Temporal Dynamics of Bose-Condensed Gases

Dissertation
zur
Erlangung des Doktorgrades (Dr. rer. nat.)
der
Mathematisch-Naturwissenschaftlichen Fakultät
der
Rheinischen Friedrich-Wilhelms-Universität Bonn

von
Mauricio Trujillo Martínez
aus
Medellín, Kolumbien

Bonn 2014

Dieser Forschungsbericht wurde als Dissertation von der
Mathematisch-Naturwissenschaftlichen Fakultät der Universität Bonn angenommen und ist
auf dem Hochschulschriftenserver der ULB Bonn
`http://hss.ulb.uni-bonn.de/diss_online` elektronisch publiziert.

1. Gutachter:	Prof. Dr. Johann Kroha
2. Gutachterin:	Prof. Dr. Corinna Kollath
Tag der Promotion:	19.03.2014
Erscheinungsjahr:	2014

Contents

Abstract

We perform a detailed quantum dynamical study of non-equilibrium trapped, interacting Bose-condensed gases. We investigate Josephson oscillations between interacting Bose-Einstein condensates confined in a finite size double-well trap and the non-trivial time evolution of a coherent state placed at the center of a two dimensional optical lattice. For the Josephson oscillations three time scales appear. We find that Josephson junction can sustain multiple undamped oscillations up to a characteristic time scale τ_c without exciting atoms out of the condensates. Beyond the characteristic time scale τ_c the dynamics of the junction are governed by fast, non-condensed particles assisted Josephson tunnelling as well as the collisions between non-condensed particles. In the non-condensed particles dominated regime we observe strong damping of the oscillations due to inelastic collisions, equilibrating the system leading to an effective loss of details of the initial conditions. In addition, we predict that an initially self-trapped BEC state will be destroyed by these fast dynamics. The time evolution of a coherent state released at the center of a two dimensional optical lattice shows a ballistic expansion with a decreasing expansion velocity for increasing two-body interactions strength and particle number. Additionally, we predict that if the two-body interactions strength exceeds a certain value, a forerunner splits up from the expanding coherent state. We also observe that this system, which is prepared far from equilibrium, can evolve to a quasistationary non-equilibrium state.

CHAPTER 1

Introduction

The concept of a Bose-Einstein-Condensate (BEC) dates back to 1925 when A. Einstein predicted a temperature driven phase transition in a gas of non-interacting bosons [1]. Einstein's work was based on a paper by the indian physicist S. N. Bose [2], which was devoted to the quantum statistical description of light. The phase transition is characterized by a macroscopic number occupying the lowest energy state. The atoms in this quantum coherent state have the same phase and can be described by a single, macroscopic wave function. Below the transition temperature, the thermal de Broglie wavelength of the atoms becomes comparable or even larger than the average distance between the atoms. Consequently, the individual wave functions of the atoms overlap and the gas has to be treated as a highly correlated quantum gas. The macroscopic wave function, which describes the BEC, can be thought of as the order parameter of this phase transition.

Due to experimental difficulties, it took about seven decades to verify Einstein's prediction. The first attempts to realize a BEC were in the early 1970s. Those involved techniques based on magnetic and optical trapping as well as cooling mechanisms. These first studies were focused on the spin polarized hydrogen, since it appeared to be the most obvious candidate because of its light mass. The experiments on hydrogen atoms were unsuccessful due to the high rate of recombination of the individual atoms to molecules [3, 4]. Later, advances using techniques based on lasers such as laser cooling and magneto-optical trapping, made it possible to cool alkali atoms to very low temperatures because of their favorable internal energy level structure. Once the atomic gas is trapped, the temperature can continue to be lowered by evaporative cooling [5, 6]. Naively, one would expect that the equilibrium configuration of the system produced in this manner could be a solid phase. In order to observe BEC, one has to maintain the system in a metastable gas phase for a sufficiently long time. An additional requirement is that the gas should be dilute enough, since three-body collisions could lead to a transition into a solid or molecular phase. All these complications were successfully overcome by Cornell and Wieman [5] and Ketterle [6] in 1995. They reported the experimental realization of a BEC of Rubidium atoms, which were cooled down to 170 nK in an atomic trap. They were awarded the Nobel prize for this work in 2001.

Since the early days, the experimental and theoretical research on this unique phenomenon has involved different areas of physics. Immediately after the discovery of superfluidity in ^{4}He in 1938 [7, 8], F. London had the intuition that it could be a manifestation of Bose-Einstein condensation [9]. In particular, the experimental achievement of a BEC was very exciting for con-

densed matter physicists. In the 1950s and 1960s, Bose-Einstein condensation was extensively studied for a weakly interacting uniform Bose gas in the context of many-body calculations as a possible model for the superfluid behavior in liquid Helium. Although theoretical approaches, which assume weak interactions in the bosonic gas are not applicable to the strongly interacting liquid Helium, these studies played an important role in the development of the theoretical framework for describing Bose superfluids. Landau proposed a phenomenological theory of superfluids in terms of the spectrum of elementary excitations of the fluid [10]. However, he argued that Bose statistics obeyed by the ^{4}He atoms were irrelevant and that his theory could be applied to any low temperature quantum liquid. For this reason, the role of Bose-Einstein condensation as the underlying basis for superfluid phenomena remained controversial for many years [11]. Later, the two-fluid hydrodynamic description formulated by Landau was proven to be related to the thermodynamic Green's function formulation of the many-body problem [12].

One of the key features of experimentally realized BECs is that they are inhomogenous finite-size systems, with fixed number of particles ranging from a few thousands to millions. The inhomogeneity arises as a consequence of the external trapping potential that confines the atoms in coordinate space. In addition, a trapped atomic gas can be regarded (in a very good approximation) as being completely isolated. These features open new possibilities for interesting studies from the experimental and theoretical point of view. They allow the systematic study of physical quantities and new phenomena which have not been accessible before, e.g. temperature dependence of the condensate, energy and density distribution, interference phenomena, etc.

Since the experimental achievement of a BEC in 1996 [5, 6], a new branch of physics has been opened. It is devoted to the study of coherence effects and fluctuation phenomena in many-body systems. There has been a huge grow in literature on the theory of Bose-Einstein condensation since then, addressing a variety of questions. Some of these questions have been answered in an extensive way. In particular, the mean field description has positioned itself as a well established theory able to provide a satisfying description of many physical phenomena exhibited by cold bosonic gases. The mean field theory is expressed in terms of a non-linear partial-differential equation for the order parameter (Gross-Pitaevskii equation). Its solutions allow the study of a diversity of physical effects such as vortices [13], solitons [14], interference [15], etc. However, experiments have achieved regimes where the standard mean field description is not applicable, revealing an incomplete understanding of the dynamics [16]. In addition, the experimental realization of colliding and collapsing condensates has attracted a lot of interest. A detailed description of the temporal dynamics of these non-equilibrium situations requires a new, different approach.

In this thesis we present a non-equilibrium field theoretical approach to situations involving inhomogeneous, weakly interacting Bose-condensed gases out of equilibrium. This theoretical description is based on the generalization of the Keldysh technique to interacting Bose gases at low temperatures and allows to treat the single particle excitations and the condensate separately. The non-equilibrium theory is expressed in terms of integro-partial-differential equations for the single particle excitations Green's function and for the order parameter. The two-particle processes described by these equations are contained in the self-energies, which are obtained from conserving approximations. The numerical analysis of this type of equations is very demanding and time consuming. This restricts their analysis to small systems and to short evolution times. The first step beyond the mean field description is the Bogoliubov-Hartree-Fock approximation. In this approximation quantum fluctuations are included and only the processes to the first order in the interatomic interaction are take into account, so

that the equations of motion reduce to system of coupled partial-differential equations for the quantum fluctuations propagator and for the order parameter. This approximation neglects multiple scatterings and is only suitable for the study of short time dynamics and weak interaction strengths. However, we have applied this approximation to various systems and have discovered very interesting effects, which are confirmed by the short time dynamics obtained from the full second-order approximation. In spite of the predicting power of the Bogoliubov-Hartree-Fock approximation, it does not take the correlations between the initial state and the intermediate states into account. In order to include these "memory effects", we take second order processes in the two-particle interactions into account. In doing so, we expect an effective loss of the initial conditions, and eventually the observation of thermalization.

In chapter 2 we review the non-equilibrium field theory formulation based on the Keldysh technique. In the subsequent chapter, this theory is generalized for Bose-condensed gases. We also discuss the conserving approximations and the self-energies derived from them. We explain how the Gross-Pitaevskii equation is obtained from the mean-field approximation and derive the equations of motion for an inhomogeneous Bose-condensed gas in a non-equilibrium situation within the framework of the Bogoliubov-Hartree-Fock approximation and the full second-order approximation. At the end of the chapter we will show how this description is connected to the semi-classical quantum Boltzmann equation.

Having the theoretical tools needed to study the temporal dynamics of a Bose-condensed gas out of equilibrium, we proceed to study non-equilibrium oscillations between two BECs. In chapter 4, we first review the mean-field description for the tunneling of particles between the condensates. The experimental realization of the Josephson junction is a non-equilibrium situation. This requires a detailed study of the temporal dynamics, including the interatomic interactions as well as the single particle excitations. In order to do so, we introduce a model which takes all these effects into account. The numerical analysis of this model within the Bogoliubov-Hartree-Fock approximation reveals the existence of a time scale at which the system undergoes a transition to a regime dominated by fast dynamics. A systematic study of this time scale depending on the system parameters is performed. Afterwards, possible mechanism of thermalization and equilibration are discussed using the full second-order approximation.

In chapter 5 we introduce the Bose-Hubbard model and some of its aspects in the case of thermodynamic equilibrium. The model is used to study cold atoms of bosonic nature placed on an optical lattice. The underlying equations of motion are derived within Bogoliubov-Hartree-Fock approximation and full second-order approximation. As a first exercise, we solve the two-site Bose-Hubbard model with the same initial conditions as the Josephson junction in chapter 4. Afterwards, we consider a coherent state released in the center of a 2-dimensional lattice. Similar systems were considered in [17, 18] for one dimension and in [19] for two dimensions.

CHAPTER 2

Non-Equilibrium Field Theory

Before we proceed to develop a theory for bosonic gases at low temperatures out of equilibrium, we first have to study how non-equilibrium situations in quantum system can be treated. In the present chapter, we will introduce the Keldysh technique, which was introduced by P. C Martin and J. Schwinger [20], J. Schwinger [21] and L. V. Keldysh [22]. Further contributions to the theory were made by Kadanoff and Baym [23–25]. A detailed review of the method can be found in [26, 27]. In this chapter we will follow closely the review provided in [26, 28].

2.1 The Closed Time Path

The standard construction of the equilibrium many-body theory (see e.g., [29–31]) involves switching "on" the interactions adiabatically in the distant past, and "off" in the distant future. The crucial assumption in this case is that starting from the ground (or equilibrium) state of the system at $t = -\infty$ one reaches the same state at $t = +\infty$ (up to some phase that was acquired along the way).

This is not necessarily the case for a non-equilibrium situation. In general one starts with an arbitrary initial state, then switches on the interactions and after a while turns them off. There is no warranty that the system will evolve into the state it was in prior the switching on of the interactions, i.e. the final state will depend on the switching procedure. The lack of knowledge about the final state spoils completely the field theoretical formulation, since the physical observables are described in terms of averages (or traces) of physical operators. In order to overcome this difficulty, one needs to find a field theoretical formulation that avoids the reference to the final state at $t = \infty$. Nonetheless, one still has to compute averages and therefore, knowledge about the final state is still needed. J. Schwinger suggested to take the final state to be the initial one, which would allow to compute averages (or traces) of products of operators associated to the physical observables. This approach is based on the idea of letting the quantum system evolve forward in time and then rewind its evolution back in time. At the end, one has to construct a field theory with the time evolution along the two-branch contour C, depicted in fig. 2.1.

In other words, independently of the final state at $t = +\infty$, the system will evolve backwards to the known initial state at $t = -\infty$. In this construction there is no switching off of the interactions in the far future, instead the interactions are switched on in the upper branch

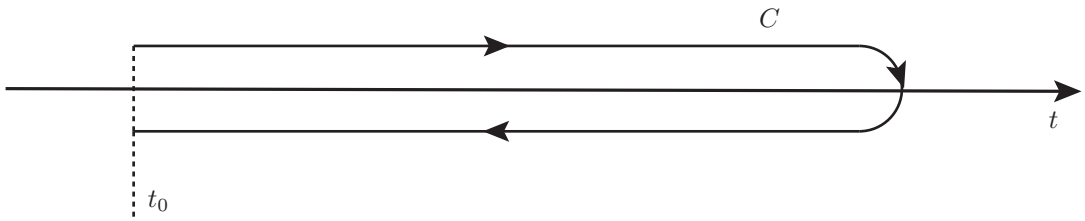

Figure 2.1: The closed time path contour C.

of the contour, which evolves forward in times, and off in the lower branch, which evolves backwards.

Now we proceed to construct a theory along the closed time path contour (CTP). With this aim, let us consider a quantum system at thermal equilibrium, which is described by the time independent Hamiltonian $\hat{H}$. The non-equilibrium problem can be formulated as follows: For times far in the past and prior an arbitrary time $t = t_0$ the system is assumed to be in equilibrium and described by $\hat{H}$. Then, at $t = t_0$ a time-dependent mechanical perturbation, associated to $\hat{H}'(t)$, is turned on, and the Hamiltonian describing the full time dependent problem becomes

$$\hat{\mathcal{H}}(t) = \hat{H} + \hat{H}'(t). \tag{2.1}$$

The non-equilibrium theory concerns the computation of statistical averages of operator products related to physical quantities for times $t > t_0$. The time evolution of an operator in the situation described above is given in terms of the unitary transformations related to Heisenberg pictures of the Hamiltonian $\hat{\mathcal{H}}(t)$ and $\hat{H}$:

$$\hat{O}_{\mathcal{H}}(t) = \hat{U}(t,t_0)^\dagger \hat{O}_S(t_0)\hat{U}(t,t_0), \qquad \hat{U}(t,t_0) = T\, e^{-i\int_{t_0}^{t} \mathrm{d}\bar{t}\, \hat{\mathcal{H}}(\bar{t})}, \tag{2.2}$$

and

$$\hat{O}_H(t) = e^{i\hat{H}(t-t_0)}\hat{O}_S(t_0)e^{-i\hat{H}(t-t_0)}, \tag{2.3}$$

where T is the time ordering operator. Here $\hat{O}_S$ is the operator in the Schrödinger picture.

Now, solving eq. 2.3 for $\hat{O}_S$ and then inserting into eq. 2.2 we obtain

$$\begin{aligned} \hat{O}_{\mathcal{H}}(t) &= \hat{U}(t,t_0)^\dagger e^{-i\hat{H}(t-t_0)}\hat{O}_H(t)e^{i\hat{H}(t-t_0)}\hat{U}(t,t_0) \\ &= \left[T\, e^{i\int_{t_0}^{t} \mathrm{d}\bar{t}\, \hat{H}'_H(\bar{t})}\right] \hat{O}_H(t) \left[T\, e^{-i\int_{t_0}^{t} \mathrm{d}\bar{t}\, \hat{H}'_H(\bar{t})}\right]. \end{aligned} \tag{2.4}$$

In other words, the interaction picture with respect to $\mathcal{H}$ is equivalent to the Heisenberg picture with respect to H.

Now we proceed to show how the transformation between the two Heisenberg pictures $\mathcal{H}$ and H can be expressed in terms of the CTP. The fact, that all times t occur later that the reference time t_0, permits us to parametrize as follows

$$T_{\overrightarrow{C}}\, e^{-i\int_{\overrightarrow{C}} \mathrm{d}\tau\, \hat{H}'_H(\tau)} = T\, e^{-i\int_{t_0}^{t} \mathrm{d}\bar{t}\, \hat{H}'_H(\bar{t})}, \tag{2.5}$$

$$T_{\overleftarrow{C}}\, e^{-i\int_{\overleftarrow{C}} \mathrm{d}\tau\, \hat{H}'_H(\tau)} = \tilde{T}\, e^{-i\int_{t}^{t_0} \mathrm{d}\bar{t}\, \hat{H}'_H(\bar{t})}, \tag{2.6}$$

where $\tau(\bar{t}) = \bar{t}$, $\bar{t} \in [t_0, t]$ and $\tilde{T}$ is the anti-time ordering operator, that rearranges all operators with arguments referring to earlier times to the left, in contrast to the time ordering operator T, which arranges them in the opposite order.

Inserting eq. 2.5 and 2.6 into eq. 2.4 and using the Cauchy product and the Binomial theorem, we can write

$$\begin{aligned}
\hat{O}_{\mathcal{H}}(t) &= \left[T_{\overleftarrow{C}}\, e^{-i\int_{\overleftarrow{C}} \mathrm{d}\tau\, \hat{H}'_H(\tau)}\right] \hat{O}_H(t) \left[T_{\overrightarrow{C}}\, e^{-i\int_{\overrightarrow{C}} \mathrm{d}\tau\, \hat{H}'_H(\tau)}\right] \\
&= \left(\sum_{k=0}^{\infty} \frac{(-i)^k}{k!} \int_{\overleftarrow{C}} \mathrm{d}\tau\, T_{\overleftarrow{C}} \left[H'_H(\tau_1) \dots H'_H(\tau_k)\right]\right) O_H(t) \\
&\quad \times \left(\sum_{m=0}^{\infty} \frac{(-i)^m}{m!} \int_{\overrightarrow{C}} \mathrm{d}\tau\, T_{\overrightarrow{C}} \left[H'_H(\tau_1) \dots H'_H(\tau_m)\right]\right) \\
&= \sum_{k=0}^{\infty} \sum_{m=0}^{k} \left(\frac{(-i)^m}{m!} \frac{(-i)^{k-m}}{(k-m)!} \int_{\overleftarrow{C}} \mathrm{d}\tau\, T_{\overleftarrow{C}} \left[H'_H(\tau_1) \dots H'_H(\tau_m)\right] \hat{O}_H(t)\right. \\
&\quad \left. \times \int_{\overrightarrow{C}} \mathrm{d}\tau\, T_{\overrightarrow{C}} \left[H'_H(\tau_1) \dots H'_H(\tau_{k-m})\right]\right) \\
&= \sum_{k=0}^{\infty} \frac{(-i)^k}{k!} \sum_{m=0}^{k} \binom{k}{m} \int_{\overleftarrow{C}} \mathrm{d}\tau\, T_{\overleftarrow{C}} \left[H'_H(\tau_1) \dots H'_H(\tau_k)\right] \hat{O}_H(t) \\
&\quad \times \int_{\overrightarrow{C}} \mathrm{d}\tau\, T_{\overrightarrow{C}} \left[H'_H(\tau_1) \dots H'_H(\tau_{k-m})\right] \\
&= \sum_{k=0}^{\infty} \frac{(-i)^k}{k!} \int_{\overrightarrow{C}+\overleftarrow{C}} \mathrm{d}\tau\, T_{\overrightarrow{C}+\overleftarrow{C}} \left[H'_H(\tau_1) \dots H'_H(\tau_k) O_H(t)\right]. \qquad (2.7)
\end{aligned}$$

$T_{\overrightarrow{C}+\overleftarrow{C}}$ is the time-ordering operator along the contour $\overrightarrow{C} + \overleftarrow{C}$. In the last equality, we joint the forward and the backward contours, in order to obtain the closed time path $C = \overrightarrow{C} + \overleftarrow{C}$. This yields the expression

$$\hat{O}_{\mathcal{H}}(t) = T_C \left[e^{-i\int_C \mathrm{d}\tau\, \hat{H}'_H(\tau)} O_H(t)\right], \qquad (2.8)$$

which is equivalent to eq. 2.4. In the following we will see that the time-ordering operator T_c is a key tool in order to study non-equilibrium situations, as it will allow us to formulate a theory that resides on the CTP.

While constructing a theory along the CTP, we have to consider Green's functions because they allow us to calculate physical quantities. We start by introducing the "lesser" and "greater" Green's functions:

$$G^{<}(1,1') = \mp i \langle \hat{\Psi}^{\dagger}_{\mathcal{H}}(1') \hat{\Psi}_{\mathcal{H}}(1) \rangle, \qquad (2.9)$$

$$G^{>}(1,1') = \quad i \langle \hat{\Psi}_{\mathcal{H}}(1) \hat{\Psi}^{\dagger}_{\mathcal{H}}(1') \rangle, \qquad (2.10)$$

where the minus(plus) sign refers to the Bose(Fermi) statistics. $\hat{\Psi}_{\mathcal{H}}$ and $\hat{\Psi}^{\dagger}_{\mathcal{H}}$ are the field operators in the Heisenberg picture of the Hamiltonian $\hat{\mathcal{H}}$ and the short hand notation $1 \equiv (\mathbf{r}_1, t_1)$ and $1' \equiv (\mathbf{r}_{1'}, t_{1'})$ is being used. It is noteworthy that it is possible to express the average probability density of the particle species described by the field $\hat{\Psi}$ in terms of the lesser

Green's function, i.e., $n(1) = \pm iG^<(1,1)$. Other physical quantities, such as the particle current and the energy density, can be expressed in terms of the lesser Green's function, as well.

Now, we define the closed time path Green's function

$$G(1,1') = -i\langle T_C \left[\hat{\Psi}_{\mathcal{H}}(1)\hat{\Psi}^\dagger_{\mathcal{H}}(1')\right]\rangle, \tag{2.11}$$

which plays an analogous role in the non-equilibrium formalism as the causal Green's function plays in the equilibrium theory. As we will discuss below, it also can be studied by the means of perturbation theory using Wick's theorem. The difficulty now resides on the fact that time labels not only lie on a forward, but also on the backwards propagating time contour. This results in a doubling of the degrees of freedom. Proper treatment of the two time labels yields four different functions:

$$G(1,1') = \begin{cases} G_{\overrightarrow{C}}(1,1'), & t_1, t_{1'} \in \overrightarrow{C} \\ G^>(1,1') & t_1 \in \overleftarrow{C},\, t_{1'} \in \overrightarrow{C} \\ G^<(1,1') & t_1 \in \overrightarrow{C},\, t_{1'} \in \overleftarrow{C} \\ G_{\overleftarrow{C}}(1,1'), & t_1, t_{1'} \in \overleftarrow{C} \end{cases}. \tag{2.12}$$

Here, we introduced the "casual" or time-ordered Green's function $G_{\overrightarrow{C}}$,

$$G_{\overrightarrow{C}}(1,1') = -i\langle T \left[\hat{\Psi}_{\mathcal{H}}(1)\hat{\Psi}^\dagger_{\mathcal{H}}(1')\right]\rangle,$$

and the anti-time-ordered Green's function,

$$G_{\overleftarrow{C}}(1,1') = -i\langle \tilde{T} \left[\hat{\Psi}_{\mathcal{H}}(1)\hat{\Psi}^\dagger_{\mathcal{H}}(1')\right]\rangle.$$

The "lesser" and "greater" were already defined in eq. 2.9 and 2.10.

Since $G_{\overrightarrow{C}} + G_{\overleftarrow{C}} = G^> + G^<$, there are only three linearly independent functions, making one of the four Green's functions redundant. There exists a variety of representations in the literature, which are all similar to each other[1], but for our discussion below and in the upcoming chapters, we will keep using $G^\gtrless$ and will define the advanced and retarded Green's functions as

$$G^{\mathrm{adv}} = -\theta(t_{1'} - t_1)\left[G^>(1,1') - G^<(1,1')\right], \tag{2.13}$$
$$G^{\mathrm{ret}} = \quad \theta(t_1 - t_{1'})\left[G^>(1,1') - G^<(1,1')\right], \tag{2.14}$$

where θ is the Heaviside step function. In this representation we observe that $G^{\mathrm{ret}} - G^{\mathrm{adv}} = G^> - G^<$. As a side remark, we want to mention that the lesser-greater formulation is very advantageous and widely used on strongly correlated electron systems at non-equilibrium when using the non-crossing approximation [32, 33].

After all these definitions, we return to the closed time path Green's function. We need to find a more tractable way to deal with eq. 2.11, and transform it, such that Wick's theorem can be used. The first step towards this aim is to perform a similar analysis to the one done in order to derive the relation between the closed time contour and the two Heisenberg pictures

[1] One can introduce a 2×2-matrix representation of the closed contour Green's function. Using similarity transformations one can find various types of representations.

for $\mathcal{H}$ and H. Inserting eq. 2.8 into eq. 2.11 yields

$$\begin{aligned} G(1,1') &= -i\langle T_{C_1}\left[e^{-i\int_{C_1}\mathrm{d}\tau\,\hat{H}'_H(\tau)}\hat{\Psi}_H(1)\right]T_{C_{1'}}\left[e^{-i\int_{C_{1'}}\mathrm{d}\tau\,\hat{H}'_H(\tau)}\hat{\Psi}^\dagger_H(1')\right]\rangle, \\ &= -i\langle T_{C_1+C_{1'}}\left[e^{-i\int_{C_1+C_{1'}}\mathrm{d}\tau\,\hat{H}'_H(\tau)}\hat{\Psi}_H(1)\hat{\Psi}^\dagger_H(1')\right]\rangle \\ &= -i\langle T_C\left[e^{-i\int_C\mathrm{d}\tau\,\hat{H}'_H(\tau)}\hat{\Psi}_H(1)\hat{\Psi}^\dagger_H(1')\right]\rangle, \end{aligned} \tag{2.15}$$

where the contour $C_1(C_{1'})$ starts at t_0, propagates forward in time, passes through $t_1(t_{1'})$, and returns to t_0. In the last equality we introduced the combined contour $C = C_1 + C_{1'}$, which starts at t_0, stretches till $\max(t_1, t_{1'})$ (or all the way to $+\infty$), and goes back again to t_0.

In order to obtain the perturbation theory expressions for the contour-ordered Green's functions, we need to performe one additional transformation. Recall that the Hamiltonian $\hat{H} = \hat{H}_0 + \hat{H}_\mathrm{i}$ consists of a term quadratic in the fields, $\hat{H}_0$, which describes the non-interacting particles, and a complicated term $\hat{H}_\mathrm{i}$, describing the interactions. However, Wick's theorem only works for $\hat{H}_0$ (i.e., quadratic Hamiltonians). After carrying out the transformation, the contour-ordered Green's function reads

$$G(1,1') = -i\langle T_C\left[e^{-i\int_C\mathrm{d}\tau\left[\hat{H}^\mathrm{i}_{H_0}(\tau)+\hat{H}'_{H_0}(\tau)\right]}\hat{\Psi}_{H_0}(1)\hat{\Psi}^\dagger_{H_0}(1')\right]\rangle. \tag{2.16}$$

This is an important result, since it is exact. The fact that the field operators appear in terms of the quadratic Hamiltonian allows us to use Wick's theorem and in particular to construct Feynman diagrams for the non-equilibrium problem.

Comparing eq. 2.16 with its equilibrium field theory analog, we observe the absence of the expectation value $\langle T_C\left[e^{-i\int_C\mathrm{d}\tau\left[\hat{H}^\mathrm{i}_{H_0}(\tau)+\hat{H}'_{H_0}(\tau)\right]}\right]\rangle$ in the denominator. This suggest that the non-equilibrium perturbation theory has a simpler structure than standard equilibrium theory, since there is no need for canceling unlinked or disconnected diagrams

Finally, it is worth mentioning that the equilibrium and non-equilibrium theory are structurally equivalent. Their only difference resides on the time integration, which is carried out along the real time axis in the equilibrium case and along the closed time contour in the non-equilibrium case.

2.2 Real-Time Formalism

In spite of the fact, that eq. 2.16 is an exact result and it is possible to compute it perturbatively, like in the equilibrium case, it lacks physical transparency. For this reason, our approach requires a way to bring back all the quantities to "real time". In the literature one can find many different formulations. For a review see [27] and the referred literature therein. Here, we will follow the analytical continuation procedure, which in the literature is also referred to as the "Langereth rules" (see [34]).

In the previous section we discussed that the contour-ordered Green's function has the same perturbative expansion as the corresponding time-ordered Green's function. Hence, provided that we can define a self-energy $\Sigma[G]$ that contains the interactions between particles, the

contour-ordered Green's function will satisfy the non-equilibrium Dyson equation

$$G(1,1') = G_0(1,1') + \int_C \mathrm{d}2\, G_0(1,2)U(2)G(2,1') + \int_C \mathrm{d}2 \int_C \mathrm{d}3\, G_0(1,2)\Sigma(2,3)G(3,1'), \quad (2.17)$$

where we assumed, that the non-equilibrium external force can be represented as a one-body potential. Here $\int_C \mathrm{d}2 \equiv \int \mathrm{d}\mathbf{r}_2 \int_C \mathrm{d}t_2$, and the subscript C refers to the time integration along the CTP.

An alternative formulation of eq. 2.17 is the equation of motion for the Green's function, which can be derived by the means of the Heisenberg equation of motion for the field operators. Making use of conserving approximations, which will be discussed in the next chapter in the context of Bose-condensed gases, we can replace the many-particle correlation function on the right hand side by a convolution of the self-energy and the one-particle Green's function. Thus,

$$\left[i\frac{\partial}{\partial t_1} + \frac{\boldsymbol{\nabla}_1^2}{2m} - V_{\mathrm{trap}}(\mathbf{r}_1) - U(1) \right] G(1,1') = \delta_C(1-1') + \int_C \mathrm{d}2\, \Sigma(1,2)G(2,1'), \quad (2.18)$$

where $H_0 = -\boldsymbol{\nabla}^2/2m + V_{\mathrm{trap}}$ is the non-interacting a Hamiltonian, and V_{trap} is a time independent trapping potential. While deriving the equation of motion, we have to take into account the four different cases originating from the proper treatment of the time arguments of the field operators. This results in the modified delta distribution

$$\delta_C(1-1') = \delta(\mathbf{r}_1 - \mathbf{r}_{1'}) \cdot \begin{cases} \delta(t_1 - t_{1'}), & t_1, t_{1'} \in \overrightarrow{C} \\ -\delta(t_1 - t_{1'}), & t_1, t_{1'} \in \overleftarrow{C} \\ 0, & \text{else} \end{cases}, \quad (2.19)$$

with $\overrightarrow{C}(\overleftarrow{C})$ being the forward(backwards) evolving branch of the closed contour.

An alternative way to obtain eq. 2.18 is to multiply eq. 2.17 by $G_0^{-1}(\bar{1},1)$, then integrate over "1", and use $\int_C \mathrm{d}1\, G_0^{-1}(\bar{1},1)G_0(1,1') = \delta_C(\bar{1}-1')$.

If we are not interested in the initial correlations, we can set $t_0 \to -\infty$, and end up with the contour C_{K}, which was introduced by Keldysh (1964). The contour C_{K}, depicted in fig. 2.2, consists of two branches: one extending from $-\infty$ to ∞ and one from ∞ to $-\infty$. The information lost by this procedure is related to the initial correlations.

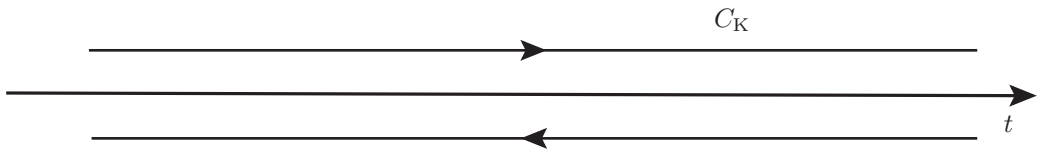

Figure 2.2: The Keldysh closed time path or real-time closed contour.

In the following chapters we will consider various non-equilibrium setups, which we will study by the means of the equation of motion for the Green's function. Evaluating eq. 2.18 we encounter terms with the structure $C = A \otimes B$, or more explicitly

$$C(t_1, t_{1'}) = \int_{C_{\mathrm{K}}} \mathrm{d}\tau\, A(t_1,\tau)B(\tau,t_{1'}) \quad (2.20)$$

and their generalizations involving convolutions of three or even more correlators. For simplicity, we will exclude the spacial dependence in following analysis, since we are presently concerned with the temporal dynamics.

Now let us assume that in eq. 2.20 t_1 is on the upper(lower) branch of the Keldysh contour $C_{\rm K}$ and $t_{1'}$ resides on the lower(upper) branch. This means that we are analyzing the "lesser"("greater") function of C. As it is explained in Appendix A, after the deformation of the integration contour $C_{\rm K}$, one obtains

$$C^{\lessgtr}(t_1,t_{1'}) = \int_{-\infty}^{\infty} \mathrm{d}t \, \left[A^{\rm ret}(t_1,t)B^{\lessgtr}(t,t_{1'}) + A^{\lessgtr}(t_1,t)B^{\rm adv}(t,t_{1'})\right]. \tag{2.21}$$

Notice, that we use greek letters for the integration variable along the closed contour and latin letters for the real time integration. We will keep this notation for the rest of this section.

Apart from the lesser/greater components, one often needs the retarded and advanced component of the convolution of two functions defined on the Keldysh contour. The required expression is obtained by using the definitions 2.13 and 2.14, and the result 2.21, and reads

$$C^{\rm adv/ret}(t_1,t_{1'}) = \int_{-\infty}^{\infty} \mathrm{d}t \, A^{\rm adv/ret}(t_1,t)B^{\rm adv/ret}(t,t_{1'}). \tag{2.22}$$

While considering various terms in the diagrammatic expansion, one may come across terms where two propagator lines run anti(parallel). In this case we have to compute the lesser/greater and the advanced/retarded components of the structures

$$D(\tau,\tau') = \quad A(\tau,\tau')B(\tau,\tau') \tag{2.23}$$
$$E(\tau,\tau') = \quad A(\tau,\tau')B(\tau',\tau), \tag{2.24}$$

where τ and τ' are contour variables. The derivation for the lesser/greater and advanced/retarded expressions is similar to the analysis done for the convolution 2.20. In table 2.1, we give the results for these expressions together with other "Langereth rules".

Using eq. 2.21 and 2.22, we can compute the equations of motion for the lesser/greater Green's functions

$$\left[i\frac{\partial}{\partial t_1} + \frac{\boldsymbol{\nabla}_1^2}{2m} - V_{\rm trap}(\mathbf{r}_1) - U(1)\right] G^{\lessgtr}(1,1') = \int_{-\infty}^{\infty} \mathrm{d}2 \, \left[\Sigma^{\rm ret}(1,2)G^{\lessgtr}(2,1') + \Sigma^{\lessgtr}(1,2)G^{\rm adv}(2,1')\right], \tag{2.25}$$

and for the retarded Green's function

$$\left[i\frac{\partial}{\partial t_1} + \frac{\boldsymbol{\nabla}_1^2}{2m} - V_{\rm trap}(\mathbf{r}_1) - U(1)\right] G^{\rm adv/ret}(1,1') = \delta(1-1') + \int_{-\infty}^{\infty} \mathrm{d}2 \, \Sigma^{\rm adv/ret}(1,2)G^{\rm adv/ret}(2,1'). \tag{2.26}$$

Eq. 2.25 and 2.26 form a set of closed integro-partial-differential-equations (IPDE), and are the main tool we will later apply to a variety non-equilibrium situations.

Contour	Real Time
$C = \int_C AB$	$C^{\lessgtr} = \int_t \left[A^{\lessgtr} B^{\mathrm{adv}} + A^{\mathrm{ret}} B^{\lessgtr} \right]$ $G^{\mathrm{ret}} = \int_t A^{\mathrm{ret}} B^{\mathrm{ret}}$
$D = \int_C ABC$	$D^{\lessgtr} = \int_t \left[A^{\mathrm{ret}} B^{\mathrm{ret}} C^{\lessgtr} + A^{\mathrm{ret}} B^{\lessgtr} C^{\mathrm{adv}} + A^{\lessgtr} B^{\mathrm{adv}} C^{\mathrm{adv}} \right]$ $D^{\mathrm{ret}} = \int_t A^{\mathrm{ret}} B^{\mathrm{ret}} C^{\mathrm{ret}}$
$D(\tau, \tau') = A(\tau, \tau') B(\tau, \tau')$	$D^{\lessgtr}(t, t') = A^{\lessgtr}(t, t') B^{\lessgtr}(t, t')$ $D^{\mathrm{ret}}(t, t') = A^{<}(t, t') B^{\mathrm{ret}}(t, t') + A^{\mathrm{ret}}(t, t') B^{<}(t, t') + A^{\mathrm{ret}}(t, t') B^{\mathrm{ret}}(t, t')$
$E(\tau, \tau') = A(\tau, \tau') B(\tau', \tau)$	$E^{\lessgtr}(t, t') = A^{\lessgtr}(t, t') B^{\gtrless}(t, t')$ $E^{\mathrm{ret}}(t, t') = A^{<}(t, t') B^{\mathrm{adv}}(t', t) + A^{\mathrm{ret}}(t, t') B^{<}(t', t)$

Table 2.1: Langereth rules.

CHAPTER 3

Non-Equilibrium Theory of a Bose Gas at Low Temperatures

In this chapter we consider a bosonic gas at low temperature, which is subject to a time-dependent trapping potential. In order to describe the dynamics of such a system, we will make use of the Keldysh formalism, which was presented in chapter 2 and has proven to be a useful approach to study non-equilibrium situations. After deriving the general set of equations of motion describing such a system, we will discuss the conserving approximations, which will provide a tractable way of dealing with the infinite hierarchy of correlators involved in the equations of motion. Towards the end of this chapter, we will introduce further approximations based on physical reasoning in order to make a connection between the general equations of motion describing a Bose-condensed gas and the Boltzmann-like equation derived by Griffin et al [35, 36].

3.1 The Kinetic Equations

A system of weakly interacting atoms of bosonic nature, which are subject to a trapping potential, is most generally described by the Hamiltonian

$$\hat{H} = \int \mathrm{d}\mathbf{r}\, \hat{\Psi}^\dagger(\mathbf{r},t) \left(-\frac{1}{2m}\boldsymbol{\nabla}^2 + V_{\mathrm{ext}}(\mathbf{r},t) \right) \hat{\Psi}(\mathbf{r},t) + \frac{g}{2} \int \mathrm{d}\mathbf{r}\, \hat{\Psi}^\dagger(\mathbf{r},t)\hat{\Psi}^\dagger(\mathbf{r},t)\hat{\Psi}(\mathbf{r},t)\hat{\Psi}(\mathbf{r},t), \quad (3.1)$$

where $\hat{\Psi}(\mathbf{r},t)$ is a bosonic field operator and V_{ext} the time-dependent trapping potential. Additionally, we have assumed a contact interaction between the bosons with $g = 4\pi a_s/m$ (a_s is the s-wave scattering length).

At low temperatures most of the bosons occupy the lowest state of energy. As a consequence, averages of normal products of the bosonic field operator $\hat{\Psi}(\mathbf{r},t)$ are not only non-vanishing, but can actually be arbitrarily large, and this should be taken into account when constructing a field theoretical approach. Therefore, the generalization of the methods of quantum field theory to the case of a system of interacting bosons at temperatures below the temperature of Bose-Einstein condensation contains large difficulties. Nevertheless, the appropriate formalism for equilibrium situations has been developed by S. T. Beliaev [37].

The treatment of non-equilibrium dynamics of a Bose-condensed gas involves the formalism

developed by Beliaev and the Schwinger-Keldysh close-time path formalism (see chapter 2). A detailed review on this approach can be found in [38] and we will follow it in this chapter.

We start by denoting the mean field or the expectation value of the operator by $\Psi_0(\mathbf{r},t) = \langle\hat{\Psi}(\mathbf{r},t)\rangle$ and the fluctuation operator by $\hat{\varphi}(\mathbf{r},t) = \hat{\Psi}(\mathbf{r},t) - \Psi_0(\mathbf{r},t)$. Physically, $|\Psi_0(\mathbf{r},t)|^2$ is the condensate density at position $\mathbf{r}$ and time t. The bosonic propagator splits into $\boldsymbol{C} + \boldsymbol{G}$, where

$$\boldsymbol{C}(1,1') = -i \begin{pmatrix} \Psi_0(1)\Psi_0^*(1') & \Psi_0(1)\Psi_0(1') \\ \Psi_0^*(1)\Psi_0^*(1') & \Psi_0^*(1)\Psi_0(1') \end{pmatrix} \tag{3.2}$$

is the propagator related to the condensate fraction of the gas, and

$$\begin{aligned} \boldsymbol{G}(1,1') = &- i \begin{pmatrix} \langle T_C\hat{\varphi}(1)\hat{\varphi}^\dagger(1')\rangle & \langle T_C\hat{\varphi}(1)\hat{\varphi}(1')\rangle \\ \langle T_C\hat{\varphi}^\dagger(1)\hat{\varphi}^\dagger(1')\rangle & \langle T_C\hat{\varphi}^\dagger(1)\hat{\varphi}(1')\rangle \end{pmatrix} \\ = & \begin{pmatrix} G(1,1') & F(1,1') \\ \overline{F}(1,1') & \overline{G}(1,1') \end{pmatrix}, \end{aligned} \tag{3.3}$$

the non-condensate particle Green's function. Here we used the short hand notation $1 \equiv (\mathbf{r},t)$, $1' \equiv (\mathbf{r}',t')$, which was introduced in chapter 2, T_C denotes the time ordering along the Keldysh contour, i.e., both Green's functions G and F become 2×2 matrices in Keldysh space with their time arguments lying on the real time contour.

The associated Dyson's equations on the CTP for $\boldsymbol{C}$ and $\boldsymbol{G}$ read

$$\int_C \mathrm{d}2\, \left[\boldsymbol{G}_0^{-1}(1,2) - \boldsymbol{S}^{HF}(1,2)\right] \boldsymbol{C}(2,1') = \int_C \mathrm{d}2\, \boldsymbol{S}(1,2)\boldsymbol{C}(2,1'), \tag{3.4}$$

$$\int_C \mathrm{d}2\, \left[\boldsymbol{G}_0^{-1}(1,2) - \boldsymbol{\Sigma}^{HF}(1,2)\right] \boldsymbol{G}(2,1') = \mathbb{1}\delta_C(1-1') + \int_C \mathrm{d}2\, \boldsymbol{\Sigma}(1,2)\boldsymbol{G}(2,1'), \tag{3.5}$$

where $\int_C \mathrm{d}1 \equiv \int \mathrm{d}\mathbf{r}_1 \int_C \mathrm{d}t_1$, $\mathbb{1}$ is the 2×2 identity matrix and the subscript C denotes the time integration along the CTP. Moreover, we have decomposed the self-energies into their Hartree-Fock local parts $\boldsymbol{S}^{HF}$ and $\boldsymbol{\Sigma}^{HF}$ and their non-local part $\boldsymbol{S}$ and $\boldsymbol{\Sigma}$, respectively. The non-local parts contain the information about collisions. Here, the bare 2×2 propagator $\boldsymbol{G}_0$ is defined by

$$\boldsymbol{G}_0^{-1}(1,1') = \left[i\boldsymbol{\tau}_3\frac{\partial}{\partial t_1} - \left(-\frac{1}{2m}\boldsymbol{\nabla}_1^2 + V_{ext}(1)\right)\mathbb{1}\right]\delta(1-1'), \tag{3.6}$$

where

$$\boldsymbol{\tau}_3 = \begin{pmatrix} 1 & 0 \\ 0 & -1 \end{pmatrix}. \tag{3.7}$$

The self-energies can be obtained within the framework of conserving approximations [12, 25, 36, 38]. We will discuss the choice of the approximation in the next section, but for the moment we will keep them unspecified.

Now, making use of real-time formalism in eq. 3.4 and 3.5 we obtain

$$\int_{-\infty}^{\infty} \mathrm{d}2\, \left[\boldsymbol{G}_0^{-1}(1,2) - \boldsymbol{S}^{HF}(1,2)\right] \boldsymbol{C}(2,1') = -i\int_{-\infty}^{t_1} \mathrm{d}2\, \boldsymbol{\gamma}(1,2)\boldsymbol{C}(2,1'), \tag{3.8}$$

$$\int_{-\infty}^{\infty} \mathrm{d}2\, \left[\boldsymbol{G}_0^{-1}(1,2) - \boldsymbol{\Sigma}^{HF}(1,2)\right] \boldsymbol{G}^{\gtrless}(2,1') = -i \int_{-\infty}^{t_1} \mathrm{d}2\, \boldsymbol{\Gamma}(1,2)\boldsymbol{G}^{\gtrless}(2,1') + i \int_{-\infty}^{t_{1'}} d2\boldsymbol{\Sigma}^{\gtrless}(1,2)\boldsymbol{A}(2,1'), \tag{3.9}$$

where the time integrations now performed along the intervals specified at the boundaries. The single particle excitations spectral function $\boldsymbol{A}$ is defined as

$$\begin{aligned} \boldsymbol{A}(1,1') &= i\left[\boldsymbol{G}^{>}(1,1') - \boldsymbol{G}^{<}(1,1')\right] \\ &= \begin{pmatrix} A^{G}(1,1') & A^{F}(1,1') \\ A^{\overline{F}}(1,1') & A^{\overline{G}}(1,1') \end{pmatrix}, \end{aligned} \tag{3.10}$$

and the for the non-local self-energies given by

$$\begin{aligned} \boldsymbol{\Gamma}(1,1') &= i\left[\boldsymbol{\Sigma}^{>}(1,1') - \boldsymbol{\Sigma}^{<}(1,1')\right] \\ &= \begin{pmatrix} \Gamma^{G}(1,1') & \Gamma^{F}(1,1') \\ \Gamma^{\overline{F}}(1,1') & \Gamma^{\overline{G}}(1,1') \end{pmatrix} \end{aligned} \tag{3.11}$$

and

$$\begin{aligned} \boldsymbol{\gamma}(1,1') &= i\left[\boldsymbol{S}^{>}(1,1') - \boldsymbol{S}^{<}(1,1')\right] \\ &= \begin{pmatrix} \gamma^{G}(1,1') & \gamma^{F}(1,1') \\ \gamma^{\overline{F}}(1,1') & \gamma^{\overline{G}}(1,1') \end{pmatrix}. \end{aligned} \tag{3.12}$$

It convenient to express the evolution equation 3.9 in terms of two independent two-point functions, which can be associated to the commutator and anticommutator of the field operators $\hat{\varphi}$ and $\hat{\varphi}^{\dagger}$ [39–41]. The reason for this will become clear in section 3.5, when we explain how to treat the terms including the non-local self-energies. Now, we introduce the single particle excitations statistical function

$$\begin{aligned} \boldsymbol{F}(1,1') =& \frac{1}{2}\left[\boldsymbol{G}^{>}(1,1') + \boldsymbol{G}^{<}(1,1')\right] \\ =& \begin{pmatrix} F^{G}(1,1') & F^{F}(1,1') \\ F^{\overline{F}}(1,1') & F^{\overline{G}}(1,1') \end{pmatrix}. \end{aligned} \tag{3.13}$$

The whole evolution of the dynamics of the non-condensed particles can be encoded in the spectral function 3.10 and the statistical propagator 3.13, which contain the information about the spectrum and the occupation number, respectively. Taking the difference and sum of eq. 3.9 for the lesser ($<$) and greater ($>$) component of $\boldsymbol{G}$, we obtain the evolution equations in terms of the spectral function and statistical propagator,

$$\int_{-\infty}^{\infty} \mathrm{d}2\, \left[\boldsymbol{G}_0^{-1}(1,2) - \boldsymbol{\Sigma}^{HF}(1,2)\right] \boldsymbol{A}(2,1') = -i \int_{t_{1'}}^{t_1} \mathrm{d}2\, \boldsymbol{\Gamma}(1,2)\boldsymbol{A}(2,1'), \tag{3.14}$$

$$\int_{-\infty}^{\infty} \mathrm{d}2\, \left[\boldsymbol{G}_0^{-1}(1,2) - \boldsymbol{\Sigma}^{HF}(1,2)\right] \boldsymbol{F}(2,1') = -i \left[\int_{-\infty}^{t_1} \mathrm{d}2\, \boldsymbol{\Gamma}(1,2)\boldsymbol{F}(2,1') - \int_{-\infty}^{t_{1'}} \mathrm{d}2\, \boldsymbol{\Pi}(1,2)\boldsymbol{A}(2,1')\right], \tag{3.15}$$

where $\boldsymbol{\Pi}$ is the statistical function related to non-local self-energy and is defined as

$$\begin{aligned}\boldsymbol{\Pi}(1,1') =& \frac{1}{2}\left[\boldsymbol{\Sigma}^{>}(1,1') + \boldsymbol{\Sigma}^{<}(1,1')\right] \\ =& \begin{pmatrix} \Pi^{G}(1,1') & \Pi^{F}(1,1') \\ \Pi^{\overline{F}}(1,1') & \Pi^{\overline{G}}(1,1') \end{pmatrix}.\end{aligned} \tag{3.16}$$

After a careful evaluation of the integrals on the left hand sides of eq. 3.14 and 3.15, we obtain

$$\left[i\boldsymbol{\tau}_3 \frac{\partial}{\partial t_1} - \left(-\frac{1}{2m}\boldsymbol{\nabla}_1^2 + V_{ext}(1)\right)\mathbb{1} - \boldsymbol{\Sigma}^{HF}(1)\right] \boldsymbol{A}(1,1') = -i \int_{t_{1'}}^{t_1} \mathrm{d}2\, \boldsymbol{\Gamma}(1,2)\boldsymbol{A}(2,1'), \tag{3.17}$$

$$\begin{aligned}\left[i\boldsymbol{\tau}_3 \frac{\partial}{\partial t_1} - \left(-\frac{1}{2m}\boldsymbol{\nabla}_1^2 + V_{ext}(1)\right)\mathbb{1} - \boldsymbol{\Sigma}^{HF}(1)\right] \boldsymbol{F}(1,1') =& -i \int_{-\infty}^{t_1} \mathrm{d}2\, \boldsymbol{\Gamma}(1,2)\boldsymbol{F}(2,1') \\ &+ i \int_{-\infty}^{t_{1'}} \mathrm{d}2\, \boldsymbol{\Pi}(1,2)\boldsymbol{A}(2,1'),\end{aligned} \tag{3.18}$$

where we have used the fact that $\boldsymbol{\Sigma}^{HF}$ is local, i.e. $\boldsymbol{\Sigma}^{HF}(1,1') = \boldsymbol{\Sigma}^{HF}(1)\delta(1-1')$. These two equations describe the full time dynamics of the non-condensed particles and are coupled to the equation of motion for the condensate propagator,

$$\left[i\boldsymbol{\tau}_3 \frac{\partial}{\partial t_1} - \left(-\frac{1}{2m}\boldsymbol{\nabla}_1^2 + V_{ext}(1)\right)\mathbb{1} - \boldsymbol{S}^{HF}(1)\right] \boldsymbol{C}(1,1') = -i \int_{-\infty}^{t_1} \mathrm{d}2\, \boldsymbol{\gamma}(1,2)\boldsymbol{C}(2,1'), \tag{3.19}$$

which was obtained by carrying out the integral on the left hand side of eq 3.8 and using the locality of $\boldsymbol{S}^{HF}$.

Now, having a general system of equations describing the temporal dynamics of a Bose-condensed gas in a trapping potential, we will proceed with the classification of the self-energy approximations which are needed in order to make the equations more tractable.

3.2 Self-Energy Approximations

In the previous section, we derived a general set of equations describing the time dependent dynamics of an interacting Bose gas at low temperatures. In the derivation we did not specify the approximations used for the self-energies. Since the progators $\boldsymbol{A}$, $\boldsymbol{F}$ and $\boldsymbol{C}$ are traced quantities, it is not possible to obtain a closed set of equations, and one gets complicated equations for an infinite hierarchy of the correlation functions [27]. In order to find a tractable way to deal with the equations of motion, one has to truncate the diagrammatic expansion for the propagators. In addition, it is necessary to treat the condensed and non-condensed particles at equal footing

[41]. This can be done using the so-called "Φ-derivable" (or conserving approximation).

3.2.1 Conserving Approximations and the Generating Functional

Before we proceed to give the self-energies corresponding to the the interatomic interactions, we review some general aspects of conserving approximations. Conserving approximations are based on self-consistent approximations for the one-particle propagator. One assumes that it is possible to find a functional, such that from its functional derivative with respect to the one-particle propagator one can obtain the self-energy function , i.e.

$$\boldsymbol{S}(1,1') = \frac{\delta\Phi}{\delta\boldsymbol{C}(1,1')} \quad \text{and} \quad \boldsymbol{\Sigma}(1,1') = \frac{\delta\Phi}{\delta\boldsymbol{G}(1,1')} \tag{3.20}$$

If one requires the intrinsic conservations laws at each vertex in the diagrammatic expansion, the existence of such a Φ is guarantied. In addition, one can prove that the density response functions related to the one-particle propagator satisfy all the over-all conservation laws [24, 25]. We now proceed to illustrate the conserving character of a "Φ-derivable" approximation by showing how the overall particle number conservation arises as consequence of requiring the existence of such a Φ.

Under variation of $\boldsymbol{C}$ and $\boldsymbol{G}$ the generating functional transforms as

$$\delta\Phi = \frac{1}{2}\int \mathrm{d}1 \int \mathrm{d}1' \,\mathrm{Tr}\left[\frac{\delta\Phi}{\delta\boldsymbol{C}(1,1')}\delta\boldsymbol{C}(1',1) + \frac{\delta\Phi}{\delta\boldsymbol{G}(1,1')}\delta\boldsymbol{G}(1',1)\right], \tag{3.21}$$

where Tr denotes the trace and the pre-factor 1/2 appears as a consequence of the spinor representation that is used.

The first-order change in Φ induced by the gauge transformation

$$\begin{aligned}\boldsymbol{C}(1,1') &\longrightarrow \tilde{\boldsymbol{C}}(1,1') \equiv e^{-i\theta(1)\boldsymbol{\tau}_3}\boldsymbol{C}(1,1')e^{i\theta(1')\boldsymbol{\tau}_3}\\ \boldsymbol{G}(1,1') &\longrightarrow \tilde{\boldsymbol{G}}(1,1') \equiv e^{-i\theta(1)\boldsymbol{\tau}_3}\boldsymbol{G}(1,1')e^{i\theta(1')\boldsymbol{\tau}_3}\end{aligned} \tag{3.22}$$

is

$$\begin{aligned}\delta\Phi =& -\frac{i}{2}\int \mathrm{d}1 \int \mathrm{d}1' \,\mathrm{Tr}\left[\boldsymbol{S}(1,1')\left(\theta(1')\boldsymbol{\tau}_3\boldsymbol{C}(1',1) - \theta(1)\boldsymbol{C}(1',1)\boldsymbol{\tau}_3\right)\right]\\ &-\frac{i}{2}\int \mathrm{d}1 \int \mathrm{d}1' \,\mathrm{Tr}\left[\boldsymbol{\Sigma}(1,1')\left(\theta(1')\boldsymbol{\tau}_3\boldsymbol{G}(1',1) - \theta(1)\boldsymbol{G}(1',1)\boldsymbol{\tau}_3\right)\right]\\ =&\frac{i}{2}\int \mathrm{d}1\,\theta(1) \int \mathrm{d}1' \,\mathrm{Tr}\left[\boldsymbol{\tau}_3\left(\boldsymbol{S}(1,1')\boldsymbol{C}(1',1) - \boldsymbol{C}(1,1')\boldsymbol{S}(1',1)\right)\right]\\ &+\frac{i}{2}\int \mathrm{d}1\,\theta(1) \int \mathrm{d}1' \,\mathrm{Tr}\left[\boldsymbol{\tau}_3\left(\boldsymbol{\Sigma}(1,1')\boldsymbol{G}(1',1) - \boldsymbol{G}(1,1')\boldsymbol{\Sigma}(1',1)\right)\right],\end{aligned} \tag{3.23}$$

where in the last equality we used the fact that the trace Tr is invariant under cyclic permutations.

The particle number conservation at each vertex in ϕ requires that the number of ingoing lines must equal the number of outgoing lines. As a consequence the functional Φ must be invariant under the transformation 3.22 and therefore the coefficient of $\theta(1)$ in eq. 3.23 must

vanish. Thus, we obtain

$$0 = \int \mathrm{d}1' \,\mathrm{Tr}\left[\boldsymbol{\tau}_3 \left(\boldsymbol{S}(1,1')\boldsymbol{C}(1',1) - \boldsymbol{C}(1,1')\boldsymbol{S}(1',1)\right)\right] + \int \mathrm{d}1' \,\mathrm{Tr}\left[\boldsymbol{\tau}_3 \left(\boldsymbol{\Sigma}(1,1')\tilde{\boldsymbol{G}}(1',1) - \boldsymbol{G}(1,1')\boldsymbol{\Sigma}(1',1)\right)\right]. \tag{3.24}$$

Finally, making use of the equations of motion 3.4 and 3.5 (or their realtime versions 3.8 and 3.9) for $\boldsymbol{C}$ and $\boldsymbol{G}$ and their hermitian conjugated versions, we get

$$0 = \int \mathrm{d}1' \,\mathrm{Tr}\left[\boldsymbol{\tau}_3 \left(\boldsymbol{G}_0^{-1}(1,1')\boldsymbol{C}(1',1) - \boldsymbol{C}(1,1')\boldsymbol{G}_0^{-1}(1',1)\right)\right] + \int \mathrm{d}1' \,\mathrm{Tr}\left[\boldsymbol{\tau}_3 \left(\boldsymbol{G}_0^{-1}(1,1')\boldsymbol{G}(1',1) - \boldsymbol{G}(1,1')\boldsymbol{G}_0^{-1}(1',1)\right)\right]. \tag{3.25}$$

Carrying out the integrations, using $\boldsymbol{G}_0^{-1}(1,1') = [i\boldsymbol{\tau}_3\partial_{t_1} + \boldsymbol{\nabla}_1^2/2m - V_{\mathrm{ext}}(1)]\delta(1-1') = [-i\boldsymbol{\tau}_3\partial_{t_{1'}} + \boldsymbol{\nabla}_{1'}^2/2m - V_{\mathrm{ext}}(1')]\delta(1-1')$ and substituting at $1' = 1^+$, the continuity equation for the particle number $n(1)$ and the particle current $\mathbf{j}(1)$ arises,

$$\frac{\partial}{\partial t_1} n(1) + \boldsymbol{\nabla}_1 \cdot \mathbf{j}(1) = 0, \tag{3.26}$$

where

$$n(1) = \frac{1}{2}\mathrm{Tr}[i\boldsymbol{C}(1,1^+) + i\boldsymbol{G}(1,1^+)], \tag{3.27}$$

$$\begin{aligned} \mathbf{j}(1) &= \frac{-i}{2m}(\boldsymbol{\nabla}_1 - \boldsymbol{\nabla}_{1'})\mathrm{Tr}[\boldsymbol{\tau}_3(i\boldsymbol{C}(1,1') + i\boldsymbol{G}(1,1'))]\Big|_{1=1'} \\ &= \boldsymbol{v}_\theta(1)n_0(1) + \frac{-i}{2m}(\boldsymbol{\nabla}_1 - \boldsymbol{\nabla}_{1'})\mathrm{Tr}[\boldsymbol{\tau}_3 i\boldsymbol{G}(1,1')]\Big|_{1=1'}, \end{aligned} \tag{3.28}$$

and $\boldsymbol{v}_\theta(1) = \boldsymbol{\nabla}_1\theta(1)/m$ is the superfluid velocity and $n_0(1)$ is the particle density of the condensate. The additional conservation laws can be proven in a similar way, provided the self-energy is defined via a generating functional Φ, which is a functional of the fully renormalized propagator. In the next section we will give the self-energies corresponding to the interatomic interaction in a Bose-condensed gas.

3.2.2 Self-Energies

Now that we have discussed the existence of a functional Φ from which we can derive the self-energies, we proceed to discussed the two approximations relevant to our work, i.e., the Bogoliubov-Hartree-Fock (BHF) *approximation* and the *full second-order approximation*. Note, that there is a variety of approximations accounting two particle interactions, which can be obtained from the functional Φ. This approach is equivalent to the Two-Particle-Irreducible (2PI) effective action [38, 41]. In this thesis we will not give the exact expression for the functionals Φ generating the self-energies. Instead we refer to the literature [36, 38, 39, 41] and limit ourselves to just giving the expressions.

The BHF approximation corresponds to a truncation of Φ retaining only the two-particle-irreducible diagrams first order in the interaction g. Alternatively, it can also be obtained by using cumulant expansions up to second order, in which the cumulants containing three

or four field operators are neglected. This approximation violates the Goldstone's theorem, but conserves energy and particle number density [41–43]. The BHF approximation neglects multiple scatterings and can be interpreted in terms of the parameter $gt < E_{\text{trap}}$ (where t is the time of evolution and E_{trap} bare energy expectation of trap) and is, therefore, suitable for the description of short time dynamics or weak interactions strengths [41, 44].

The self-energies within the BHF approximations are

$$\boldsymbol{S}^{HF}(1,1') = ig\left(\frac{1}{2}\text{Tr}\left[\boldsymbol{C}(1,1')\right] + \left\{\frac{1}{2}\text{Tr}[\boldsymbol{G}(1,1')]\mathbb{1} + \boldsymbol{G}(1,1')\right\}\right)\delta(1-1') \tag{3.29}$$

for the condensate fraction,

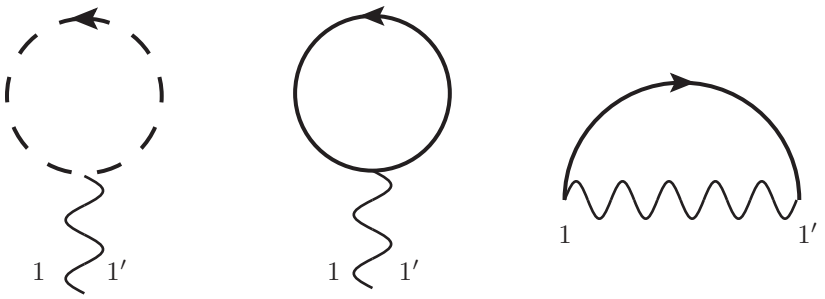

Figure 3.1: The solid and dashed lines represent the 2×2 non-condensed particles propagator and the condensate propagator, respectively. The wavy are associated to the interatomic potential $g\delta(1-1')$.

and

$$\boldsymbol{\Sigma}^{HF}(1,1') = ig\left(\left\{\frac{1}{2}\text{Tr}\left[\boldsymbol{C}(1,1')\right]\mathbb{1} + \boldsymbol{C}(1,1')\right\} + \left\{\frac{1}{2}\text{Tr}\left[\boldsymbol{G}(1,1')\right]\mathbb{1} + \boldsymbol{G}(1,1')\right\}\right)\delta(1-1'). \tag{3.30}$$

for the non-condensed particles.

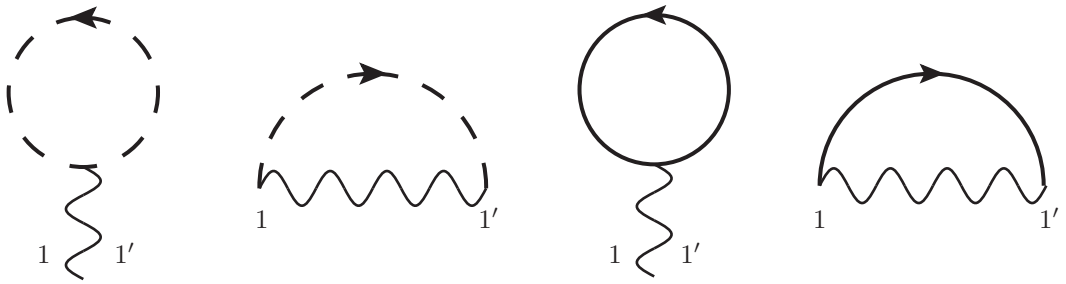

Figure 3.2: The solid and dashed lines represent the 2×2 non-condensed particles propagator and the condensate propagator, respectively. The wavy lines are associated to the interatomic potential $g\delta(1-1')$.

The Feynman diagrams representing the first order BHF approximation are shown in fig. 3.1 and 3.2 for the condensate self-energy and the non-condensate self-energy, respectively. Their analytical expressions are given in eq. 3.29 and 3.30. The order of the contributing terms in those equations matches the order of the diagrams in fig. 3.1 and 3.2.

To obtain the full second-order contributions to the self-energy, the terms second-order in g must be included in the functional Φ. In doing so, one obtains the following expression for the

self-energy related to the non-condensed particles

$$\begin{aligned}\boldsymbol{\Sigma}(1,1') = -\frac{g^2}{2}\{&\boldsymbol{G}(1,1')\mathrm{Tr}\left[\boldsymbol{C}(1',1)\boldsymbol{G}(1,1')\right] + \boldsymbol{G}(1,1')\mathrm{Tr}\left[\boldsymbol{C}(1,1')\boldsymbol{G}(1',1)\right] \\ &+ \boldsymbol{C}(1,1')\mathrm{Tr}\left[\boldsymbol{G}(1,1')\boldsymbol{G}(1',1)\right] + \boldsymbol{G}(1,1')\mathrm{Tr}\left[\boldsymbol{G}(1,1')\boldsymbol{G}(1',1)\right] \\ &+ 2\boldsymbol{G}(1,1')\boldsymbol{G}(1',1)\mathbf{C}(1,1') + 2\boldsymbol{C}(1,1')\boldsymbol{G}(1',1)\boldsymbol{G}(1,1') \\ &+ 2\boldsymbol{G}(1,1')\boldsymbol{C}(1',1)\boldsymbol{G}(1,1') + 2\boldsymbol{G}(1,1')\boldsymbol{G}(1',1)\boldsymbol{G}(1,1')\}\,. \end{aligned} \tag{3.31}$$

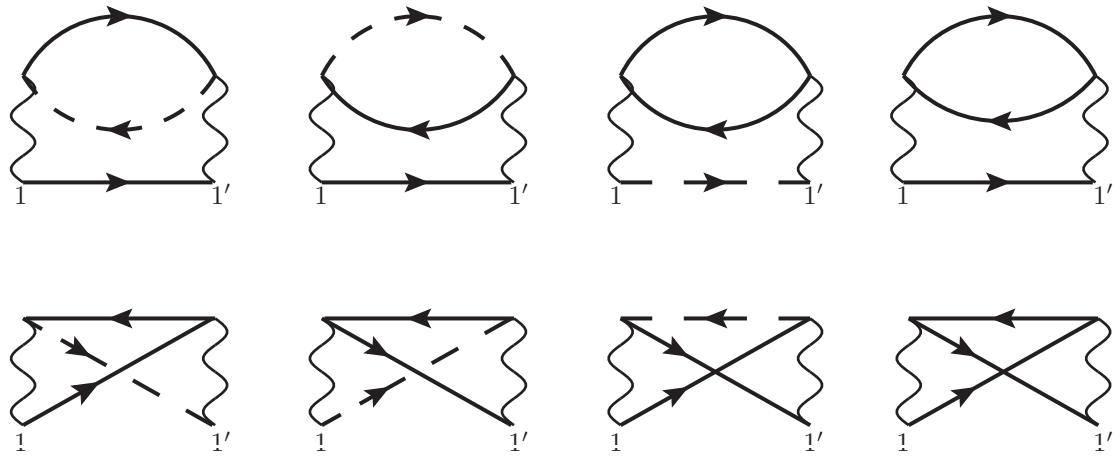

Figure 3.3: The solid and dashed lines represent the 2×2 non-condensed particles propagator and the condensate propagator, respectively. The wavy lines are associated to the interatomic potential $g\delta(1-1')$.

The diagrammatic representation of equation 3.31 is shown in fig. 3.3. Again, the order of the terms entering eq. 3.31 corresponds to the order of the diagrams in the figure.

Finally, the condensate self-energy is given by

$$\boldsymbol{S}(1,1') = -\frac{g^2}{2}\left\{\boldsymbol{G}(1,1')\mathrm{Tr}\left[\boldsymbol{G}(1,1')\boldsymbol{G}(1',1)\right] + 2\boldsymbol{G}(1,1')\boldsymbol{G}(1',1)\boldsymbol{G}(1,1')\right\}, \tag{3.32}$$

where the first term in the brackets corresponds to the fourth diagram in the upper row and the second term to the fourth diagram in the lower row of fig. 3.3.

In spite of the fact that only terms up to second order in g are kept, one can go beyond the second-order truncation by solving the equations in a self-consistent way. The second order contributions lead to a system of IPDE, which depend on the time history of the system. Taking all these memory effects into account is equivalent to the self-consistent solution of the problem.

3.3 Gross-Pitaevskii Equation

As it was pointed out in section 3.1, at low temperatures most of the atoms in a bosonic gas occupy the lowest energy state. This implies that the expectation value of the field operator $\Psi_0(1) = \langle\hat{\Psi}(1)\rangle$ does not vanish and can take arbitrary large values. We will refer from now on to $\Psi_0(1)$ as the macroscopic condensate wave function. At the same time Ψ_0 is the associated order parameter describing the phase transition to Bose-Einstein condensation.

Now let us consider the situation, where a trapped, weakly interacting bosonic gas is at zero temperature. In this case, it is a good approximation to neglect the quantum fluctuations and constrain our analysis to the macroscopic wave function Ψ_0. The equation of motion for the order parameter can be obtained from eq. 3.19 for the condensate propagator by neglecting all terms involving the quantum fluctuations,

$$\left[i\boldsymbol{\tau}_3\frac{\partial}{\partial t_1} - \left(-\frac{1}{2m}\boldsymbol{\nabla}_1^2 + V_{ext}(1)\right)\mathbb{1} - \boldsymbol{S}^{HF}(1)\right]\boldsymbol{C}(1,1') = 0. \tag{3.33}$$

The upper left component of equation 3.33 reads

$$\left[i\frac{\partial}{\partial t_1} - \left(-\frac{1}{2m}\boldsymbol{\nabla}_1^2 + V_{ext}(1) + g|\Psi_0(1)|^2\right)\right]\Psi_0(1)\Psi_0^*(1') = 0. \tag{3.34}$$

Since there is no differential operator acting on the function $\Psi_0^*(1')$, we can divide both sides of the equation by it and obtain the Gross-Pitaevskii-equation (GPE)

$$\left[i\frac{\partial}{\partial t_1} - \left(-\frac{1}{2m}\boldsymbol{\nabla}_1^2 + V_{ext}(1) + g|\Psi_0(1)|^2\right)\right]\Psi_0(1) = 0. \tag{3.35}$$

This equation was derived independently by Gross and Pitaevskii and is one of the most frequently used theoretical tools for investigating non-uniform dilute Bose gases at low temperatures [45]. Coherence and interaction effects can be investigated within the framework of the GPE. It has the form of a mean field equation where the order parameter must be calculated in a self-consistent way. The GPE can also be obtained from the functional integral formalism by requiring that the action is stationary with respect to variations of the mean field Ψ_0 [46].

As we discussed in section 3.1, the macroscopic wave function $\Psi_0(1)$ is related to the condensate particle density $n_0(1)$. Thus, it is normalized to the total condesate particle number

$$N_0(t_1) = \int \mathrm{d}\mathbf{r}_1\, |\Psi_0(\mathbf{r}_1, t_1)|^2. \tag{3.36}$$

This implies that the order parameter $\Psi_0(1)$ is equal to the square root of the condensate density $n_0(1)$ up to a multiplicative factor, i.e.

$$\Psi_0(1) = e^{i\theta(1)}\sqrt{n_0(1)}, \tag{3.37}$$

where $\theta(1)$ is the phase of the condensate wave function.

This mean field approximation is also a conserving approximation. The overall conservation laws are guaranteed. We want to illustrate the conserving character of the GPE by proving the particle number conservation.

Inserting the definition of the order parameter 3.37 into eq. 3.35 and equating the real and imaginary parts, we obtain

$$\frac{\partial}{\partial t_1}n_0(1) + \boldsymbol{\nabla}_1 \cdot (n_0(1)\boldsymbol{v}_\theta(1)) = 0, \tag{3.38}$$

$$\frac{\partial}{\partial t_1}\theta(1) + \frac{1}{2}m\boldsymbol{v}_\theta(1)^2 + V_{\mathrm{ext}}(1) + gn_0(1) - \frac{\boldsymbol{\nabla}_1^2\sqrt{n_0(1)}}{2m\sqrt{n_0(1)}} = 0 \tag{3.39}$$

where $\boldsymbol{v}_\theta$ is the superfluid velocity as defined at the end of section 3.2.1. It is also worth noticing

that the continuity equation for the condensate at the mean field level can be recovered by neglecting the quantum fluctuations in eq. 3.26. Moreover, the equations for n_0 and θ form a closed set of coupled hydrodynamic equations, exactly equivalent to the GPE. The term proportional to the gradient of the density in eq. 3.39 is called the "quantum pressure" and is a consequence of the Heisenberg uncertainty principle [45].

The small oscillations of the condensate are sound waves, according to the set of hydrodynamic equations 3.38 and 3.39 and the Goldstone's theorem. Quantum mechanically, these oscillations correspond to phonons and can be well described by a proper quantization of the dynamical variables of the system, which are the density n_0 and the phase θ. At the semi-classical level the hydrodynamic equations can be obtained by making use of the Hamilton formalism. Equating the Poisson bracket of the overlying Hamilton function with the corresponding dynamical variable, one gets the hydrodynamic equations 3.38 and 3.39. This means that the Poisson bracket of n_0 and θ is non-zero and these variables are canonical conjugated. After proper quantization one obtains

$$\hat{n}_0(\mathbf{r}_1, t_1)\hat{\theta}(\mathbf{r}_{1'}, t_{1'}) - \hat{\theta}(\mathbf{r}_{1'}, t_{1'})\hat{n}_0(\mathbf{r}_1, t_1) = i\delta(\mathbf{r}_1 - \mathbf{r}_{1'}). \tag{3.40}$$

Here we used the "hat" in order to differentiate the quantized operators $\hat{n}_0$ and $\hat{\theta}$ from the dynamical variables n_0 and θ. The quantization has the advantage of making the theory applicable to highly-correlated systems.

3.4 Bogoliubov-Hartree-Fock Approximation

The first step going beyond the mean-field approximation described in the previous section, is to include the quantum fluctuations and retain only the terms first order in g. In doing so, one ends up with a system of coupled partial-differential equations

$$\left[i\boldsymbol{\tau}_3\frac{\partial}{\partial t_1} - \left(-\frac{1}{2m}\boldsymbol{\nabla}_1^2 + V_{ext}(1)\right)\mathbb{1} - \boldsymbol{\Sigma}^{HF}(1)\right]\boldsymbol{A}(1,1') = 0, \tag{3.41}$$

$$\left[i\boldsymbol{\tau}_3\frac{\partial}{\partial t_1} - \left(-\frac{1}{2m}\boldsymbol{\nabla}_1^2 + V_{ext}(1)\right)\mathbb{1} - \boldsymbol{\Sigma}^{HF}(1)\right]\boldsymbol{F}(1,1') = 0 \tag{3.42}$$

for non-condensed particles and

$$\left[i\boldsymbol{\tau}_3\frac{\partial}{\partial t_1} - \left(-\frac{1}{2m}\boldsymbol{\nabla}_1^2 + V_{ext}(1)\right)\mathbb{1} - \boldsymbol{S}^{HF}(1)\right]\boldsymbol{C}(1,1') = 0 \tag{3.43}$$

for the condesate. The equations are coupled via the BHF self-energies $\boldsymbol{S}^{HF}$ and $\boldsymbol{\Sigma}^{HF}$, which are given by eq. 3.29 and 3.30, respectively. Expressing the self-energies in terms of the spectral and statistical function on the real time contour, one gets

$$\begin{aligned}\boldsymbol{S}^{HF}(1) \equiv & \begin{pmatrix} S^{HF}(1) & W^{HF}(1) \\ \overline{W}^{HF}(1) & \overline{S}^{HF}(1)\end{pmatrix} \\ =& ig\left(\frac{1}{2}\mathrm{Tr}\left[\boldsymbol{C}(1,1^+)\right]\mathbb{1} + \left\{\frac{1}{2}\mathrm{Tr}\Big[\boldsymbol{F}(1,1^+)\Big]\mathbb{1} + \boldsymbol{F}(1,1^+)\right\}\right),\end{aligned} \tag{3.44}$$

$$\begin{aligned}\boldsymbol{\Sigma}^{HF}(1) \equiv & \begin{pmatrix}\Sigma^{HF}(1) & \Omega^{HF}(1)\\ \overline{\Omega}^{HF}(1) & \overline{\Sigma}^{HF}(1)\end{pmatrix}\\ =& ig\left(\left\{\frac{1}{2}\mathrm{Tr}\left[\boldsymbol{C}(1,1^+)\right]\mathbb{1}+\boldsymbol{C}(1,1^+)\right\}+\left\{\frac{1}{2}\mathrm{Tr}\left[\boldsymbol{F}(1,1^+)\right]\mathbb{1}+\boldsymbol{F}(1,1^+)\right\}\right).\end{aligned} \tag{3.45}$$

It is worth mentioning that these self-energies only contain the symmetrized two-point propagators evaluated at equal points in time and space instead of the time-ordered Green's functions $G^<$ and $F^<$. Expressing the time ordered propagator $\boldsymbol{G}^<$ in terms of the spectral function $\boldsymbol{A}$ and statistical function $\boldsymbol{F}$ at equal times, one obtains

$$\boldsymbol{G}^<(1,1')\big|_{t_1=t_{1'}} = \boldsymbol{F}(1,1')\big|_{t_1=t_{1'}} + i\frac{\delta(\mathbf{r}_1-\mathbf{r}_{1'})}{2}\mathbb{1} \tag{3.46}$$

This introduces terms proportional to $\delta(\mathbf{r}_1-\mathbf{r}_1)=\delta(0)$ in the diagonal components of the self-energies $\boldsymbol{S}^{HF}$ and $\boldsymbol{\Sigma}^{HF}$ when inserting into eq. 3.29 and 3.30. These terms can be made to disappear by shifting the energy scale in the Hamiltonian, leading to the expressions eq. 3.44 and 3.45 for the selfenergies.

Taking a closer look at the equations 3.42 and 3.43, we observe that they decoupled from the equation for the spectral function 3.41, since the $\boldsymbol{A}$ does not appear in the self-energies 3.44 and 3.45. We therefore restrict our further analysis within the framework of BHF approximation to the equations for statistical function $\boldsymbol{F}$ and the condensate propagator $\boldsymbol{C}$. In addition, all the appearing quantities in the selfenergies are evaluated at equal coordinates, so that it is not necessary to evolve the equations of motion for different arguments 1 and $1'$. Equating the evolution of the statistical function $\boldsymbol{F}$ for equal arguments requires special attention. In order to find the equations that describe the time evolution of the components of $\boldsymbol{F}$, we equate the difference and sum of eq 3.42 with its hermitian conjugated version and then evaluate them at equal arguments. This yields,

$$\begin{aligned}i\left(\boldsymbol{\tau}_3\frac{\partial}{\partial t_1}\boldsymbol{F}(1,1')+\frac{\partial}{\partial t_{1'}}\boldsymbol{F}(1,1')\boldsymbol{\tau}_3\right)\Big|_{1=1'} =& \boldsymbol{\nabla}_1\cdot\left(-\frac{1}{2m}\left[\boldsymbol{\nabla}_1-\boldsymbol{\nabla}_{1'}\right]\boldsymbol{F}(1,1')\right)\Big|_{1=1'}\\ &+\boldsymbol{\Sigma}^{HF}(1)\boldsymbol{F}(1,1)-\boldsymbol{F}(1,1)\boldsymbol{\Sigma}^{HF}(1),\end{aligned} \tag{3.47}$$

$$\begin{aligned}i\left(\boldsymbol{\tau}_3\frac{\partial}{\partial t_1}\boldsymbol{F}(1,1')-\frac{\partial}{\partial t_{1'}}\boldsymbol{F}(1,1')\boldsymbol{\tau}_3\right)\Big|_{1=1'} =& \boldsymbol{\nabla}_1\cdot\left(-\frac{1}{2m}\left[\boldsymbol{\nabla}_1+\boldsymbol{\nabla}_{1'}\right]\boldsymbol{F}(1,1')\right)\Big|_{1=1'}\\ &+2V_{\mathrm{ext}}(1)\boldsymbol{F}(1,1)+\boldsymbol{\Sigma}^{HF}(1)\boldsymbol{F}(1,1)+\boldsymbol{F}(1,1)\boldsymbol{\Sigma}^{HF}(1).\end{aligned} \tag{3.48}$$

Due to the fact that the statistical function is a symmetrized two-point correlation function, we only need to consider two of its for components. The remaining two can be expressed in terms of the initial ones by making use of the symmetries of $\boldsymbol{F}$. In section 3.5, where we go beyond the BHF approximation, we will exploit these symmetries in order find a tractable way to deal with the higher-order terms and, therefore, will also give a complete review on these symmetries. For the moment we just refer to them, and equate the evolution equations for the upper-left and upper-right components of $\boldsymbol{F}$. The equation for $F^G(1,1)$ is obtained by taking

the upper-left component of eq. 3.47,

$$i\frac{\partial}{\partial t_1}F^G(1,1) = \boldsymbol{\nabla}_1 \cdot \left(\frac{-1}{2m}\left[\boldsymbol{\nabla}_1 - \boldsymbol{\nabla}_{1'}\right] F^G(1,1')\right)\Big|_{1=1'} - \Omega^{HF}(1)F^F(1,1)^* - F^F(1,1)\Omega^{HF}(1)^*, \tag{3.49}$$

and the equation for $F^F(1,1)$ is extracted from the upper right component of eq. 3.48,

$$\begin{aligned} i\frac{\partial}{\partial t_1}F^F(1,1) = \boldsymbol{\nabla}_1 \cdot \left(\frac{-1}{2m}\left[\boldsymbol{\nabla}_1 + \boldsymbol{\nabla}_{1'}\right] F^F(1,1')\right)\Big|_{1=1'} + 2\left(V_{\text{ext}}(1) + \Sigma^{HF}(1)\right) F^F(1,1) \\ - \Omega^{HF}(1)F^G(1,1)^* + F^G(1,1)\Omega^{HF}(1), \end{aligned} \tag{3.50}$$

with

$$\Sigma^{HF}(1) = 2g|\Psi_0(1)|^2 + 2igF^G(1,1), \tag{3.51}$$

$$\Omega^{HF}(1) = g\left(\Psi_0(1)\right)^2 + gF^F(1,1). \tag{3.52}$$

The equations of motion for F^G and F^F are coupled to the GPE, which is now modified due to the presence of the non-condensate particles. This modified GPE is extracted from the upper-left component of eq. 3.43 ,

$$i\frac{\partial}{\partial t_1}\Psi_0(1) = \left(-\frac{1}{2m}\boldsymbol{\nabla}_1^2 + V_{ext}(1) + g|\Psi_0(1)|^2 + 2igF^G(1,1)\right)\Psi_0(1) + igF^F(1,1)\Psi_0^*(1). \tag{3.53}$$

Eq. 3.49, 3.50 and 3.53 form a closed set of evolution equations. They can be used, as it was pointed out before, to study of a weakly interacting Bose gas. The smaller the interaction parameter, the further in time the BHF approximation will be valid.

3.4.1 Conservation Laws

For any closed system, the particle number and the energy are conserved quantities. The particle number conservation arises as a consequence of the invariance of the Hamiltonian with respect to a global phase change. The mean density of particles can be expressed in terms of the condensate wave function Ψ_0 and the statistical function F^G, as follows

$$n(1) = |\Psi_0(1)|^2 + i\left(F^G(1,1) + \frac{i}{2}\right). \tag{3.54}$$

The particle number conservation arises as a consequence of self-consistency of the equations of motion. Now we proceed to prove the conservation of the particle number within the framework of the BHF approximation. In order to do so, we take the time derivative of 3.54 and make use of the eq. 3.49 and 3.53,

$$\begin{aligned} \frac{\partial}{\partial t_1}n(1) &= -\boldsymbol{\nabla}_1 \cdot \left(\frac{-i}{2m}\left[\boldsymbol{\nabla}_1 - \boldsymbol{\nabla}_{1'}\right]\Psi_0^*(1')\Psi_0(1)\right)\Big|_{1=1'} - \boldsymbol{\nabla}_1 \cdot \left(\frac{-i}{2m}\left[\boldsymbol{\nabla}_1 - \boldsymbol{\nabla}_{1'}\right] iF^G(1,1')\right)\Big|_{1=1'} \\ &= -\boldsymbol{\nabla}_1 \cdot \left(n_0(1)\boldsymbol{v}_\theta(1) + \frac{-i}{2m}\left[\boldsymbol{\nabla}_1 - \boldsymbol{\nabla}_{1'}\right] iF^G(1,1')\right)\Big|_{1=1'}, \end{aligned} \tag{3.55}$$

where in the last equality we expressed Ψ_0 in terms of the phase θ and the density n_0, according to eq. 3.37. Note that all term proportional to g cancel with each other and the expression in

the brackets in the last equality corresponds to the particle current density.

It is known that the solution of an isolated system excludes dissipation. However the consideration of a non-conserving approximation may introduce some dissipation into the system. If the self-energies $\boldsymbol{S}^{HF}$ and $\boldsymbol{\Sigma}^{HF}$ are derived by the means of a conserving approximation (see section 3.2.2), for instance from a "ϕ-derivable" functional, the mean energy

$$\langle H\rangle = \langle H\rangle_{\rm c} + \langle H\rangle_{\rm exc} \tag{3.56}$$

can be proven to be conserved. The mean energy of the condensate fraction is given by

$$\langle H\rangle_{\rm c} = \frac{i}{2}{\rm Tr}\left[\int {\rm d}\mathbf{r}_1 \left\{\left(-\frac{\boldsymbol{\nabla}_1^2}{2m} + V_{\rm ext}(1)\right)\mathbb{1} + \frac{1}{2}\boldsymbol{S}^{HF}(1)\right\}\boldsymbol{C}(1,1^+)\right], \tag{3.57}$$

and the single particle excitations energy by

$$\langle H\rangle_{\rm exc} = \frac{i}{2}{\rm Tr}\left[\int {\rm d}\mathbf{r}_1 \left\{\left(-\frac{\boldsymbol{\nabla}_1^2}{2m} + V_{\rm ext}(1)\right)\mathbb{1} + \frac{1}{2}\boldsymbol{\Sigma}^{HF}(1)\right\}\boldsymbol{F}(1,1^+)\right]. \tag{3.58}$$

In section 3.5 we will extend these results to the full-second order approximation. But now, before we proceed to include the higher order terms in g, we will discuss the BHF approximation for a system at equilibrium.

3.4.2 Equilibrium Properties

Within the BHF approximation, there is only one situation in which we expect an equilibrium solution: when the system has never been disturbed and it remains in its equilibrium state. We will discuss now how this solution looks like and how it can be obtained from our previous considerations.

For the equilibrium situation the time dependence of the order parameter is given by

$$\Psi_0(\mathbf{r},t) = \Psi_0(\mathbf{r})e^{-i\mu t}, \tag{3.59}$$

with μ being the chemical potential. This becomes clearer once we take the average over stationary states in $\Psi_0 = \langle\hat{\Psi}\rangle$, whose time dependence is governed by the law e^{-iEt}. Then the chemical potential reads $\mu = E(N) - E(N-1) \sim \partial E/\partial N$. In addition, the energies of the non-condensed particles are measured with respect to the ground state energy, which is μ. Hence,

$$\hat{\varphi}(\mathbf{r},t) \longrightarrow \hat{\varphi}(\mathbf{r},t)e^{-i\mu t}. \tag{3.60}$$

All this corresponds to using the grand canonical Ensemble instead of the canonical, as we have done so far. In the equilibrium case, the propagator $\boldsymbol{F}$ depends on the difference of the two time arguments rather than on each of them individually. This allow us to take the Fourier transform of 3.42 with respect to the time difference.

$$\left[\boldsymbol{\tau}_3\omega - \left(-\frac{1}{2m}\boldsymbol{\nabla}_{\mathbf{r}}^2 + V_{ext}(\mathbf{r}) - \mu\right)\mathbb{1} - \boldsymbol{\Sigma}^{HF}(\mathbf{r})\right]\boldsymbol{F}(\mathbf{r},\mathbf{r}';\omega) = 0, \tag{3.61}$$

where $\boldsymbol{F}(\mathbf{r},\mathbf{r}';\omega) = \int_{-\infty}^{\infty}{\rm d}(t_1 - t_{1'})\, e^{-i\omega(t_1-t_{1'})}\boldsymbol{F}(1,1')$. The appearance of μ in 3.61 is due to the time evolution of the quantum fluctuations, described in eq. 3.60. Notice that neither $V_{\rm ext}(\mathbf{r})$

nor $\boldsymbol{\Sigma}^{HF}(\mathbf{r})$ are time dependent.

The quasiparticle energy spectrum can be obtain from the zeros of the inverse of the Green's function

$$\boldsymbol{G}^{-1}(\mathbf{r};\omega) = \begin{pmatrix} \omega - \mu + \frac{\boldsymbol{\nabla}_{\mathbf{r}}^2}{2m} - V_{ext}(\mathbf{r}) - \Sigma^{HF}(\mathbf{r}) & -\Omega^{HF}(\mathbf{r}) \\ -\Omega^{HF}(\mathbf{r})^* & -\omega - \mu + \frac{\boldsymbol{\nabla}_{\mathbf{r}}^2}{2m} - V_{ext}(\mathbf{r}) - \Sigma^{HF}(\mathbf{r}) \end{pmatrix}. \quad (3.62)$$

The additional argument related to the coordinate $\mathbf{r}'$ was dropped, because $\boldsymbol{G}^{-1}(\mathbf{r},\mathbf{r}') = \boldsymbol{G}^{-1}(\mathbf{r})\delta(\mathbf{r}-\mathbf{r}')$. In order to close the system of equations, we insert eq. 3.59 into the modified GPE (eq. 3.53) and get

$$\mu\Psi_0(\mathbf{r}) = \left(-\frac{1}{2m}\boldsymbol{\nabla}_1^2 + V_{ext}(\mathbf{r}) + g|\Psi_0(\mathbf{r})|^2 + 2igF^G(\mathbf{r},\mathbf{r})\right)\Psi_0(\mathbf{r}) + igF^F(\mathbf{r},\mathbf{r})\Psi_0^*(\mathbf{r}), \quad (3.63)$$

where $F^G(\mathbf{r},\mathbf{r}') = \int \mathrm{d}\omega F^G(\mathbf{r},\mathbf{r}';\omega)/2\pi$ and similarly for F^F. Eq. 3.62 and 3.63 form a system of self-consistent equations. At each iteration the chemical potential μ is fixed by equation 3.63 and then inserted into the eigenvalue problem defined by eq. 3.62.

According to the Hungenholtz-Pines theorem, an interacting Bose gas does not exhibit an energy gap. However, the BHF approximation violates this theorem, because the single-particle Green's function $\boldsymbol{G}$ does not have the required phonon-like spectrum at long wavelengths.

This violation of the Hungenholtz-Pines and Goldstone's theorems can be overcome by implementing the Popov-Hartree-Fock (PHF)- or "gapless"-aproximation, where the anomalous density $F^F(\mathbf{r},\mathbf{r}')$ is neglected [35, 36]. It is intensely studied in the context of Bose-Einstein condensation in atomic gases and has been applied to the equilibrium density profile of the gas below the critical temperature. The PHF theory describes the condensate in the presence of a static cloud of non-condensed particles.

One special case of the PHF approximation is the Bogoliubov theory. In this theory all the cubic and quartic terms of the quantum fluctuations $\hat{\varphi}$ in the Hamiltonian are neglected. This approach is only valid for small fluctuations of the condensate and can not be applied to liquid helium, but it is expected to be valid for a weakly interacting atomic gas at sufficiently low temperatures. The Bogoliubov theory can not only make predictions for the condensate density $n_0(1) = |\Psi_0|^2$, but also for the collective modes of the condensate. Theoretically, the eigenfrequencies of the collective modes are again determined by the poles of the one particle Green's function $\boldsymbol{G}$. In order to understand more clearly how this can be done, we limit our study to a homogeneous Bose gas [30, 45].

For a homogenous gas we can exploit that the Green's function 3.62 depends on the relative space coordinate, instead on the two arguments independently. We, therefore, obtain for the Fourier coefficients of 3.62

$$\boldsymbol{G}^{-1}(\mathbf{k};\omega) = \begin{pmatrix} \omega - \frac{\mathbf{k}^2}{2m} - g|\Psi_0|^2 & -g(\Psi_0)^2 \\ -g(\Psi_0^*)^2 & -\omega - \frac{\mathbf{k}^2}{2m} - g|\Psi_0|^2 \end{pmatrix}, \quad (3.64)$$

where we used that eq. 3.63 within the framework of the Bogoliubov theory for a homogenous gas reduces to

$$\mu = g|\Psi_0|^2. \quad (3.65)$$

The energy spectrum of the system is given by the zeros of eq. 3.64:

$$\omega_{\mathbf{k}} = \sqrt{\left(\frac{\mathbf{k}^2}{2m}\right)^2 + 2g|\Psi_0|^2\left(\frac{\mathbf{k}^2}{2m}\right)}. \tag{3.66}$$

This is the so called "Bogoliubov dispersion relation" of the collective modes.

For small momenta $|\mathbf{k}| \ll mc$ the dispersion law of the quasiparticle takes a phonon-like form $\omega_{\mathbf{k}} \approx c|\mathbf{k}|$, with $c = \sqrt{g|\Psi_0|^2/m}$ as the sound velocity. This means that the Bogoliubov approximation predicts that the long wave excitations of a weakly interacting Bose gas are sound waves. They can be regarded as the Goldstone's modes associated to the breaking of the gauge symmetry caused by the Bose-Einstein condensation. In the opposite limit, $|\mathbf{k}| \gg mc$, the dispersion relation approaches the free particle law $\omega_{\mathbf{k}} \approx \mathbf{k}^2/2m + g|\Psi_0|^2$. With this we conclude our discussion of the BHF approximation. In the following we will extend our analysis and include higher order terms.

3.5 Beyond Bogoliubov-Hartree-Fock Approximation

At the begining of this chapter, we introduced the spectral function $\boldsymbol{A}$ and the statistical function $\boldsymbol{F}$, defined in eq. 3.10 and eq. 3.13. Similar definitions followed for the non-local self-energies (see eq. 3.11, 3.12 and 3.16). The reason we expressed the equation of motion in the language of symmetrized and antisymmetrized two-point correlation functions, instead of the commonly used time-ordered propagators, is that we can exploit the bosonic commutation relations. This will become clearer when we explain how do we propagate in time the correlation functions evaluated at equal times while solving the equations of motion numerically. Moreover, in section 3.4 we pointed out that it is possible to give the whole system of equations in terms of the upper-left and upper-right components of $\boldsymbol{A}$ and $\boldsymbol{F}$, because the remaining two components can be expressed in terms of the upper ones. Making use of these symmetries, it is only necessary to consider the two upper components of the self-energies, because the remaining two can be also expressed in terms of the upper ones. This allows us to finally rewrite the terms involving higher order processes as a sort of "memory integral". All this will become clearer in our discussion below.

Consider now the function $A^{\overline{G}}$,

$$\begin{aligned} A^{\overline{G}}(1,1') &= i\left(\overline{G}^{>}(1,1') - \overline{G}^{<}(1,1')\right) \\ &= -i\left(G^{>}(1,1') - G^{<}(1,1')\right) \\ &= -A^{G}(1,1'). \end{aligned} \tag{3.67}$$

Similar relations can be found using the bosonic commutation relations in the statistical averages in the definitions of the time-ordered correlators. A list of these relations is provided in table 3.1.

Now expressing the full second-order self-energies 3.32 and 3.31 in the language of the spectral and statistical functions and using the symmetry relations listed in the table 3.1, for the components of spectral function $\boldsymbol{\gamma}$ of the non-local condensate self-energy (see eq. 3.12) we

	Spectral Function $\boldsymbol{A}$	Statistical Function $\boldsymbol{F}$
$\overline{G}$-component	$A^{\overline{G}}(1,1') = -A^{G}(1,1')^{*}$	$F^{\overline{G}}(1,1') = -F^{G}(1,1')^{*}$
	$= -A^{G}(1',1)$	$= \ F^{G}(1',1)$
$\overline{F}$-component	$A^{\overline{F}}(1,1') = -A^{F}(1,1')^{*}$	$F^{\overline{F}}(1,1') = -F^{F}(1,1')^{*}$
	$= \ A^{F}(1',1)^{*}$	$= -F^{F}(1',1)^{*}$

Table 3.1: Symmetry relations for the symmetrized and antisymmetrized two-point correlation functions.

obtain

$$\begin{aligned}\gamma^{G}(1,1') = g^{2}\Big(&F^{G}(1,1')\left\{4\Lambda[F,F^{*}](1,1') + 2\Lambda[G,G^{*}](1,1')\right\}\\ &+ A^{G}(1,1')\left\{4\Xi[F,F^{*}](1,1') + 2\Xi[G,G^{*}](1,1')\right\}\Big), \qquad (3.68)\\ \gamma^{F}(1,1') = g^{2}\Big(&F^{F}(1,1')\left\{4\Lambda[G,G^{*}](1,1') + 2\Lambda[F,F^{*}](1,1')\right\}\\ &+ A^{G}(1,1')\left\{4\Xi[G,G^{*}](1,1') + 2\Xi[F,F^{*}](1,1')\right\}\Big). \qquad (3.69)\end{aligned}$$

Analogously, for the spectral function $\boldsymbol{\Gamma}$ of the non-condesate self-energy we get

$$\begin{aligned}\Gamma^{G}(1,1') = {}&2ig^{2}\left(2\Psi_{0}^{*}(1)\Psi_{0}^{*}(1')\Lambda[F,G](1,1') + \Psi_{0}^{*}(1)\Psi_{0}(1')\Lambda[G,G](1,1')\right.\\ &\left.-2\Psi_{0}(1)\Psi_{0}(1')\Lambda[F^{*},G](1,1') - 2\Psi_{0}(1)\Psi_{0}^{*}(1')\left\{\Lambda[G,G^{*}](1,1') + \Lambda[F,F^{*}](1,1')\right\}\right)\\ &+ g^{2}\Big(F^{G}(1,1')\left\{4\Lambda[F,F^{*}](1,1') + 2\Lambda[G,G^{*}](1,1')\right\}\\ &+ A^{G}(1,1')\left\{4\Xi[F,F^{*}](1,1') + 2\Xi[G,G^{*}](1,1')\right\}\Big), \qquad (3.70)\\ \Gamma^{F}(1,1') = {}&2ig^{2}\left(2\Psi_{0}^{*}(1)\Psi_{0}(1')\Lambda[F,G](1,1') + \Psi_{0}^{*}(1)\Psi_{0}^{*}(1')\Lambda[F,F](1,1')\right.\\ &\left.-2\Psi_{0}(1)\Psi_{0}^{*}(1')\Lambda[F,G^{*}](1,1') - 2\Psi_{0}(1)\Psi_{0}(1')\left\{\Lambda[G,G^{*}](1,1') + \Lambda[F,F^{*}](1,1')\right\}\right)\\ &+ g^{2}\Big(F^{F}(1,1')\left\{4\Lambda[G,G^{*}](1,1') + 2\Lambda[F,F^{*}](1,1')\right\}\\ &+ A^{G}(1,1')\left\{4\Xi[G,G^{*}](1,1') + 2\Xi[F,F^{*}](1,1')\right\}\Big) \qquad (3.71)\end{aligned}$$

with the definitions

$$\Lambda[f,g](1,1') = A^{f}(1,1')F^{g}(1,1') + A^{g}(1,1')F^{f}(1,1') \qquad (3.72)$$

$$\Xi[f,g](1,1') = F^{f}(1,1')F^{g}(1,1') - \frac{1}{4}A^{f}(1,1')A^{g}(1,1'), \qquad (3.73)$$

where $g, f \in \{G, F, G^{*}, F^{*}\}$, and $A^{g^{*}} = (A^{g})^{*}$.

Similarly, for the components of the statistical function $\boldsymbol{\Pi}$ of the non-condensate self-energy

we obtain

$$\begin{aligned}\Pi^G(1,1') = 2ig^2 &\left(2\Psi_0^*(1)\Psi_0^*(1')\Xi[F,G](1,1') + \Psi_0^*(1)\Psi_0(1')\Xi[G,G](1,1')\right.\\ &-2\Psi_0(1)\Psi_0(1')\Xi[F^*,G](1,1') - 2\Psi_0(1)\Psi_0^*(1')\left\{\Xi[G,G^*](1,1') + \Xi[F,F^*](1,1')\right\})\\ &+ g^2\left(F^G(1,1')\left\{4\Xi[F,F^*](1,1') + 2\Xi[G,G^*](1,1')\right\}\right.\\ &\left.\left.-\frac{1}{2}A^G(1,1')\left\{2\Lambda[F,F^*](1,1') + \Lambda[G,G^*](1,1')\right\}\right), \qquad (3.74)\\ \Pi^F(1,1') = 2ig^2 &\left(2\Psi_0^*(1)\Psi_0(1')\Xi[F,G](1,1') + \Psi_0^*(1)\Psi_0^*(1')\Xi[F,F](1,1')\right.\\ &-2\Psi_0(1)\Psi_0^*(1')\Xi[F,G^*](1,1') - 2\Psi_0(1)\Psi_0(1')\left\{\Xi[G,G^*](1,1') + \Xi[F,F^*](1,1')\right\})\\ &+ g^2\left(F^F(1,1')\left\{4\Xi[G,G^*](1,1') + 2\Xi[F,F^*](1,1')\right\}\right.\\ &\left.\left.-\frac{1}{2}A^G(1,1')\left\{2\Lambda[G,G^*](1,1') + \Lambda[F,F^*](1,1')\right\}\right). \qquad (3.75)\end{aligned}$$

Like in the case of the spectral and statistical functions $A^{G/F}$ and $F^{G/F}$, the additional two components of the spectral and statistical functions of the self-energies can be expressed in terms of their upper-left and upper-right components. They satisfy similar symmetry relations to those satisfied by the components of $\boldsymbol{A}$ and $\boldsymbol{F}$. In table 3.2 we summarize them all.

	Spectral Self-energy Function $\boldsymbol{\Gamma}$ ($\boldsymbol{\gamma}$)	Statistical Self-energy Function $\boldsymbol{\Pi}$
$\overline{G}$-component	$\Gamma^{\overline{G}}(1,1') = -\Gamma^G(1,1')^*$ $= -\Gamma^G(1',1)$ $\gamma^{\overline{G}}(1,1') = -\gamma^G(1,1')^*$ $= -\gamma^G(1',1)$	$\Pi^{\overline{G}}(1,1') = -\Pi^G(1,1')^*$ $= \Pi^G(1',1)$
$\overline{F}$-component	$\Gamma^{\overline{F}}(1,1') = -\Gamma^F(1,1')^*$ $= \gamma^F(1',1)^*$ $\gamma^{\overline{F}}(1,1') = -\gamma^F(1,1')^*$ $= \gamma^F(1',1)^*$	$\Pi^{\overline{F}}(1,1') = -\Pi^F(1,1')^*$ $= -\Pi^F(1',1)^*$

Table 3.2: Symmetry relations for the symmetrized and antisymmetrized two-point correlation functions.

The equations of motion involving the non-local self-energies were already given at the begining of this chapter (see eq. 3.17, 3.18 and 3.19). In the BHF approximation, one does not have to keep track of any "memory effects" and spacial correlation, and the underlying system of equations reduces to a system of coupled, non-linear partial-differential equations for the condensate wave function and for the two-point functions evaluated at equal points in space and time. Unlike BHF approximation, once we include the terms of higher order in g, we have to evolve the equations taking into account the correlations between the initial and the intermediate states as well as spacial correlations.

Taking the upper-left and upper-right components of eq. 3.17, we obtain

$$\begin{aligned} i\frac{\partial}{\partial t_1}A^G(1,1') &= \left[-\tfrac{1}{2m}\boldsymbol{\nabla}_1^2 + V_{ext}(1) + \Sigma^{HF}(1)\right]A^G(1,1') - \Omega^{HF}(1)A^F(1,1')^* \\ &\quad -i\int_{t_{1'}}^{t_1} \mathrm{d}2\,\left[\Gamma^G(1,2)A^G(2,1') + \Gamma^F(1,2)A^{\overline{F}}(2,1')\right], \end{aligned} \tag{3.76}$$

$$\begin{aligned} i\frac{\partial}{\partial t_1}A^F(1,1') &= \left[-\tfrac{1}{2m}\boldsymbol{\nabla}_1^2 + V_{ext}(1) + \Sigma^{HF}(1)\right]A^F(1,1') - \Omega^{HF}(1)A^G(1,1')^* \\ &\quad -i\int_{t_{1'}}^{t_1} \mathrm{d}2\,\left[\Gamma^G(1,2)A^F(2,1') + \Gamma^F(1,2)A^{\overline{G}}(2,1')\right]. \end{aligned} \tag{3.77}$$

The equations for F^G and F^F are extracted from eq. 3.18 in the same way:

$$\begin{aligned} i\frac{\partial}{\partial t_1}F^G(1,1') &= \left[-\tfrac{1}{2m}\boldsymbol{\nabla}_1^2 + V_{ext}(1) + \Sigma^{HF}(1)\right]F^G(1,1') - \Omega^{HF}(1)F^F(1,1')^* \\ &\quad -i\int_{-\infty}^{t_1} \mathrm{d}2\,\left[\Gamma^G(1,2)F^G(2,1') + \Gamma^F(1,2)F^{\overline{F}}(2,1')\right] \\ &\quad +i\int_{-\infty}^{t_{1'}} \mathrm{d}2\,\left[\Pi^G(1,2)A^G(2,1') + \Pi^F(1,2)A^{\overline{F}}(2,1')\right] \end{aligned} \tag{3.78}$$

$$\begin{aligned} i\frac{\partial}{\partial t_1}F^F(1,1') &= \left[-\tfrac{1}{2m}\boldsymbol{\nabla}_1^2 + V_{ext}(1) + \Sigma^{HF}(1)\right]F^F(1,1') - \Omega^{HF}(1)F^G(1,1')^* \\ &\quad -i\int_{-\infty}^{t_1} \mathrm{d}2\,\left[\Gamma^G(1,2)F^F(2,1') + \Gamma^F(1,2)F^{\overline{G}}(2,1')\right] \\ &\quad +i\int_{-\infty}^{t_{1'}} \mathrm{d}2\,\left[\Pi^G(1,2)A^F(2,1') + \Pi^F(1,2)A^{\overline{G}}(2,1')\right]. \end{aligned} \tag{3.79}$$

And finally, the "generalized" GPE reads

$$\begin{aligned} i\frac{\partial}{\partial t_1}\Psi_0(1) &= \left(-\tfrac{1}{2m}\boldsymbol{\nabla}_1^2 + V_{ext}(1) + g|\Psi_0(1)|^2 + 2igF^G(1,1)\right)\Psi_0(1) + igF^F(1,1)\Psi_0^*(1) \\ &\quad -i\int_{-\infty}^{t_1} \mathrm{d}2\,\left[\gamma^G(1,2)\Psi_0(2) + \gamma^F(1,2)\Psi_0^*(2)\right]. \end{aligned} \tag{3.80}$$

Notice, that with the help of the symmetry relations in table 3.1 and 3.2 we can rewrite all appearing two-point functions in the integrals on the right hand side of eq. 3.76 - 3.80 with the argument related to the later time on the left side (see Appendix B). This implies, that we only need to know the solution of the previous steps while evolving the equations in time. We will take advantage of this property in the numerical implementation of the equations of motion for a system of two Bose-condensed gases trapped in a double well potential and the non-trivial time evolution of an expanding Bose-condensed gas on an optical lattice in chapters 4 and 5, respectively.

Time propagation of the eq. 3.76 - 3.79 for the two-point correlation functions $A^{G/F}$ and $F^{G/F}$ evaluated at equal times requires additional care, as it was pointed out in section 3.4. In the case of the spectral functions $A^{G/F}$, it is rather simple. The spectral functions involve the expectation value of the commutator of the quantum fluctuations field operators $\hat{\varphi}$ and $\hat{\varphi}^\dagger$. For equal time arguments these commutators have fixed values due to the bosonic commutation

relations. Hence, we get

$$i\frac{\partial}{\partial t_1}A^G(1,1')\Big|_{t_1=t_{1'}} = 0, \tag{3.81}$$

$$i\frac{\partial}{\partial t_1}A^F(1,1')\Big|_{t_1=t_{1'}} = 0. \tag{3.82}$$

The equations of motion for the statistical function $F^{G/F}$ are obtained in the same way as eq. 3.49 and 3.50 in the BHF approximation. The only difference is that we have to keep track of the spacial correlations while evolving for equal times and include the integrals involving higher order terms in g on the right hand side of the equations.

Now that we have derived the full set of coupled IPDE that describe the dynamics of a bosonic gas in a non-equilibrium situation within the full second-order approximation, we will proceed to the following section to show that they satisfy the conservation laws.

3.5.1 Conservation Laws

In section 3.4.1 we proved that the particle number within the framework of the BHF approximation is conserved and gave the expression for the mean energy of the isolated gas confined in a trapping potential. Now we want to prove the particle number conservation within the framework of the full second-order approximation and finally provide the general expression for the mean energy of the bosonic gas.

While deriving the continuity equation (see eq. 3.55) in the BHF approximation, we argued that all the terms first order in g cancel with each other, what becomes clear after inserting the expressions for the self-energy components Σ^{HF} and Ω^{HF} into the equation of motion for F^G evaluated at equal points in time and space. At first sight, it is not obvious that all the terms second order in g will cancel when inserting the expressions for the full-second-order self-energies. In order to demonstrate that this is the case, we start with the equation of motion for the particle density of the non-condensed particles

$$\begin{aligned} i\frac{\partial}{\partial t_1}F^G(1,1) = {} & \boldsymbol{\nabla}_1 \cdot \left(\frac{-1}{2m}\left[\boldsymbol{\nabla}_1 - \boldsymbol{\nabla}_{1'}\right]F^G(1,1')\right)\Big|_{1=1'} - \Omega^{HF}(1)F^F(1,1)^* - F^F(1,1)\Omega^{HF}(1)^* \\ & + i\int_{-\infty}^{t_1} \mathrm{d}2\, \left[\Gamma^G(1,2)F^G(1,2)^* + \Gamma^F(1,2)F^F(1,2)^* + \Pi^G(1,2)A^G(1,2)^* + \Pi^F(1,2)A^F(1,2)^*\right] \\ & - i\int_{-\infty}^{t_1} \mathrm{d}2\, \left[F^G(1,2)\Gamma^G(1,2)^* + F^F(1,2)\Gamma^F(1,2)^* + A^G(1,2)\Pi^G(1,2)^* + A^F(1,2)\Pi^F(1,2)^*\right], \end{aligned} \tag{3.83}$$

where we used the symmetries listed in tables 3.1 and 3.2 to rewrite all quantities appearing in the integrals such that the arguments are in the same order. Inserting the expressions for the full second-order self-energies, 5.52 - 5.55, and collecting the terms proportional to $\Psi_0\Psi_0^*$,

$\Psi_0^*\Psi_0^*$ and similar, we obtain

$$\begin{aligned} i\frac{\partial}{\partial t_1}F^G(1,1) = & \boldsymbol{\nabla}_1 \cdot \left(\frac{-1}{2m}\left[\boldsymbol{\nabla}_1 - \boldsymbol{\nabla}_{1'}\right] F^G(1,1')\right)\Big|_{1=1'} - \Omega^{HF}(1)F^F(1,1)^* - F^F(1,1)\Omega^{HF}(1)^* \\ & + \int_{-\infty}^{t_1} \mathrm{d}2 \left[\{4\Lambda[G,G^*] + 2\Lambda[F,F^*]\}\, F^F + \{4\Xi[G,G^*] + 2\Xi[F,F^*]\}\, A^F\right] \Psi_0^*(2)\Psi_0^*(1) \\ & + \int_{-\infty}^{t_1} \mathrm{d}2 \left[\{4\Lambda[F,F^*] + 2\Lambda[G,G^*]\}\, F^G + \{4\Xi[F,F^*] + 2\Xi[G,G^*]\}\, A^G\right] \Psi_0(2)\Psi_0^*(1) \\ & + \int_{-\infty}^{t_1} \mathrm{d}2 \left[\{4\Lambda[G,G^*] + 2\Lambda[F,F^*]\} \left(F^F\right)^* + \{4\Xi[G,G^*] + 2\Xi[F,F^*]\} \left(A^F\right)^*\right] \Psi_0(2)\Psi_0(1) \\ & + \int_{-\infty}^{t_1} \mathrm{d}2 \left[\{4\Lambda[F,F^*] + 2\Lambda[G,G^*]\} \left(F^G\right)^* + \{4\Xi[F,F^*] + 2\Xi[G,G^*]\} \left(F^G\right)^*\right] \Psi_0^*(2)\Psi_0(1), \end{aligned} \tag{3.84}$$

where the arguments of all two-point correlation functions are $(1,2)$, which were omitted for simplicity. Taking a closer look at the integrals, we observe that the terms contained in the square brackets can be identified with the full second-order condensate self-energies. Thus,

$$\begin{aligned} i\frac{\partial}{\partial t_1}F^G(1,1) = & \boldsymbol{\nabla}_1 \cdot \left(\frac{-1}{2m}\left[\boldsymbol{\nabla}_1 - \boldsymbol{\nabla}_{1'}\right] F^G(1,1')\right)\Big|_{1=1'} - \Omega^{HF}(1)F^F(1,1)^* - F^F(1,1)\Omega^{HF}(1)^* \\ & + \int_{-\infty}^{t_1} \mathrm{d}2 \left[\gamma^F\Psi_0^*(2)\Psi_0^*(1) + \gamma^G\Psi_0(2)\Psi_0^*(1) + \left(\gamma^F\right)^*\Psi_0(2)\Psi_0(1) + \left(\gamma^G\right)^*\Psi_0^*(2)\Psi_0(1)\right]. \end{aligned} \tag{3.85}$$

Again, we omitted the arguments of the quantities related to the non-condensate particles in the integrals.

Using the generalized GPE (eq. 3.80) to compute the equation of motion for the condensate density, we get

$$\begin{aligned} \frac{\partial}{\partial t_1}\Psi_0^*(1)\Psi_0(1) = & -\boldsymbol{\nabla}_1 \cdot \left(\frac{-i}{2m}\left[\boldsymbol{\nabla}_1 - \boldsymbol{\nabla}_{1'}\right]\Psi_0^*(1')\Psi_0(1)\right)\Big|_{1=1'} + \left(g(\Psi_0^*(1))^2F^F(1,1) + \text{c.c.}\right) \\ & - \int_{-\infty}^{t_1} \mathrm{d}2 \left[\left(\gamma^G\right)^*\Psi_0^*(2)\Psi_0(1) + \left(\gamma^F\right)^*\Psi_0(2)\Psi_0(1) + \gamma^G\Psi_0(2)\Psi_0^*(1) + \gamma^F\Psi_0^*(2)\Psi_0^*(1)\right], \end{aligned} \tag{3.86}$$

where c.c. refers to the complex conjugated quantity of the other term in the brackets.

Adding eq. 3.85 and 3.86 all the terms of first order in g or higher cancel. The remaining terms yield the continuity equation for the mean density of gas

$$\frac{\partial}{\partial t_1}n(1) = -\boldsymbol{\nabla}_1 \cdot \left(\frac{-i}{2m}\left[\boldsymbol{\nabla}_1 - \boldsymbol{\nabla}_{1'}\right]\Psi_0^*(1')\Psi_0(1)\right)\Big|_{1=1'} - \boldsymbol{\nabla}_1 \cdot \left(\frac{-i}{2m}\left[\boldsymbol{\nabla}_1 - \boldsymbol{\nabla}_{1'}\right] iF^G(1,1')\right)\Big|_{1=1'}, \tag{3.87}$$

which agrees with the continuity equation derived previously in section 3.4.1.

Including terms of higher order in g also for the mean energy yields,

$$\langle H\rangle_{\mathrm{c}} = \frac{i}{2}\mathrm{Tr}\left[\int \mathrm{d}\mathbf{r}_1 \left\{\left(-\frac{\boldsymbol{\nabla}_1^2}{2m} + V_{\mathrm{ext}}(1)\right)\mathbb{1} + \frac{1}{2}\boldsymbol{S}^{HF}(1)\right\}\boldsymbol{C}(1,1^+)\right] + \frac{1}{4}\mathrm{Tr}\left[\int_{-\infty}^{t_1} \mathrm{d}2\,\boldsymbol{\gamma}(1,2)\boldsymbol{C}(2,1^+)\right] \tag{3.88}$$

and

$$\langle H\rangle_{\mathrm{exc}} = \frac{i}{2}\mathrm{Tr}\left[\int \mathrm{d}\mathbf{r}_1 \left\{\left(-\frac{\boldsymbol{\nabla}_1^2}{2m} + V_{\mathrm{ext}}(1)\right)\mathbb{1} + \frac{1}{2}\boldsymbol{\Sigma}^{HF}(1)\right\}\boldsymbol{F}(1,1^+)\right] + \frac{1}{4}\mathrm{Tr}\left[\int_{-\infty}^{t_1} \mathrm{d}2\,\left\{\boldsymbol{\Gamma}(1,2)\boldsymbol{F}(2,1^+) - \boldsymbol{\Pi}(1,2)\boldsymbol{A}(2,1^+)\right\}\right]. \tag{3.89}$$

for the mean energy of the condensate fraction $\langle H\rangle_{\mathrm{c}}$ and the energy of the single particle excitations $\langle H\rangle_{\mathrm{exc}}$, respectively. Their sum can be proven to be constant by inserting the expressions for the second-order self-energies.

3.6 Quantum-Boltzmann Equation

From the previous considerations, it is clear that the full non-equilibrium quantum dynamics of a Bose gas are described by a closed set of coupled IPDE, which are very difficult to solve. As an alternative, one can introduce approximations based on physical considerations. In order to make some progress, one can use time scale separations, if they are well justified. This can break the hierarchy of coupled equations, and one obtains a quantum kinetic equation, which resembles the classical Boltzmann equation, but additionally includes quantum features. This equation is commonly called Quantum-Boltzmann equation (QBE). For the derivation of the QBE we will follow the approach used by Zeremba, Nikuni and Griffin [35, 47] and we will therefore use throughout this section the time-ordered non-condensate propagators $\boldsymbol{G}^{\gtrless}$ instead of the spectral function $\boldsymbol{A}$ and statistical function $\boldsymbol{F}$.

Assuming that we can separate the fast from the slow processes, we can use the "Wigner-coordinates" and write the correlation function in terms of the center-of-mass coordinate $(\mathbf{R}, T)$ and the relative coordinate $(\mathbf{r}, \tau)$ given by

$$\mathbf{R} = \tfrac{1}{2}\left(\mathbf{r}_1 + \mathbf{r}_{1'}\right), \quad T = \frac{1}{2}\left(t_1 + t_{1'}\right) \tag{3.90}$$

$$\mathbf{r} = \mathbf{r}_1 - \mathbf{r}_{1'}, \qquad \tau = t_1 - t_{1'}. \tag{3.91}$$

The center-of-mass coordinates describe the macroscopic properties of the system, governed by the non-equilibrium features of the state under consideration, as result of an applied external force, while the relative coordinates describe the microscopic properties of the system.

If the external force applied to the system causes perturbances with a wavelength much longer than the thermal wavelengths, the propagators $\boldsymbol{G}^{\gtrless}(1,1') \equiv \boldsymbol{G}^{\gtrless}(\mathbf{R}, T; \mathbf{r}, \tau)$ are supposed to vary slowly as a function of $(\mathbf{R}, T)$ and to be dominated by small values of $(\mathbf{r}, \tau)$. This assumption

means that the system is slightly perturbed away from equilibrium. As we will see, this is an important assumption for the derivations of the QBE.

However, in the presence of a condensate the order parameter $\langle\hat{\Psi}\rangle = \Psi_0$ can be express in terms of the condensate density n_0 and the phase θ, according to eq. 3.37. In equilibrium the gradient of the phase is related to the superfluid velocity and its time derivative to the chemical potential. Extending these relations to non-equilibrium yields

$$\boldsymbol{\nabla}_1\theta(1) = m\boldsymbol{v}_\theta, \tag{3.92}$$

$$\frac{\partial}{\partial t_1}\theta(1) = -\left(\mu(1) + \frac{1}{2}m\boldsymbol{v}_\theta^2\right). \tag{3.93}$$

It can be seen that $\theta(1)$ is a rapidly varying function of the center-of-mass coordinates $(\mathbf{R}, T)$, what induces strong variations in the off-diagonal elements of the propagators $\boldsymbol{C}$ and $\boldsymbol{G}^{\gtrless}$. We, therefore, need to remove this strong dependence on the center-of-mass coordinates associated to the phase θ. In order to do so, we apply the gauge transformation

$$\begin{aligned}\boldsymbol{C}(1,1') &\longrightarrow \tilde{\boldsymbol{C}}(1,1') \equiv e^{-i\theta(1)\boldsymbol{\tau}_3}\boldsymbol{C}(1,1')e^{i\theta(1')\boldsymbol{\tau}_3},\\ \boldsymbol{G}^{\gtrless}(1,1') &\longrightarrow \tilde{\boldsymbol{G}}^{\gtrless}(1,1') \equiv e^{-i\theta(1)\boldsymbol{\tau}_3}\boldsymbol{G}^{\gtrless}(1,1')e^{i\theta(1')\boldsymbol{\tau}_3},\end{aligned} \tag{3.22}$$

which was introduced in section 3.2.1. In this gauge the non-condensed particles are moving with the average velocity $\boldsymbol{v}_\theta$ with respect to the static condensate and we expect the quantities $\tilde{\boldsymbol{C}}$, $\tilde{\boldsymbol{G}}^{\gtrless}$ and $\boldsymbol{v}_\theta$ to be slowly varying with respect to the coordinates $(\mathbf{R}, T)$. Notice that the gauge-transformed condensate propagator now reads

$$\tilde{\boldsymbol{C}}(1,1') = -i\sqrt{n_0(1)n_0(1')}\begin{pmatrix}1 & 1\\ 1 & 1\end{pmatrix}, \tag{3.94}$$

and the equations of motion 3.8 and 3.9 remain invariant if we replace $\boldsymbol{G}_0^{-1}$ by

$$\tilde{\boldsymbol{G}}_0^{-1}(1,1') = \left[i\boldsymbol{\tau}_3\frac{\partial}{\partial t_1} - \frac{\partial\theta(1)}{\partial t_1} - \left(-\frac{1}{2m}\left[\boldsymbol{\nabla}_1 + i\boldsymbol{\tau}_3\boldsymbol{\nabla}_1\theta(1)\right]^2 + V_{ext}(1)\right)\mathbb{1}\right]\delta(1-1'). \tag{3.95}$$

Since throughout the rest of this section we will use the gauge-transformed functions exclusively, we will drop the "tildes" to simplify the notation.

We now focus on the single particle excitations and will derive the QBE for the quasiparticles. The QBE for the quasiparticles is coupled to a "generalized" GPE. Under the slow varying perturbances approximation, which we are considering in this section, this GPE will look slightly different with respect to the equation derived in section 3.5.

Now let us proceed to derive the QBE for the quasiparticles. We first take the difference of eq. 3.9 with its hermitian conjugated version

$$\begin{aligned}\left[\boldsymbol{G}_0^{-1} - \boldsymbol{\Sigma}^{HF}\overset{\otimes}{,}\boldsymbol{G}^{\gtrless}\right](1,1') = &-i\int_{-\infty}^{t_1}\mathrm{d}2\,\boldsymbol{\Gamma}(1,2)\boldsymbol{G}^{\gtrless}(2,1') + i\int_{-\infty}^{t_{1'}}d2\,\boldsymbol{\Sigma}^{\gtrless}(1,2)\boldsymbol{A}(2,1')\\ &-i\int_{-\infty}^{t_{1'}}\mathrm{d}2\,\boldsymbol{G}^{\gtrless}(1,2)\boldsymbol{\Gamma}(2,1') + i\int_{-\infty}^{t_1}d2\,\boldsymbol{A}(1,2)\boldsymbol{\Sigma}^{\gtrless}(2,1')\end{aligned} \tag{3.96}$$

where we introduced the notation $\left[\boldsymbol{A}\overset{\otimes}{,}\boldsymbol{B}\right] = \boldsymbol{A}\otimes\boldsymbol{B} - \boldsymbol{B}\otimes\boldsymbol{A}$ with $\otimes$ refering to the convolution

of two two-point functions, $(\boldsymbol{A}\otimes\boldsymbol{B})(1,1') = \int_{-\infty}^{\infty} \mathrm{d}2\, \boldsymbol{A}(1,2)\boldsymbol{B}(2,1')$.

We now express the the correlation functions in terms of the center-of-mass and relative coordinates, as given by eq. 3.90 and 3.91. Since $\boldsymbol{\Sigma}^{\gtrless}$ is a function of $\boldsymbol{G}^{\gtrless}$, it happens to be dominated by small values of the relative coordinates $(\mathbf{r},\tau)$ (or high momenta and frequencies). Using these properties we can write 3.96 in terms of the center-of-mass and relative coordinates,

$$\begin{aligned}\left[\boldsymbol{G}_0^{-1} - \boldsymbol{\Sigma}^{HF}\overset{\otimes}{,}\boldsymbol{G}^{\gtrless}\right](\mathbf{R},T;\mathbf{r},\tau) \;\approx\; &\tfrac{1}{2}\int_{-\infty}^{\infty}\mathrm{d}\bar{t}\int\mathrm{d}\bar{\mathbf{r}}\,\big[\boldsymbol{\Sigma}^{>}(\mathbf{R},T;\mathbf{r}-\bar{\mathbf{r}},\tau-\bar{t})\boldsymbol{G}^{<}(\mathbf{R},T;\bar{\mathbf{r}},\bar{t})\\ &-\boldsymbol{\Sigma}^{<}(\mathbf{R},T;\mathbf{r}-\bar{\mathbf{r}},\tau-\bar{t})\boldsymbol{G}^{>}(\mathbf{R},T;\bar{\mathbf{r}},\bar{t})\big]\\ &+\tfrac{1}{2}\int_{-\infty}^{\infty}\mathrm{d}\bar{t}\int\mathrm{d}\bar{\mathbf{r}}\,\big[\boldsymbol{G}^{<}(\mathbf{R},T;\mathbf{r}-\bar{\mathbf{r}},\tau-\bar{t})\boldsymbol{\Sigma}^{>}(\mathbf{R},T;\bar{\mathbf{r}},\bar{t})\\ &-\boldsymbol{G}^{>}(\mathbf{R},T;\mathbf{r}-\bar{\mathbf{r}},\tau-\bar{t})\boldsymbol{\Sigma}^{<}(\mathbf{R},T;\bar{\mathbf{r}},\bar{t})\big]\,. \end{aligned}\tag{3.97}$$

Taking the Fourier transform of eq. 3.97 with respect to the relative coordinates $(\mathbf{r},\tau)$, we obtain

$$\begin{aligned}&\left[\boldsymbol{G}_0^{-1} - \boldsymbol{\Sigma}^{HF}\overset{\otimes}{,}\boldsymbol{G}^{\gtrless}\right](\mathbf{R},T;\mathbf{p},\omega)\\ &= \frac{1}{2}\left[\boldsymbol{\Sigma}^{>}(\mathbf{R},T;\mathbf{p},\omega)\boldsymbol{G}^{<}(\mathbf{R},T;\mathbf{p},\omega) - \boldsymbol{\Sigma}^{<}(\mathbf{R},T;\mathbf{p},\omega)\boldsymbol{G}^{>}(\mathbf{R},T;\mathbf{p},\omega)\right]\\ &\quad+\frac{1}{2}\left[\boldsymbol{G}^{<}(\mathbf{R},T;\mathbf{p},\omega)\boldsymbol{\Sigma}^{>}(\mathbf{R},T;\mathbf{p},\omega) - \boldsymbol{G}^{>}(\mathbf{R},T;\mathbf{p},\omega)\boldsymbol{\Sigma}^{<}(\mathbf{R},T;\mathbf{p},\omega)\right],\end{aligned}\tag{3.98}$$

with $\boldsymbol{G}^{\gtrless}(\mathbf{R},T;\mathbf{p},\omega) = \int_{-\infty}^{\infty}\mathrm{d}\tau\int\mathrm{d}\mathbf{r}\, e^{i(\omega\tau-\mathbf{p}\cdot\mathbf{r})}\boldsymbol{G}^{\gtrless}(\mathbf{R},T;\mathbf{r},\tau)$, and analogously for the self-energy $\boldsymbol{\Sigma}^{\gtrless}$. The Fourier transformation of the bracket $\left[\cdot\overset{\otimes}{,}\cdot\right]$ was computed within the "gradient approximation"[1], and is given by

$$\begin{aligned}&\left[\boldsymbol{A}\overset{\otimes}{,}\boldsymbol{B}\right](\mathbf{R},T;\mathbf{p},\omega)\\ &\quad=\left[1+\frac{i}{2}\left(\frac{\partial^1}{\partial\omega}\frac{\partial^2}{\partial T}-\frac{\partial^1}{\partial T}\frac{\partial^2}{\partial\omega}-\boldsymbol{\nabla}^1_{\mathbf{p}}\cdot\boldsymbol{\nabla}^2_{\mathbf{R}}+\boldsymbol{\nabla}^1_{\mathbf{R}}\cdot\boldsymbol{\nabla}^2_{\mathbf{p}}\right)\right](\boldsymbol{AB}-\boldsymbol{BA})(\mathbf{R},T;\mathbf{p},\omega).\end{aligned}\tag{3.99}$$

Since $\boldsymbol{A}$ and $\boldsymbol{B}$ do not commute, we have to differentiate on which of the matrices the derivative is acting. This is done by the superscript appearing in the derivatives, i.e. 1 refers to the case where the differential operator acts on the matrix appearing left in the multiplication and 2 to the matrix appearing on the right [27].

Now we take the trace of eq. 3.98,

$$\begin{aligned}&\mathrm{Tr}\left[\frac{\partial}{\partial\omega}\left(\boldsymbol{G}_0^{-1}-\boldsymbol{\Sigma}^{HF}\right)\frac{\partial\boldsymbol{G}^{\gtrless}}{\partial T}-\frac{\partial}{\partial T}\left(\boldsymbol{G}_0^{-1}-\boldsymbol{\Sigma}^{HF}\right)\frac{\partial\boldsymbol{G}^{\gtrless}}{\partial\omega}\right]\\ &\quad-\mathrm{Tr}\left[\boldsymbol{\nabla}_{\mathbf{p}}\left(\boldsymbol{G}_0^{-1}-\boldsymbol{\Sigma}^{HF}\right)\cdot\boldsymbol{\nabla}_{\mathbf{R}}\boldsymbol{G}^{\gtrless}-\boldsymbol{\nabla}_{\mathbf{R}}\left(\boldsymbol{G}_0^{-1}-\boldsymbol{\Sigma}^{HF}\right)\cdot\boldsymbol{\nabla}_{\mathbf{p}}\boldsymbol{G}^{\gtrless}\right]\\ =&(-i)\mathrm{Tr}\left[\boldsymbol{\Sigma}^{>}\boldsymbol{G}^{<}-\boldsymbol{\Sigma}^{<}\boldsymbol{G}^{>}\right],\end{aligned}\tag{3.100}$$

where we omitted the arguments $(\mathbf{R},T;\mathbf{p},\omega)$ of all correlation functions for readability, and the

[1] In this approximation, we expand the correlation functions in the bracket $\left[\cdot\overset{\otimes}{,}\cdot\right]$ around small values of the relative coordinates $(\mathbf{r},\tau)$ and keep the terms up to first order.

Fourier transform of the inverse of the non-interacting propagator reads

$$\boldsymbol{G}_0^{-1}(\mathbf{R},T;\mathbf{p},\omega) = [\omega - \mathbf{p}\cdot\boldsymbol{v}_\theta(\mathbf{R},T)]\,\boldsymbol{\tau}_3 - \frac{\boldsymbol{p}^2}{2m} - V_{\text{ext}}(\mathbf{R},T) + \mu(\mathbf{R},T). \tag{3.101}$$

Inserting eq. 3.101 in 3.100 and expressing the left hand side in terms of the components of $\boldsymbol{G}^{\gtrless}$ and $\boldsymbol{\Sigma}^{HF}$, we obtain

$$\begin{aligned}\mathcal{L}\,G^{\gtrless} + \overline{\mathcal{L}}\,\overline{G}^{\gtrless} + \frac{\partial\Omega^{HF}}{\partial T}\frac{\partial\overline{F}^{\gtrless}}{\partial\omega} + \frac{\partial\overline{\Omega}^{HF}}{\partial T}\frac{\partial F^{\gtrless}}{\partial\omega} - \boldsymbol{\nabla}_{\mathbf{R}}\Omega^{HF}\cdot\boldsymbol{\nabla}_{\mathbf{p}}\overline{F}^{\gtrless} - \boldsymbol{\nabla}_{\mathbf{R}}\overline{\Omega}^{HF}\cdot\boldsymbol{\nabla}_{\mathbf{p}}F^{\gtrless}\\ = (-i)\mathrm{Tr}\left[\boldsymbol{\Sigma}^{>}\boldsymbol{G}^{<} - \boldsymbol{\Sigma}^{<}\boldsymbol{G}^{>}\right],\end{aligned} \tag{3.102}$$

where

$$\mathcal{L} = \left(\frac{\partial}{\partial T} + \frac{\partial}{\partial T}\left(\tilde{\epsilon}_{\mathbf{p}} + \mathbf{p}\cdot\boldsymbol{v}_\theta\right)\frac{\partial}{\partial\omega} + \boldsymbol{\nabla}_{\mathbf{p}}\left(\tilde{\epsilon}_{\mathbf{p}} + \mathbf{p}\cdot\boldsymbol{v}_\theta\right)\cdot\boldsymbol{\nabla}_{\mathbf{R}} - \boldsymbol{\nabla}_{\mathbf{R}}\left(\tilde{\epsilon}_{\mathbf{p}} + \mathbf{p}\cdot\boldsymbol{v}_\theta\right)\cdot\boldsymbol{\nabla}_{\mathbf{p}}\right), \tag{3.103}$$

$$\overline{\mathcal{L}} = \left(-\frac{\partial}{\partial T} + \frac{\partial}{\partial T}\left(\tilde{\epsilon}_{\mathbf{p}} - \mathbf{p}\cdot\boldsymbol{v}_\theta\right)\frac{\partial}{\partial\omega} + \boldsymbol{\nabla}_{\mathbf{p}}\left(\tilde{\epsilon}_{\mathbf{p}} - \mathbf{p}\cdot\boldsymbol{v}_\theta\right)\cdot\boldsymbol{\nabla}_{\mathbf{R}} - \boldsymbol{\nabla}_{\mathbf{R}}\left(\tilde{\epsilon}_{\mathbf{p}} - \mathbf{p}\cdot\boldsymbol{v}_\theta\right)\cdot\boldsymbol{\nabla}_{\mathbf{p}}\right). \tag{3.104}$$

The Hartree-Fock selfenergies in the language of the time-ordered two-point functions are given by

$$\Sigma^{HF}(1) = 2g|\Psi_0(1)|^2 + 2igG^{<}(1,1), \tag{3.105}$$

$$\Omega^{HF}(1) = g\left(\Psi_0(1)\right)^2 + giF^{<}(1,1). \tag{3.106}$$

Here $\tilde{\epsilon}_{\mathbf{p}}$ is the renormalized single particles excitation energy and is defined as

$$\tilde{\epsilon}_{\mathbf{p}}(\mathbf{R},T) = \frac{\boldsymbol{p}^2}{2m} + V_{\text{ext}}(\mathbf{R},T) + \Sigma^{HF}(\mathbf{R},T) - \mu(\mathbf{R},T). \tag{3.107}$$

A bosonic gas can either be described in terms of the distribution functions of the physical atoms directly or in the language of the quasiparticle excitations. In section 3.4.2 we discussed the properties of a trapped Bose gas at equilibrium and mentioned that is possible to describe the system in terms of quasiparticles by solving the eigenvalue problem constituted by eq. 3.62. Similarly, we can transformed the equation of motion for the single particle excitations into a kinetic equation for the quasiparticle distribution. This appears to be a convenient description, if one is dealing with a Bose gas at low temperatures. In the Bogoliubov theory for trapped Bose gases at low temperature, one introduces the quasiparticles by expressing the field operators $\hat{\varphi}$ related to the quantum fluctuations as a coherent superposition of the creation and annihilation operators, $\hat{b}^\dagger_{\mathbf{p}}$ and $\hat{b}_{\mathbf{p}}$ associated to Bose quasiparticles, with the weights $u_{\mathbf{p}}$ and $v_{\mathbf{p}}$ being the eigenvectors of the eigenvalue problem posed, for instant, by eq. 3.62 and usually referred to in the literature as the Bogoliubov coherent factors:

$$\hat{\varphi}(\mathbf{R},T) = \int\frac{\mathrm{d}\mathbf{p}}{(2\pi)^2}\left[u_{\mathbf{p}}(\mathbf{R},T)\hat{b}_{\mathbf{p}}e^{-iE_{\mathbf{p}}t} - v^*_{\mathbf{p}}(\mathbf{R},T)\hat{b}^\dagger_{\mathbf{p}}e^{iE_{\mathbf{p}}t}\right]. \tag{3.108}$$

The annihilation and creation operators of the Bogoliubov quasiparticles satisfy the bosonic commutation relations and their distribution can be express in terms of the statistical average [30, 35, 45], i.e. $f_q(\mathbf{p}) = \langle\hat{b}^\dagger_{\mathbf{p}}\hat{b}_{\mathbf{p}}\rangle$. The distribution function of the physical atoms is related to

the diagonal term of the non-condensate propagator (see eq. 3.27 and 3.54), namely

$$f(\mathbf{R},T;\mathbf{p},\omega) = iG^{<}(\mathbf{R},T;\mathbf{p},\omega). \tag{3.109}$$

The distribution function entering in the usual Boltzmann equation is the Wigner distribution $f_W(\mathbf{R},T;\mathbf{p})$. The fact that the Wigner distribution is associated to the position and momentum of the atoms at same time confines the treatment to a semiclassical approximation. Since we are deriving a kinetic equation for quasiparticles at low temperatures, where the semiclassical limit is no longer valid, we have to include quantum effects in the formalism. This is done by adding an additional variable ω to the quasiparticle distribution $f_q(\mathbf{R},T;\mathbf{p},\omega)$, according to [12, 23, 35]:

$$\boldsymbol{G}^{<}(\mathbf{R},T;\mathbf{p},\omega) = -i\boldsymbol{A}(\mathbf{R},T;\mathbf{p},\omega) f_q(\mathbf{R},T;\mathbf{p},\omega) \tag{3.110}$$

$$\boldsymbol{G}^{>}(\mathbf{R},T;\mathbf{p},\omega) = -i\boldsymbol{A}(\mathbf{R},T;\mathbf{p},\omega)\left[1 + f_q(\mathbf{R},T;\mathbf{p},\omega)\right], \tag{3.111}$$

where $\boldsymbol{A}$ is the spectral function defined in eq. 3.10. The semiclassical Wigner distribution function can be recovered by integrating over ω.

Taking the difference of the greater and lesser component in equation 3.102, we obtain

$$\mathcal{L}\,A^{G} + \overline{\mathcal{L}}\,A^{\overline{G}} + \frac{\partial\Omega^{HF}}{\partial T}\frac{\partial A^{\overline{F}}}{\partial\omega} + \frac{\partial\overline{\Omega}^{HF}}{\partial T}\frac{\partial A^{F}}{\partial\omega} - \boldsymbol{\nabla}_{\mathbf{R}}\Omega^{HF}\cdot\boldsymbol{\nabla}_{\mathbf{p}}A^{\overline{F}} - \boldsymbol{\nabla}_{\mathbf{R}}\overline{\Omega}^{HF}\cdot\boldsymbol{\nabla}_{\mathbf{p}}A^{F} = 0. \tag{3.112}$$

Using 3.102 and 3.112, we can rewrite the the original kinetic equation for $\boldsymbol{G}^{<}$, in order to obtain the a new kinetic equation of the quasiparticle distribution $f_q(\mathbf{R},T;\mathbf{p})$:

$$\begin{aligned} &A^{G}\,\mathcal{L}f_q + A^{\overline{G}}\,\overline{\mathcal{L}}f_q + A^{\overline{F}}\,\frac{\partial\Omega^{HF}}{\partial T}\frac{\partial f_q}{\partial\omega} + A^{F}\,\frac{\partial\overline{\Omega}^{HF}}{\partial T}\frac{\partial f_q}{\partial\omega} - A^{\overline{F}}\,\boldsymbol{\nabla}_{\mathbf{R}}\Omega^{HF}\cdot\boldsymbol{\nabla}_{\mathbf{p}}f_q \\ &\quad - A^{F}\,\boldsymbol{\nabla}_{\mathbf{R}}\overline{\Omega}^{HF}\cdot\boldsymbol{\nabla}_{\mathbf{p}}f_q = (-i)\mathrm{Tr}\left[f\,\boldsymbol{\Sigma}^{>}\boldsymbol{A} - (1+f)\,\boldsymbol{\Sigma}^{<}\boldsymbol{A}\right] \end{aligned} \tag{3.113}$$

It is worth mentioning that the additional variable ω in the distribution function results in the appearance of terms involving the derivative with respect to ω itself. According to [23], this is the result of the change in the average energy of a particle at $(\mathbf{R},T)$ caused by the time variation of the potential field through which it moves.

In the derivation of eq. 3.113, the only approximation made was that the external perturbation varies slowly in time and space, what allowed us to make a time scale separation. Moreover, we found out that all physically relevant quantities vary slowly as functions of the centre-of-mass-coordinates $(\mathbf{R},T)$. In addition, it was also necessary to assume that one can define a distribution function f_q for the quasiparticles.

In section 3.4.2 we explained that within the framework of a conserving approximation, such as the BHF, the Hungelholtz-Pines theorem is violated and one needs to assume a vanishing anomalous density $F^{<}(1,1^{+})$ in order to get a gapless quasiparticle spectrum. Now we proceed according to the "Popov-Bogoliubov"-approximation and require that the anomalous density equals zero. Within this approximation the quasiparticle spectral densities read

$$A^{G}(\mathbf{R},T;\mathbf{p},\omega) = 2\pi\left[u_{\mathbf{p}}^{2}\delta(\omega - \mathbf{p}\cdot\boldsymbol{v}_\theta - E_{\mathbf{p}}) - v_{\mathbf{p}}^{2}\delta(\omega - \mathbf{p}\cdot\boldsymbol{v}_\theta + E_{\mathbf{p}})\right], \tag{3.114}$$

$$A^{F}(\mathbf{R},T;\mathbf{p},\omega) = 2\pi u_{\mathbf{p}}v_{\mathbf{p}}\left[\delta(\omega - \mathbf{p}\cdot\boldsymbol{v}_\theta - E_{\mathbf{p}}) - \delta(\omega - \mathbf{p}\cdot\boldsymbol{v}_\theta + E_{\mathbf{p}})\right]. \tag{3.115}$$

The additional two components can be given in terms of A^G and A^F, according to the table 3.1. From the Bose commutation relations for the quasiparticle field operators, we see $u_{\mathbf{p}}^2 - v_{\mathbf{p}}^2 = 1$. It is therefore not necessary to give the expression for both factors, because each can be expressed in terms of the other one. The Bogoliubov coherent factor $u_{\mathbf{p}}$ is given by

$$u_{\mathbf{p}}^2 = \frac{\tilde{\epsilon}_{\mathbf{p}}(\mathbf{R},T) + E_{\mathbf{p}}(\mathbf{R},T)}{2E_{\mathbf{p}}} \tag{3.116}$$

and the quasiparticle energy by

$$E_{\mathbf{p}}(\mathbf{R},T) = \sqrt{\tilde{\epsilon}_{\mathbf{p}}(\mathbf{R},T) - (gn_0(\mathbf{R},T))^2}. \tag{3.117}$$

Inserting 3.114 and 3.115 into the general kinetic equation 3.113 and integrating over $\int \mathrm{d}\omega/(2\pi)$, we get

$$\left(\frac{\partial}{\partial T} + \boldsymbol{\nabla}_{\mathbf{p}}\left(E_{\mathbf{p}} + \mathbf{p}\cdot\boldsymbol{v}_\theta\right)\cdot\boldsymbol{\nabla}_{\mathbf{R}} - \boldsymbol{\nabla}_{\mathbf{R}}\left(E_{\mathbf{p}} + \mathbf{p}\cdot\boldsymbol{v}_\theta\right)\cdot\boldsymbol{\nabla}_{\mathbf{p}}\right) f_q(\mathbf{R},T;\mathbf{p},\omega)\Big|_{\omega=E_{\mathbf{p}}+\mathbf{p}\cdot\boldsymbol{v}_\theta} = I[f_q] \tag{3.118}$$

after some algebra. This is the so called Zeremba-Nikuni-Griffin equation (ZNG), which is named after the authors [35, 47]. Similar quasiparticle kinetic equations have been derived before [12, 48, 49].

The collision integral $I[f_q]$ is given by

$$\begin{aligned} I[f] = -2g^2 n_0(\mathbf{R},T) \int \frac{\mathrm{d}\mathbf{p}_1\mathrm{d}\mathbf{p}_2\mathrm{d}\mathbf{p}_3}{(2\pi)^2} |S(2,3;1)|^2 \delta(\mathbf{p}_1 - \mathbf{p}_2 - \mathbf{p}_3)\delta(E_1 - E_2 - E_3) \\ \left[\delta(\mathbf{p}-\mathbf{p}_1) - \delta(\mathbf{p}-\mathbf{p}_2) - \delta(\mathbf{p}-\mathbf{p}_3)\right]\left[(1+f_{\mathbf{p}_1})f_{\mathbf{p}_2}f_{\mathbf{p}_3} - f_{\mathbf{p}_1}(1+f_{\mathbf{p}_2})(1+f_{\mathbf{p}_3})\right], \end{aligned} \tag{3.119}$$

where we used the simplified notation $f_q(\mathbf{R},T;\mathbf{p},\omega = E_{\mathbf{p}} + \mathbf{p}\cdot\boldsymbol{v}_\theta) = f_{\mathbf{p}}$. The quantity $S(2,3;1)$ is the scattering amplitude and is given in terms of the coherence factor $u_{\mathbf{p}}$ and $v_{\mathbf{p}}$

$$\begin{aligned} S(2,3;1) \quad &= (u_{\mathbf{p}_3} - v_{\mathbf{p}_3})(u_{\mathbf{p}_1}u_{\mathbf{p}_2} + v_{\mathbf{p}_1}v_{\mathbf{p}_2}) + (u_{\mathbf{p}_2} - v_{\mathbf{p}_2})(u_{\mathbf{p}_1}u_{\mathbf{p}_3} + v_{\mathbf{p}_1}v_{\mathbf{p}_3}) \\ &\quad -(u_{\mathbf{p}_1} - v_{\mathbf{p}_1})(u_{\mathbf{p}_2}u_{\mathbf{p}_3} + v_{\mathbf{p}_2}v_{\mathbf{p}_3}). \end{aligned} \tag{3.120}$$

Notice, that the collision integral involves only terms containing three quasiparticles distribution functions and one condensate density. The reason is that at very low temperatures we can neglect processes where two incoming quasiparticles result in two outgoing quasiparticles. In addition, we used that for a slowly varying external disturbance the Fourier transform of the condensate propagator 3.94 reads

$$\boldsymbol{C}(\mathbf{R},T;\mathbf{p},\omega) = -i(2\pi)^4 n_0(\mathbf{R},T)\delta(\mathbf{p})\delta(\omega)\begin{pmatrix}1 & 1\\ 1 & 1\end{pmatrix}, \tag{3.121}$$

if we neglect second derivatives of the density $n_0(\mathbf{R},T)$.

The appearance of the condensate density in the quasiparticle energy $E_{\mathbf{p}}$ and the collision integral $I[f_q]$ implies that eq. 3.118 is coupled to an equation of motion for the condensate density. In order to derive the equation of motion for the condensate density, we consider the

general GPE (see eq. 3.80) for the order parameter $\Psi_0(\mathbf{r},t)$ in the local rest frame

$$\left(i\frac{\partial}{\partial t_1}-\frac{\partial\theta(1)}{\partial t_1}+\frac{1}{2m}\left[\boldsymbol{\nabla}_1+im\boldsymbol{v}_\theta\right]^2-V_{ext}(1)+g|\Psi_0(1)|^2+2igG^<(1,1^+)\right)\Psi_0(1)$$
$$=-i\int_{-\infty}^{t_1}\mathrm{d}2\,\left[\gamma^G(1,2)\Psi_0(2)+\gamma^F(1,2)\Psi_0^*(2)\right]. \tag{3.122}$$

Here the anomalous density $F^<(1,1^+)$ was neglected according to the Popov-Bogoliubov approach and the spectral functions of the condensate self-energies $\gamma^{G/F}$ are expressed in terms of the time ordered two-point correlation functions.

Working in the slow varying disturbances approximation, we can assume that the correlation functions $\gamma^{G/F}$ appearing in the integral are dominated by small values of their relative coordinates $1-2\equiv(\mathbf{r}_1-\mathbf{r}_2,t_1-t_2)$, thus making it possible to approximate $\gamma^{G/F}$ in eq. 3.123 by $\gamma^{G/F}(1-2,1)$. In addition, since we are working in the local rest frame, we have $\Psi_0=\Psi_0^*$, which yields

$$\left(i\frac{\partial}{\partial T}-\frac{\partial\theta(\mathbf{R},T)}{\partial T}+\frac{1}{2m}\left[\boldsymbol{\nabla}_{\mathbf{R}}+im\boldsymbol{v}_\theta\right]^2-V_{ext}+g|\Psi_0(\mathbf{R},t)|^2+2igG^<(\mathbf{R},T)\right)\Psi_0(\mathbf{R},T)$$
$$=-i\Psi_0(\mathbf{R},T)\int_{-\infty}^{T}\mathrm{d}\bar{t}\,\mathrm{d}\bar{\mathbf{r}}\,\left[\gamma^G(\mathbf{R}-\bar{\mathbf{r}},T-\bar{t};\mathbf{R},T)+\gamma^F(\mathbf{R}-\bar{\mathbf{r}},T-\bar{t};\mathbf{R},T)\right]$$
$$=-i\Psi_0(\mathbf{R},T)\int\frac{\mathrm{d}\mathbf{p}\,\mathrm{d}\omega}{(2\pi)^4}\left[\gamma^G(\mathbf{R},T;\mathbf{p},\omega)+\gamma^F(\mathbf{R},T;\mathbf{p},\omega)\right]\int_{-\infty}^{T}\mathrm{d}\bar{t}\,\mathrm{d}\bar{\mathbf{r}}\,e^{i(\mathbf{p}\cdot(\mathbf{R}-\bar{\mathbf{r}})-\omega(T-\bar{t})} \tag{3.123}$$

after relabeling $(\mathbf{r}_1,t_1)\longrightarrow(\mathbf{R},T)$.

Now using the identity

$$\lim_{\rho\to0^+}\int_{-\infty}^{T}\mathrm{d}\bar{t}\,e^{-i(\omega+i\rho)(T-\bar{t})}=\pi\delta(\omega)+i\mathrm{P}\left(\frac{1}{\omega}\right), \tag{3.124}$$

with P referring to the principal value, we can evaluate the right hand side

$$\left(i\frac{\partial}{\partial T}-\frac{\partial\theta(\mathbf{R},T)}{\partial T}+\frac{1}{2m}\left[\boldsymbol{\nabla}_{\mathbf{R}}+im\boldsymbol{v}_\theta\right]^2-V_{ext}+g|\Psi_0(\mathbf{R},t)|^2+2igG^<(\mathbf{R},T)\right)\Psi_0(\mathbf{R},T)$$
$$=-i\Psi_0(\mathbf{R},T)\left[\gamma^G(\mathbf{R},T;\mathbf{p}=\mathbf{0},\omega=0)+\gamma^F(\mathbf{R},T;\mathbf{p}=\mathbf{0},\omega=0)\right] \tag{3.125}$$

where we keep only the real part of eq. 3.124. Keeping in mind that in the local rest frame we have $\Psi_0(\mathbf{R},T)=\sqrt{n_0(\mathbf{R},T)}$, we finally obtain the equation for the condensate density

$$i\frac{\partial}{\partial T}\sqrt{n_0(\mathbf{R},T)}=\Big(-\frac{\partial\theta(\mathbf{R},T)}{\partial T}+\frac{1}{2m}\left[\boldsymbol{\nabla}_{\mathbf{R}}+im\boldsymbol{v}_\theta\right]^2-V_{ext}$$
$$+g|\Psi_0(\mathbf{R},t)|^2+2igG^<(\mathbf{R},T)-iR(\mathbf{R},T)\Big)\sqrt{n_0(\mathbf{R},T)}. \tag{3.126}$$

This equation contains a dissipative term $R(\mathbf{R},T)$, which is related to the collision integral

$I[f_q]$ in the ZNG equation and reads

$$R(\mathbf{R}, T) = \int \frac{\mathrm{d}\mathbf{p}}{(2\pi)^3} \frac{I[f_q]}{2n_0(\mathbf{R}, T)}. \tag{3.127}$$

This term is associated to the damping of the condensate cloud due to collisions with thermally excited atoms.

In this thesis we will not study the solutions of the ZNG equation, instead we refer to [35] and the citations therein.

With this we conclude our review of the non-equilibrium approach for Bose-condensed gases. In the following chapters we will proceed to apply the techniques developed in this chapter to Bose gases at low temperatures in different non-equilibrium situations.

CHAPTER 4

Non-Equilibrium Josephson Oscillations in Bose-Condensed Gases

A remarkable manifestation of quantum mechanics at a macroscopic scale is the particle current induced by the phase difference between two coherent wave functions connected by a weak link, known as the Josephson effect [50]. This effect was originally predicted for superconductors separated by a thin insulating layer, and subsequently observed in between two superfluid ^{3}He as well as ^{4}He reservoirs coupled through nano-apertures [51, 52]. However, the experimental realization of a BEC, and the possibility to cool down atoms and manipulate them in atomic traps, opened the possibility to study the Josephson effect in gaseous BEC of cold atoms.

An oscillatory exchange of particles between two weakly linked BECs was described already in 1986 [53]. Due to the stringent cooling conditions and the technical difficulties manipulating cold atoms, the experimental realization remained elusive until 2005 [54]. In addition to the oscillatory behavior of the particle density, a wide range of new curious effects, such as macroscopic quantum self-trapping, were successfully confirmed in this experiment. Two condensates were prepared in a double-well potential with different initial population imbalances. This resulted in different oscillatory regimes. The left panel of fig. 4.1 shows the time evolution of the atomic density distribution in a symmetric Bose Josephson junction for two different initial population imbalances. For an initial population imbalance chosen well below a critical value, Josephson oscillations occur, i.e., the particles tunnel left and right over the time. The discrepancy between the period of the oscillations observed in the experiment and the period expected from non-interacting atoms in a double-well potential is a consequence of the interatomic interactions. A different manifestation of the interactions is the macroscopic self-trapped state, which exhibits an unchanged population imbalance over the evolution time.

Even though the Josephson effect in atomic gases is very similar to the one exhibited by superconductors, there are important physical differences. The conventional Josephson junction in superconductors is an open quantum many-body system driven by a bias voltage. In contrast, a Bose Josephson junction is (to a good approximation) a closed system with fixed total number of atoms and is not necessarily in the thermodynamic limit. Nevertheless, a direct equivalent of a superconducting a.c. Josephson effect was realized in a single BEC Josephson junction in 2007 [55, 56] (see also discussion in [57]).

In the experiments [54–56] the Josephson junctions are prepared in a non-equilibrium situation by ramping up the barrier between the condensates suddenly, in a non-adiabatic way.

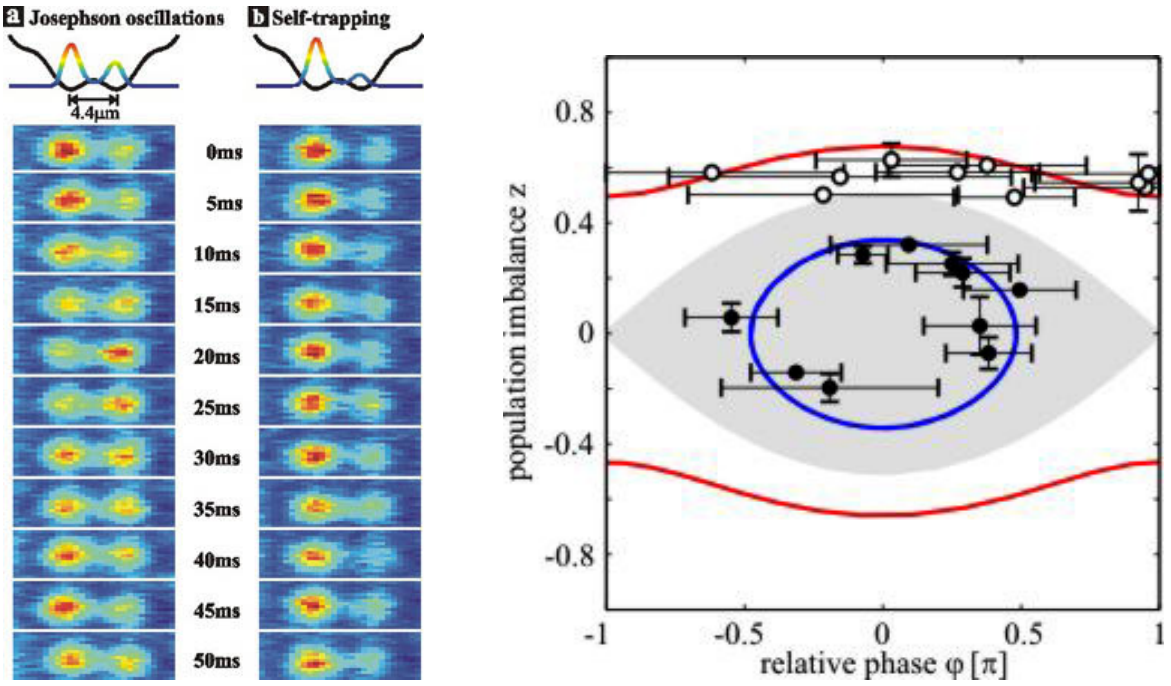

Figure 4.1: The left panel shows the time evolution of the particle density of a BEC trapped in a double-well potential for two different initial interwell population imbalances. For an initial population imbalance below a critical value the system displays Josephson oscillations and particles tunnel left and right. Above the critical value the particle imbalance remains unchanged over the time. The right panel summarizes the dynamics in the phase-space portrait of the two variable describing the system. Figures take from [54].

The behavior of the system when the two condensates are connected presents a fundamental problem in non-equilibrium macroscopic quantum mechanics. Previous theoretical studies [58, 59] suggest a damping of the Josephson oscillations due to quasiparticle excitations, which is not observed in small traps [54, 60]. Much is known about the equilibrium states in the weakly and strongly interacting regimes. However, it remains a challenge to probe the dynamics by which these equilibrium states are reached.

The canonical description of a Bose Josephson junction is given in terms of the eigenstate $|z\rangle$, referring to the interwell population imbalance. This eigenstate can be written as the coherent superposition of all possible relative phases θ between the left and right condensates,

$$|z\rangle = \int_{\pi}^{-\pi} \frac{\mathrm{d}\theta}{2\pi} e^{iz\theta} |\theta\rangle. \tag{4.1}$$

As long as the condensates are completely isolated from each other and the particle tunneling is suppressed, the system poses no problems[1]. The situation changes when the condensates are

[1] Hofferberth et al. [61] presented a detailed experimental study of the time evolution of the phase randomization of a BEC. As initial setup, they considered a BEC, which was abruptly splitted into two fractions separated by a barrier. The barrier was chose high and broad enough to completely suppressed the tunneling and sufficiently low to provide a weak link between the condensates. After some time they released the trap, permitting the condensates to mix. Taking pictures of the matter waves interference patters, they were able to extract the

linked by changing the shape of the trapping potential. This induces a Josephson-like tunneling of particles from one condensate to the other. Consequently, decoherence sets in and the relative phase can be measured.

The bosonic Josephson oscillations have been already studied in the context of the two-mode approximation [62–64] and the two-site Bose-Hubbard model (TSBH) [65]. The two-mode approximation is restricted to the low-energy regime and is expressed in terms of the GPE. The dynamics of the system are well described in terms of the interwell population imbalance and the relative phase. Smerzi et al. [62] showed that the underlying equations of motion can be mapped onto equations describing a "mathematical pendulum" (see also sec. 4.1). The results were experimentally confirmed by Oberthaler et al. [54] and can be nicely summarized in a phase-space portrait of the canonical conjugated variables (see right panel of fig. 4.1 and both panels of fig. 4.4). Moreover, studies of the TSBH described the quantum nature of the system. Without any further approximation, this approach is limited to small particle numbers. In this thesis, we will also study the TSBH using the non-equilibrium extension of the Bogoliubov theory for Bosons below the critical temperature.

An understanding of how the Bose Josephson junctions work is crucial for various applications, such as quantum optics with interacting matter waves [66–68], atomic circuits [69], which is an important step towards the realization of an atomic superconducting quantum interference device (SQUID). The realization of Josephson junctions and its physics is also relevant for the merging of BECs, and the production of a continuous source of condensed atoms [70–72].

In this chapter we present a detailed study of the temporal non-equilibrium dynamics of two Josephson-coupled BECs after non-adiabatically switching on the Josephson coupling, including interatomic interactions as well as single particle excitations. Now, we proceed to discuss the two-mode approximation, which provides the ground for our non-equilibrium extensions.

4.1 Two-Mode or Mean-Field Approximation

Now, we proceed to investigate the coherent tunneling of particles between two BEC's with very large number of atoms ($\sim 10^3 - 10^5$) at zero temperature. In order to do so, we consider two completely isolated condensates, that were brought adiabatically in contact, permitting the exchange of particles. Lets say the condensates are initially trapped in the separated wells of a double-well potential. The barrier separating them is assumed to be infinitely high, so that they can be regarded as isolated. Then, we lower the barrier adiabatically and end up with a system consisting of two BECs separated by finite potential barrier. The tunneling of particles between two BEC's is represented by the overlap of their macroscopic wave functions. This overlap is exponentially suppressed in the region of the barrier, but it still has a finite value.

In this section we want to develop a theory that describes the coherent exchange of particles between the condensates. This description is based on the mean-field approximation introduced in section 3.3. We consider condensates with a large number of particles that are brought into contact adiabatically. This allows us to regard the density of quantum fluctuations as negligible small, and justifies the replacement of the bosonic field operator $\hat{\Psi}(\mathbf{r}, t)$ with its expectation value $\Psi_0 = \langle \hat{\Psi} \rangle$ in the Hamiltonian 3.1. As we are concerned with the temporal dynamics of

relative phase between the condensates. Repetition of the experiment yielded a phase randomization, which increased with the time waited before mixing the condensates and with the heights and widths of the barrier.

the junction, we use the Ansatz

$$\begin{aligned}\Psi_0(\mathbf{r},t) &= \sum_{\alpha=1,2}\phi_\alpha(\mathbf{r})a_\alpha(t)\\ &= \phi_1(\mathbf{r})a_1(t)+\phi_2(\mathbf{r})a_2(t),\end{aligned} \tag{4.2}$$

for the order parameter, with $a_\alpha(t)=\sqrt{N_\alpha(t)}e^{i\theta_\alpha(t)}$ as the uniform amplitudes of the condensates. Note that the subscript 0 on the left side of the equation refers to the order parameter, and 1 and 2 on the right side to the left and right condensates, respectively. $\phi_1(\mathbf{r})$ and $\phi_2(\mathbf{r})$ are linear combinations of the symmetric and antisymmetric solutions of the stationary double-well trap, which correspond to the lowest eigenvalues, i.e. $\int \mathrm{d}\mathbf{r}\,\phi_\alpha\phi_\beta=\delta_{\alpha\beta}$. For simplicity we assume these functions to be real. Throughout this chapter, we will use greek indices to refer to the left (1) and right (2) condensates. The reason for this will become clear in the succeeding section, when we extent our analysis in order to include the quantum fluctuations.

Inserting the Ansatz 4.2 into the Hamilton operator 3.1, we obtain the mean-field Hamiltonian,

$$H=\sum_{\alpha,\beta}E_{\alpha\beta}\,a_\alpha^*a_\beta+\frac{1}{2}\sum_{\alpha,\beta}\sum_{\gamma,\delta}U_{\alpha\beta\gamma\delta}\,a_\alpha^*a_\beta^*a_\gamma a_\delta, \tag{4.3}$$

where

$$E_{\alpha\beta}=\int \mathrm{d}\mathbf{r}\,\phi_\alpha(\mathbf{r})\left(-\frac{\boldsymbol{\nabla}^2}{2m}+V_{\mathrm{ext}}(\mathbf{r})\right)\phi_\beta(\mathbf{r}), \tag{4.4}$$

and

$$U_{\alpha\beta\gamma\delta}=g\int \mathrm{d}\mathbf{r}\,\phi_\alpha(\mathbf{r})\phi_\beta(\mathbf{r})\phi_\gamma(\mathbf{r})\phi_\delta(\mathbf{r}). \tag{4.5}$$

From now on, we will assume the trap to be symmetric and set the on-site energies $E_{11}=E_{22}=0$. Additionally, we will consider only on-site repulsion, i.e. $U_{\alpha\beta\gamma\delta}=U$, for $\alpha=\beta=\gamma=\delta$. Thus, we obtain

$$H = -J\left(a_1^*a_2+a_2^*a_1\right)+\frac{U}{2}\left[\left(a_1^*a_1\right)^2+\left(a_2^*a_2\right)^2\right] \tag{4.6}$$

$$= -J\left(a_1^*a_2+a_2^*a_1\right)+\frac{U}{4}\left(a_1^*a_1+a_2^*a_2\right)^2+\frac{U}{4}\left(a_1^*a_1-a_2^*a_2\right)^2, \tag{4.7}$$

where $E_{12}=E_{21}=-J$ is the "Josephson coupling". Notice that the Hamiltonian 4.6 is equivalent to the TSBH Hamiltonian within the mean-field approximation. We will discuss the TSBH in more detail in chapter 5. Replacing the uniform amplitudes $a_\alpha(t)$ by $\sqrt{N_\alpha}e^{i\theta_\alpha(t)}$, we get

$$H=-J\sqrt{N^2-(N_1-N_2)^2}\cos\theta+\frac{U}{4}N^2+\frac{U}{4}\left(N_1-N_2\right)^2, \tag{4.8}$$

where $N=N_1+N_2$ is the total particle number and $\theta=\theta_1-\theta_2$ is the relative phase difference between the condensates. In order to absorb the large factors due to the large particle number, we introduce the dimensionless mean-field Hamiltonian,

$$H\equiv\left(\frac{H}{JN}\right)=-\sqrt{1-z^2}\cos\theta+\frac{u}{4}z^2, \tag{4.9}$$

with $u = UN/J$ and

$$z = \frac{N_1 - N_2}{N} \tag{4.10}$$

as the dimensionless interaction parameter and the normalized interwell population imbalance, respectively.

Note that the term proportional N^2 does not appear in eq. 4.9. The conservation of the total particle number allows us to perform an adequate rotation of the amplitudes a_α in order to get rid of the terms proportional to N.

The variables z and θ are canonically conjugated and their time evolution can be computed from the Hamilton's equations,

$$\dot{z} = -\frac{\partial H}{\partial \theta}, \quad \text{and} \quad \dot{\theta} = \frac{\partial H}{\partial z}, \tag{4.11}$$

which are given by

$$\dot{z} = -\sqrt{1 - z^2}\sin\theta, \tag{4.12}$$

$$\dot{\theta} = \frac{z}{\sqrt{1 - z^2}}\cos\theta + \frac{u}{2}z. \tag{4.13}$$

In a simple classical mechanics analogy, this system of non-linear coupled differential equations for θ and z corresponds to a "non-rigid pendulum", of tilt angle θ and a length proportional to $\sqrt{1 - z^2}$, that decreases with the "angular momentum" z [62]. Moreover, these equations for the dynamical variables resemble (apart from their non-linear generalizations) the equations describing a superconductor Josephson junction [63]. There are, however, differences between the physics of Bose Josephson junctions and superconductor Josephson junctions. The superconductor Josephson junctions are often discussed in terms of a rigid pendulum analogy, while the description of Bose Josephson junctions requires the extension of this analogy to the non-rigid pendulum. Nevertheless, the question arises, wether a boson Josephson junction can exhibit the full range of effects of a superconductor Josephson junction or not. For a brief summary on the different effects exhibited by the superconductor Josephson junctions we refer to [63]. At the first glance, it appears not to be the case, because of the charge neutrality of the atoms trapped in the double-well potential. Nonetheless, the experimentalist's ability to customize atomic traps and the interactions between the condensate particles compensates the electric neutrality of the atoms, i.e., an initial asymmetric preparation of the population of the two wells can be regarded as the analogous to the applied bias voltage in a superconductor Josephson junction. In addition, the non-linear interatomic interaction $\sim uz^2$ plays the role of a junction capacitance energy [63].

A detailed analysis of eq. 4.12 and 4.13 requires the study of the interplay between the three parameters: the initial interwell population imbalance $z(0)$ and relative phase between the two condensates $\theta(0)$, and the dimensionless on-site repulsion u. The analytic solutions for θ and z can be given in terms of the Jacobian and Weierstrassian elliptic function [63]. In the following, we will consider three different regimes for an initial relative phase $\theta(0) = 0$. We refer to [63] for a review on the π-junctions ($\theta(0) = \pi$),

Non-interaction regime

In this limit we consider negligibly small interatomic interaction ($u \approx 0$). Rabi-like

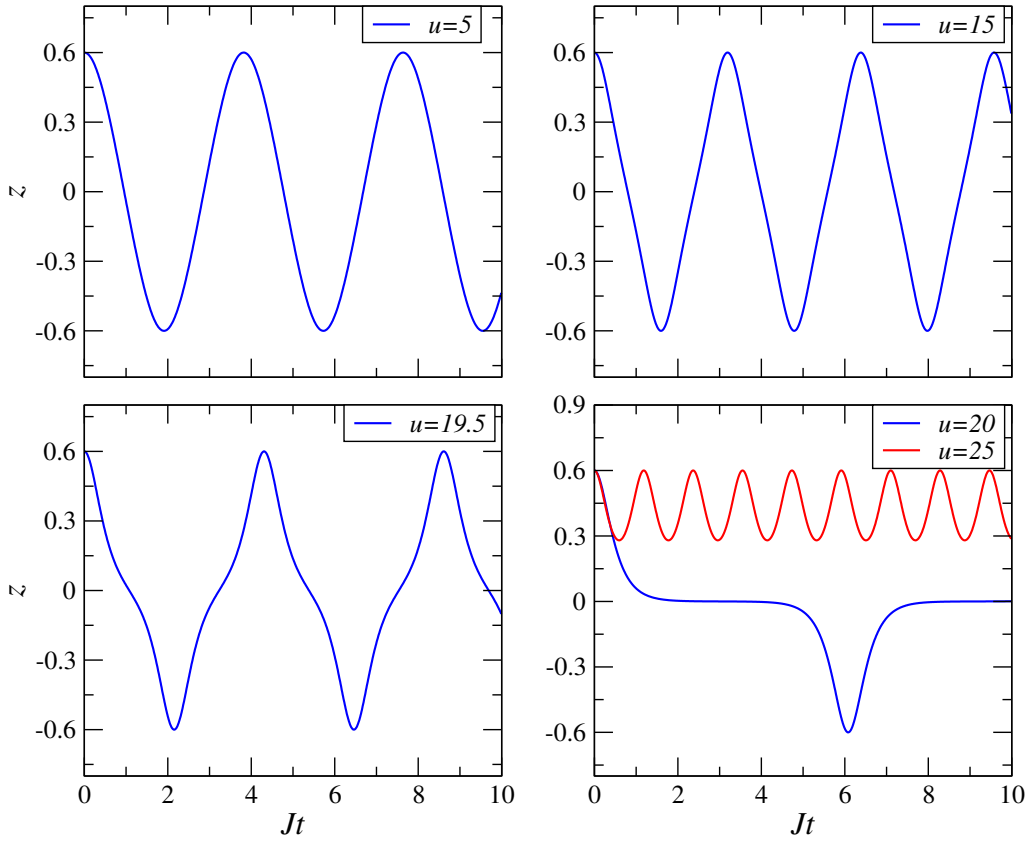

Figure 4.2: Interwell population imbalance z as function of time t for increasing interactomic interactions parameter u and fixed initial imbalance $z(0) = 0.6$.

oscillations in the population of each trap with the frequency

$$\omega_{\mathrm{R}} = J \tag{4.14}$$

are exhibited by eq. 4.12 and 4.13. These oscillations are equivalent of a single-atom dynamics, rather than a Josephson effect arising from the interaction between BECs.

Linear regime

For small amplitude oscillations ($|z| \ll 1$ and $|\theta| \ll 1$), the eq. 4.12 and 4.13 become

$$\dot{z} \approx -\theta, \tag{4.15}$$

$$\dot{\theta} \approx \left(1 + \frac{u}{2}\right) z. \tag{4.16}$$

These equations describe small amplitude or plasma oscillations for a sinusoidal $z(t)$ with frequency

$$\omega_{\mathrm{L}} = \sqrt{J^2 + \frac{NUJ}{2}}, \tag{4.17}$$

and show interwell atomic tunneling dynamics with a zero time-averaged phase across the junction, i.e. $\langle\theta(t)\rangle = 0$ and $\langle z(t)\rangle = 0$.

Moreover, we can justify the neglect of the spatial variations of the z and θ, since the Josephson-like length $\lambda_J = 1/\sqrt{2mJ}$, which governs the spatial variations along the junction, is much larger than the length that characterized by the junction area.

Non-linear regime

Numerical solutions of eq. 4.12 and 4.13 show a non-sinusoidal behavior for the interwell population imbalance z, which can be understood as an anharmonic generalization of the sinusoidal Josephson effec that is exhibited in the regime of small amplitude oscillations. The anharmonicity in the solutions increases with the initial population imbalance $z(0)$ for a fixed interatomic interaction u (fig. 4.3), or with u for a fixed $z(0)$ (fig. 4.2). In the non-rigid pendulum analogy these anharmonic oscillations correspond to large amplitude oscillations of the pendulum.

In addition to these large amplitude oscillations, other remarkable effects happen in Bose Josephson junctions. For instance, if the interaction parameter u exceeds a critical value u_c for a fixed initial population imbalance, the junction will exhibit a "self-locked" population imbalance. In other words, the populations become "macroscopically self-trapped" with a non-zero time-averaged population imbalance, i.e., $\langle z\rangle \neq 0$.

The macroscopic self-trapped state can be understood in terms of the pendulum analogy. Assume, that the initial population imbalance is prepared such, that it corresponds to an initial kinetic energy $uz(0)^2$ that exceeds the potential barrier represented by the vertically displaced ($\theta = \pi$) pendulum orientation. In this the case, a steady self sustained pendulum rotation will happen with a non-vanishing time-averaged angular momentum $\langle z\rangle$.

We will use the pendulum analogy to formulate an expression for the critical value u_c of the interaction parameter. According to the pendulum analogy the system can only be macroscopically self-trapped, if its total energy is larger than the hopping energy, i.e., if it is larger than the energy corresponding to the Josephson junction effect. Consequently, we can write

$$H(z(0),\theta(0)) = -\sqrt{1-z(0)^2}\cos\theta(0) + \frac{u}{4}z(0)^2 > 1, \tag{4.18}$$

where we used the energy conservation and $H(z(0),\theta(0))$ is the energy at $t = 0$. Finally, the condition for the macroscopic self-trapping in terms of the interactions parameter reads

$$u > u_c \equiv \frac{1+\sqrt{1-z(0)^2}\cos\theta(0)}{z(0)^2/4}. \tag{4.19}$$

The macroscopic self-trapped state can be achieved by preparing a series of experiments with fixed initial population imbalance $z(0)$ and relative phase $\theta(0)$ for different interaction parameters u. This can be done by changing the geometry of the trap or varying the total number of atoms involved in the experiments [54].

Alternatively, for fixed trap geometry, total number of particles and relative phase difference, the macroscopic self-trapped state can be realized by varying the initial interwell population imbalance. This procedure defines a critical population imbalance z_c, that describes the transition from large amplitude oscillations with $\langle z\rangle = 0$ to the macroscopic self-trapped state for increasing initial population imbalances.

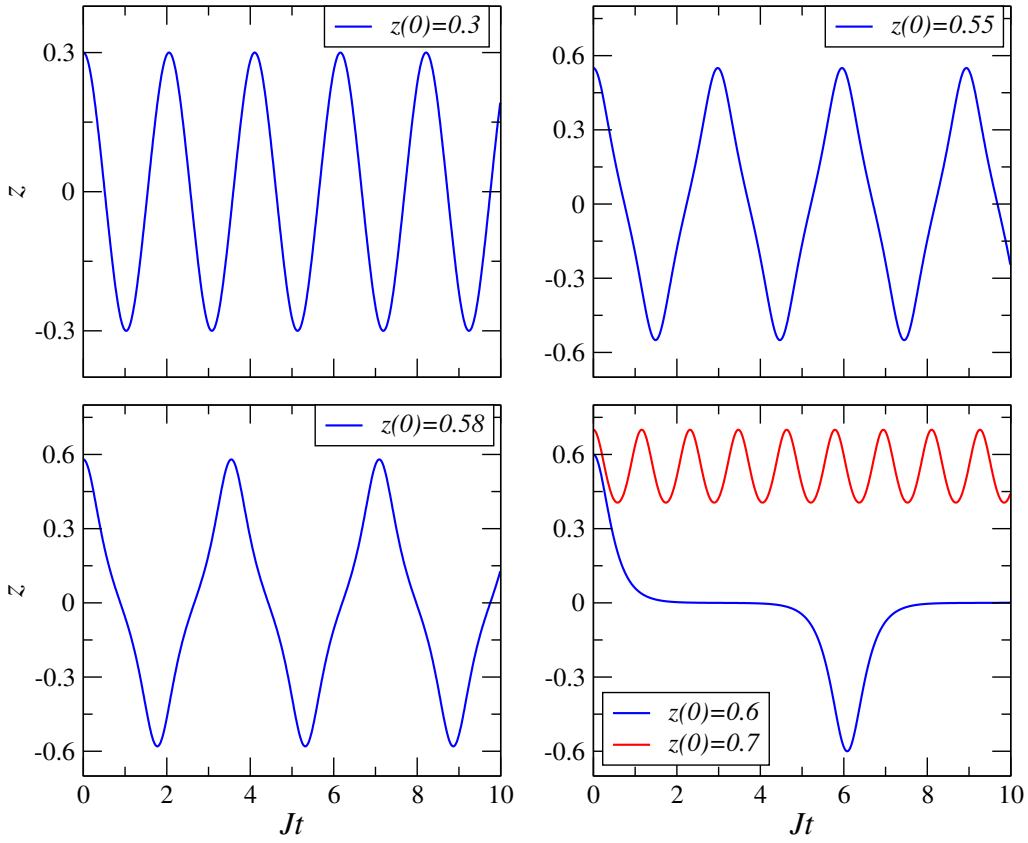

Figure 4.3: Population imbalance z between the two wells as a function of time for increasing initial imbalance $z(0)$ for a fixed interaction parameter $u = 20$.

The dynamical behavior of a Bose Josephson junction can be summarized quite conveniently in terms of a phase-space portrait of the two dynamical variables, z and θ, as shown in fig. 4.4. The upper panel shows the trajectories for different interaction parameters u and fixed initial population imbalance $z(0) = 0.6$. The closed trajectories (violet, orange and green lines) show the dynamics of the system for the phase θ and imbalance z oscillating around zero. The violet line ($u = 5$) corresponds to the linear regime, when the amplitude oscillations are small, i.e. $|\theta| \ll 1$ and $|z| \ll 1$. Increasing the interaction parameter the trajectories become anharmonic (orange and green line for $u = 15$ and $u = 19.5$, respectively) until we observe large amplitude oscillations in the dynamical variables. The blue trajectory corresponds to the critical interactions parameter $u_c = 20$, and describes the transition to the self-trapped state for increasing u. We observe that above u_c that the trajectory is not closed. The time average of the population imbalance has a non-zero value and the relative phase increases as function of time. In the pendulum analogy, this corresponds to a self-sustained rotation. Similarly, in the lower panel we show the phase-space portrait for fixed interaction $u = 20$ for different initial population imbalances $z(0)$. The closed trajectories describe the linear regime for small amplitude oscillations (violate line for $z(0) = 0.3$) and the anharmonic Bose Josephson oscillations between the condensates (orange and green lines for $z(0) = 0.55$ and $z(0) = 0.58$).

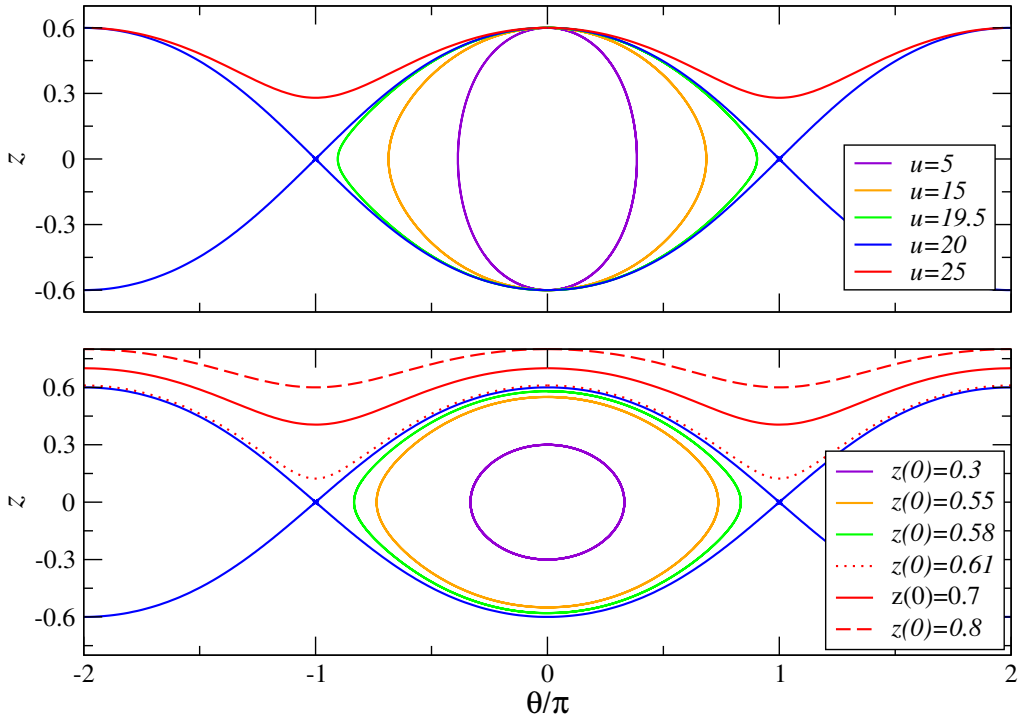

Figure 4.4: Phase-space portraits of the dynamical variables z and θ. In the upper panel the trajectories are given for fixed initial population imbalance $z(0) = 0.6$ and increasing interaction parameter u. In the lower panel the interaction parameter $u = 20$ is kept fix for increasing initial population imbalance $z(0)$.

The blue line ($z(0) = 0.6$) shows the large amplitude oscillations of the interwell population imbalance around zero, and describes the transition into the self-trapped regime. The critical initial population imbalance $z_c(0)$ is obtained by solving eq. 4.19 in favor of $z(0)$. The three red trajectories at the top of the lower panel correspond to macroscopic self-trapped states.

4.2 Beyond the Two-Mode Approximation

The two-mode approximation, which we reviewed in the previous section, provides a good a description of the dynamics of Bose Josephson junctions. However, experimentally the Josephson junction is prepared in a non-equilibrium situation by suddenly ramping up the barrier between the condensates, in a non-adiabatic way. The damping of the Josephson oscillations due to quasiparticle excitations has been estimated for this situation [59]. Nevertheless, this damping has not been observed for small traps [54, 56], revealing an incomplete understanding of the non-equilibrium dynamics.

Now we proceed to develop a detailed theory of the temporal dynamics of two non-adiabatically

Josephson-coupled BECs. Interactomic interactions and single particle excitations are included in our analysis. Initially, the experiment is prepared, such that the barrier between two wells can be regarded as infinitely high, so that the coherent tunneling of particles is completely suppressed. Moreover, we assume all the bosons to be condensed, and both condensates to be in the equilibrium state. Suddenly, at time $t = 0$ the barrier is lowered and the Josephson weak link between the two wells is established. This non-adiabatic switching on of the interwell tunneling drives the system out of thermodynamic equilibrium.

In order to develop a general non-equilibrium theory for this situation and analyze its dynamics, we represent the Hamiltonian 3.1 in a complete basis of the exact single particle eigenstates of the double-well potential $V_{\rm ext}(\mathbf{t}, t > 0)$ after switching on the Josephson coupling J. In this basis the field operator reads

$$\hat{\Psi}(\mathbf{r}, t) = \phi_1(\mathbf{r})a_1(t) + \phi_2(\mathbf{r})a_2(t) + \sum_{n\neq 0} \varphi_n(\mathbf{r})\hat{b}_n(t), \tag{4.20}$$

where $\phi_1(\mathbf{r})$, $\phi_2(\mathbf{r})$ are linear combinations of the symmetric and antisymmetric solutions, which correspond to the lowest eigenvalues of the stationary double-well trap after lowering the barrier. They were introduced in the previous section in the context of the two-mode approximation.The "c-numbers", $a_\alpha(t) = \sqrt{N_\alpha(t)}e^{i\theta_\alpha(t)}$, $\alpha = 1, 2$, are the corresponding condensate amplitudes. This semiclassical treatment of the BECs neglects phase fluctuations and is justified for the experiments [54] with fixed phase relation and sufficiently large number of particles. The single particle excitations dynamics will be treated quantum mechanically. The index $n \neq 0$ enumerates the exact single particle excited states, with $\varphi_n(\mathbf{r})$ and $\hat{b}_n(t)$ as the corresponding eigenfunctions and bosonic destruction operators, respectively. Including the single particle excitations, we go beyond the two-mode approximation (see Section 4.1).

Inserting the field operator 4.20 into the Hamiltonian 3.1, we get

$$\hat{H} = H_{\rm BEC} + \hat{H}_{\rm qp} + \hat{H}_{\rm mix}, \tag{4.21}$$

for $t > 0$. $H_{\rm BEC}$ describes the condensate particles,

$$H_{\rm BEC} = \sum_{\alpha,\beta} E_{\alpha\beta}\, a^*_\alpha a_\beta + \frac{1}{2}\sum_{\alpha,\beta}\sum_{\gamma,\delta} U_{\alpha\beta\gamma\delta}\, a^*_\alpha a^*_\beta a_\gamma a_\delta, \tag{4.3}$$

where $E_{\alpha\beta}$ are $U_{\alpha\beta\gamma\delta}$ are defined by eqs. 4.4 and 4.5, respectively. Note, that the hat is missing, because $H_{\rm BEC}$ only involves the condensate amplitudes, which are c-numbers. $\hat{H}_{\rm qp}$ corresponds to the single particle excitations,

$$\hat{H}_{\rm qp} = \sum_{n,m\neq 0} E_{nm}\, \hat{b}^\dagger_n \hat{b}_m + \frac{1}{2}\sum_{n,m}\sum_{\ell,s} V_{nm\ell s}\, \hat{b}^\dagger_n \hat{b}^\dagger_m \hat{b}_\ell \hat{b}_s, \tag{4.22}$$

where

$$E_{nm} = \int \mathrm{d}\mathbf{r}\, \varphi_n(\mathbf{r}) \left(-\frac{\boldsymbol{\nabla}^2}{2m} + V_{\rm ext}(\mathbf{r}) \right) \varphi_m(\mathbf{r}) = E_n \delta_{nm} \tag{4.23}$$

are the (bare) energy levels of the excited states, and

$$V_{nm\ell s} = g \int \mathrm{d}\mathbf{r}\, \varphi_n(\mathbf{r})\varphi_m(\mathbf{r})\varphi_\ell(\mathbf{r})\varphi_s(\mathbf{r}) \tag{4.24}$$

is the repulsive interaction between non-condensed particles. The mixing between the BECs and the excited states is described by

$$\begin{aligned}\hat{H}_{\rm mix} &= \frac{1}{2}\sum_{\alpha,\beta}\sum_{n,m} K_{\alpha\beta nm}\left[\left(a_\alpha^* a_\beta^* \hat{b}_n \hat{b}_m + \text{h.c.}\right) + 4 a_\alpha^* \hat{b}_n^\dagger a_\beta \hat{b}_m\right] \\ &\quad + \sum_{\alpha}\sum_{n,m,s} R_{\alpha nms}\left[a_\alpha^* \hat{b}_n^\dagger \hat{b}_m \hat{b}_s + \text{h.c.}\right], \end{aligned} \tag{4.25}$$

where

$$K_{\alpha\beta nm} = g\int \mathrm{d}\mathbf{r}\, \phi_\alpha(\mathbf{r})\phi_\beta(\mathbf{r})\varphi_n(\mathbf{r})\varphi_m(\mathbf{r}), \tag{4.26}$$

$$R_{\alpha nm} = g\int \mathrm{d}\mathbf{r}\, \phi_\alpha(\mathbf{r})\varphi_n(\mathbf{r})\varphi_m(\mathbf{r})\varphi_s(\mathbf{r}) \tag{4.27}$$

are the overlap matrix elements involving two and three non-condensed particles, respectively. Note, that we use greek indices, i.e. $\alpha, \beta = 1, 2$ to denote the left and right condensate, and the latin indices $n, m \neq 0$ to enumerate the exact single particle excited states. In Fig. 4.5 we show the elementary processes corresponding to each of the different terms in eq. 4.25, and the two-particle interaction terms in eqs. 4.3 and 4.22. Note that only terms quadratic, cubic, and quartic in the single particle operators $\hat{b}_n$ and $\hat{b}_m^\dagger$ appear in eq. 4.21.

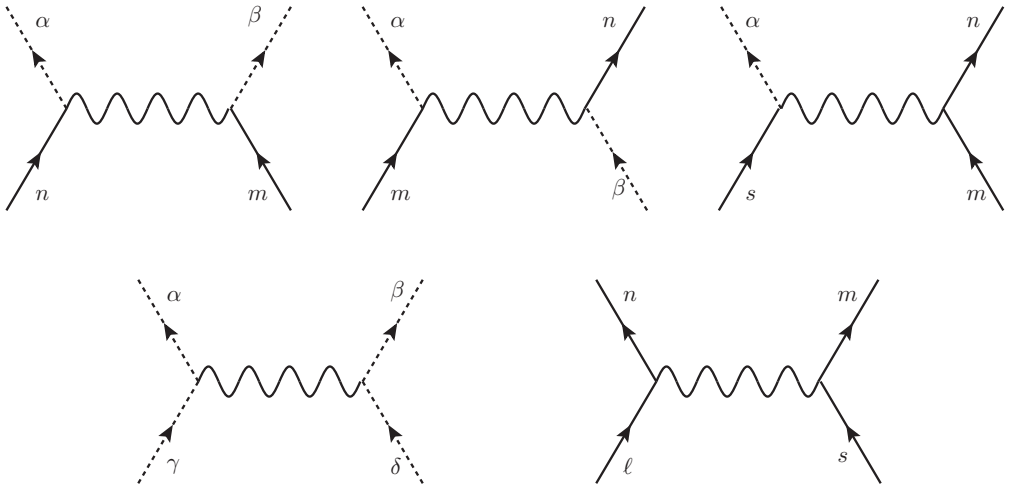

Figure 4.5: The dotted and solid lines represent the condensate and non-condensate particles, respectively. The greek labels attached to the condensate lines refer to the left and right condensate, and the latin letters attached to the solid lines to the excited levels. The wavy lines are associated to the interatomic potential, i.e., $K_{\alpha\beta nm}$ for the first two diagrams in the upper row, $R_{\alpha n\ell s}$ for the last in the upper row. $U_{\alpha\beta\gamma}$ and $V_{nm\ell s}$ for the left and right diagrams in the lower row.

From now on, we restrict our analysis to symmetric double-well potentials. We set $E_{11} = E_{22} = 0$, according to section 4.1 and introduce the Josephson coupling $E_{12} = E_{21} = -J$. In addition, we distinguish between processes involving two condensate particles associated to the

same condensate and two condensate particles associated to different condensates:

$$K_{\alpha\beta nm} = \begin{cases} K/2, & \alpha = \beta \\ J'/2, & \alpha \neq \beta \end{cases}, \quad \forall n, m \neq 0. \tag{4.28}$$

Here, the coupling constant J' can be regarded as a quasiparticle assisted Josephson tunneling, as well as a pairwise "simultaneous" quasiparticle creation or destruction out both condensates. K represents the density-density interaction of condensed and non-condensed particles and the pairwise quasiparticle creation or destruction out of each condensate.

The experimental realization of double-well potential involves the overlap of a three dimensional harmonic confinement and a one dimensional periodic potential with a sufficiently large period [54, 60]. This allows us to assume that the wave functions of the excited states extend over both wells, as it is shown in fig. 4.6. For simplicity, we suppose that energy levels of the excited states coincide with the higher states of the three dimensional harmonic confinement and are, therefore, equidistant. The level spacing is given by

$$\Delta = E_{n+1} - E_n. \tag{4.29}$$

In general, the overlap matrix elements $K_{\alpha\beta nm}$, $U_{\alpha\beta\gamma}$ and $R_{\alpha nms}$ depend on the trap geometry and total number of particles. Consequently, they should be computed from the solutions of the stationary GPE for a double-well trap. Nevertheless, this is not the subject of our discussion and in order to keep things manageable for our numerical analysis, we will overestimate the two-body processes described by $K_{\alpha\beta nm}$, $V_{nm\ell s}$ and $R_{\alpha mms}$ by setting them equal to their respective maximal values[2]. They will be considered as input parameters of our model. After these simplifications, the contributions to the Hamiltonian 4.21 read

$$H_{\mathrm{BEC}} = -J\left(a_1^* a_2 + a_2^* a_1\right) + \frac{U}{2}\sum_{\alpha} a_\alpha^* a_\alpha^* a_\alpha a_\alpha, \tag{4.30}$$

$$\hat{H}_{\mathrm{qp}} = \sum_n E_n \hat{b}_n^\dagger \hat{b}_n + \frac{U'}{2}\sum_{n,m}\sum_{\ell,s} \hat{b}_n^\dagger \hat{b}_m^\dagger \hat{b}_\ell \hat{b}_s, \tag{4.31}$$

$$\begin{aligned} \hat{H}_{\mathrm{mix}} = {} & J'\sum_{n,m}\left[\left(a_1^* a_2 + a_2^* a_1\right)\hat{b}_n^\dagger \hat{b}_m + \frac{1}{2}\left(a_1^* a_2^* \hat{b}_n \hat{b}_m + \mathrm{h.c}\right)\right] \\ & + K\sum_{\alpha}\sum_{n,m}\left[a_\alpha^* a_\alpha \hat{b}_n^\dagger \hat{b}_m + \frac{1}{4}\left(a_\alpha^* a_\alpha^* \hat{b}_n \hat{b}_m + \mathrm{h.c}\right)\right] \\ & + R\sum_{\alpha}\sum_{n,m,s}\left[a_\alpha^* \hat{b}_n^\dagger \hat{b}_m \hat{b}_s + \mathrm{h.c.}\right]. \end{aligned} \tag{4.32}$$

In order to describe the non-equilibrium dynamics of the system, we proceed according to the methods presented in chapter 3. Using the bosonic field operator 4.20, we obtain

$$\boldsymbol{C}(1,1') = \sum_{\alpha,\beta=1}^{2} \phi_\alpha(\mathbf{r})\phi_\beta(\mathbf{r}')\boldsymbol{C}_{\alpha\beta}(t,t') \tag{4.33}$$

[2] The solution of the stationary symmetric double-well potential are symmetric and antisymmetric functions. Inserting these eigenfunctions in the definitions of $K_{\alpha\beta nm}$, $V_{nm\ell s}$ and $R_{\alpha mms}$ will yield forbidden transitions between some of the levels. A more realistic model requires the computations of the these eigenfunctions prior solving the time-dependent problem.

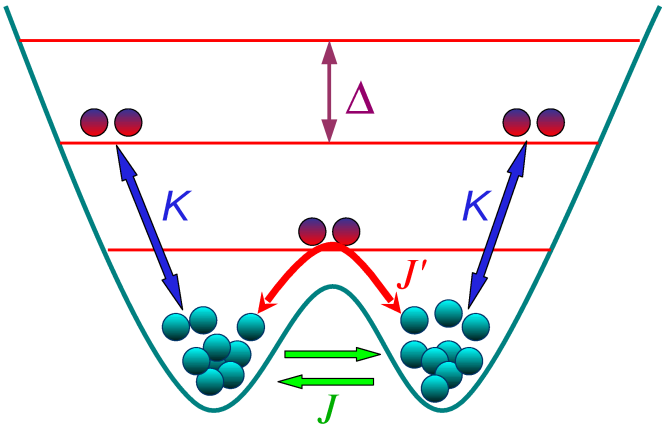

Figure 4.6: A BEC in a double-well potential after abrupt decrease of the barrier height. The definitions of the parameters are explained in the text, see eqs. 4.30 - 4.32. Figure taken from [44]

and

$$\boldsymbol{G}(1,1') = \sum_{n,m\neq 0} \varphi_m(\mathbf{r})\varphi_n(\mathbf{r}')\boldsymbol{G}_{nm}(t,t') \tag{4.34}$$

for the condensate propagator 3.2 and the non-condensate propagator 3.3 , respectively. The time-depentent parts of the propagators, read

$$\boldsymbol{C}_{\alpha\beta}(t,t') = -i\begin{pmatrix} a_\alpha(t)a^*_\beta(t') & a_\alpha(t)a_\beta(t') \\ a^*_\alpha(t)a^*_\beta(t') & a^*_\alpha(t)a_\beta(t') \end{pmatrix}, \tag{4.35}$$

$$\begin{aligned} \boldsymbol{G}_{nm}(t,t') &= -i\begin{pmatrix} \langle T_C \hat{b}_n(t)\hat{b}^\dagger_m(t')\rangle & \langle T_C \hat{b}_n(t)\hat{b}(t')\rangle \\ \langle T_C \hat{b}^\dagger_n(t)\hat{b}^\dagger_m(t')\rangle & \langle T_C \hat{b}^\dagger_n(t)\hat{b}_m(t')\rangle \end{pmatrix} \\ &= \begin{pmatrix} G_{nm}(t,t') & F_{nm}(t,t') \\ \overline{F}_{nm}(t,t') & \overline{G}_{nm}(t,t') \end{pmatrix}. \end{aligned} \tag{4.36}$$

T_C was introduced in chapter 2 and denotes the time ordering operator along the CTP. Using the real-time formalism (see section 2.2) for the associated Dyson's equations on the real time contour yields

$$\int_{-\infty}^{\infty} \mathrm{d}\bar{t}\,\left[\boldsymbol{G}^{-1}_{0,\alpha\gamma}(t,\bar{t}) - \boldsymbol{S}^{HF}_{\alpha\gamma}(t,\bar{t})\right]\boldsymbol{C}_{\gamma\beta}(\bar{t},t') = -i\int_{-\infty}^{t} \mathrm{d}\bar{t}\,\boldsymbol{\gamma}_{\alpha\gamma}(t,\bar{t})\boldsymbol{C}_{\gamma\beta}(\bar{t},t'), \tag{4.37}$$

$$\begin{aligned} \int_{-\infty}^{\infty} \mathrm{d}\bar{t}\,\left[\boldsymbol{G}^{-1}_{0,n\ell}(t,\bar{t}) - \boldsymbol{\Sigma}^{HF}_{n\ell}(t,\bar{t})\right]\boldsymbol{G}^{\gtrless}_{\ell m}(\bar{t},t') &= -i\int_{-\infty}^{t} \mathrm{d}\bar{t}\,\boldsymbol{\Gamma}_{n\ell}(t,\bar{t})\boldsymbol{G}^{\gtrless}_{\ell m}(\bar{t},t') \\ &\quad + i\int_{-\infty}^{t'} \mathrm{d}\bar{t}\,\boldsymbol{\Sigma}^{\gtrless}_{n\ell}(t,\bar{t})\boldsymbol{A}_{\ell m}(\bar{t},t'), \end{aligned} \tag{4.38}$$

where we summed over all greek indices appearing twice in every term from 1 to 2, which refer

to the left and right condensates. The summation over the latin is take over the excited states. Here we decomposed the self-energies into the Hartree-Fock local parts $\boldsymbol{S}^{HF}_{\alpha\beta}(\boldsymbol{\Sigma}^{HF}_{nm})$ and the non-local parts $\boldsymbol{S}_{\alpha\beta}(\boldsymbol{\Sigma}_{nm})$. The inverse propagators on the left side of eq. 4.37 and 4.38 are given by

$$\boldsymbol{G}^{-1}_{0,\alpha\beta}(t,t') = \left[i\boldsymbol{\tau}_3\delta_{\alpha\beta}\frac{\partial}{\partial t} - E_{\alpha\beta}\mathbb{1}\right]\delta(t-t') \tag{4.39}$$

and

$$\boldsymbol{G}^{-1}_{0,nm}(t,t') = \left[i\boldsymbol{\tau}_3\delta_{nm}\frac{\partial}{\partial t} - E_{nm}\mathbb{1}\right]\delta(t-t') \tag{4.40}$$

respectively. $\boldsymbol{\tau}_3$ denotes the third Pauli matrix and is defined in eq. 3.7. We also introduced the non-condensate particles spectral function

$$\begin{aligned}\boldsymbol{A}_{nm}(t,t') &= i\left[\boldsymbol{G}^{>}_{nm}(t,t') - \boldsymbol{G}^{<}_{nm}(t,t')\right] \\ &= \begin{pmatrix} A^{G}_{nm}(t,t') & A^{F}_{nm}(t,t') \\ -A^{F}_{nm}(t,t')^* & -A^{G}_{nm}(t,t')^*\end{pmatrix},\end{aligned} \tag{4.41}$$

and the spectral function of the non-local self-energies are given by

$$\begin{aligned}\boldsymbol{\gamma}_{\alpha\beta}(t,t') &= i\left[\boldsymbol{S}^{>}_{\alpha\beta}(t,t') - \boldsymbol{S}^{<}_{\alpha\beta}(t,t')\right] \\ &= \begin{pmatrix} \gamma^{G}_{\alpha\beta}(t,t') & \gamma^{F}_{\alpha\beta}(t,t') \\ -\gamma^{F}_{\alpha\beta}(t,t')^* & -\gamma^{G}_{\alpha\beta}(t,t')^*\end{pmatrix}\end{aligned} \tag{4.42}$$

and

$$\begin{aligned}\boldsymbol{\Gamma}_{nm}(t,t') &= i\left[\boldsymbol{\Gamma}^{>}_{nm}(t,t') - \boldsymbol{\Gamma}^{<}_{nm}(t,t')\right] \\ &= \begin{pmatrix} \Gamma^{G}_{nm}(t,t') & \Gamma^{F}_{nm}(t,t') \\ -\Gamma^{F}_{nm}(t,t')^* & -\Gamma^{G}_{nm}(t,t')^*\end{pmatrix}.\end{aligned} \tag{4.43}$$

Here, we exploited the symmetries listed in the tables 3.1 and 3.2.

In chapter 3 we discussed that it is convenient to express the dynamics of the system in terms of two-point correlators associated to the commutator and anti-commutator of the bosonic field operators. Thus, we introduce in addition to the spectral functions the non-condensate particles statistical function

$$\begin{aligned}\boldsymbol{F}_{nm}(t,t') &= \frac{1}{2}\left[\boldsymbol{G}^{>}_{nm}(t,t') + \boldsymbol{G}^{<}_{nm}(t,t')\right] \\ &= \begin{pmatrix} F^{G}_{nm}(t,t') & F^{F}_{nm}(t,t') \\ -F^{F}_{nm}(t,t')^* & -F^{G}_{nm}(t,t')^*\end{pmatrix}.\end{aligned} \tag{4.44}$$

The non-condensate non-local self-energy statistical function reads

$$\begin{aligned}\boldsymbol{\Pi}_{nm}(t,t') &= \frac{1}{2}\left[\boldsymbol{\Sigma}^{>}_{nm}(t,t') + \boldsymbol{\Sigma}^{<}_{nm}(t,t')\right] \\ &= \begin{pmatrix} \Pi^{G}_{nm}(t,t') & \Pi^{F}_{nm}(t,t') \\ -\Pi^{F}_{nm}(t,t')^* & -\Pi^{G}_{nm}(t,t')^*\end{pmatrix},\end{aligned} \tag{4.45}$$

Here, we used the symmetry relations in tables 3.1 and 3.2 in order to express the lower components in terms of the upper components.

Expressing the Dyson's equations 4.37 and 4.38 in terms of the spectral and statistical function 4.41 - 4.45, and carefully evaluating the time integration on the left side, we obtain

$$\left[i\boldsymbol{\tau}_3\delta_{\alpha\gamma}\frac{\partial}{\partial t} - E_{\alpha\gamma}\mathbb{1} - \boldsymbol{S}^{HF}_{\alpha\gamma}(t)\right]\boldsymbol{C}_{\gamma\beta}(t,t') = -i\int_0^t \mathrm{d}\bar{t}\,\boldsymbol{\gamma}_{\alpha\gamma}(t,\bar{t})\boldsymbol{C}_{\gamma\beta}(\bar{t},t'), \tag{4.46}$$

$$\left[i\boldsymbol{\tau}_3\delta_{n\ell}\frac{\partial}{\partial t} - E_{n\ell}\mathbb{1} - \boldsymbol{\Sigma}^{HF}_{n\ell}(t)\right]\boldsymbol{A}_{\ell m}(t,t') = -i\int_{t'}^t \mathrm{d}\bar{t}\,\boldsymbol{\Gamma}_{n\ell}(t,\bar{t})\boldsymbol{A}_{\ell m}(\bar{t},t'), \tag{4.47}$$

$$\begin{aligned}\left[i\boldsymbol{\tau}_3\delta_{n\ell}\frac{\partial}{\partial t} - E_{n\ell}\mathbb{1} - \boldsymbol{\Sigma}^{HF}_{n\ell}(t)\right]\boldsymbol{F}_{\ell m}(t,t') &= -i\int_0^t \mathrm{d}\bar{t}\,\boldsymbol{\Gamma}_{n\ell}(t,\bar{t})\boldsymbol{F}_{\ell m}(\bar{t},t') \\ &\quad + i\int_0^{t'} \mathrm{d}\bar{t}\,\boldsymbol{\Pi}_{n\ell}(t,\bar{t})\boldsymbol{A}_{\ell m}(\bar{t},t'),\end{aligned} \tag{4.48}$$

where we use the fact, that the Hartree-Fock self-energies are local in the time arguments, i.e. $\boldsymbol{S}^{HF}_{\alpha\beta}(t,t') = \boldsymbol{S}^{HF}_{\alpha\beta}(t)\delta(t-t')$, and similar for $\boldsymbol{\Sigma}^{HF}_{nm}$. Moreover, some of the integrals start at 0 instead of $-\infty$. This is due to the choice of boundary conditions. Prior $t = 0$ the system is assume to be in equilibrium. These equations of motion describe the dynamics of the system after switching on of the Josephson coupling.

Before we proceed in the succeeding sections to analyze eqs. 4.46 - 4.48 numerically within the framework of the BHF and the full second-order approximation, we want to take a closer look at the conserved quantities. In section 3.4.1, we mentioned that for any isolated system the particle number and the energy are conserved. The mean particle number is expressed in terms of the condensate amplitudes and the diagonal components of the single particle excitations statistical function, i.e.,

$$\begin{aligned}N(t) &= N_1(t) + N_2 + \sum_{n\neq 0} N_b^{(n)} \\ &= \sum_{\alpha=1,2} a^*_\alpha(t)a_\alpha(t) + \sum_{n\neq 0} i\left[F^G_{nn}(t,t) - \frac{1}{2}\right].\end{aligned} \tag{4.49}$$

It can be proven to be constant by making use of the equations of motion for a_α and F^G_{nn}. N is also a convenient quantity for checking the correctness of our numerical calculations.

A closed system (like the double-well potential we considering) excludes dissipation. Working within the framework of a conserving approximation (see section 3.2.1) we can prove that the mean energy,

$$\langle\hat{H}\rangle = \langle\hat{H}\rangle_{\mathrm{BEC}} + \langle\hat{H}\rangle_{\mathrm{qp}}, \tag{4.50}$$

is conserved. The energies of the condensate fraction and the single particle excitations are given by

$$\langle\hat{H}\rangle_{\mathrm{BEC}}(t) = \frac{i}{2}\mathrm{Tr}\left[\left(E_{\alpha\beta}\mathbb{1} + \frac{1}{2}\boldsymbol{S}^{HF}_{\alpha\beta}(t)\right)\boldsymbol{C}_{\beta\alpha}(t,t)\right] + \frac{1}{2}\mathrm{Tr}\left[\int_0^t \mathrm{d}\bar{t}\,\boldsymbol{\gamma}_{\alpha\beta}(t,\bar{t})\boldsymbol{C}_{\beta\alpha}(\bar{t},t)\right] \tag{4.51}$$

and

$$\begin{aligned}\langle \hat{H} \rangle_{\rm qp}(t) &= \frac{i}{2}\mathrm{Tr}\left[\left(E_{nm}\mathbb{1} + \frac{1}{2}\boldsymbol{\Sigma}^{HF}_{nm}(t)\right)\boldsymbol{F}_{nm}(t,t)\right] \\ &\quad + \frac{1}{2}\mathrm{Tr}\left[\int_0^t \mathrm{d}\bar{t}\,\left(\boldsymbol{\Gamma}_{nm}(t,\bar{t})\boldsymbol{F}_{mn}(\bar{t},t) - \boldsymbol{\Pi}_{nm}(t,\bar{t})\boldsymbol{A}_{mn}(\bar{t},t)\right)\right] \\ &\quad + \frac{1}{2}\mathrm{Tr}\left[\int_0^t \mathrm{d}\bar{t}\,\left(\boldsymbol{F}_{nm}(t,\bar{t})\boldsymbol{\Gamma}_{mn}(\bar{t},t) - \boldsymbol{A}_{nm}(t,\bar{t})\boldsymbol{\Pi}_{mn}(\bar{t},t)\right)\right], \end{aligned} \tag{4.52}$$

respectively. Again, we sum over all indices appearing twice in every term according the to the previous explanations.

4.2.1 The Bogoliubov-Hartree-Fock Approximation and the Critical Time τ_c

In section 3.4, we discussed the range of validity of the BHF approximation. In spite of its limitations, such as its failure to include thermalization effects due to the collisions between single particles excitations, it provides a good insight into the non-equilibrium dynamics of Bose Josephson junctions for short times and weak interactions. As we discussed in [44], the initially empty energy levels above the condensates (and the barrier separating them) can be populated by changing the shape of the trapping potential in a non-adiabatic way. The population of these higher energy levels may lead, for instance, to the destruction of an initially prepared localized state due to fast single particle excitations assisted transitions from one well to the other. We reported that beyond a characteristic time τ_c, the dynamics of the system are well explained by rabi-like oscillations between the non-condesate particle levels and the condensates.

In the previous section, we gave a detailed derivation of the Hamiltonian 4.21 describing a system of two condensates in a double-well potential after being non-adiabatically coupled. In addition, we summarized the dynamics of the system in terms of the non-condensate particle spectral function $\boldsymbol{A}_{nm}$ and the statistical function $\boldsymbol{F}_{nm}$, which provide the information about the energy spectrum and the occupation number, respectively. The time evolution of the condensate fraction is characterized by the condensate amplitudes a_α, which are contained in the condensate propagator $\boldsymbol{C}_{\alpha\beta}$. The derivation of the equations of motion 4.46 - 4.48 was general, since we did not specify the self-energies. In this section we analyze the BHF approximation and the effects described by it. In order to do so, we retain only the diagrams first order in the interactions (see figs. 3.1 and 3.2). In section 4.2.2, we will take the higher order processes into account.

Now, dropping the integrals on the right side of eqs. 4.46 - 4.48, we obtain the equations of motion for the two-point correlators in the BHF approximation, i.e.,

$$\left[i\boldsymbol{\tau}_3\delta_{\alpha\gamma}\frac{\partial}{\partial t} - E_{\alpha\gamma}\mathbb{1} - \boldsymbol{S}^{HF}_{\alpha\gamma}(t)\right]\boldsymbol{C}_{\gamma\beta}(t,t') = 0, \tag{4.53}$$

$$\left[i\boldsymbol{\tau}_3\delta_{n\ell}\frac{\partial}{\partial t} - E_{n\ell}\mathbb{1} - \boldsymbol{\Sigma}^{HF}_{n\ell}(t)\right]\boldsymbol{A}_{\ell m}(t,t') = 0, \tag{4.54}$$

$$\left[i\boldsymbol{\tau}_3\delta_{n\ell}\frac{\partial}{\partial t} - E_{n\ell}\mathbb{1} - \boldsymbol{\Sigma}^{HF}_{n\ell}(t)\right]\boldsymbol{F}_{\ell m}(t,t') = 0, \tag{4.55}$$

where

$$\begin{aligned}\boldsymbol{S}^{HF}_{\alpha\beta}(t) &\equiv \begin{pmatrix} S^{HF}_{\alpha\beta}(t) & W^{HF}_{\alpha\beta}(t) \\ W^{HF}_{\alpha\beta}(t)^* & S^{HF}_{\alpha\beta}(t)^* \end{pmatrix} \\ &= i\left(\sum_{\gamma,\delta}\frac{U_{\alpha\beta\gamma\delta}}{2}\mathrm{Tr}\left[\boldsymbol{C}_{\gamma\delta}(t,t)\right]\mathbb{1} + \sum_{\ell,s}K_{\alpha\beta\ell s}\left\{\boldsymbol{F}_{\ell s}(t,t) + \frac{1}{2}\mathrm{Tr}\left[\boldsymbol{F}_{\ell s}(t,t)\right]\mathbb{1}\right\}\right)\end{aligned} \tag{4.56}$$

and

$$\begin{aligned}\boldsymbol{\Sigma}^{HF}_{nm}(t,t') &\equiv \begin{pmatrix} \Sigma^{HF}_{\alpha\beta}(t) & \Omega^{HF}_{\alpha\beta}(t) \\ \Omega^{HF}_{\alpha\beta}(t)^* & \Sigma^{HF}_{\alpha\beta}(t)^* \end{pmatrix} \\ &= i\left(\sum_{\alpha,\beta}K_{nm\alpha\beta}\left\{\boldsymbol{C}_{\alpha\beta}(t,t) + \frac{1}{2}\mathrm{Tr}\left[\boldsymbol{C}_{\alpha\beta}(t,t)\right]\mathbb{1}\right\}\right. \\ &\qquad \left. + \sum_{\ell,s}V_{nm\ell s}\left\{\boldsymbol{F}_{\ell s}(t,t) + \frac{1}{2}\mathrm{Tr}\left[\boldsymbol{F}_{\ell s}(t,t)\right]\mathbb{1}\right\}\right)\end{aligned} \tag{4.57}$$

are the BHF self-energies. Here, we made use of the symmetry relations in table 3.1 to express the two lower components of the self-energies in terms of the upper components. Notice that the only non-condensate related quantity entering the self-energies $\boldsymbol{S}^{HF}$ and $\boldsymbol{\Sigma}^{HF}$ is the non-condensate particle statistical function $\boldsymbol{F}_{nm}$. Consequently, the equation for propagator $\boldsymbol{C}_{\alpha\beta}$ is only coupled to the equation for $\boldsymbol{F}_{nm}$ and decouples from the equation for the spectral function $\boldsymbol{A}_{nm}$. Moreover, due to the absence of the higher order processes, it is not necessary to propagate the solutions for different time arguments (see discussion in section 3.4). In addition, the time evolution of the spectral function $\boldsymbol{A}_{nm}$ for equal time arguments is trivial, since it is fixed for all times due to the bosonic commutation relations. This also justifies the fact, that the system of equations decouples from the equation for $\boldsymbol{A}_{nm}$.

The equation of motion for the condensate amplitude is obtained from the upper left component of eq. 4.53 and dividing by $a^*_\beta(t')$. Thus, we get

$$i\frac{\partial}{\partial t}a_\alpha(t) = \left[E_{\alpha\gamma} + S^{HF}_{\alpha\gamma}(t)\right]a_\gamma(t) + W^{HF}_{\alpha\gamma}(t)a^*_\gamma(t). \tag{4.58}$$

Computing the evolution of $\boldsymbol{F}_{nm}$ for equal time arguments requires special attention. Now, we proceed exactly like in section 3.4, and take the difference and sum of eq. 4.55 with its hermitian conjugated version:

$$i\left(\boldsymbol{\tau}_3\frac{\partial}{\partial t}\boldsymbol{F}_{nm}(t,t') + \frac{\partial}{\partial t'}\boldsymbol{F}_{nm}(t,t')\boldsymbol{\tau}_3\right) = \boldsymbol{\Sigma}^{HF}_{n\ell}(t)\boldsymbol{F}_{\ell m}(t,t') - \boldsymbol{F}_{n\ell}(t,t') + \boldsymbol{\Sigma}^{HF}_{\ell m}(t), \tag{4.59}$$

$$i\left(\boldsymbol{\tau}_3\frac{\partial}{\partial t}\boldsymbol{F}_{nm}(t,t') - \frac{\partial}{\partial t'}\boldsymbol{F}_{nm}(t,t')\boldsymbol{\tau}_3\right) = 2E_n\boldsymbol{F}_{nm}(t,t') + \boldsymbol{\Sigma}^{HF}_{n\ell}(t)\boldsymbol{F}_{\ell m}(t,t') + \boldsymbol{F}_{n\ell}(t,t')\boldsymbol{\Sigma}^{HF}_{\ell m}(t) \tag{4.60}$$

where we used $E_{nm} = E_n\delta_{nm}$, according to eq. 4.23. The symmetry relations for the components of $\boldsymbol{F}_{nm}$ listed in tab. 3.1, allow us to describe the full dynamics of the non-condensed particles in terms of the two upper components of the statistical function. The equation for

F^G_{nm} is obtained from the upper left component of eq. 4.59, evaluated at equal times. Thus, we get

$$i\frac{\partial}{\partial t}F^G_{nm}(t,t) = \Sigma^{HF}_{n\ell}(t)F^G_{\ell m}(t,t) - F^G_{n\ell}(t,t)\Sigma^{HF}_{\ell m}(t) - \Omega^{HF}_{n\ell}(t)F^F_{\ell m}(t,t)^* - F^F_{n\ell}(t,t)\Omega^{HF}_{\ell m}(t)^*. \quad (4.61)$$

Similarly, taking the upper right component of eq. 4.60 and setting $t = t'$, we obtain

$$\begin{aligned} i\frac{\partial}{\partial t}F^F_{nm}(t,t) =& 2E_n F^F_{nm}(t,t) + \Sigma^{HF}_{n\ell}(t)F^F_{\ell m}(t,t) + F^F_{n\ell}(t,t)\Sigma^{HF}_{\ell m}(t) \\ & - \Omega^{HF}_{n\ell}(t)F^G_{\ell m}(t,t)^* + F^G_{n\ell}(t,t)\Omega^{HF}_{\ell m}(t)^*, \end{aligned} \quad (4.62)$$

where components of the non-condensate self-energy are given by eq. 4.57, and read

$$\Sigma^{HF}_{nm}(t) = K(N_1+N_2) + J'(a_1^* a_2 + a_2^* a_1) + 2iU'\sum_{s,\ell} F^G_{s\ell}(t,t), \quad (4.63)$$

$$\Omega^{HF}_{nm}(t) = \frac{K}{2}\sum_{\alpha} a_\alpha a_\alpha + J' a_2 a_1 + iU'\sum_{s,\ell} F^F_{s\ell}(t,t). \quad (4.64)$$

Here, we omitted the time arguments of the condensate amplitudes a_α and wrote $N_\alpha = a^*_\alpha a_\alpha$ for particle number in the condensate α.

The system of equations is closed by inserting the explicit expressions for the condensate self-energies into the equation of motion for the condensate amplitude. Hence, we get

$$\begin{aligned} i\frac{\partial}{\partial t}a_1(t) =& \left[UN_1(t) + iK\sum_{n,m} F^G_{nm}(t,t)\right]a_1(t) - \left[J - iJ'\sum_{n,m} F^G_{nm}(t,t)\right]a_2(t) \\ & + i\left[\frac{K}{2}a_1^*(t) + \frac{J'}{2}a_2^*(t)\right]\sum_{n,m} F^F_{nm}(t,t). \end{aligned} \quad (4.65)$$

The equation for the $a_2(t)$ is obtained from eq. 4.65 by $a_1 \rightleftarrows a_2$.

Numerical Analysis and Initial Conditions

Initially the two condensates are completely isolated from each other. Then, at time $t = 0$ the Josephson link between the condensates as well as the interactions with single particle excitations are turned on. The initial conditions expressed in the language of the condensate amplitudes and statistical functions for the non-condensate particles read

$$a_\alpha(0) = \sqrt{N_\alpha(0)}e^{i\theta_\alpha(0)}, \quad (4.66)$$

$$F^G_{nm}(0,0) = -\frac{i}{2}\delta_{nm}, \quad (4.67)$$

$$F^F_{nm}(0,0) = 0, \quad (4.68)$$

where $N_\alpha(0)$ is the initial particle number in condensate α and $\theta_\alpha(0)$ its corresponding macroscopic phase. In addition, we have $A^G_{nm}(0,0) = \delta_{nm}$ and $A^F_{nm}(0,0) = 0$ for the spectral functions.

Taking a look at the different terms in the Hamiltonian describing the system (see eqs. 4.30 - 4.32), we notice that our model is rich in parameters. This makes a systematic study

of all features very extensive. We, therefore, should analyze how the interplay between the parameters affects the system and if it is possible to fix some of them. According to [41, 44, 62] it is convenient to give all the energies in terms of the Josephson coupling J and absorb the large particle numbers appearing in the eqs. 4.61 - 4.65 into the dimensionless parameters $u = NU/J$, $k = NK/J$, $j' = NJ'/J$, $u' = NU'/J$ and $n_b^{(n)} = N_b^{(n)}/N$, where N is the total number of particles. The parameter R is excluded in the present discussion, because it only appears beyond the BHF approximation. It will be included in the next section when we address the question of thermalization and equilibration. From the eqs. 4.61, 4.62 and 4.65 we compute the time evolution of the occupation numbers of the bosons out of the condensates, $n_b^{(n)}(t)$ and $n_b(t) = \sum n_b^{(n)}(t)$, the condensate population imbalance $z(t) = [N_1(t) - N_2(t)]/N$, and the relative phase difference $\theta(t) = \theta_1(t) - \theta_2(t)$ as well as the condensate mean energy $\langle \hat{H} \rangle_{\mathrm{BEC}}(t)$ and single particle excitations mean energy $\langle \hat{H} \rangle_{\mathrm{qp}}(t)$.

At the level of the two-mode approximation ($k = j' = u' = 0$) the interplay between the initial population imbalance $z(0)$ and the interaction parameter u has already been studied [62]. The dynamics exhibited by Bose Josephson junctions for fixed initial population imbalance $z(0)$ and varying interactions u are very similar to those observed for fixed u and varying $z(0)$ (section 4.1). This permits us, for instance, to fix $z(0)$ and study the interplay between u and the other parameters. Neglecting the coupling with the single particle excitations $k = j' = 0$, the system exhibits a macroscopic self-trapped and a delocalized regime, with a Josephson oscillation frequency of

$$\omega_{\mathrm{L}} = \sqrt{J^2 + \frac{NUJ}{2}} \tag{4.17}$$

in the linear regime. When, however, $k \neq 0, j' \neq 0$, particles are excited out of the condensates, $N_b(t) > 0$, the Josephson tunneling term in H_{mix} becomes active (J' term in equation 4.32). One then expects an enhanced Josephson frequency, with roughly J replaced by $J\,[1 - j' n_b(t)]$ in equation 4.17. Simultaneously, Rabi-like oscillations of the $N_b^{(n)}(t)$, i.e., of non-condensate particles pairs between the BECs and the excited levels, with frequencies $\omega_{\mathrm{R}} \approx 2E_n$ set in, c.f. eq. 4.62. As a result, in this non-condensate particles dominated regime one expects complex, high-frequency anharmonic oscillatory behavior.

When we discussed the various approximations in our model (see eqs. 4.30 - 4.32), we explained that the experimental realization of the double-well potential is achieved by the overlap of a harmonic confinement with a sinusoidal potential with large period, with one of its maxima placed at the center of the harmonic confinement. Our model assumes that the wave functions of the excited states extend over the two condensates and the barrier separating them. We, therefore, assume that the excited energy levels coincide with the energy levels of the harmonic confinement. Typically, the oscillator frequency of the harmonic trap has experimental values of $\Delta \equiv \omega_{\mathrm{HO}} \sim 100\,\mathrm{Hz}$ [73]. The experimental value of the Josephson coupling J is roughly $10\,\mathrm{Hz}$ [62], and therefore the bare single particle excitations level spacing $\Delta \sim 10J$ in terms of J.

The complete numerical solution of the equations of motion 4.61, 4.62 and 4.65 for a finite-size trap with $N = 5 \cdot 10^5$ particles, taking 5 excited levels into account[3] are shown for typical parameter values in figs. 4.7 and 4.8 for an initially prepared delocalized state and in figs. 4.9 and 4.10 for the initially prepared self-trapped state. In order to get a better insight

[3] We have performed similar calculations for 2, 3 and 4 excited levels with fixed Δ. It was verified that generic behavior described in the text, in particular the values of τ_c, are essentially independent of the number of excited levels take into account [44]

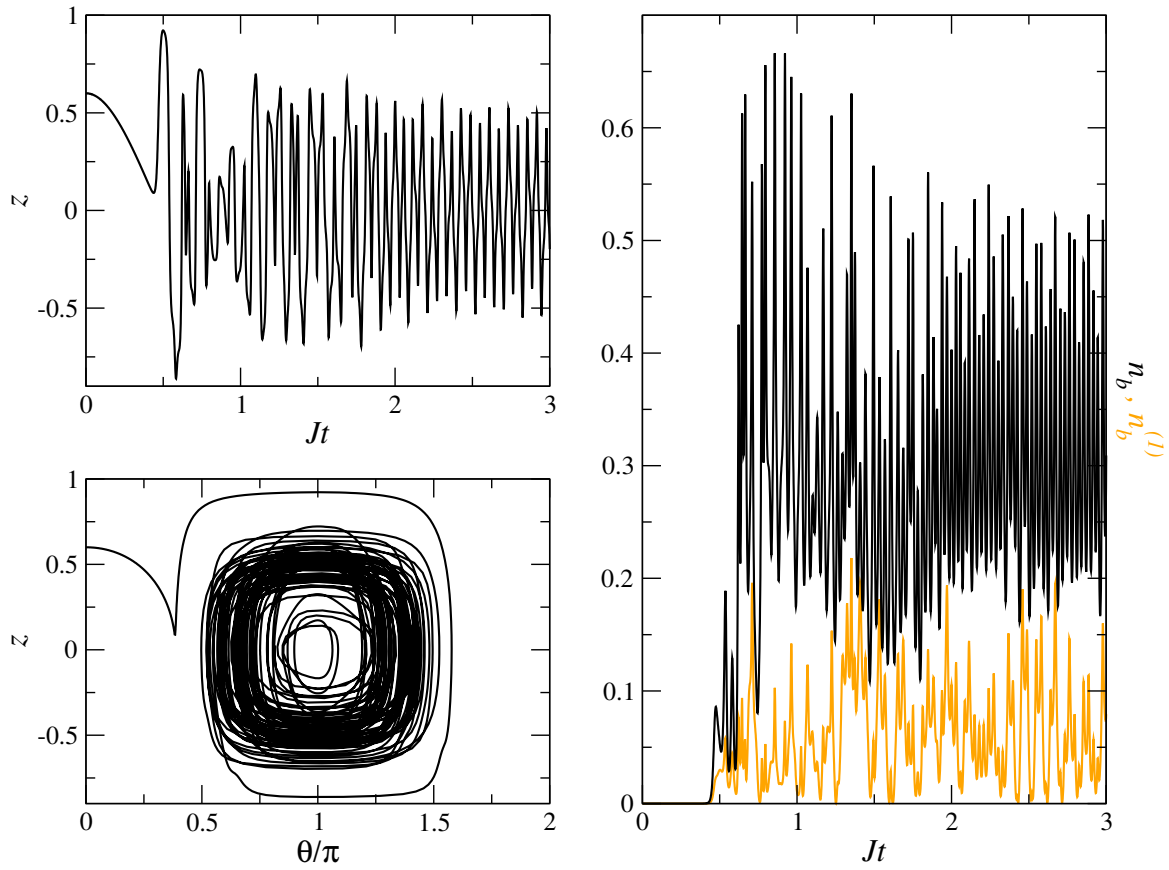

Figure 4.7: Time evolution of condensed and non-condensed particles for initial conditions $z(0) = 0.6$, $\theta(0) = 0$, $\Delta = 10J$ and interactions parameters $u = u' = 5$, $j' = 60$, $k = 0$ for $N = 5 \cdot 10^5$ (delocalized regime). In the upper left panel, the dynamics of the BEC population imbalance $z(t)$ is shown. The lower left panel shows the phase-space portrait of the dynamical variables z and θ. The right plot displays the time evolution of the non-condensate particle population. The orange line shows the particle occupation of the first excited level $n_b^{(1)}$, while the black line is the sum of all levels n_b.

into the dynamics of the system, we computed the quasiparticle energies by diagonalizing the Hamiltonian 4.30 - 4.32 at every time step. The time evolution of the eigenenergies is plotted in the left panels of figs. 4.8 and 4.10. The highest lying level is repulsed upwards in both cases for initial time $t = 0$. This effect is similar to the one observed in the two-level model [74].

The results reproduce the expected behavior discussed above in the regime with finite population of single particle excitations. The values for the equidistant energy level spacing Δ were chosen such that the first excited level lies the above the largest condensate energy eigenvalue, which is obtained from the diagonalization of the condensate Hamiltonian 4.30 at time $t = 0$. This ensures the assumption that the single particle wave functions extend over both condensates and the barrier separating them. The most striking and most important feature observed in figs. 4.7 and 4.8 for an initially prepared delocalized state and in figs. 4.9 and 4.10 for the initially prepared self-trapped state is that for times greater than a characteristic time τ_c the

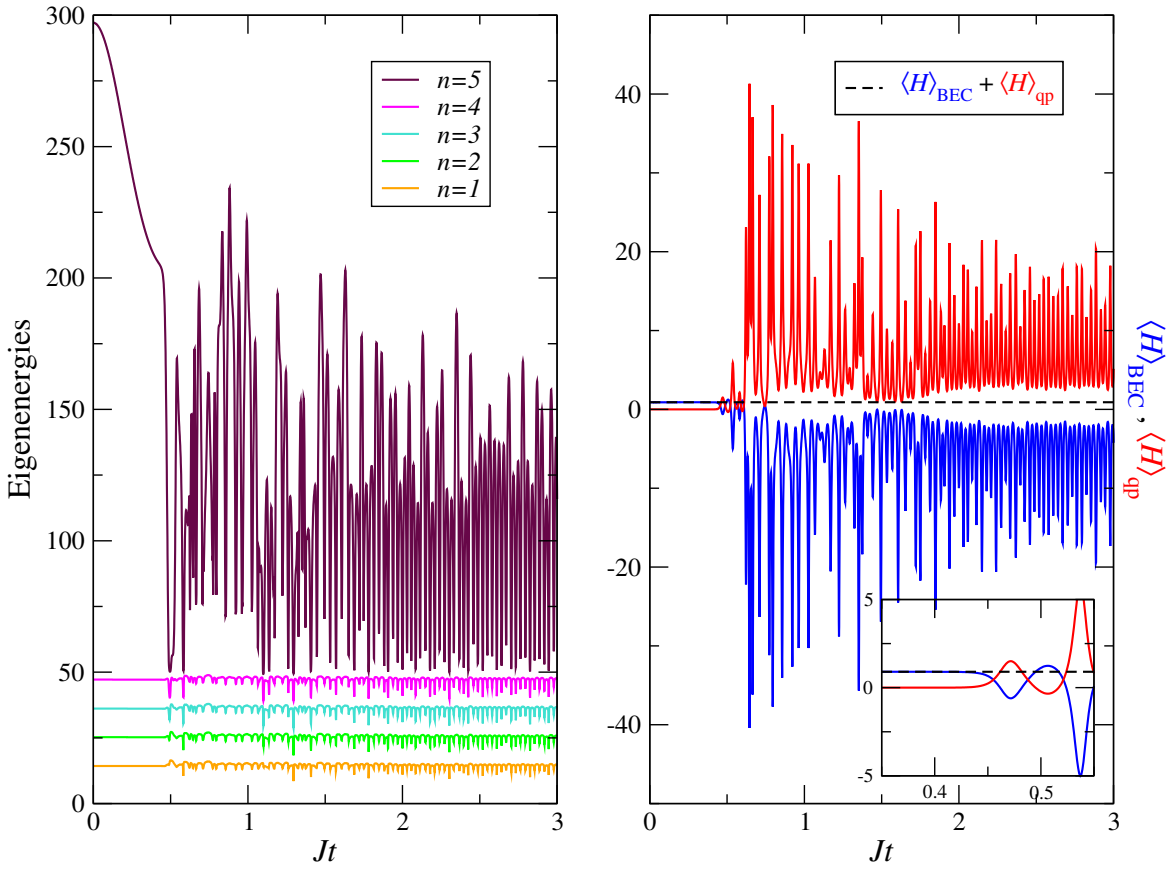

Figure 4.8: Time evolution of the instantaneous eigenenergies and mean energies for initial conditions as in fig. 4.7 (delocalized regime). On the left, we plotted the instantaneous quasiparticle energies obtained from the diagonalization of the Hamiltonian 4.30 - 4.32 at the every time step. The right plot shows the mean energies of the condensate fraction $\langle H\rangle_{\mathrm{BEC}}$ (blue line) and the single particle excitations $\langle H\rangle_{\mathrm{qp}}$ (red line). The black dashed line corresponds to the total mean energy of the system.

highly non-linear dynamics of the system makes the excitation of particles out of the condensate possible. In this regime the finite occupation number $n_b(t)$ of the single particle excitations and fast oscillations of the BEC population imbalance $z(t)$ stabilize each other mutually: $n_b(t) > 0$ implies an enhancement of the Josephson frequency, and the resulting fast oscillations of $z(t)$ can efficiently excite particles out of the BECs via the mixing Hamiltonian 4.32.

The fast, non-condensate particles induced dynamics implies two further features. (1) As seen from fig. 4.7 an initially prepared self-trapped state is destroyed and the system changes to a delocalized state at the same time when the non-condensate occupation $n_b(t)$ becomes sizable. A similar behavior is observed in the analysis of Bose Josephson junctions in the context TSBH model , as it is discussed in section 5.3. (2) At the onset of the fast dynamics the system changes from a $\theta = 0$ to $\theta = \pi$ Josephson junction (see the phase-space portraits in lower left panels of figs. 4.7 and 4.9). This can be understood qualitatively, in that the large phase difference $\theta(t) \approx \pi$ is required to sustain the large Josephson current in the regime with fast dynamics.

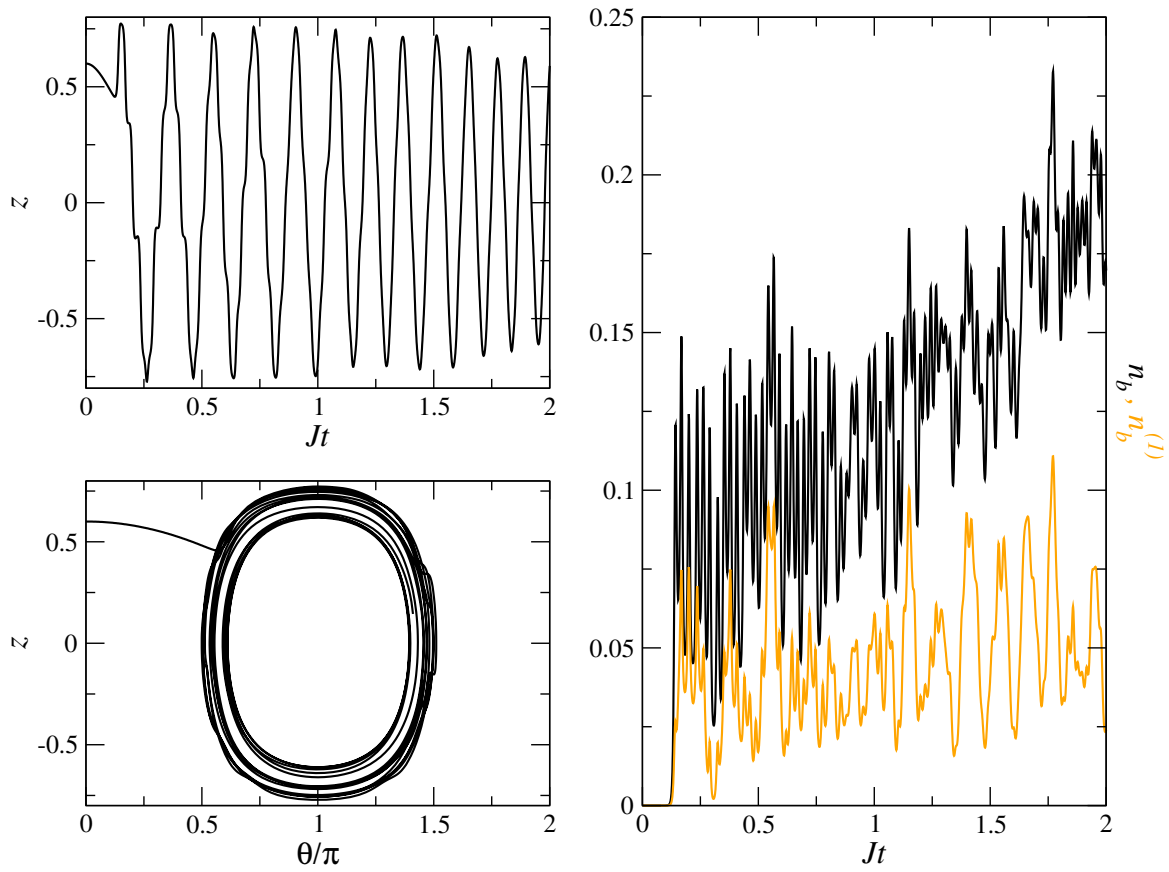

Figure 4.9: Time evolution of condensed and non-condensed particles for initial conditions $z(0) = 0.6$, $\theta(0) = 0$, $\Delta = 25J$ and interactions parameters $u = u' = 25$, $j' = 60$, $k = 0$ for $N = 5 \cdot 10^5$ (self-trapped regime). In the upper left panel, the dynamics of the BEC population imbalance $z(t)$ is shown. The lower left panel shows the phase-space portrait of the dynamical variables z and θ. The right plot displays the time evolution of the non-condensate particle population. The orange line shows the particle occupation of the first excited level $n_b^{(1)}$, while the black line is the sum of all levels n_b.

Since the transition to the non-condensate particles dominated regime is not described by a Fermi golden rule, it is hard to analyze the time scale τ_c analytically. We defined τ_c numerically as the time scale where the occupation number of the non-condensate particles, $n_b(t)$, first exceeds 0.05 and extracted it from our solutions[4]. The fact that the non-condensate particles dynamics does not become sizable immediately after the switching on of the Josephson coupling and sets in in an "avalanche" manner, allows us to define τ_c in this way. The dependence of $(J\tau_c)^{-1}$ on the parameters j' and k and fixed $\Delta = 10J$ for an initially prepared delocalized state is presented in figs. 4.11a and 4.11b for total particle numbers $N = 5 \cdot 10^3$ and $N = 5 \cdot 10^5$, respectively. We observe that for a given k and increasing j', the avalanche behavior sets in earlier. The larger k, the longer is the system able to sustain undamped Josephson oscillations

[4] We have defined τ_c as the time scale where $n_b(t)$ first exceeds 0.03, 0.05 and 0.07. It was verified that the generic behavior of τ_c as a function of the system's parameters, is qualitatively the same for all these definitions

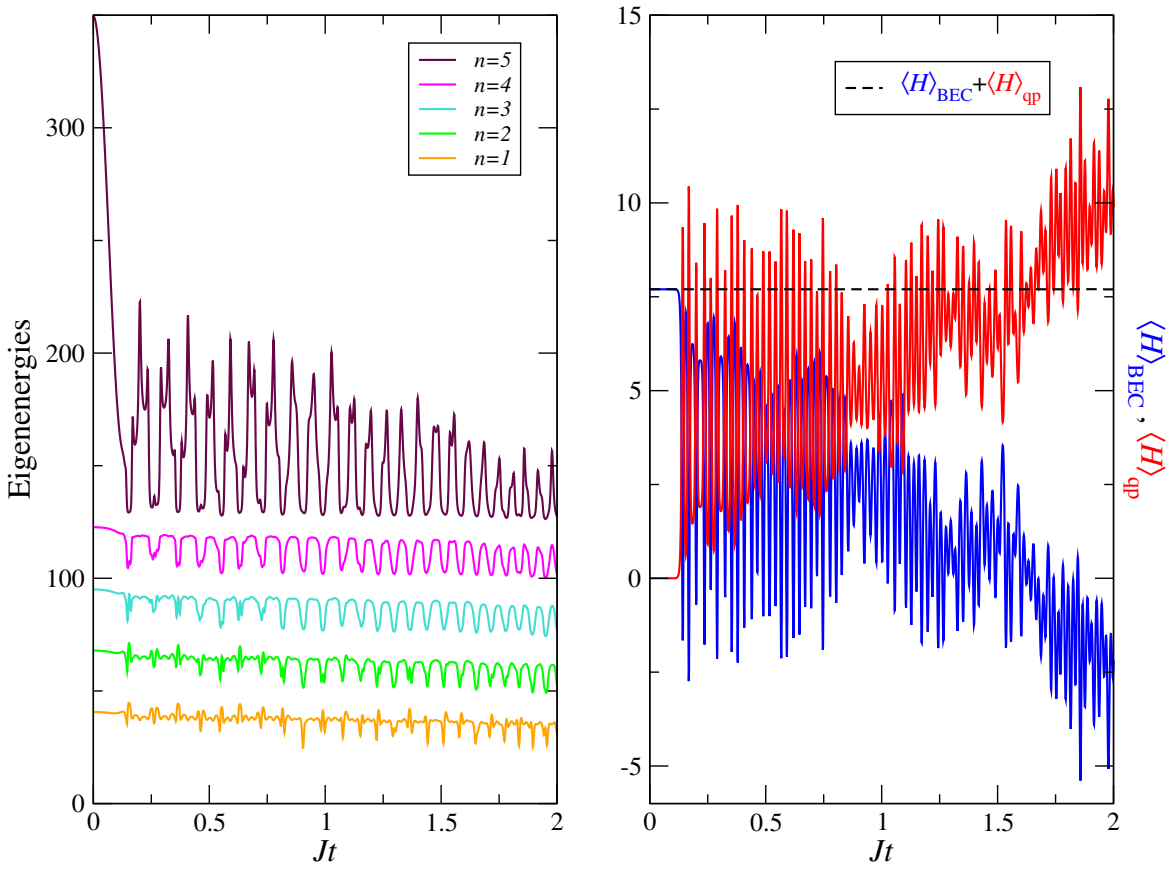

Figure 4.10: Time evolution of the instantaneous eigenenergies and mean energies for initial conditions as in fig. 4.9 (self-trapped regime). On the left, we plotted the instantaneous quasiparticle energies obtained from the diagonalization of the Hamiltonian 4.30 - 4.32 at the every time step. The right plot shows the mean energies of the condensate fraction $\langle H\rangle_{\mathrm{BEC}}$ (blue line) and the single particle excitations $\langle H\rangle_{\mathrm{qp}}$ (red line). The black dashed line corresponds to the total mean energy of the system.

for a given j', provided the transition to the non-condensate particles dominated regime takes place for those parameters. The missing data points for small j' in every curve correspond to j' and k values for which τ_c was not found within the time interval $0 \leq Jt \leq 25$. In addition, the comparison of fig. 4.11a with fig. 4.11b yields, that τ_c increases with the total number of particles.

In figs. 4.12 and 4.13, we plot the inverse of the time scale τ_c as a function of the level spacing Δ and the parameter j' for an initially prepared delocalized state and an initially self-trapped state, respectively. In both cases, τ_c increases with the level spacing Δ and decreases with parameter j'. Again, the missing data points in the curves correspond to j' and Δ values for which τ_c was not found within the time interval $0 \leq Jt \leq 25$. For an initially prepared delocalized state, $(J\tau_c)^{-1}$ shows qualitatively a similar behavior as a function of Δ and j' for different particle numbers N (see figs. 4.12a and 4.12b). However, we observed that τ_c increases with N. This explains why the sudden drop in $(J\tau_c)^{-1}$ happens at smaller values of Δ for a

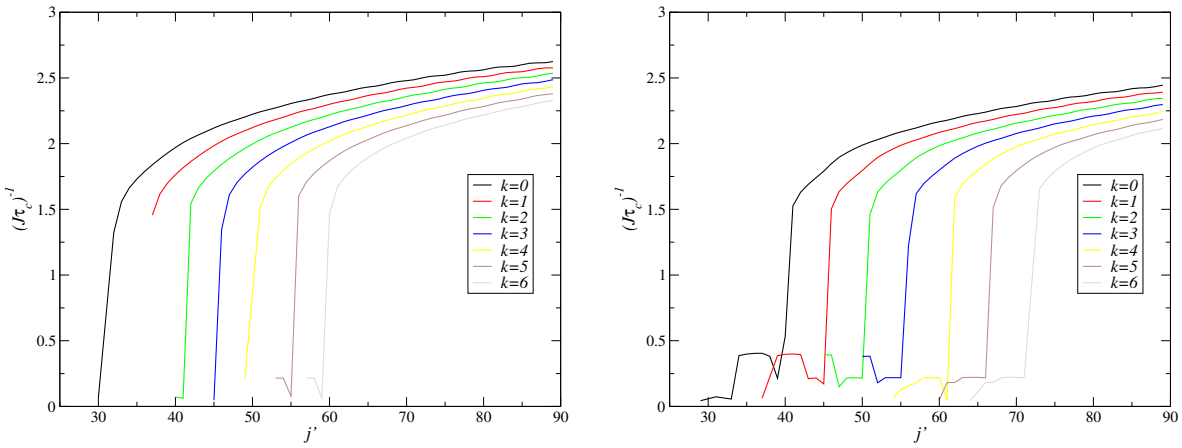

(a) $N = 5 \cdot 10^3$ (b) $N = 5 \cdot 10^5$

Figure 4.11: Dependence of the inverse time scale $(J\tau_c)^{-1}$ on two main parameters j' and k, for the initial conditions as in fig. 4.7 and for total particle number $N = 5 \cdot 10^3$ and $N = 5 \cdot 10^5$. The scatter is due to the ambiguity in the numerical definition of τ_c.

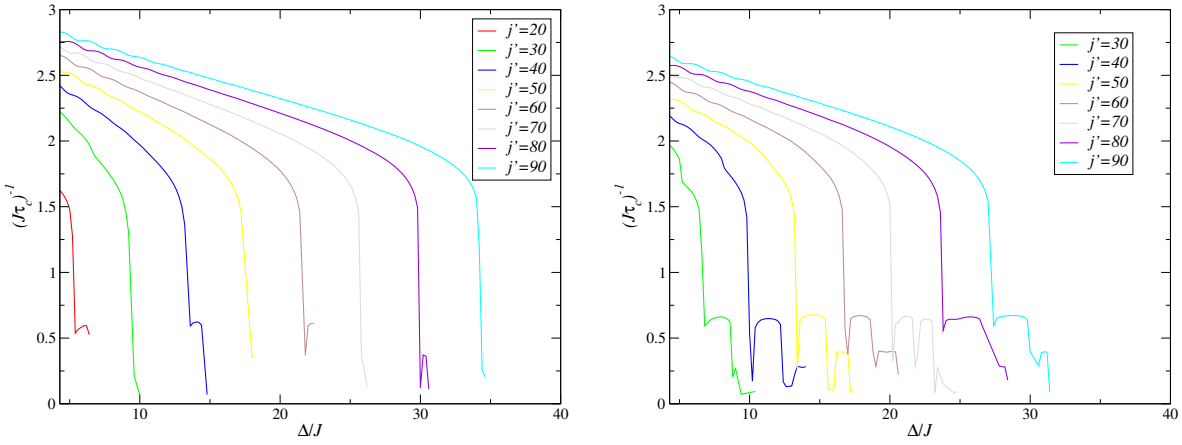

(a) $N = 5 \cdot 10^3$ (b) $N = 5 \cdot 10^5$

Figure 4.12: Dependence of the inverse time scale $(J\tau_c)^{-1}$ on the parameter j' and the single particle excitations energy spacing Δ, for the initial conditions as in fig. 4.7 and for total particle number $N = 5 \cdot 10^3$ and $N = 5 \cdot 10^5$. The scatter is due to the ambiguity in the numerical definition of τ_c.

given j' in a system with a larger particle number. An initially self-trapped state also shows a larger τ_c for increasing number of particles, as seen from the comparison of figs. 4.12a with 4.12b. The sudden drop in the inverse of τ_c occurs for $j' < 60$ at similar values of Δ. The transition to the non-condensate particle dominated regime for an initially self-trapped state happens simultaneously with its destruction and change to a delocalized state. The smaller the particle number, the higher the percentage of particles excited out of the condensates for

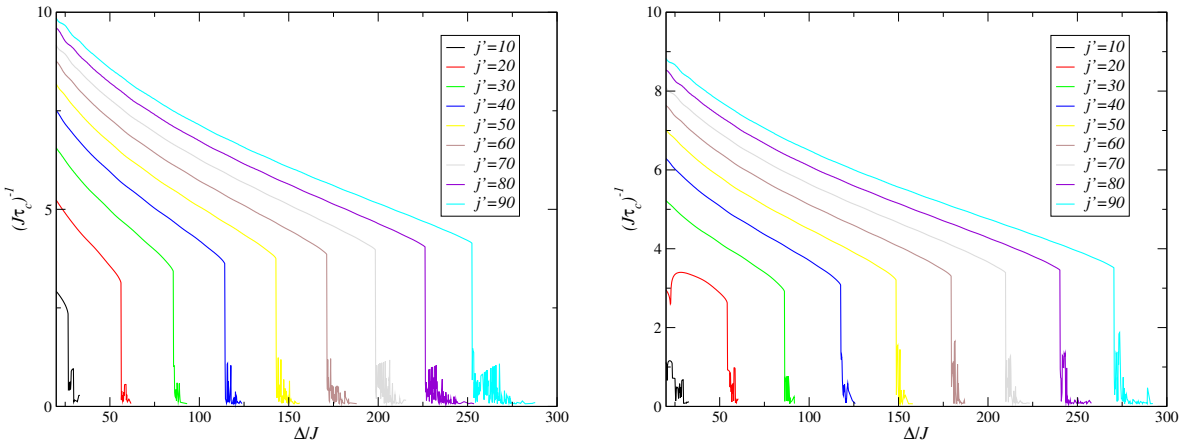

(a) $N = 5 \cdot 10^3$ (b) $N = 5 \cdot 10^5$

Figure 4.13: Dependence of the inverse time scale $(J\tau_c)^{-1}$ on the parameter j' and the single particle excitations energy spacing Δ, for the initial conditions as in fig. 4.9 and for total particle number $N = 5 \cdot 10^3$ and $N = 5 \cdot 10^5$. The scatter is due to the ambiguity in the numerical definition of τ_c.

given j' and Δ. Consequently, we expect a larger enhancement of the Josephson frequency, which is responsible for the transition into the delocalized regime. This explains why the drop in $(J\tau_c)^{-1}$ happens at larger Δ values for $j' > 60$ in systems with larger particle numbers.

Now that we have studied the characteristic time τ_c until which the system can sustain undamped Josephson oscillations as a function of the system's parameter, the question remains about what is the origin of the transition into the single particle excitations dominated regime. We also want to understand why does $(J\tau_c)^{-1}$ present a sudden drop(increase) as a function of $\Delta(j')$. In fig. 4.14 we plot the inverse of τ_c as a function of the single particle energy level spacing Δ for $j' = 60$. The insets show the time evolution of the lowest quasiparticle energy level and the two condensate eigenenergies for three different Δ's along the curve (see the dots on the curve). The condensate eigenenergies are obtained from the diagonalization of the BEC part of the Hamiltonian 4.30 - 4.32. We observe that particles get excited out of the condensates as an avalanche when the lowest quasiparticle energy (orange line in the insets) becomes equal the highest condensate eigenenergy (green line in the insets). This crossing of the eigenenergies defines the transition into the non-condesate particles dominated regime. From the time evolution of the condensate eigenenergies for $\Delta = 18J$ and $\Delta = 20.6J$, we see that their unperturbed period of oscillation is roughly $JT \approx 1$. We also observed that the sudden increase(drop) of $(J\tau_c)^{-1}$ as a function of $j'(\Delta)$ in figs. 4.11 and 4.12 happens for $J\tau_c \approx 1$. This allows us to conjecture that the drop in $(J\tau_c)^{-1}$ for increasing Δ occurs when τ_c is roughly the unperturbed period of oscillations of the condensate eigenenergies. In other words, if the system is able to sustain at least one oscillation in the condensate eigenenergies, it will likely be able sustain multiple undamped Josephson oscillations.

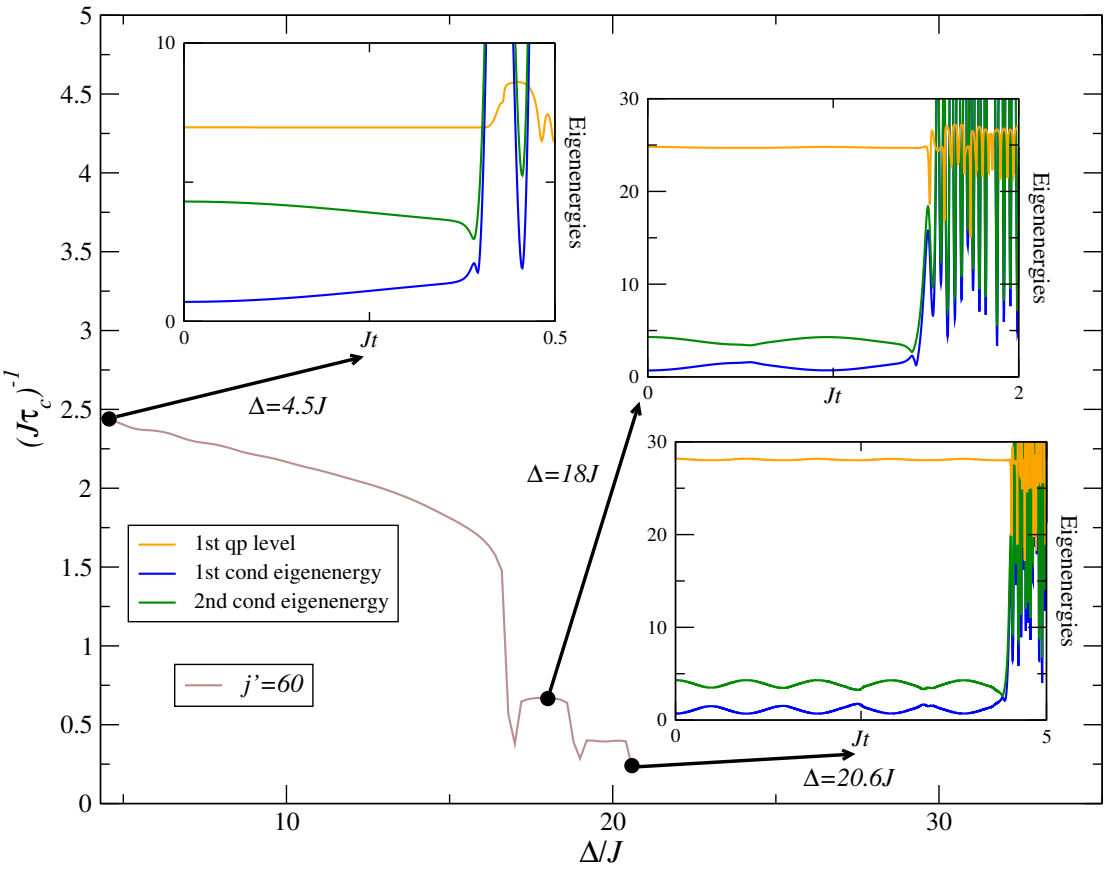

Figure 4.14: τ_c^{-1} as a function of the single particle excitations energy spacing Δ for fixed $k = 0$ and $j' = 60$, as in fig. 4.12b. The insets correspond to the time evolution of the instantaneous condensates and first excited level eigenenergies marked by the dots on the curve. τ_c coincides with the time at which the higher condensate eigenenergy crosses lowest quasiparticle energy.

4.2.2 Full 2nd-order Approximation and "Thermalization Effects"

In section 4.2, we derived a Hamiltonian 4.21 describing two initially isolated in thermal equilibrium BECs in a double-well potential, which are subject to a non-adiabatic perturbation that couples them, allowing the exchange of atoms. In addition we gave the underlying equations of motion for the condensate propagator and the non-condensate two-point correlation functions $\boldsymbol{A}_{nm}$ and $\boldsymbol{F}_{nm}$, which describe the single particle spectrum and the occupation number, respectively. In the derivation of the equations of motion, we did not specify self-energies. In section 4.2.1, we discussed the solutions of the Hamiltonian 4.21 obtained using the BHF approximation, and gave the analytical expressions for the local self-energies $\boldsymbol{S}^{HF}$ and $\boldsymbol{\Sigma}^{HF}$ (see eqs. 4.56 and 4.57). The numerical analysis showed that after a characteristic time τ_c, particles get excited out of the condensates as an avalanche and the behavior changes abruptly to a regime of fast Josephson and Rabi oscillations. Only in this single particle excitations dominated regime we expect strong damping of the oscillations due to inelastic collisions between the non-condensed particles, equilibrating and thermalizing the system. Thus, it is necessary

to include the higher order terms in the interatomic interaction. This will be done according to the discussion of the full second-order approximation in section 3.5.

Similar to analysis of the BHF approximation in the last section, we can express the full dynamics of the system in terms of the upper left and upper right components of the spectral function $\boldsymbol{A}_{nm}$ and the statistical function $\boldsymbol{F}_{nm}$. The remaining components can be obtained using the relations listed in table 3.1. Rewriting the $\boldsymbol{\gamma}$ in the basis 4.20, we obtain

$$\begin{aligned}
\gamma^G_{\alpha\alpha'}(t,t') &= \sum_{n,\ell,s}\sum_{n',\ell',s'} R_{\alpha n\ell s}R_{n'\ell's'\alpha'}\Big(F^G_{nn'}(t,t')\left\{4\Lambda^{\ell\ell'}_{ss'}[F,F^*](t,t')+2\Lambda^{\ell\ell'}_{ss'}[G,G^*](t,t')\right\} \\
&\quad + A^G_{nn'}(t,t')\left\{4\Xi^{\ell\ell'}_{ss'}[F,F^*](t,t')+2\Xi^{\ell\ell'}_{ss'}[G,G^*](t,t')\right\}\Big), \qquad (4.69)\\
\gamma^F_{\alpha\alpha'}(t,t') &= \sum_{n,\ell,s}\sum_{n',\ell',s'} R_{\alpha n\ell s}R_{n'm's'\alpha'}\Big(F^F_{nn'}(t,t')\left\{4\Lambda^{\ell\ell'}_{ss'}[G,G^*](t,t')+2\Lambda^{\ell\ell'}_{ss'}[F,F^*](t,t')\right\} \\
&\quad + A^F_{nn'}(t,t')\left\{4\Xi^{\ell\ell'}_{ss'}[G,G^*](t,t')+2\Xi^{\ell\ell'}_{ss'}[F,F^*](t,t')\right\}\Big) \qquad (4.70)
\end{aligned}$$

where we used that R is independent of the order of its indices, because the wave functions appearing in the overlap matrix element 4.27 were assumed to be real. Here, we defined

$$\begin{aligned}
\Lambda^{\ell\ell'}_{ss'}[f,g](t,t') &= A^f_{\ell\ell'}(t,t')F^g_{ss'}(t,t')+F^f_{\ell\ell'}(t,t')A^g_{ss'}(t,t'), \qquad (4.71)\\
\Xi^{\ell\ell'}_{ss'}[f,g](t,t') &= F^f_{\ell\ell'}(t,t')F^g_{ss'}(t,t')-\frac{1}{4}A^f_{\ell\ell'}(t,t')A^g_{ss'}(t,t'), \qquad (4.72)
\end{aligned}$$

where $g,f\in\{G,F,G^*,F^*\}$ and $A^{g^*}=(A^g)^*$. It is sufficient to give only the expressions for the upper components of $\boldsymbol{\gamma}$, since the remaining two components are obtained using the symmetry relations listed in tab. 3.2.

Analogously, for the spectral function $\boldsymbol{\Gamma}_{nm}$ of the non-condensate self-energy we get

$$\begin{aligned}
\Gamma^G_{nn'}(t,t') &= 2i\sum_{\alpha,\ell,s}\sum_{\alpha',\ell',s'} R_{n\alpha\ell s}R_{\ell's'\alpha'n'}\Big(2a^*_\alpha(t)a^*_{\alpha'}(t')\Lambda^{\ell\ell'}_{ss'}[G,F](t,t') \\
&\quad +a^*_\alpha(t)a_{\alpha'}(t')\Lambda^{\ell\ell'}_{ss'}[G,G](t,t')-2a_\alpha(t)a_{\alpha'}(t')\Lambda^{\ell\ell'}_{ss'}[F^*,G](t,t') \\
&\quad -2a_\alpha(t)a^*_{\alpha'}(t')\left\{\Lambda^{\ell\ell'}_{ss'}[G,G^*](t,t')+\Lambda^{\ell\ell'}_{ss'}[F,F^*](t,t')\right\}\Big) \\
&\quad +\sum_{m,\ell,s}\sum_{m',\ell',s'} V_{nm\ell s}V_{m'\ell's n'}\Big(F^G_{mm'}(t,t')\left\{4\Lambda^{\ell\ell'}_{ss'}[F,F^*](t,t')+2\Lambda^{\ell\ell'}_{ss'}[G,G^*](t,t')\right\} \\
&\quad + A^G_{mm'}(t,t')\left\{4\Xi^{\ell\ell'}_{ss'}[F,F^*](t,t')+2\Xi^{\ell\ell'}_{ss'}[G,G^*](t,t')\right\}\Big), \qquad (4.73)\\
\Gamma^F_{nn'}(t,t') &= 2i\sum_{\alpha,\ell,s}\sum_{\alpha',\ell',s'} R_{n\alpha\ell s}R_{\ell's'\alpha'n'}\Big(2a^*_\alpha(t)a_{\alpha'}(t')\Lambda^{\ell\ell'}_{ss'}[G,F](t,t') \\
&\quad +a^*_\alpha(t)a^*_{\alpha'}(t')\Lambda^{\ell\ell'}_{ss'}[F,F](t,t')-2a_\alpha(t)a^*_{\alpha'}(t')\Lambda^{\ell\ell'}_{ss'}[G^*,F](t,t') \\
&\quad -2a_\alpha(t)a_{\alpha'}(t')\left\{\Lambda^{\ell\ell'}_{ss'}[G,G^*](t,t')+\Lambda^{\ell\ell'}_{ss'}[F,F^*](t,t')\right\}\Big) \\
&\quad +\sum_{m,\ell,s}\sum_{m',\ell',s'} V_{nm\ell s}V_{m'\ell's n'}\Big(F^F_{mm'}(t,t')\left\{4\Lambda^{\ell\ell'}_{ss'}[G,G^*](t,t')+2\Lambda^{\ell\ell'}_{ss'}[F,F^*](t,t')\right\} \\
&\quad + A^F_{mm'}(t,t')\left\{4\Xi^{\ell\ell'}_{ss'}[G,G^*](t,t')+2\Xi^{\ell\ell'}_{ss'}[F,F^*](t,t')\right\}\Big). \qquad (4.74)
\end{aligned}$$

For the components of the statistical function $\mathbf{\Pi}_{nm}$ of the non-condensate self-energy we obtain

$$\begin{aligned}
\Pi^G_{nn'}(t,t') &= 2i \sum_{\alpha,\ell,s} \sum_{\alpha',\ell',s'} R_{n\alpha\ell s} R_{\ell' s' \alpha' n'} \Big(2a^*_\alpha(t) a^*_{\alpha'}(t') \Xi^{\ell\ell'}_{ss'}[G,F](t,t') \\
&\quad + a^*_\alpha(t) a_{\alpha'}(t') \Xi^{\ell\ell'}_{ss'}[G,G](t,t') - 2a_\alpha(t) a_{\alpha'}(t') \Xi^{\ell\ell'}_{ss'}[F^*,G](t,t') \\
&\quad - 2a_\alpha(t) a^*_{\alpha'}(t') \left\{ \Xi^{\ell\ell'}_{ss'}[G,G^*](t,t') + \Xi^{\ell\ell'}_{ss'}[F,F^*](t,t') \right\} \Big) \\
&\quad + \sum_{m,\ell,s} \sum_{m',\ell',s'} V_{nm\ell s} V_{m'\ell' s n'} \Big(F^G_{mm'}(t,t') \left\{ 4\Xi^{\ell\ell'}_{ss'}[F,F^*](t,t') + 2\Xi^{\ell\ell'}_{ss'}[G,G^*](t,t') \right\} \\
&\quad + \frac{1}{2} A^G_{mm'}(t,t') \left\{ 2\Xi^{\ell\ell'}_{ss'}[F,F^*](t,t') + \Xi^{\ell\ell'}_{ss'}[G,G^*](t,t') \right\} \Big) , \qquad (4.75) \\
\Pi^F_{nn'}(t,t') &= 2i \sum_{\alpha,\ell,s} \sum_{\alpha',\ell',s'} R_{n\alpha\ell s} R_{\ell' s' \alpha' n'} \Big(2a^*_\alpha(t) a_{\alpha'}(t') \Xi^{\ell\ell'}_{ss'}[G,F](t,t') \\
&\quad + a^*_\alpha(t) a^*_{\alpha'}(t') \Xi^{\ell\ell'}_{ss'}[F,F](t,t') - 2a_\alpha(t) a^*_{\alpha'}(t') \Xi^{\ell\ell'}_{ss'}[G^*,F](t,t') \\
&\quad - 2a_\alpha(t) a_{\alpha'}(t') \left\{ \Xi^{\ell\ell'}_{ss'}[G,G^*](t,t') + \Xi^{\ell\ell'}_{ss'}[F,F^*](t,t') \right\} \Big) \\
&\quad + \sum_{m,\ell,s} \sum_{m',\ell',s'} V_{nm\ell s} V_{m'\ell' s n'} \Big(F^F_{mm'}(t,t') \left\{ 4\Xi^{\ell\ell'}_{ss'}[G,G^*](t,t') + 2\Xi^{\ell\ell'}_{ss'}[F,F^*](t,t') \right\} \\
&\quad + \frac{1}{2} A^F_{mm'}(t,t') \left\{ 2\Lambda^{\ell\ell'}_{ss'}[G,G^*](t,t') + \Lambda^{\ell\ell'}_{ss'}[F,F^*](t,t') \right\} \Big) . \qquad (4.76)
\end{aligned}$$

Here, we also used the fact that the functions appearing in the overlap matrix elements are real, so that R and V are independent of the order of their indices.

Like in the case of the spectral and statistical functions $A^{G/F}_{nm}$ and $F^{G/F}_{nm}$, the additional two components of the spectral and statistical functions of the self-energies can be expressed in terms of their upper left and upper right components. They satisfy similar symmetry relations to those satisfied by the components of $\boldsymbol{A}_{nm}$ and $\boldsymbol{F}_{nm}$ (see table 3.2). This is very convenient, because we can express all the appearing quantities in the equations of motion with the argument related to the later time on the left side. In appendix B, we show how one can exploit these relations in order to simplify the numerical analysis.

Finally, the equations of motion for the components of the single particle excitations spectral function read

$$\begin{aligned}
i\frac{\partial}{\partial t} A^G_{nm}(t,t') &= \left[E_{n\ell} + \Sigma^{HF}_{n\ell}(t) \right] A^G_{\ell m}(t,t') - \Omega^{HF}_{n\ell}(t) A^F_{\ell m}(t,t')^* \\
&\quad - i \int_{t'}^{t} \mathrm{d}\bar{t} \left[\Gamma^G_{n\ell}(t,\bar{t}) A^G_{\ell m}(\bar{t},t') + \Gamma^F_{n\ell}(t,\bar{t}) A^{\overline{F}}_{\ell m}(\bar{t},t') \right] , \qquad (4.77) \\
i\frac{\partial}{\partial t} A^F_{nm}(t,t') &= \left[E_{n\ell} + \Sigma^{HF}_{n\ell}(t) \right] A^F_{\ell m}(t,t') - \Omega^{HF}_{n\ell}(t) A^G_{\ell m}(t,t')^* \\
&\quad - i \int_{t'}^{t} \mathrm{d}\bar{t} \left[\Gamma^G_{n\ell}(t,\bar{t}) A^F_{\ell m}(\bar{t},t') + \Gamma^F_{n\ell}(t,\bar{t}) A^{\overline{G}}_{\ell m}(\bar{t},t') \right] , \qquad (4.78)
\end{aligned}$$

for the components of the statistical function

$$
\begin{aligned}
i\frac{\partial}{\partial t}F^G_{nm}(t,t') &= \left[E_{n\ell}+\Sigma^{HF}_{n\ell}(t)\right]F^G_{\ell m}(t,t') - \Omega^{HF}_{n\ell}(t)F^F_{\ell m}(t,t')^* \\
&\quad - i\int_0^t \mathrm{d}\bar{t}\left[\Gamma^G_{n\ell}(t,\bar{t})F^G_{\ell m}(\bar{t},t') + \Gamma^F_{n\ell}(t,\bar{t})F^{\overline{F}}_{\ell m}(\bar{t},t')\right] \\
&\quad + i\int_0^{t'} \mathrm{d}\bar{t}\left[\Pi^G_{n\ell}(t,\bar{t})A^G_{\ell m}(\bar{t},t') + \Pi^F_{n\ell}(t,\bar{t})A^{\overline{F}}_{\ell m}(\bar{t},t')\right], \qquad (4.79)\\
i\frac{\partial}{\partial t}F^F_{nm}(t,t') &= \left[E_{n\ell}+\Sigma^{HF}_{n\ell}(t)\right]F^F_{\ell m}(t,t') - \Omega^{HF}_{n\ell}(t)F^G_{\ell m}(t,t')^* \\
&\quad - i\int_0^t \mathrm{d}\bar{t}\left[\Gamma^G_{n\ell}(t,\bar{t})F^F_{\ell m}(\bar{t},t') + \Gamma^F_{n\ell}(t,\bar{t})F^{\overline{G}}_{\ell m}(\bar{t},t')\right] \\
&\quad + i\int_0^{t'} \mathrm{d}\bar{t}\left[\Pi^G_{n\ell}(t,\bar{t})A^F_{\ell m}(\bar{t},t') + \Pi^F_{n\ell}(t,\bar{t})A^{\overline{G}}_{\ell m}(\bar{t},t')\right]. \qquad (4.80)
\end{aligned}
$$

The equations 4.77 - 4.80 are coupled to equations for the condensate amplitudes

$$
i\frac{\partial}{\partial t}a_\alpha(t) = \left[E_{\alpha\gamma}+S^{HF}_{\alpha\gamma}(t)\right]a_\gamma(t) + W^{HF}_{\alpha\gamma}(t)a^*_\gamma(t) - i\int_0^t \mathrm{d}\bar{t}\left[\gamma^G_{\alpha\gamma}(t,\bar{t})a_\gamma(\bar{t}) + \gamma^F_{\alpha\beta}(t,\bar{t})a^*_\gamma(\bar{t})\right]. \qquad (4.81)
$$

The equations for the spectral functions do not decoupled from the rest of the equations, as happens in the BHF approximation. In addition, we have to propagate the equations of motion for different time arguments, as it was pointed out in section 3.5. The propagation of the solutions for equal time arguments requires special care.

Numerical Analysis

In section 4.2.1, we studied the BHF dynamics of two initially completely isolated BECs, that are linked by a Josephson coupling in a non-adiabatic way. Although the BHF approximation excludes the memory effects that could lead to the establishment of an non-equilibrium steady state, we found a very interesting behavior: particles do not get excited immediately after switching on the Josephson coupling. Instead, there is a certain characteristic time τ_c after which the system undergoes a transition to a non-condensate particles dominated regime. However, the high-frequency anharmonic behavior in this regime, hints that the theoretical description requires an extension in order to able to address the question of "thermalization".

As it is discussed in [40, 75, 76], the equations of motion derived within the full second-order approximation can be applied to study thermalization and equilibration in situations away from equilibrium. In section 4.2.2 we gave a detailed derivation of the full second-order equations of motion for our model (see eqs. 4.77 - 4.81). Note, that the numerical solution of these equations requires the knowledge of all previous time steps. Thus, it is necessary to include $\boldsymbol{A}_{nm}$ into our analysis. In appendix B we explain the numerical scheme used to solve the equations of motion 4.77 - 4.81.

The initial setup is exactly the same as in section 4.2.1 and is expressed in the language of the

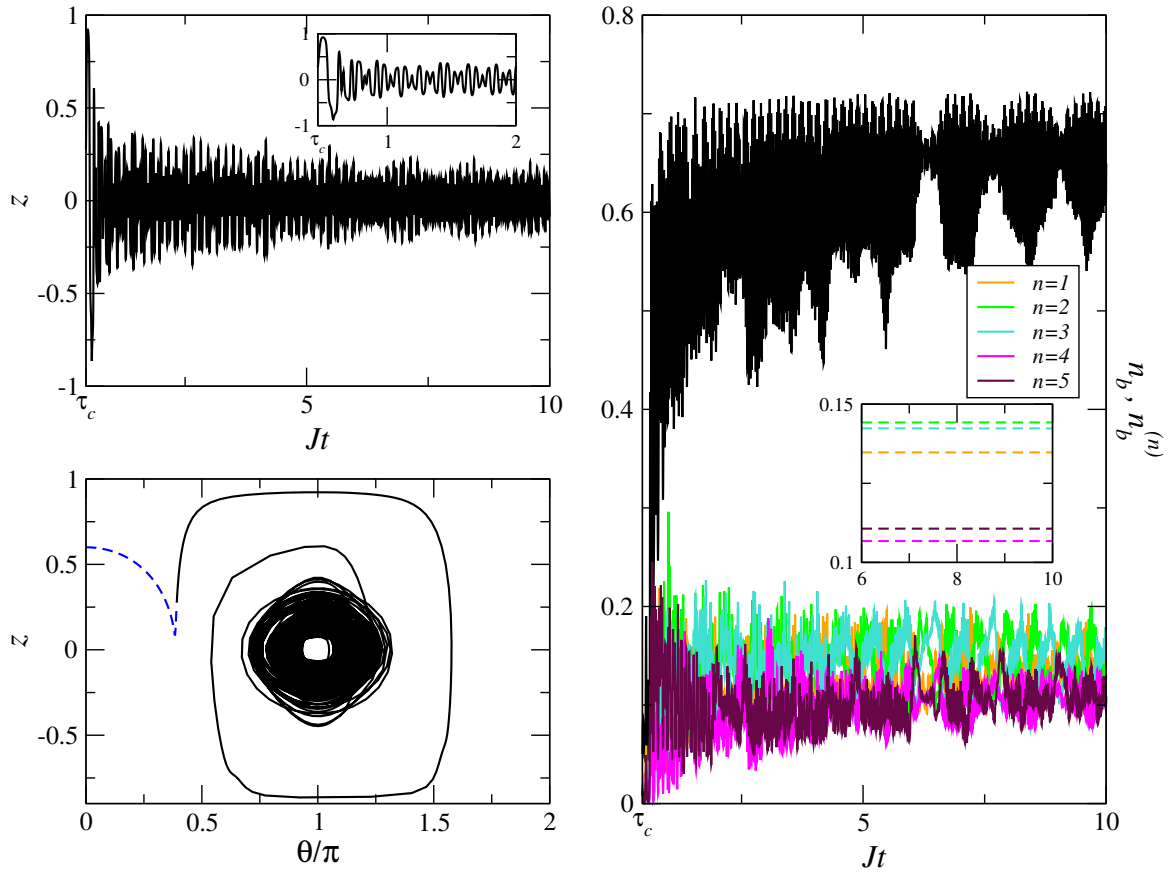

Figure 4.15: Time evolution of condensed and non-condensed particles for initial conditions as in fig. 4.7 for $r = u_c = 60$ (delocalized regime). In the upper left panel, the dynamics of the BEC population imbalance $z(t)$ is shown. The lower left panel shows the phase-space portrait of the dynamical variables z and θ, where the dashed blue line corresponds to the trajectory prior τ_c. The right plot displays the occupation number $n_b^{(n)}$ of the excited levels as a function of time. The black curve corresponds to their sum. The inset shows the time average of each occupation number for the time interval $6 \leq Jt \leq 10$.

two-time correlators and the condensate amplitudes according to eqs. 4.66 - 4.68. Again, all relevant energies are given in terms of the Josephson coupling J and we absorb the large factors appearing the eqs. 4.77 - 4.81 into the dimensionless parameters $u = NU/J$, $k = NK/J$, $j' = NJ'/J$, $u' = NU'/J$, $r = NR/J$ and $n_b^{(n)} = N_b^{(n)}/N$. In addition we will to treat the two-body second-order processes between non-condensate particles with the parameter $u_c = NU_c/J \neq u'$ and consider it as an additional input parameter of the system[5].

From the solutions of the equations of motion we compute the time evolution occupation numbers for the bosons out of the condensate, $n_b^{(n)}(t)$ and $n_b(t) = \sum n_b^{(n)}(t)$, the condensate population imbalance $z(t) = [N_1(t) - N_2(t)]/N$, and the relative phase difference $\theta(t) = \theta_1(t) - \theta_2(t)$ as well as the real part of the diagonal elements of the single particle excitations spectral function $\mathrm{Re}\left[A^G_{nn}(t, \tau_c)\right]$. We plot all the the quantities for times $t \geq \tau_c$, since no sizable

[5] u_c must be equal to u' according to the definition of the overlap matrix element $V_{nms\ell}$ in eq. 4.24

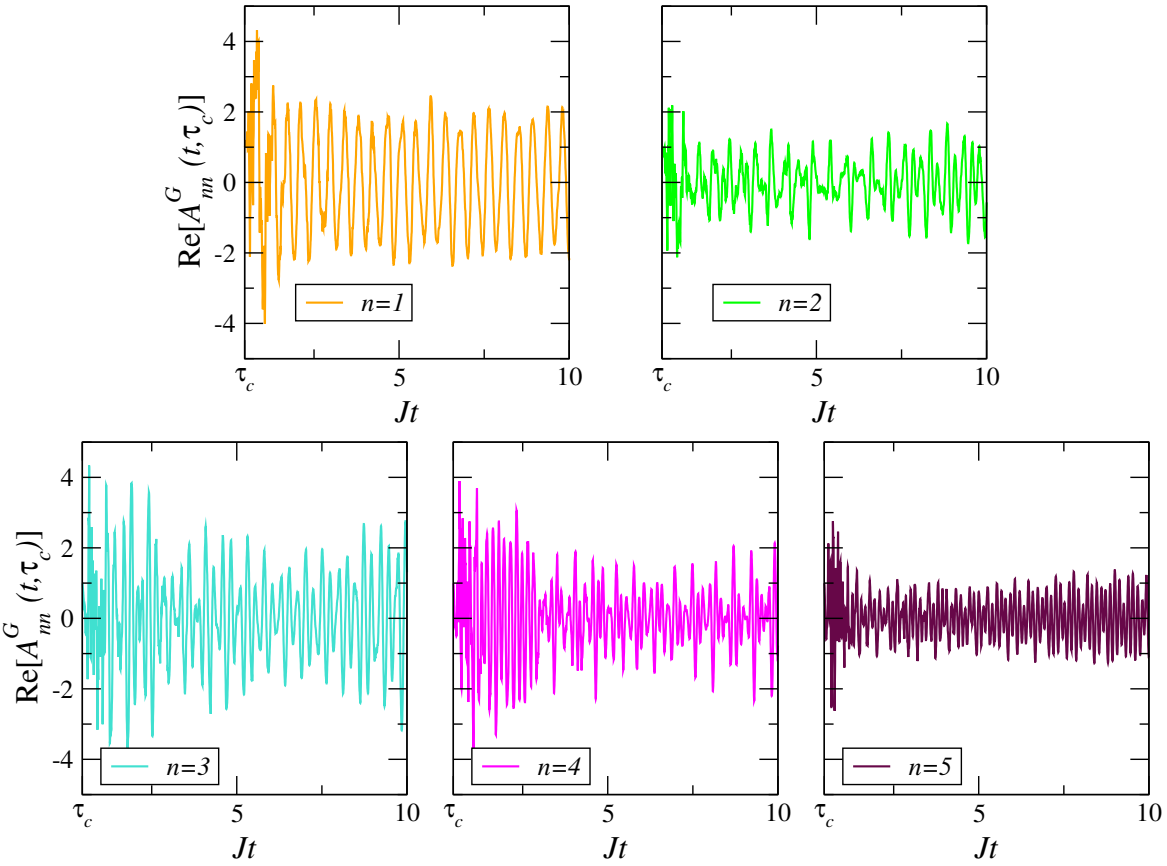

Figure 4.16: Time evolution of the single particle excitations spectral function Re $\left[A^G_{nn}(t,\tau_c)\right]$ for $t > \tau_c$ with initial conditions as in fig. 4.15

deviations are observed from the results obtained using BHF approximation for times prior τ_c.

Figs. 4.15 and 4.17 show the time evolution of the condensate population imbalance $z(t)$ and the population of the excited levels $n_b^{(n)}$ as well as the phase-space portrait of the variable $z(t)$ and $\theta(t)$ for the initial conditions as in fig. 4.7 and fig. 4.9, respectively. The parameters r and u_c describing the second-order processes were chose equal in each of the figures. We observe in that in both figures the population imbalance is damped and that the sum of the occupation numbers of the excited levels has a tendency to saturate with damped oscillations. Those effects are more pronounced for a larger parameter $r = u_c$. Naively, we expect the occupation number of the lowest excited level to approach the highest value and the higher levels approach values in descending order. This is not seen in left panel of fig. 4.15, but a tendency is visible in fig. 4.17 (see the time average of each occupation number in the insets). The reason for this could be that we were not able to propagate the solutions long enough in order to observe thermalization. Unfortunately, the computational cost is so high, that it would require very long simulation times. The trajectory in the phase-space portrait is contracted after switching to a π junction. This is due to the damped oscillations of the BEC population imbalance.

The temporal behavior of the real part of the two-time spectral function Re $\left[A^G_{nn}(t,\tau_c)\right]$

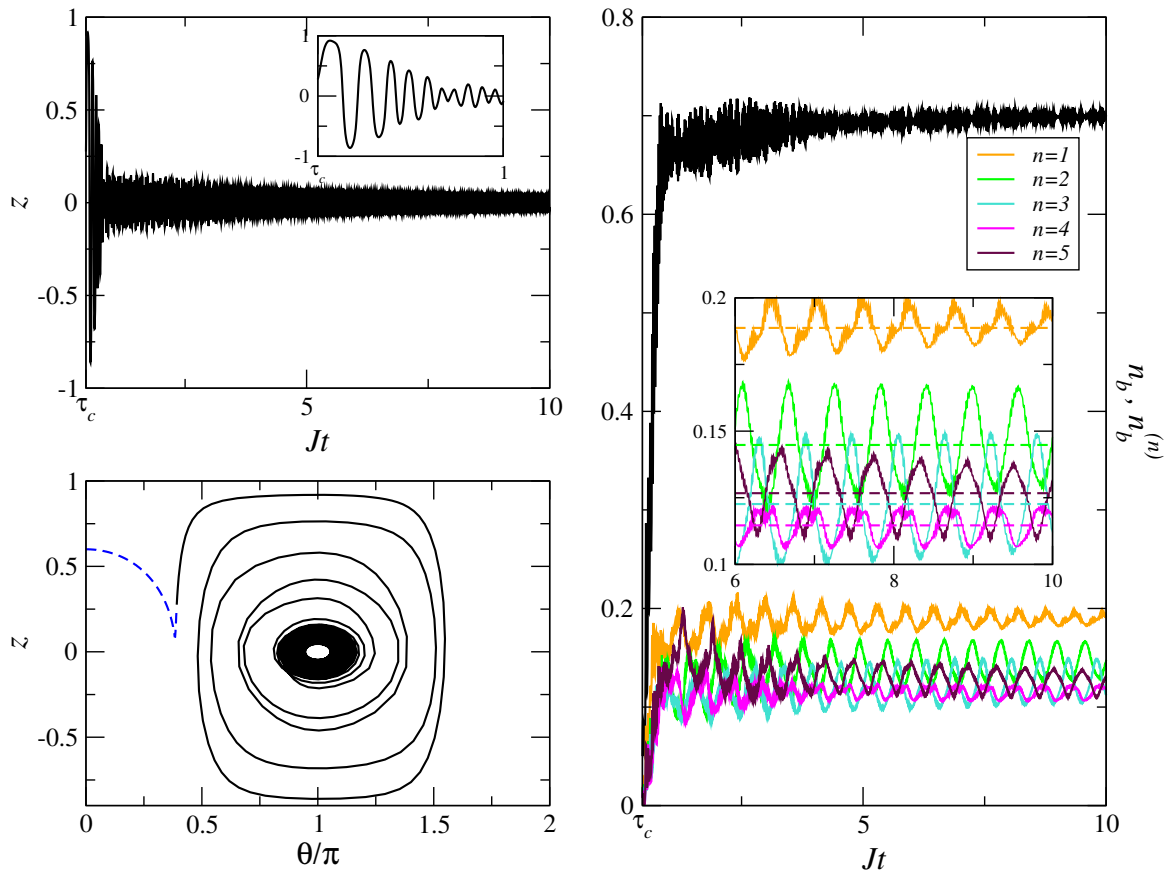

Figure 4.17: Time evolution of condensed and non-condensed particles for initial conditions as in fig. 4.7 for $r = u_c = 60$ (delocalized regime). In the upper left panel, the dynamics of the BEC population imbalance $z(t)$ is shown. The lower left panel shows the phase-space portrait of the dynamical variables z and θ, where the dashed blue line corresponds to the trajectory prior τ_c. The right plot displays the occupation number $n_b^{(n)}$ of the excited levels as a function of time. The black curve corresponds to their sum. The inset shows the time average of each occupation number for the time interval $6 \leq Jt \leq 10$.

provides an idea about the correlations between $t = \tau_c$ and the intermediate states for $t > \tau_c$. We observe that for smaller parameters r and u_c, a damping of the temporal oscillations of the spectral function is barely evident (see fig. 4.16). This suggest the presence of large memory effects. In contrast, fig. 4.18 shows a damping of the oscillations for an increased r and u_c for the time evolution of the spectral function. This damping becomes less pronounced for the higher excited levels. This can be understood as a partial loss of information about the state at $t = \tau_c$ and a suppression of the correlations between it and the later states.

4.3 Discussion

To conclude, we have presented a detailed quantum dynamical study of the non-linear Josephson dynamics of the BECs confined in a finite-size double-well potential, including the coupling

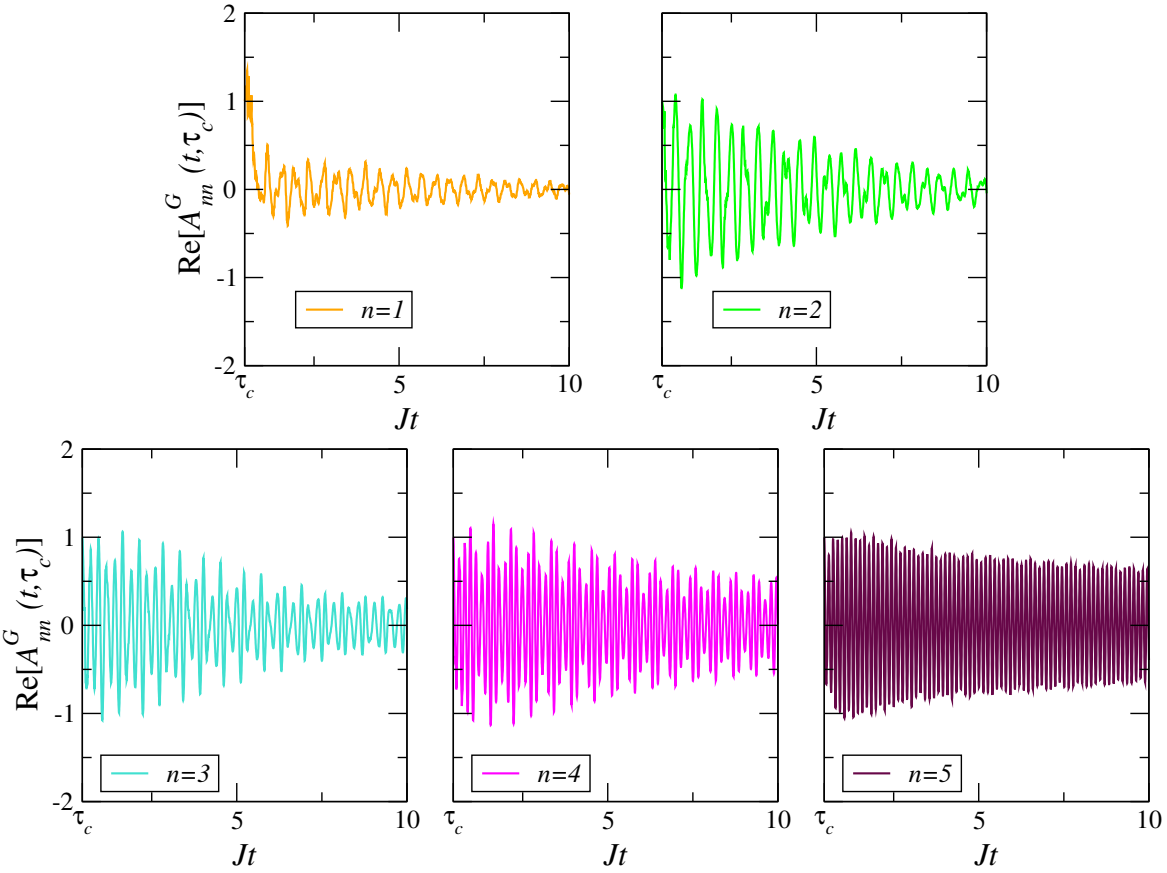

Figure 4.18: Time evolution of the single particle excitations spectral function Re $\left[A^G_{nn}(t,\tau_c)\right]$ for $t > \tau_c$ with initial conditions as in fig. 4.17

to the non-condensate particles. Remarkably, the system can sustain multiple, undamped Josephson oscillations for an extended time period before particles get excited out of the condensates and the behavior changes abruptly to a regime of fast Josephson and Rabi oscillations. The number of undamped Josephson oscillations depends on the trap geometry and number of particles in the system. We have conducted a quantitative and qualitative study on the time scale at which the dynamics of the system changes into non-condensate particles dominated regime. The time scale describes the transition to the high-frequency anharmonic state in a satisfactory way, despite of the ambiguities in its numerical definition. At the transition, we observe that particles get excited out of the condensate as an avalanche, as a consequence of the crossing of the lowest quasiparticle energy and the highest condensate eigenenergy. In the regime dominated by the single particle excitations we observe two main features. First, a state initially prepared in the self-trapped regime undergoes a transition to the delocalized regime simultaneously with the transition to the non-condensate particles dominated regime. Second, at the onset of the fast dynamics the system changes from a "0" to a "π" Josephson junction in order to sustain the large Josephson current in the state of fast dynamics.

Only in the non-condensate particles dominated regime we observed strong damping of oscil-

lations due to inelastic non-condensate particles collisions and a tendency towards equilibration of the system. The parameters describing the second-order processes were chosen very large in order to observe a "pre-thermalization". The study of the two-time spectral function suggests that the lowest excited level has the largest effective loss of information about the initial reference state.

CHAPTER 5

Non-Equilibrium Dynamics of the Bose-Hubbard-Model

Despite of the considerable amount of time many physicists have invested in studying the Bose-Hubbard model, it remains a source of fascination. Perhaps the fact that the Bose-Hubbard model is the simplest many-body model one can write down, which cannot be reduced to a single-particle theory, keeps attracting remarkable amount of interest.

In chapter 3 we presented the theoretical tools to analyze the temporal dynamics of a Bose-condensed gas. In the following we want to apply them to the Bose-Hubbard model to study the non-trivial time evolution of a coherent state loaded in the center of an optical lattice, which is subsequently driven out of equilibrium by suddenly turning on the tunneling between neighboring sites. But before we proceed to do so, we will first introduce the Bose-Hubbard model and discuss its equilibrium properties. Then, we will derive the equations of motion describing non-equilibrium situations of this model. As a first example, we will apply this non-equilibrium description to the TSBH model, and compare the result with the model we postulated in chapter 4 to describe non-equilibrium Josephson oscillations between two BECs. After that, we will proceed to study the expansion dynamics of a coherent state on a two dimensional optical lattice.

5.1 The Bose-Hubbard Model

We begin our analysis by considering a system of interacting atoms of bosonic nature trapped in an external potential. The second-quantized Hamiltonian describing such a system in the grand canonical ensemble is given by

$$\hat{H} = \int \mathrm{d}\mathbf{r}\, \hat{\Psi}^\dagger(\mathbf{r},t) \left(-\frac{1}{2m}\boldsymbol{\nabla}^2 + V_{\mathrm{ext}}(\mathbf{r},t) - \mu \right) \hat{\Psi}(\mathbf{r},t) + \frac{g}{2} \int \mathrm{d}\mathbf{r}\, \hat{\Psi}^\dagger(\mathbf{r},t)\hat{\Psi}^\dagger(\mathbf{r},t)\hat{\Psi}(\mathbf{r},t)\hat{\Psi}(\mathbf{r},t), \tag{3.1}$$

where μ is the chemical potential, and all other appearing quantities were introduced in section 3.1. Moreover, throughout this chapter we will consider a trapping potential periodic in space, i.e., $V_{\mathrm{ext}}(\mathbf{r}) = V_{\mathrm{ext}}(\mathbf{r}+\mathbf{X})$ with the periodicity $\mathbf{X}$. According to the discussion in chap. 4, a periodic potential for an atomic gas can be created using standing waves of laser light [46].

It is well known that according to Bloch's theorem the eigenstates of a periodic Hamiltonian

can be represented in form of Bloch waves, $\phi_{\mathbf{k},\mathbf{n}}(\mathbf{r}) = e^{i\mathbf{k}\cdot\mathbf{r}} u_{\mathbf{k},\mathbf{n}}(\mathbf{r})$, where the components of the lattice momentum $\mathbf{k}$ are restricted to values inside the first Brillouin zone, $k_a \in [-\pi/X_a, \pi/X_a]$, with X_a being the respective components of $\mathbf{X}$. The index $\mathbf{n}$ labels the separated energy bands of the lattice, and the functions $u_{\mathbf{kn}}(\mathbf{r}) = u_{\mathbf{k},\mathbf{n}}(\mathbf{r}+\mathbf{X})$ have the same periodicity as the lattice.

Now let us consider the case where the potential minima located at the sites $\mathbf{X}_i$ of the lattice are well separated. In this case the weight of the atoms moving on the potential are tightly bound to the lattice minima. Thus, it is convenient to represent the Hamiltonian 3.1 in a basis that reflects the atomic orbital states of the isolated lattice minima. One can show that for each energy band $\mathbf{n}$ a set of Wannier functions $w_{\mathbf{n}}(\mathbf{r}-\mathbf{X}_i)$ exits, such that the Bloch functions can be written as

$$\phi_{\mathbf{k},\mathbf{n}}(\mathbf{r}) = \sum_i e^{i\mathbf{k}\cdot\mathbf{r}} w_{\mathbf{n}}(\mathbf{r}-\mathbf{X}_i). \tag{5.1}$$

The Wannier functions form a set of orthonormal functions for the different bands $\mathbf{n}$ and lattice sites i, i.e. $\int \mathrm{d}\mathbf{r}\, w^*_{\mathbf{n}}(\mathbf{r}-\mathbf{X}_i) w_{\mathbf{n}'}(\mathbf{r}-\mathbf{X}_{i'}) = \delta_{\mathbf{n}\mathbf{n}'}\delta_{ii'}$.

Now we can expand the second-quantized field operators $\hat{\Psi}(\mathbf{r},t)$ in terms of the Wannier functions as follows,

$$\hat{\Psi}(\mathbf{r},t) = \sum_{\mathbf{n},i} \hat{b}_{\mathbf{n},i}(t) w_{\mathbf{n}}(\mathbf{r}-\mathbf{X}_i), \tag{5.2}$$

where the $\hat{b}_{\mathbf{n},i}(t)$ are the expansion coefficients and correspond to the annihilation operators of an atom in the Wannier state represented by the function $w_{\mathbf{n}}(\mathbf{r}-\mathbf{X}_i)$. The Wannier functions of an optical lattice can be approximated by harmonic oscillator states on each lattice site, provided we are considering the tight-binding limit. If this is the case, the quantum states at each lattice site will be represented by the quantum numbers n_x, n_y and n_z, corresponding to three dimensional harmonic oscillators in Cartesian coordinates. If the system under consideration is prepared at low temperatures, the atoms will only occupy the lowest energy state, i.e., $\mathbf{n} = \mathbf{0}$, at each site. Consequently, we can restrict the summation over the quantum states $\mathbf{n}$ in equation 5.2 to the $\mathbf{n} = \mathbf{0}$ terms.

Inserting 5.2 into the Hamiltonian 3.1, we obtain

$$\hat{H} = \sum_i (\epsilon_i - \mu)\hat{b}^\dagger_i \hat{b}_i - \sum_{i\neq j} J_{ij}\hat{b}^\dagger_i \hat{b}_j + \frac{1}{2}\sum_{i,j}\sum_{i',j'} U_{iji'j'}\hat{b}^\dagger_i \hat{b}^\dagger_j \hat{b}_{i'}\hat{b}_{j'}, \tag{5.3}$$

with the on-site energies

$$\epsilon_i = \int \mathrm{d}\mathbf{r}\, w^*_{\mathbf{0}}(\mathbf{r}-\mathbf{X}_i)\left[-\frac{1}{2m}\boldsymbol{\nabla}^2 + V_{\mathrm{ext}}(\mathbf{r})\right] w_{\mathbf{0}}(\mathbf{r}-\mathbf{X}_i), \tag{5.4}$$

the tunneling or hopping amplitude between the sites i and j

$$J_{ij} = -\int \mathrm{d}\mathbf{r}\, w^*_{\mathbf{0}}(\mathbf{r}-\mathbf{X}_i)\left[-\frac{1}{2m}\boldsymbol{\nabla}^2 + V_{\mathrm{ext}}(\mathbf{r})\right] w_{\mathbf{0}}(\mathbf{r}-\mathbf{X}_j), \tag{5.5}$$

and

$$U_{iji'j'} = g\int \mathrm{d}\mathbf{r}\int \mathrm{d}\mathbf{r}'\, w^*_{\mathbf{0}}(\mathbf{r}-\mathbf{X}_i) w^*_{\mathbf{0}}(\mathbf{r}'-\mathbf{X}_j)\delta(\mathbf{r}-\mathbf{r}') w_{\mathbf{0}}(\mathbf{r}'-\mathbf{X}_{i'}) w_{\mathbf{0}}(\mathbf{r}-\mathbf{X}_{j'}) \tag{5.6}$$

representing the interactions energy between two atoms. In general it does not only contain the on-site two-particle interactions, but also interactions between atoms on different sites. The

later can be neglected, because they are usually exponentially suppressed.

The summation in eq. 5.3 related to the hopping of atoms from one site to another extends over all possible combinations of $i \neq j$. Assuming that the lattice is deep enough, the major contributions will come from the hopping to the nearest neighbor, while the others will be exponentially suppressed. This allows us to restrict the summation to the nearest-neighbor hopping terms, which we will denote by $\sum_{\langle i,j \rangle}$ and its corresponding hopping amplitude J. With all these approximations, the Hamiltonian now reads

$$\begin{aligned} \hat{H} &= -J \sum_{\langle i,j \rangle} \hat{b}_i^\dagger \hat{b}_j + \sum_i (\epsilon_i - \mu) \hat{b}_i^\dagger \hat{b}_i + \frac{U}{2} \sum_i \hat{b}_i^\dagger \hat{b}_i^\dagger \hat{b}_i \hat{b}_i \\ &= -J \sum_{\langle i,j \rangle} \hat{b}_i^\dagger \hat{b}_j + \sum_i (\epsilon_i - \mu) \hat{b}_i^\dagger \hat{b}_i + \frac{U}{2} \sum_i \hat{n}_i \left(\hat{n}_i - 1 \right), \end{aligned} \tag{5.7}$$

where in the last equality we used the bosonic commutation relations in order to rewrite the term related to the two-particle interactions in terms of the occupation operator $\hat{n}_i = \hat{b}_i^\dagger \hat{b}_i$.

The simplified Hamiltonian 5.7 is known as "Bose-Hubbard model". It could have been postulated phenomenologically: atoms that tunnel between the potential minima $(\epsilon_i - \mu)$ of the optical lattice with the hopping amplitude J, while multiple occupancy of a single site results in an energy penalty proportional to U.

5.1.1 Superfluid-Mott Insulator Transition

At zero temperature the Bose-Hubbard model features two different phases, the superfluid and the Mott insulator phase. The former is characterized by a hopping amplitude J that exceeds the on-site repulsion U, which results in a kinetic energy dominated regime. In contrast to the superfluid phase, the Mott insulator phase is the result of an on-site repulsion that overwhelms the tunneling between lattice sites. These two phases can be understood as the competition of the parameters J and U. The hopping amplitude J, which is related to the kinetic energy, tries to delocalize the atoms, while the on-site repulsion U tries to localize them and suppresses the on-site particle number fluctuations.

In the following we want to study the transition between the two phases that characterize the Bose-Hubbard model at zero temperature [16, 46, 77, 78]. In analogy to the Bogoliubov approach, we first introduce the superfluid order parameter

$$\Psi = \sqrt{n_0} = \langle \hat{b}_i^\dagger \rangle = \langle \hat{b}_i \rangle, \tag{5.8}$$

where n_0 is the condensate fraction $\langle N_0 \rangle / N_s$ per site, and N_s is the number of sites. Notice, that Ψ can be chosen to be real, because the model is translational invariant and one can choose a global gauge transformation to absorb its complex phase.

Now, aiming towards the construction of a consistent mean-field theory, we make the substitution

$$\hat{b}_i^\dagger \hat{b}_j \approx \langle \hat{b}_i^\dagger \rangle \hat{b}_j + \hat{b}_i^\dagger \langle \hat{b}_j \rangle - \langle \hat{b}_i^\dagger \rangle \langle \hat{b}_j \rangle = \Psi \left(\hat{b}_i^\dagger + \hat{b}_j \right) - \Psi^2 \tag{5.9}$$

in the hopping term of eq. 5.7. Thus, we obtain the effective Hamiltonian

$$\begin{aligned}\hat{H}^{eff} &= zJ\Psi^2 N_s + \frac{U}{2}\sum_i \hat{n}_i\left(\hat{n}_i - 1\right) - \mu\sum_i \hat{b}_i^\dagger \hat{b}_i - zJ\sum_i \Psi\left(\hat{b}_i^\dagger + \hat{b}_j\right) \\ &= zJ\sum_i \left[-\overline{\mu}\hat{n}_i + \frac{\overline{U}}{2}\hat{n}_i\left(\hat{n}_i - 1\right) + \Psi^2 - \Psi\left(\hat{b}_i^\dagger + \hat{b}_j\right)\right] \end{aligned} \tag{5.10}$$

where z is the number of nearest-neighbors. In the last equality we introduced $\overline{U} = U/zJ$ and $\overline{\mu} = \mu/zJ$. Note that the summand in the second line is the same for every single site. Hence, we can drop the index i when studying a single site. In addition, all energies in the summand are scaled by the factor $1/zJ$, making them dimensionless.

With the purpose of deriving the phase diagram analytically, we consider a single site on the lattice, which is described by the dimensionless Hamiltonian

$$\begin{aligned}\hat{H} &= \hat{H}^{(0)} + \Psi\hat{V} \\ &= \left[-\overline{\mu}\hat{n} + \frac{\overline{U}}{2}\hat{n}\left(\hat{n} - 1\right) + \Psi^2\right] - \Psi\left(\hat{b}^\dagger + \hat{b}\right), \end{aligned} \tag{5.11}$$

where we split the Hamiltonian in an exact solvable part $\hat{H}^{(0)}$ and a perturbation $\Psi\hat{V}$.

From perturbation theory analysis of the Hamiltonian, we observe that in the occupation number basis all the energy corrections with odd powers of Ψ are zero. Denoting the unperturbed energy of the state with exactly n particles by $E_n^{(0)}$, we obtain

$$E_g^{(0)} = \min\left\{E_n^{(0)} \,|\, \forall n \in \mathbb{N}\right\} \tag{5.12}$$

for the unperturbed ground state energy. Comparison between the energies $E_n^{(0)}$ and $E_{n+1}^{(0)}$ yields

$$E_g^{(0)} = \begin{cases} 0, & \overline{\mu} < 0 \\ \frac{\overline{U}}{2}g(g-1) - \overline{\mu}g, & \overline{U}(g-1) < \overline{\mu} < \overline{U}g \end{cases}. \tag{5.13}$$

Inserting this in the standard formula for the second-order correction to the energy [74], we get

$$E_g^{(2)} = \Psi^2\left[\frac{g}{\overline{U}(g-1) - \overline{\mu}} + \frac{g+1}{\overline{\mu} - \overline{U}g}\right]. \tag{5.14}$$

If we write the energy ground state as an expansion in Ψ as

$$E_g(\Psi) = a\left(g, \overline{U}, \overline{\mu}\right) + b\left(g, \overline{U}, \overline{\mu}\right)\Psi^2 + \mathcal{O}\left(\Psi^4\right) \tag{5.15}$$

according the usual Landau procedure for second order phase transitions, and minimize it as a function of the superfluid order parameter, we obtain $\Psi = 0$ for $b\left(g, \overline{U}, \overline{\mu}\right) > 0$ and $\Psi \neq 0$ for $b\left(g, \overline{U}, \overline{\mu}\right) < 0$. This implies that the boundary between the superfluid phase and the Mott insulator phase is defined by $b\left(g, \overline{U}, \overline{\mu}\right) = 0$, which yields

$$\overline{\mu}_\pm = \frac{1}{2}\left(\overline{U}(2g-1) - 1\right) \pm \frac{1}{2}\sqrt{\overline{U}^2 - 2\overline{U}(2g+1) + 1}. \tag{5.16}$$

The subscript $\pm$ refers to the upper and lower halves of the Mott insulating regions in the phase diagram depicted in fig. 5.1. In order to obtain the smallest value $\overline{U}$ can take in each of the "lobes", we set $\overline{\mu}_+$ equal to $\overline{\mu}_-$ and solve for $\overline{U}$. This critical value will be denoted by $\overline{U}_c$ and reads

$$\overline{U}_c = 2g + 1 + \sqrt{(2g+1)^2 - 1}. \tag{5.17}$$

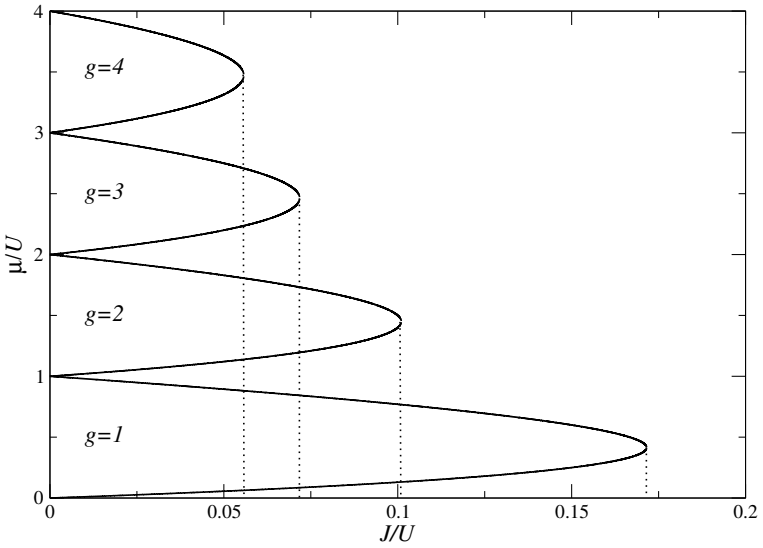

Figure 5.1: The solid lines depict the transition between the superfluid phase and the Mott insulator phase as computed from the second order perturbation theory. The vertical dotted lines indicated the critical values of J for different fillings.

In Figure 5.1 we show the phase diagram of the Bose-Hubbard model as obtained from the second order perturbation theory. Note that we plotted the chemical potential depicting the transition between the two phases as a function of the tunneling amplitude J, instead of the interatomic interactions U. This is easily done by using $\mu = zJ\overline{\mu}$ and $U = zJ\overline{U}$. The quantities on the axis are given in units of U. The dotted lines in the figure indicate the maximal value J_c that the hopping amplitude J can take in each of the lobes.

Up to this point we have discussed a translational invariant Bose-Hubbard Hamiltonian. However, in order to describe experiments we need to take the influence of the external trapping potential into account. In a simple approximation, the effect of the confining potential can be described by defining a local chemical potential $\mu(\mathbf{r}) = \mu - V_{\text{ext}}(\mathbf{r})$, where $V_{\text{ext}}(\mathbf{r})$ is the trapping potential. Assume, for instance, that the change of the mean particle number between neighboring sites is small. In this case, the system can be treated locally as a homogeneous system. Since the chemical potential is fixed by the particle density, the system can undergo a phase transition from superfluid to Mott insulator phase locally by changing the ration J/U. This provides an insight in the density profile of atoms spread on optical lattice and confined by an external trapping potential. If the trapping potential looks like a harmonic trap, the density profile across the full lattice will resemble a "wedding-cake" [79–82]. Moving outwards from

the center of the lattice, one will encounter rings of Mott insulating regions with decreasing particle density.

5.2 Equations of Motion

Having introduced the Bose-Hubbard model and its zero temperature phase transition from superfluid to Mott-insulator, we proceed to derive the kinetic equations necessary to study non-equilibrium situations of bosonic atoms on an optical lattice. The equations of motion will be derived within the framework of the self-consistent approximations presented in section 3.2. Once the mathematical tools are developed, we will apply them to the TSBH model and use them to describe the temporal dynamics of an expanding coherent state on a two dimensional lattice.

We begin our analysis considering the Bose-Hubbard Hamiltonian 5.7 in the canonical ensemble:

$$\hat{H} = -J \sum_i \left(\hat{b}_i^\dagger \hat{b}_{i+\{1\}} + \hat{b}_{i+\{1\}}^\dagger \hat{b}_i \right) + \frac{U}{2} \sum_i \hat{b}_i^\dagger \hat{b}_i^\dagger \hat{b}_i \hat{b}_i, \tag{5.18}$$

where we set all on-site energy to zero, i.e., $\epsilon_i = 0$, and $\pm\{1\}$ denotes all jumps to the nearest neighbors. For simplicity we will write from now on ± 1 instead.

Now we proceed similar to the analysis in section 3.1 and denote the mean field or the expectation value of the field operator by $a_i(t) = \langle \hat{b}_i \rangle$ and the fluctuation operator by $\hat{\varphi}_i(t) = \hat{b}_i(t) - a_i(t)$. Physically, $|a_i(t)|^2$ is related to the condensate population at site i. As a consequence of representing the bosonic operators $\hat{b}_i$ in terms of the mean field and the fluctuation operator, the full bosonic propagator splits into $\boldsymbol{C} + \boldsymbol{G}$, where

$$\boldsymbol{C}_{ij}(t_i, t_j) = -i \begin{pmatrix} a_i(t_i) a_j^*(t_j) & a_i(t_i) a_j(t_j) \\ a_i^*(t_i) a_j^*(t_j) & a_i^*(t_i) a_j(t_j) \end{pmatrix} \tag{5.19}$$

is the propagator related to the mean field, and

$$\begin{aligned} \boldsymbol{G}_{ij}(t_i, t_j) = & -i \begin{pmatrix} \langle T_C \hat{\varphi}_i(t_i) \hat{\varphi}_j^\dagger(t_j) \rangle & \langle T_C \hat{\varphi}_i(t_i) \hat{\varphi}_j(t_j) \rangle \\ \langle T_C \hat{\varphi}_i^\dagger(t_i) \hat{\varphi}_j^\dagger(t_j) \rangle & \langle T_C \hat{\varphi}_i^\dagger(t_i) \hat{\varphi}_j(t_j) \rangle \end{pmatrix} \\ = & \begin{pmatrix} G_{ij}(t_i, t_j) & F_{ij}(t_i, t_j) \\ \overline{F}_{ij}(t_i, t_j) & \overline{G}_{ij}(t_i, t_j) \end{pmatrix}, \end{aligned} \tag{5.20}$$

the propagator related to the fluctuations. T_C denotes the time ordering along the CTP, shown in fig. 2.2. Note that in the time arguments we used the same indices as the subscripts related to the lattice sites. In fact, it is not necessary to do so, but this allow us to simplify the notation in our further analysis. For the rest of this chapter, we will write

$$\boldsymbol{G}_{ij}(t_i, t_j) \equiv \boldsymbol{G}_{ij}, \tag{5.21}$$

and similarly for $\boldsymbol{C}$. When the two time variables are evaluated at equal times for different lattice sites $i \neq j$, we will mention it explicitly.

Using the real-time formalism discussed in section 2.2, the associated Dyson's equations on

the real time contour yields

$$\sum_k \int_{-\infty}^{\infty} \mathrm{d}t_k \left[\boldsymbol{G}_{0,ik}^{-1} - \boldsymbol{S}_{ik}^{HF}\right] \boldsymbol{C}_{kj} = -i \sum_k \int_{-\infty}^{t_i} \mathrm{d}t_k \, \boldsymbol{\gamma}_{ik} \boldsymbol{C}_{kj}, \tag{5.22}$$

$$\sum_k \int_{-\infty}^{\infty} \mathrm{d}t_k \left[\boldsymbol{G}_{0,ik}^{-1} - \boldsymbol{\Sigma}_{ik}^{HF}\right] \boldsymbol{G}_{kj}^{\gtrless} = -i \sum_k \int_{-\infty}^{t_i} \mathrm{d}t_k \, \boldsymbol{\Gamma}_{ik} \boldsymbol{G}_{kj}^{\gtrless} + i \sum_k \int_{-\infty}^{t_j} \mathrm{d}t_k \, \boldsymbol{\Sigma}_{ik}^{\gtrless} \boldsymbol{A}_{kj}, \tag{5.23}$$

where the k summation is taken over all lattice sites and the integration extends according to the intervals specified at the boundaries. We also decomposed the self-energies into the Hartree-Fock local part $\boldsymbol{S}_{ij}^{HF}(\boldsymbol{\Sigma}_{ij}^{HF})$ and its non-local part $\boldsymbol{S}_{ij}(\boldsymbol{\Sigma}_{ij})$. The inverse propagator on the left side reads

$$\boldsymbol{G}_{0,ij}^{-1} \equiv \boldsymbol{G}_{0,ij}^{-1}(t,t') = \left[i\boldsymbol{\tau}_3 \delta_{ij} \frac{\partial}{\partial t} + J\left(\delta_{i,j+1} + \delta_{i,j-1}\right) \mathbb{1}\right] \delta(t-t'), \tag{5.24}$$

where the time arguments were used without the indices, in order to avoid misinterpretations. In accordance to the analysis of chapter 3, we introduce the symmetrized and antisymmetrized correlation functions

$$\begin{aligned} \boldsymbol{A}_{ij} &= i\left[\boldsymbol{G}_{ij}^{>} - \boldsymbol{G}_{ij}^{<}\right] \\ &= \begin{pmatrix} A_{ij}^{G} & A_{ij}^{F} \\ A_{ij}^{F} & A_{ij}^{G} \end{pmatrix}, \end{aligned} \tag{5.25}$$

$$\begin{aligned} \boldsymbol{F}_{ij} &= \frac{1}{2}\left[\boldsymbol{G}_{ij}^{>} + \boldsymbol{G}_{ij}^{<}\right] \\ &= \begin{pmatrix} F_{ij}^{G} & F_{ij}^{F} \\ F_{ij}^{F} & F_{ij}^{G} \end{pmatrix}, \end{aligned} \tag{5.26}$$

related to the fluctuations. Similarly,

$$\begin{aligned} \boldsymbol{\gamma}_{ij} &= i\left[\boldsymbol{S}_{ij}^{>} - \boldsymbol{S}_{ij}^{<}\right] \\ &= \begin{pmatrix} \gamma_{ij}^{G} & \gamma_{ij}^{F} \\ \gamma_{ij}^{F} & \gamma_{ij}^{G} \end{pmatrix} \end{aligned} \tag{5.27}$$

for the spectral function of mean field self-energy, and

$$\begin{aligned} \boldsymbol{\Gamma}_{ij} &= i\left[\boldsymbol{\Sigma}_{ij}^{>} - \boldsymbol{\Sigma}_{ij}^{<}\right] \\ &= \begin{pmatrix} \Gamma_{ij}^{G} & \Gamma_{ij}^{F} \\ \Gamma_{ij}^{F} & \Gamma_{ij}^{G} \end{pmatrix}, \end{aligned} \tag{5.28}$$

$$\begin{aligned} \boldsymbol{\Pi}_{ij} &= \frac{1}{2}\left[\boldsymbol{\Sigma}_{ij}^{>} + \boldsymbol{\Sigma}_{ij}^{<}\right] \\ &= \begin{pmatrix} \Pi_{ij}^{G} & \Pi_{ij}^{F} \\ \Pi_{ij}^{F} & \Pi_{ij}^{G} \end{pmatrix}, \end{aligned} \tag{5.29}$$

for the spectral and statistical functions of the fluctuation's self-energies.

Rewriting the eqs. 5.22 and 5.23 in terms of the symmetrized and antisymmetrized correlators and carefully evaluating the integral on the left hand side of both equations, we get

$$i\boldsymbol{\tau}_3 \frac{\partial}{\partial t_i}\boldsymbol{C}_{ij} = -J\left(\boldsymbol{C}_{i+1,j}+\boldsymbol{C}_{i-1,j}\right)+\boldsymbol{S}_i^{HF}\boldsymbol{C}_{ij}-i\sum_k\int_0^{t_i}\mathrm{d}t_k\,\boldsymbol{\gamma}_{ik}\boldsymbol{C}_{kj}, \tag{5.30}$$

$$i\boldsymbol{\tau}_3 \frac{\partial}{\partial t_i}\boldsymbol{A}_{ij} = -J\left(\boldsymbol{A}_{i+1,j}+\boldsymbol{A}_{i-1,j}\right)+\boldsymbol{\Sigma}_i^{HF}\boldsymbol{A}_{ij}-i\sum_k\int_{t_j}^{t_i}\mathrm{d}t_k\,\boldsymbol{\Gamma}_{ik}\boldsymbol{A}_{kj}, \tag{5.31}$$

$$i\boldsymbol{\tau}_3 \frac{\partial}{\partial t_i}\boldsymbol{F}_{ij} = -J\left(\boldsymbol{F}_{i+1,j}+\boldsymbol{F}_{i-1,j}\right)+\boldsymbol{\Sigma}_i^{HF}\boldsymbol{F}_{ij}-i\sum_k\int_0^{t_i}\mathrm{d}t_k\,\boldsymbol{\Gamma}_{ik}\boldsymbol{F}_{kj}+i\sum_k\int_0^{t_j}\mathrm{d}t_k\,\boldsymbol{\Pi}_{ik}\boldsymbol{A}_{kj}. \tag{5.32}$$

Here we used the locality of the Hartree-Fock self-energies in time arguments as well as in the indices related to the lattice sites, i.e. $\boldsymbol{S}_{ij}^{HF}=\boldsymbol{S}_i^{HF}\delta_{ij}\delta(t_i-t_j)$ and similar for $\boldsymbol{\Sigma}^{HF}$. Note, that the integrals involving higher order terms in U on the right side of eqs. 5.30 and 5.32 start at 0 instead $-\infty$. Similar to the analysis performed in chapter 4, this is a consequence of the choice of the boundary conditions. In the systems we will be considering later in this chapter, we can formulate the boundary conditions such, that the system of equations 5.30 - 5.32 becomes an initial value problem.

Before we proceed to discuss the various approximations that we will consider in this chapter, we will give the expressions for the conserved quantities that are relevant to us. A bosonic gas of cold atoms trapped in an optical lattice can be regarded (in a very good approximation) as being completely isolated. The total particle number conservation arises as a consequence of the global phase invariance of the system. It can be proven that the total particle number

$$\begin{aligned} N &= \sum_i\left[N_i^{(0)}+N_i^{(\varphi)}\right] \\ &= \sum_i\left[|a_i|^2+i\left(F_{ii}^G+\frac{i}{2}\right)\right] \end{aligned} \tag{5.33}$$

is constant by making use of the eqs. 5.30 and 5.32. $N_i^{(0)}$ and $N_i^{(\varphi)}$ are the mean field and fluctuations particle number, respectively, and their sum defines the population at site i. The total particle number is a suitable quantity to test our numerics.

Although the total energy is conserved for an isolated system, the inclusion of dissipative terms in the chosen approximation for the self-energies can break the energy conservation. The particle number conservation can be proven just by using the self-consistency of the equations of motion without giving any explicit expression for the self-energies. This is however not the case for the energy. Making use of the full second-order approximation (see fig. 3.3 and eqs. 3.31 and 3.32), we can prove the mean energy of the atoms $\langle\hat{H}\rangle=\langle\hat{H}\rangle_{\mathrm{c}}+\langle\hat{H}\rangle_{\mathrm{exc}}$ to be conserved, where

$$\langle\hat{H}\rangle_{\mathrm{c}} = \frac{i}{2}\sum_i\mathrm{Tr}\left[-J\left(\boldsymbol{C}_{i+1,i}+\boldsymbol{C}_{i-1,i}\right)+\frac{1}{2}\boldsymbol{S}_i^{HF}\boldsymbol{C}_{ii}+\frac{1}{2}\sum_k\int_0^{t_i}\mathrm{d}t_k\,\boldsymbol{\gamma}_{ik}\boldsymbol{C}_{ki}\right] \tag{5.34}$$

and

$$\langle \hat{H} \rangle_{\text{exc}} = \frac{i}{2} \sum_i \text{Tr} \left[-J \left(\boldsymbol{F}_{i+1,i} + \boldsymbol{F}_{i-1,i} \right) + \frac{1}{2} \boldsymbol{\Sigma}_i^{HF} \boldsymbol{F}_{ii} + \frac{1}{2} \sum_k \int_0^{t_i} \mathrm{d}t_k \, \{ \boldsymbol{\Gamma}_{ik} \boldsymbol{F}_{ki} - \boldsymbol{\Pi}_{ik} \boldsymbol{A}_{ki} \} \right] \tag{5.35}$$

are the mean energies related to the mean field and the fluctuations, respectively.

In addition to the mean energies and the mean field and the fluctuations particle numbers $N_i^{(0)}$ and $N_i^{(\varphi)}$, we introduce the quasi-momentum distribution of the atoms released on the optical lattice. This quantity is easily accessible experimentally and is defined as

$$n_k(t) = \frac{1}{I^d} \sum_{i,j} e^{ik(i-j)} \langle \hat{b}_i^\dagger(t) \hat{b}_j(t) \rangle, \tag{5.36}$$

where $\hat{b}_i^\dagger = a_i^* + \hat{\varphi}_i^\dagger$ and $\hat{b}_i = a_i + \hat{\varphi}_i$ are the bosonic creation and annihilation operators, and the quasi-momentum $k \in \frac{2\pi}{aI} \mathbb{Z}^d$. I is the number of lattice sites in one direction and d is the dimension of the lattice[1]. Furthermore, the memory effects described within the higher order approximations can be quantified with the help of the single particle spectral function $\boldsymbol{A}_{ij}$. The quantity

$$A_k^G(t,0) = \frac{1}{I^d} \sum_{i,j} e^{ik(i-j)} A_{ij}^G(t,0) \tag{5.37}$$

is a good measure for the correlations between the states at time t and the initial condition.

5.2.1 Mean-Field Approximation

Having derived the general equations of motion describing the temporal dynamics of the Bose-Hubbard model, we proceed to study the three approximations we will be considering in the rest of this chapter. We begin with the simplest approximation. If we neglect the quantum fluctuations and constraint the analysis to the mean fields $a_i = \langle \hat{b}_i \rangle$, the system of equations simplify, leaving us only with the equation of motion for the propagator related to the mean field:

$$i \boldsymbol{\tau}_3 \frac{\partial}{\partial t_i} \boldsymbol{C}_{ij} = -J \left(\boldsymbol{C}_{i+1,j} + \boldsymbol{C}_{i-1,j} \right) + \boldsymbol{S}_i^{HF} \boldsymbol{C}_{ij}, \tag{5.38}$$

with the Hartree-Fock self-energy

$$\boldsymbol{S}_i^{HF} = i \frac{U}{2} \text{Tr} \left[\boldsymbol{C}_{ii} \right] \mathbb{1}. \tag{5.39}$$

The upper right component of equation 5.38, reads

$$i \frac{\partial}{\partial t_i} a_i = -J \left(a_{i+1} + a_{i-1} \right) + U |a_i|^2 a_i. \tag{5.40}$$

In other words, the mean field amplitudes satisfy a discrete non-linear Schrödinger equation (DNLSE).

[1] We will only consider equal numbers of lattice sites in every direction for systems with $d > 1$.

5.2.2 Bogoliubov-Hartree-Fock Approximation

The simplest conserving approximation that includes the fluctuations is the BHF approximation. In section 3.4 we discussed its range of validity and properties. The BHF approximation encompasses only the processes involving the fluctuations up to first order in the interaction parameter U. Thus it is equivalent to neglect the integrals on the right side of eqs. 5.30 - 5.32. In doing so, the equations of motion for the spectral and statistical function of the fluctuations reduce to

$$i\boldsymbol{\tau}_3 \frac{\partial}{\partial t_i} \boldsymbol{A}_{ij} = -J\left(\boldsymbol{A}_{i+1,j} + \boldsymbol{A}_{i-1,j}\right) + \boldsymbol{\Sigma}_i^{HF} \boldsymbol{A}_{ij}, \tag{5.41}$$

$$i\boldsymbol{\tau}_3 \frac{\partial}{\partial t_i} \boldsymbol{F}_{ij} = -J\left(\boldsymbol{F}_{i+1,j} + \boldsymbol{F}_{i-1,j}\right) + \boldsymbol{\Sigma}_i^{HF} \boldsymbol{F}_{ij} \tag{5.42}$$

where the Hartree-Fock self-energy in terms of the statistical function is given by

$$\begin{aligned} \boldsymbol{\Sigma}_i^{HF} &\equiv \begin{pmatrix} \Sigma_i^{HF} & \Omega_i^{HF} \\ \overline{\Omega}_i^{HF} & \overline{\Sigma}_i^{HF} \end{pmatrix} \\ &= iU\left(\left\{\frac{1}{2}\mathrm{Tr}\left[\boldsymbol{C}_{ii}\right]\mathbb{1} + \boldsymbol{C}_{ii}\right\} + \left\{\frac{1}{2}\mathrm{Tr}\left[\boldsymbol{F}_{ii}\right]\mathbb{1} + \boldsymbol{F}_{ii}\right\}\right). \end{aligned} \tag{5.43}$$

The equations for the fluctuations two-time correlators are coupled to an equation for the mean-field amplitude. This equation is obtained by inserting the self-energy

$$\begin{aligned} \boldsymbol{S}_i^{HF} &\equiv \begin{pmatrix} S_i^{HF} & W_i^{HF} \\ \overline{W}_i^{HF} & \overline{S}_i^{HF} \end{pmatrix} \\ &= iU\left(\frac{1}{2}\mathrm{Tr}\left[\boldsymbol{C}_{ii}\right]\mathbb{1} + \left\{\frac{1}{2}\mathrm{Tr}[\boldsymbol{F}_{ii}]\mathbb{1} + \boldsymbol{F}_{ii}\right\}\right) \end{aligned} \tag{5.44}$$

into equation 5.38. The upper right component the reads

$$i\frac{\partial}{\partial t_i} a_i = -J\left(a_{i+1} + a_{i-1}\right) + \left(U|a_i|^2 + 2iUF_{ii}^G\right) a_i + iUF_{ii}^F a_i^*. \tag{5.45}$$

Due to the fact that $\boldsymbol{F}_{ii}$ is the only quantum fluctuations related quantities appearing in the Hartree-Fock self-energies 5.44 and 5.43, the equations for the components of the spectral function $\boldsymbol{A}_{ij}$ decouple from the system of equations. In addition, since the integrals containing the higher order terms in U do not appear in the equations of motions within the framework of the BHF approximation, it is sufficient to propagate the solutions for the two-time correlation function evaluated at equal times. Following the discussion in sections 3.4 and 4.2.1, for the components of the statistical function we obtain

$$\begin{aligned} i\frac{\partial}{\partial t_i} F_{ij}^G &= -J\left(F_{i+1,j}^G + F_{i-1,j}^G\right) + J\left(F_{i,j+1}^G + F_{i,j-1}^G\right) \\ &\quad + \Sigma_i^{HF} F_{ij}^F - F_{ij}^F \Sigma_j^{HF} - \Omega_i^{HF}\left(F_{ij}^F\right)^* - F_{ij}^F\left(\Omega_j^{HF}\right)^*, \end{aligned} \tag{5.46}$$

$$\begin{aligned} i\frac{\partial}{\partial t_i} F_{ij}^F &= -J\left(F_{i+1,j}^F + F_{i-1,j}^F\right) - J\left(F_{i,j+1}^F + F_{i,j-1}^F\right) \\ &\quad + \Sigma_i^{HF} F_{ij}^F + F_{ij}^F \Sigma_j^{HF} - \Omega_i^{HF}\left(F_{ij}^G\right)^* + F_{ij}^G \Omega_j^{HF}, \end{aligned} \tag{5.47}$$

where all the two-time quantities are evaluated at equal times and

$$\Sigma_i^{HF} = 2U|a_i|^2 + 2iUF_{ii}^G, \tag{5.48}$$
$$\Omega_i^{HF} = U\left(a_i\right)^2 + iUF_{ii}^F. \tag{5.49}$$

When solving the system of equations 5.45, 5.46 and 5.47, one exploits that fact that they are already discrete in space. This reduces the system to a non-linear set of ordinary differential equations, which can be numerically solved by the means of the Runge-Kutta method.

5.2.3 Full Second-Order Approximation

In the derivation of the equations 5.30 - 5.32, the only assumption made was that we were working within the framework of a conserving approximation. This allowed us to write the terms involving higher order processes in the interatomic interactions as a convolution of the self-energy and the one-particle propagator. In section 3.2.2, we presented the Feynman diagrams contributing to the full second-order approximation (see fig. 3.3), which were obtained from a ϕ-derivable functional.

In sections 3.5 and 4.2.2, it was stated that the full dynamics of the fluctuations can be described in terms of the upper-left and upper-right component of $\boldsymbol{A}_{ij}$ and $\boldsymbol{F}_{ij}$, since the remaining two are obtained from the relations listed in tab. 3.1. Similar symmetry relations also apply to the self-energies (see tab. 3.2). We therefore only give the expressions for the upper-left and upper-right components of the spectral function of the mean field self-energy:

$$\gamma_{ij}^G = U^2\left(F_{ij}^G\left\{4\Lambda[F,F^*]_{ij} + 2\Lambda[G,G^*]_{ij}\right\} + A_{ij}^G\left\{4\Xi[F,F^*]_{ij} + 2\Xi[G,G^*]_{ij}\right\}\right), \tag{5.50}$$
$$\gamma_{ij}^F = U^2\left(F_{ij}^F\left\{4\Lambda[G,G^*]_{ij} + 2\Lambda[F,F^*]_{ij}\right\} + A_{ij}^G\left\{4\Xi[G,G^*]_{ij} + 2\Xi[F,F^*]_{ij}\right\}\right), \tag{5.51}$$

where $\Lambda[\cdot,\cdot]_{ij}$ and $\Xi[\cdot,\cdot]_{ij}$ are the discrete version of eqs. 3.72 and 3.73.

The relations for the components of the spectral function of the fluctuations self-energies are given by

$$\begin{aligned}\Gamma_{ij}^G = {} & 2iU^2\Big(2a_i^*a_j^*\Lambda[F,G]_{ij} + a_i^*a_j\Lambda[G,G]_{ij} \\ & -2a_ia_j\Lambda[F^*,G]_{ij} - 2a_ia_j^*\left\{\Lambda[G,G^*]_{ij} + \Lambda[F,F^*]_{ij}\right\}\Big) \\ & +U^2\left(F_{ij}^G\left\{4\Lambda[F,F^*]_{ij} + 2\Lambda[G,G^*]_{ij}\right\} + A_{ij}^G\left\{4\Xi[F,F^*]_{ij} + 2\Xi[G,G^*]_{ij}\right\}\right),\end{aligned} \tag{5.52}$$

$$\begin{aligned}\Gamma_{ij}^F = {} & 2iU^2\Big(2a_i^*a_j\Lambda[F,G]_{ij} + a_i^*a_j^*\Lambda[F,F]_{ij} \\ & -2a_ia_j^*\Lambda[F,G^*]_{ij} - 2a_ia_j\left\{\Lambda[G,G^*]_{ij} + \Lambda[F,F^*]_{ij}\right\}\Big) \\ & +U^2\left(F_{ij}^F\left\{4\Lambda[G,G^*]_{ij} + 2\Lambda[F,F^*]_{ij}\right\} + A_{ij}^G\left\{4\Xi[G,G^*]_{ij} + 2\Xi[F,F^*]_{ij}\right\}\right),\end{aligned} \tag{5.53}$$

and similarly the for the components of the statistical function,

$$\begin{aligned}\Pi_{ij}^{G} &= 2iU^2\Big(2a_i^*a_j^*\Xi[F,G]_{ij} + a_i^*a_j\Xi[G,G]_{ij} \\ &\quad -2a_ia_j\Xi[F^*,G]_{ij} - 2a_ia_j^*\left\{\Xi[G,G^*]_{ij} + \Xi[F,F^*]_{ij}\right\}\Big) \\ &\quad +U^2\left(F_{ij}^{G}\left\{4\Xi[F,F^*]_{ij} + 2\Xi[G,G^*]_{ij}\right\} - \frac{1}{2}A_{ij}^{G}\left\{2\Lambda[F,F^*]_{ij} + \Lambda[G,G^*]_{ij}\right\}\right), \quad (5.54)\\ \Pi_{ij}^{F} &= 2iU^2\Big(2a_i^*a_j\Xi[F,G]_{ij} + a_i^*a_j^*\Xi[F,F]_{ij} \\ &\quad -2a_ia_j^*\Xi[F,G^*]_{ij} - 2a_ia_j\left\{\Xi[G,G^*]_{ij} + \Xi[F,F^*]_{ij}\right\}\Big) \\ &\quad +U^2\left(F_{ij}^{F}\left\{4\Xi[G,G^*]_{ij} + 2\Xi[F,F^*]_{ij}\right\} - \frac{1}{2}A_{ij}^{G}\left\{2\Lambda[G,G^*]_{ij} + \Lambda[F,F^*]_{ij}\right\}\right). \quad (5.55)\end{aligned}$$

Finally, the equations of motion for the components of the fluctuations spectral function read

$$i\frac{\partial}{\partial t_i}A_{ij}^{G} = -J\left(A_{i+1,j}^{G} + A_{i-1,j}^{G}\right) + \Sigma_i^{HF}A_{ij}^{G} - \Omega_i^{HF}\left(A_{ij}^{F}\right)^* - i\sum_k\int_{t_j}^{t_i}\mathrm{d}t_k\,\left[\Gamma_{ik}^{G}A_{kj}^{G} + \Gamma_{ik}^{F}A_{kj}^{\overline{F}}\right], \quad (5.56)$$

$$i\frac{\partial}{\partial t_1}A_{ij}^{F} = -J\left(A_{i+1,j}^{F} + A_{i-1,j}^{F}\right) + \Sigma_i^{HF}A_{ij}^{F} - \Omega_i^{HF}\left(A_{ij}^{G}\right)^* - i\sum_k\int_{t_j}^{t_i}\mathrm{d}t_k\,\left[\Gamma_{ik}^{G}A_{kj}^{F} + \Gamma_{ik}^{F}A_{kj}^{\overline{G}}\right], \quad (5.57)$$

and for the components of the statistical function

$$\begin{aligned}i\frac{\partial}{\partial t_i}F_{ij}^{G} &= -J\left(F_{i+1,j}^{G} + F_{i-1,j}^{G}\right) + \Sigma_i^{HF}F_{ij}^{G} - \Omega_i^{HF}\left(F_{ij}^{F}\right)^* \\ &\quad -i\sum_k\int_0^{t_i}\mathrm{d}t_k\,\left[\Gamma_{ik}^{G}F_{kj}^{G} + \Gamma_{ik}^{F}F_{kj}^{\overline{F}}\right] + i\sum_k\int_0^{t_j}\mathrm{d}t_k\,\left[\Pi_{ik}^{G}A_{kj}^{G} + \Pi_{ik}^{F}A_{kj}^{\overline{F}}\right] \quad (5.58)\\ &\quad (5.59)\end{aligned}$$

$$\begin{aligned}i\frac{\partial}{\partial t_i}F_{ij}^{F} &= -J\left(F_{i+1,j}^{F} + F_{i-1,j}^{F}\right)\Sigma_i^{HF}F_{ij}^{F} - \Omega_i^{HF}\left(F_{ij}^{G}\right)^* \\ &\quad -i\sum_k\int_0^{t_i}\mathrm{d}t_k\,\left[\Gamma_{ik}^{G}F_{kj}^{F} + \Gamma_{ik}^{F}F_{kj}^{\overline{G}}\right] + i\sum_k\int_0^{t_j}\mathrm{d}t_k\,\left[\Pi_{ik}^{G}A_{kj}^{F} + \Pi_{ik}^{F}A_{kj}^{\overline{G}}\right]. \quad (5.60)\end{aligned}$$

The equations 5.56 - 5.60 are coupled to the discrete version of the "generalized" GPE

$$i\frac{\partial}{\partial t_i}a_i = -J\left(a_{i+1} + a_{i-1}\right) + \left(U|a_i|^2 + 2iUF_{ii}^{G}\right)a_i + iUF_{ii}^{F}a_i^* - i\sum_k\int_0^{t_i}\mathrm{d}t_k\,\left[\gamma_{ik}^{G}a_k + \gamma_{ik}^{F}a_k^*\right]. \quad (5.61)$$

Notice, that in the integrals on the right side we do not used the symmetry relations listed in tab. 3.1 to express the equations only in terms of the upper components. In appendix B we

explain how to treat the evolution of the two-time correlation functions numerically, and how the integrals can be computed.

5.3 Temporal Dynamics of the Two-Site Hubbard Model

As a first exercise we want to consider the TSBH. In section 4.1 we mentioned that the Hamilton function 4.6 obtained within the two-mode approximation in the context of a BEC loaded on a double-well potential is equivalent to the mean field approximation of the Hamiltonian 5.18. In the following we want to study the Bose-Hubbard model in the context of Josephson oscillations between two condensates. The aim is to compare the dynamics described by TSBH with the results obtained for the model we proposed in section 4.2 for the non-equilibrium description of a BEC confined in a double-well trap of finite size.

The situation under consideration is exactly as depicted in section 4.2: two initially completely isolated BECs, that are suddenly linked by a Josephson coupling. The difference to the model proposed in section 4.2 resides in the description of the single-particle excitations. While the model described by the Hamiltonian 4.21 assumes that for a trap of finite size, such as the one prepared in the experiment [54, 60], the single particle excitations energy levels extend over the two BECs above the barrier, the single particle excitations in the Bose-Hubbard model are described in the Wannier basis 5.2, which in the case of a double-well trap correspond to the symmetrized and antisymmetrized solutions of the potential.

The underlying equations of motion for the TSBH are given by eqs. 5.56 - 5.61 with indices i, j, k taking only the values $1, 2$ corresponding to the left and right condensate[2]. The initial conditions for the setup under consideration read

$$a_i(0) = \sqrt{N_i(0)}e^{i\theta_i(0)}, \tag{5.62}$$

$$F^G_{ij}(0,0) = -i\frac{\delta_{ij}}{2}, \tag{5.63}$$

$$F^F_{ij}(0,0) = 0, \tag{5.64}$$

where $N_i(0)$ and $\theta_i(0)$ are the initial population and macroscopic phase of the condensate in the well i, respectively. Apart from the relations 5.62 - 5.64, we have the initial values for components of the non-condensate spectral function, i.e. $A^G_{ij}(0,0) = \delta_{ij}$ and $A^F_{ij}(0,0) = 0$. These values are fixed for $A^{G/F}$ evaluated at equal times, due to the bosonic commutation relations.

Apart from the initial conditions, the TSBH has two additional input parameters, the tunneling amplitude or Josephson coupling J and the interaction parameter U. However, it is convenient to give all the energies of the system in terms of the Josephson coupling J and absorb the large particle numbers appearing in the equations of motion 5.56 - 5.61 into the dimensionless parameter $u = NU/J$, where $N = N_1 + N_2$ is the total particle number.

In the discussion of the two-mode approximation in section 4.1, we pointed out that the system displays two different regimes for fixed initial particle imbalance $z(0) = [N_1(0) - N_2(0)]/N$ and the relative phase difference $\theta(0) = \theta_1(0) - \theta_2(0)$ between the condensates, and varying interaction parameter u. Similar behavior was observe for fixed u and $\theta(0)$ and varying $z(0)$. This permits us to fix the initial population imbalance and relative phase and study the effects

[2] The summation index k should not be confused with the quasi-momentum introduced in eq. 5.36

of varying u, in order to be able to compare directly with the results obtain for the model presented in section 4.2.

In the following we analyze the effects the inclusion of the quantum fluctuations has on the dynamics of atoms in a finite size double-well potential. For this purpose we will consider different initial setups consisting of different number of bosons loaded on a two-site lattice, such that the initial particle imbalance $z(0)$ and initial relative phase $\theta(0)$ is the same for all these setups. In section 4.1 we discussed within the two-mode approximation that the condition for the macroscopic self-trapping can be expressed solely in terms of the interaction parameter u, and depends only on the initial interwell condensate population imbalance and not on the total particle number for a fixed initial relative phase difference between the condensates (see eq. 4.19). This allows us to restrict our study to the three different regimes discussed in the context of the two-mode approximation for different total numbers of atoms, since neglecting the quantum fluctuations yields the system of equations derived in section 4.1. The dynamics will be summarized in terms of the time evolution of the interwell condensate particle imbalance $z(t)$, the fluctuations particle number per site $N_i^{(\varphi)}$ and their sum normalized to the total particle number N, and the phase space portrait of the dynamical variable z and θ. In addition, the quasi-momentum distribution $n_k(t)$ provides a good insight in the dynamics as well as the single particle excitations spectral function, which we will use to study the correlations between the intermediate states and the initial conditions.

The basic features of the results can be summarized as follows:

Initially prepared delocalized state ($z(0) = 0.6$, $\theta(0) = 0$ and $u = 5$)

In fig. 5.2 we present the time evolution of the particle imbalance z, the fluctuations particle number per site $N_i^{(\varphi)}$ and their sum, and the corresponding phase space portraits for systems consisting of different total number of atoms $N = 50, 5000, 50000$. The initial conditions and interaction parameter $u = 5$ were chosen such that in the two-mode approximation the results would correspond to the delocalized regime (dashed blue lines in z vs. Jt and z vs. θ/π plots). We observe that for such a relatively *small* interaction parameter u, single particle excitations are immediately excited for the system consisting of $N = 50$ particles. After a short time the overall single particle excitations number keeps oscillating between 10% and 20% of the total particle number of the system. This depletion of the condensate manifests itself as a damping of the time-oscillations of the condensate population imbalance z and a deviation from the trajectory obtained in the two-mode approximation in the phase space plot. We observe that the larger the particle number N, the longer it takes for the system to excite single particle excitations, and the smaller the condensates depletion (see the plots for $N_i^{(\varphi)}$ as function of time for $N = 5000, 50000$). Consequently, the time-oscillations of the population imbalance are less damped and the deviations in the phase space trajectories are smaller compared to those for systems with a smaller total particle number.

The time evolution of the quasi-momentum distribution shows similar behavior for both large and small total particle number (see upper row in both panels fig. 5.3. For the lower quasi-momentum mode ($k = 0$) the distribution $n_{k=0}$ oscillates in time around a higher occupation number than the distribution of the higher mode $k = \pi/a$, where a is the distance between the two wells. These oscillations are damped, and the time this damping sets in coincides with the time the number of single particle excitations increases abruptly, as it is shown in the lower row of fig. 5.2. Moreover, we observe that

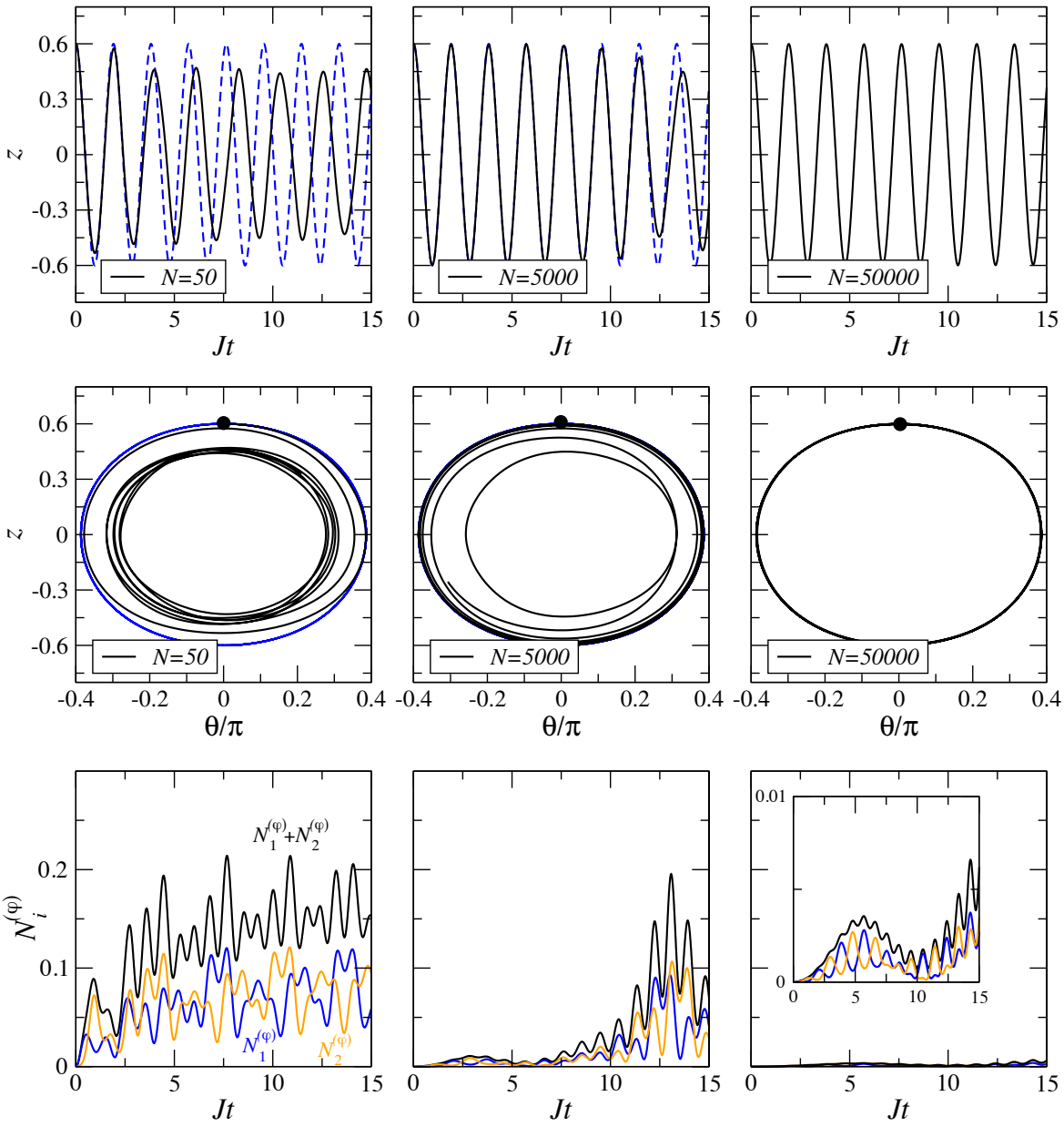

Figure 5.2: In the first row the population imbalance z is plotted as a function of time for initial total number of particles $N = 50, 5000, 50000$ and an initially prepared delocalized state ($z(0) = 0.6$ and $u = 5$). The blue dashed lines correspond to the solutions obtained from the two-mode approximation and serve as references. In the second row, the phase space portraits of the dynamical variable z and θ are shown. Again, the dashed blue lines correspond to the two-mode approximation solutions. At the bottom, the fluctuations particle number per site is plotted as functions of time (blue and orange lines), as well as the total fluctuations particle number (black line).

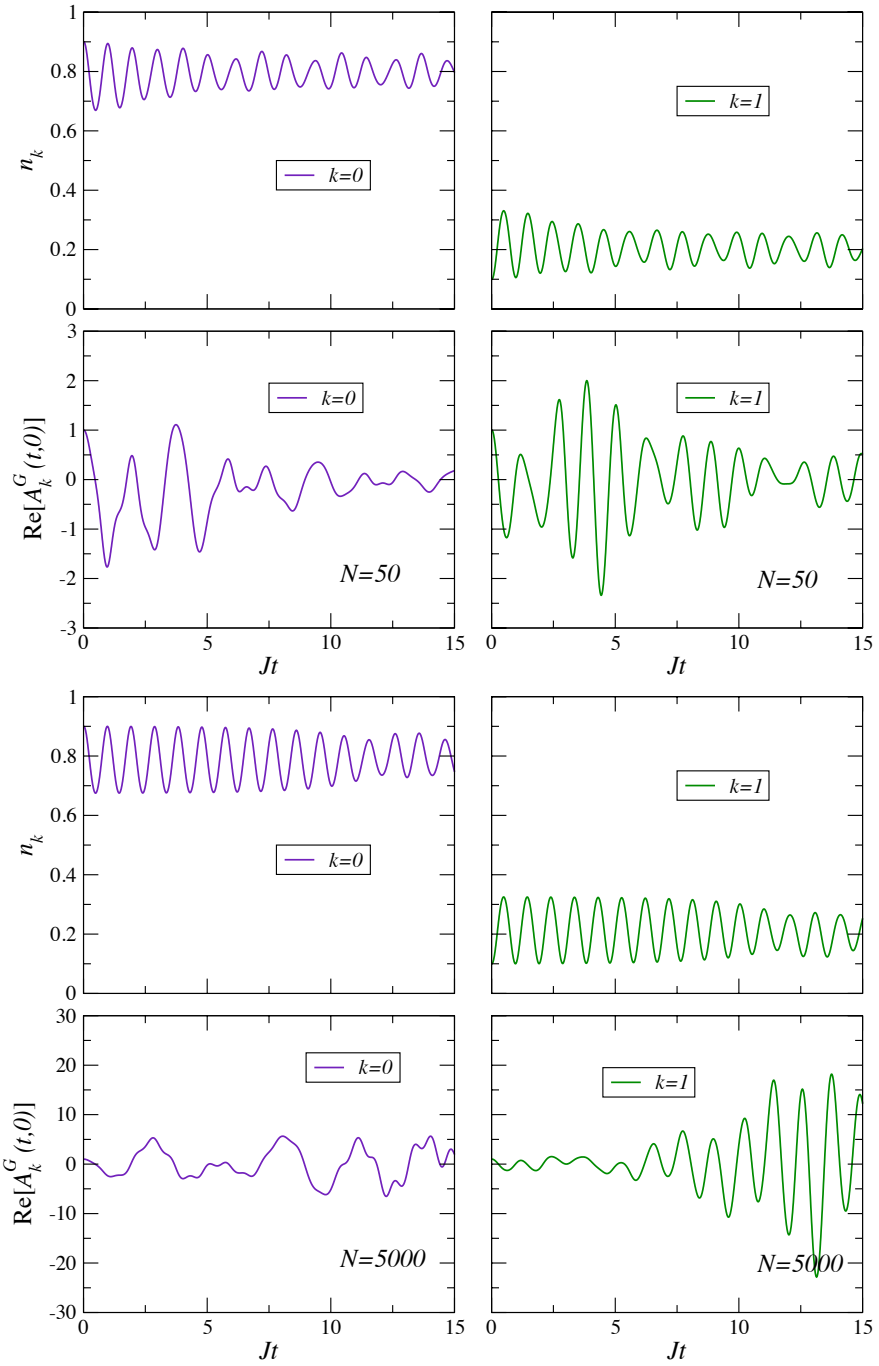

Figure 5.3: In the upper panel the quasi-momentum distribution n_k and the real part of the Fourier components of the two-time single particle excitations spectral function $\mathrm{Re}[A_k^G(t,0)]$ are plotted as a function of time for initial total number of particles $N = 50$ and an initially prepared delocalized state ($z(0) = 0.6$ and $u = 5$). The violet and green lines correspond to the $k = 0$ and $k = \pi/a \equiv 1$ quasi-momentum, respectively. In the lower panel the same quantities are plotted for initial an particle number $N = 5000$.

this damping is stronger for the system with $N = 50$ than for the system $N = 5000$ particles.

The temporal behavior of the real part of the Fourier component of the two-time fluctuations spectral function $\mathrm{Re}\left[A_k^G(t,0)\right]$, shown in the lower row of the upper panels in fig. 5.3), suggests that for the system with $N = 50$ particles the correlations between the intermediate states and the initial conditions are damped for both quasi-momentum modes $k = 0, \pi/a$. This is not the case for the system with $N = 5000$ particles (see the lower row in the lower panel). Apparently, the memory effects for such a large number of particles distributed among two sites increases with the time.

Initially prepared *critical* state ($z(0) = 0.6$, $\theta(0) = 0$ and $u = 20$)

In the following, we will refer to a state that is initially prepared at the boundary between the delocalized and macroscopic self-trapped regimes, as initially prepared *critical* state. The time evolution of the condensate population imbalance z, of the fluctuations particle number per site and of the condensates depletion exhibit a very interesting behavior for an initially prepared *critical* state while taking the quantum fluctuations under consideration. In the two-mode approximation, the condensate particle imbalance oscillates anharmonic and with a large amplitude around 0 (blue dashed lines in the upper and middle row of fig. 5.4). Once the quantum fluctuations are taken into account, the initially prepared critical state undergoes a transition into the delocalized regime, where the relative phase oscillates around $\langle\theta\rangle = 2\pi$. This transition occurs almost immediately after switching on the Josephson coupling J and occurs simultaneously to the abrupt increase of the condensate depletion $N_1^{(\varphi)} + N_2^{(\varphi)}$ (black line in the lower row of fig. 5.4). For the system with $N = 50$ particles, the condensate depletion shows damped oscillation and appears to approach a constant value, unlike the depletion for the systems with $N = 5000, 50000$ particles, which display a strong anharmonic behavior.

The quasi-momentum distribution shows a repeated crossing of the occupation numbers of the lower $k = 0$ and higher $k = \pi/a$ quasi-momentum mode for the systems with $N = 50, 5000$ particles (violet and green lines in the upper row of both panels in fig. 5.5). The distribution of the two quasi-momentum modes is damped, stronger for the system containing $N = 50$ particles. Once again, the damping sets in simultaneously with an abrupt increase of the quantum fluctuations particle number. Furthermore, in both cases the higher quasi-momentum mode appears to be reaching a higher occupation number than the lower momentum mode. This tendency is more pronounced for the $N = 50$ particles system, than for the system with $N = 5000$ particles. This behavior explains the transition into the delocalized regime and can be well understood by taking a glance at the real part of the Fourier components of the two-time single particle spectral function (violet and green lines in the lower row of both panels in fig. 5.5). For the $N = 50$ particles system, the time oscillations of $\mathrm{Re}\left[A_k^G(t,0)\right]$ are strongly suppressed for both quasi momentum modes, reaching a zero value. This means that the correlations between the initial and the intermediate states decay rapidly for both momentum modes. Unlike the behavior of the $N = 50$ particles system, the system with $N = 5000$ shows large memory effects. $\mathrm{Re}\left[A_k^G(t,0)\right]$ does not show any decay at all in the time interval under consideration, what explains the less pronounced damping in the quasi-momentum distribution and tendency of the occupation number of the higher mode to reach a higher value.

Initially prepared self-trapped state ($z(0) = 0.6$, $\theta(0) = 0$ and $u = 25$)

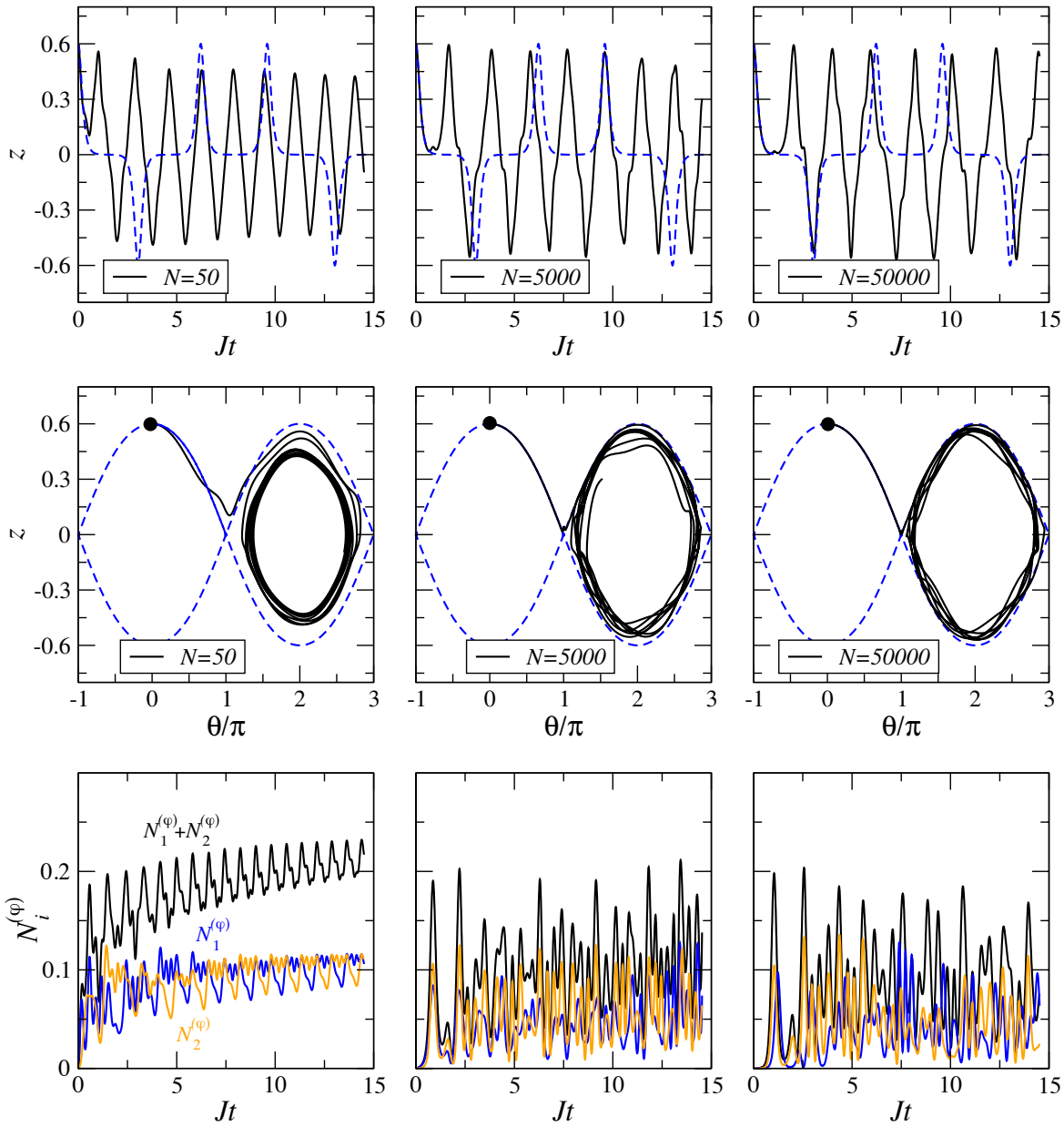

Figure 5.4: In the first row, the population imbalance z is plotted as a function of time for an initial total number of particles $N = 50, 5000, 50000$ and initially prepared *critical* state ($z(0) = 0.6$ and $u = 20$). The blue dashed lines correspond to the solutions obtained from the two-mode approximation and serve as references. In the second row, the phase space portraits of the dynamical variable z and θ are shown. Again, the dashed blue lines correspond to the two mode approximation solutions. At the bottom, the fluctuations particle number per site is plotted as functions of time (blue and orange lines) as well as the total fluctuations particle number (black line).

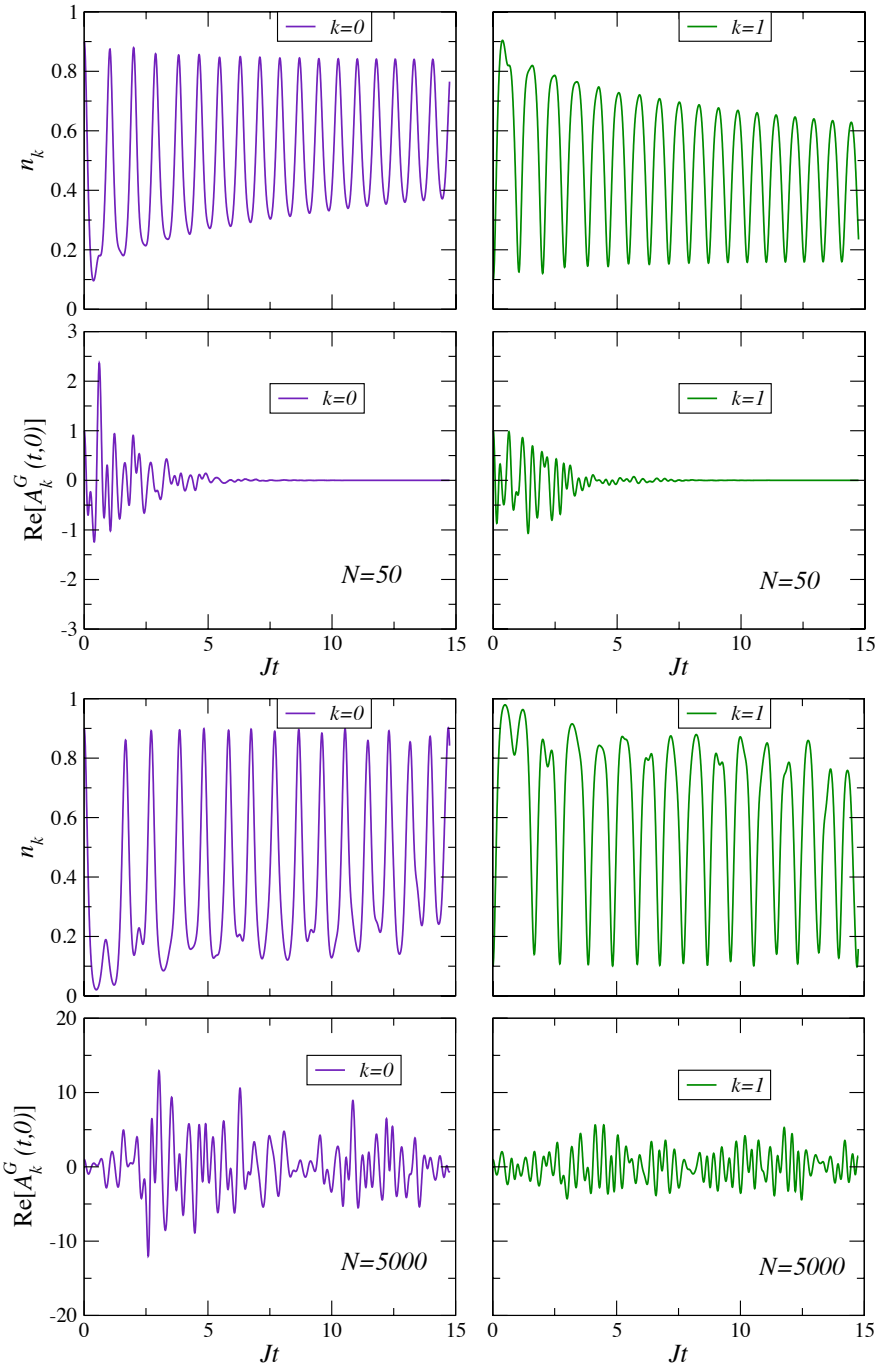

Figure 5.5: In the upper panel the quasi-momentum distribution n_k and the real part of the Fourier components of the two-time single particle excitations spectral function $\mathrm{Re}[A_k^G(t,0)]$ are plotted as a function of time for an initial total number of particles $N = 50$ and initially prepared *critical* state ($z(0) = 0.6$ and $u = 20$). The violet and green lines correspond to the $k = 0$ and $k = \pi/a \equiv 1$ quasi-momentum, respectively. In the lower panel, the same quantities are plotted for an initial particle number $N = 5000$.

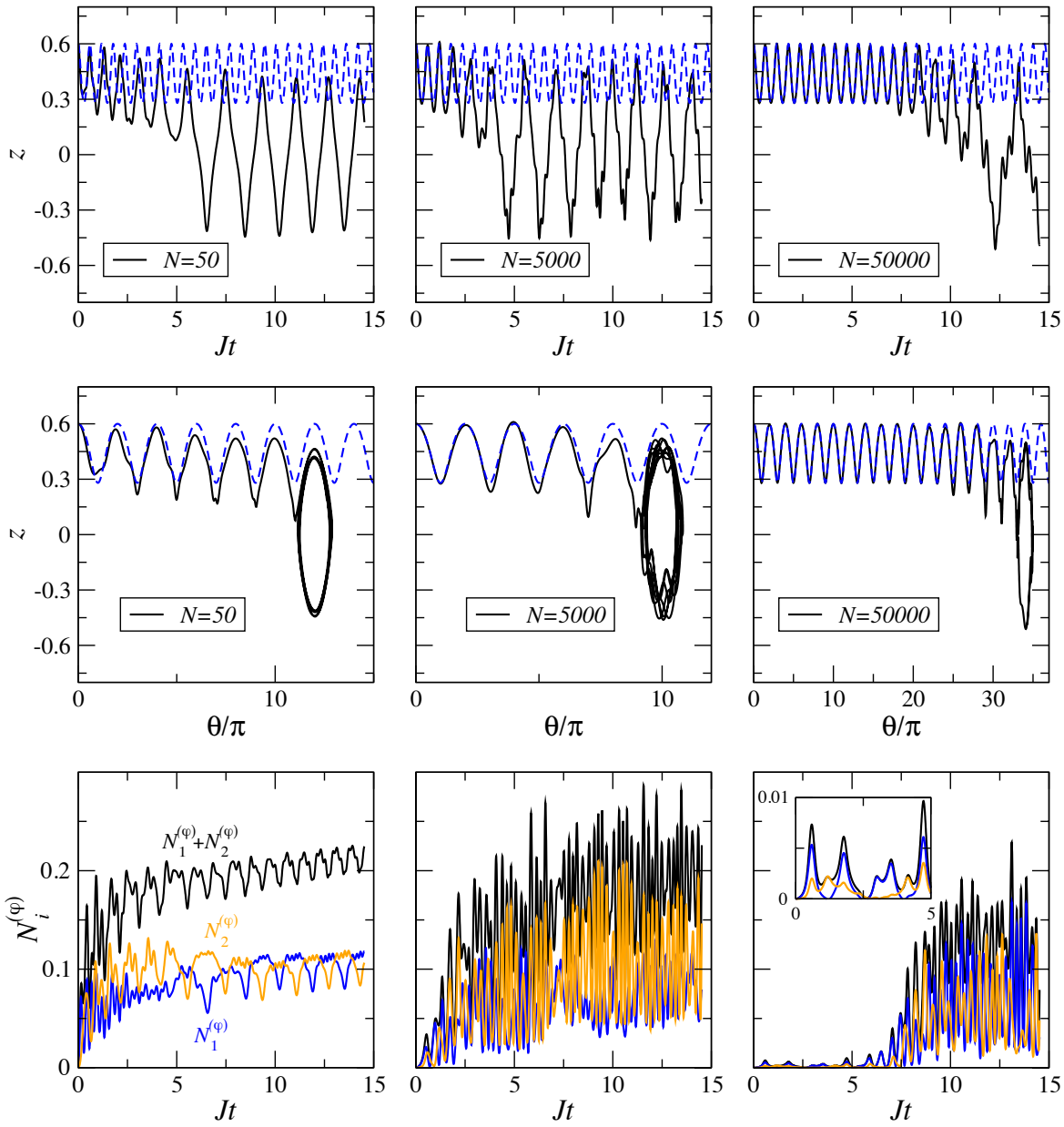

Figure 5.6: In the first row the population imbalance z is plotted as a function of time for initial total number of particles $N = 50, 5000, 50000$ and an initially prepared self-trapped state ($z(0) = 0.6$ and $u = 25$). The blue dashed lines correspond to the solutions obtained from the two-mode approximation and serve as references. In the second row, the phase space portraits of the dynamical variable z and θ are shown. Again, the dashed blue lines correspond to the two mode approximation solutions. At the bottom, the fluctuations particle number per site is plotted as functions of time (blue and orange lines) as well as the total fluctuations particle number (black line).

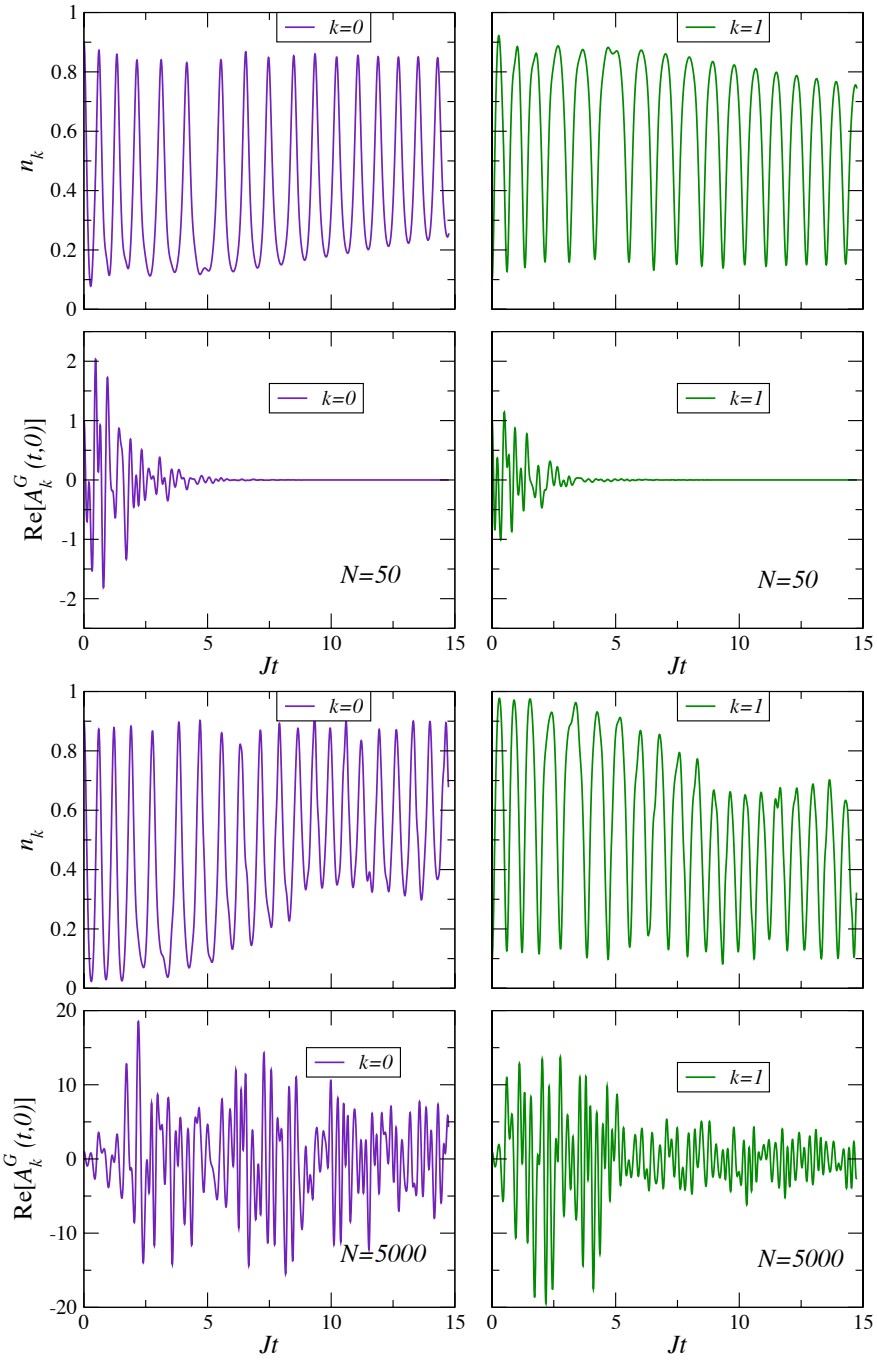

Figure 5.7: In the upper panel the quasi-momentum distribution n_k and the real part of the Fourier components of the two-time single particle excitations spectral function $\mathrm{Re}[A_k^G(t,0)]$ are plotted as a function of time for an initial total number of particles $N = 50$ and initially prepared self-trapped state ($z(0) = 0.6$ and $u = 25$). The violet and green lines correspond to the $k = 0$ and $k = \pi/a \equiv 1$ quasi-momentum, respectively. In the lower panel, the same quantities are plotted for an initial particle number $N = 5000$.

Similar to the initially prepared critical state, the initially prepared self-trapped state undergoes a transition to the delocalized regime due to the condensates depletion. This

is shown in the time evolution of the condensate particle imbalance z and the space space portrait, depicted in the upper and middle row of fig. 5.6. The dashed blue lines corresponds to the results obtained in the two-mode approximation and serve as references. We observe that the system, independent of the number of particles contained in it, can sustain a couple of time oscillations of the condensate imbalance z around a non-zero value before it switches to oscillations around zero. This means that the self-trapped state persists for some time with some deviations from the behavior predicted by two-mode approximation before it undergoes the transition to the delocalized state. While the self-trapped state persists, the relative phase difference between the condensates increases with time as expected and then starts oscillating around an even multiple of π. The deviations appear as soon as the condensate depletion becomes non-zero (see the lower row of fig. 5.6). For $N = 50000$ particles the self-trapped state persists the longest. Naively one expects that for $N = 5000$ particles, the self-trapped state should be sustained longer than for $N = 50$ particles, which we do not observe. We guess that this is due to commensurability issues. Unfortunately the time consuming calculations did not allow us to pursue an investigation in this direction.

The quasi-momentum distribution as a function of time displays a damping for both momentum modes (upper rows in both panels in fig. 5.7). The repeated crossing of the occupation numbers appears once the condensate depletion increases, and the tendency of the occupation number of the higher momentum $k = \pi/a$ to reach higher number than the one of the lower momentum $k = 0$ becomes more pronounce after the transition to the delocalized state has happened.

Comparing the data for the real part of the Fourier components of the two-time spectral function for $N = 50$ and $= 5000$ particles, we observe that correlations between the initial and the intermediate states are strongly suppressed for the system with smaller particle number (lower row in both panels in fig. 5.7). For $N = 5000$ particles, there is barely a damping visible, which can be understood as the presence of large memory effects.

5.3.1 Discussion

In the previous sections we studied the non-equilibrium effects of Josephson oscillations between two BECs in the context of the TSBH. We studied systems that were initially prepared in one of the three relevant regimes discussed in the context of the two-mode approximation in section 4.1, and the effects resulting from the inclusion of quantum fluctuations. We treated the quantum fluctuation within the full-second order approximation, which takes memory effects into account, unlike the BHF approximation. The systems under consideration were initially prepared with different total particle numbers, but with the same initial normalized condensate population imbalance $z(0)$ and relative phase difference between the condensates $\theta(0)$. This made a direct comparison of the dynamics for different total particle numbers possible in the three cases under consideration. We conducted the analysis by studying the condensate population imbalance, the total condensate depletion, and the quasi-momentum distribution as functions of time. In addition the phase space portrait of the condensate imbalance and the relative phase provided a good point of comparison to the results obtained in the two-mode approximation [62, 63]. We also used the Fourier components of the fluctuations two-time spectral function as a measure of the capability of the system to maintain correlations between the initial and intermediate states.

For an initially prepared delocalized state, we observe a damping and a slow down of the Josephson oscillations between of the condensates, which is most pronounce for the system with the smallest particle number under consideration. A transition from the initially prepared critical as well as from the self-trapped state to the delocalized state occurs. In the case of the initially critical state, this happens almost instantaneously after switching on the Josephson coupling J. The initially prepared self-trapped state was able to sustain macroscopic self-trapping for a couple of oscillations of the condensate particle imbalance, but it then underwent the transition to the delocalized state. The transition occurred earlier for the system with the smallest number of particles under consideration. For both of these cases, the occupation number of the higher quasi-momentum mode appears to have a tendency to reach a higher number than the one of the lower momentum mode after the transition to the delocalized state has occurred. This suggest that Josephson oscillations for the initially prepared critical and self-trapped state are dominated by the higher quasi-momentum mode.

Studying the correlations between the initial and intermediate states by means of the Fourier components of the single particle spectral function, we recognize that the system with the smallest particle number shows a strong decay of these correlations in the time interval under consideration, unlike the systems with particle number two and three orders of magnitude larger. We think that for such large particle numbers in a double-well potential, the TSBH is not a suitable approach to study non-equilibrium effects and one should take the actual geometry of the trap into account.

5.4 Temporal Dynamics of a BEC Placed on a 2-Dimensional Optical Lattice

Having discussed the Bose-Hubbard model in the context of non-equilibrium Josephson oscillations in the previous section, we now want to turn our attention to the temporal dynamics of the Bose-Hubbard model in the context of a BEC placed at the center of a 2-dimensional lattice with finite and equal number of the lattice-sites in each direction, which is driven out of equilibrium by suddenly switching on the tunneling amplitude J. The initial condition is shown by the cartoon in fig. 5.8. Such a system has been experimentally realized in one dimension [83]. The initial condition is not described by an eigenstate of the Bose-Hubbard Hamiltonian 5.18, and consequently will evolve in time in a non-trivial way after the tunneling is switched on [41]. At a first sight, one expects the mean field description to provide a good insight into the dynamics of the system. However, if the kinetic energy is about the same magnitude as the interaction energy, the interatomic collisions will play a crucial role [41]. Nevertheless, the mean field description as well as the BHF approximation still provide reliable results for short times.

A proper description of the quantum dynamics of the situation depicted above requires the proper treatment of scattering processes between particles. An exact solution of the problem is possible, but it is restricted to a small number of particles and lattice sites. In section 5.2 we performed a detailed derivation of the underlying equations of motion for the Bose-Hubbard model within the framework of conserving approximations. In the succeeding sections we gave the explicit equations of motion for the mean field description, BHF, and the full second-order approximation. These approaches allow us to study the temporal dynamics of the of Bose condensed gases placed on optical lattices. They also have been applied to problems in gravitation and cosmology [84, 85], particles and fields [86], and condensed matter systems as

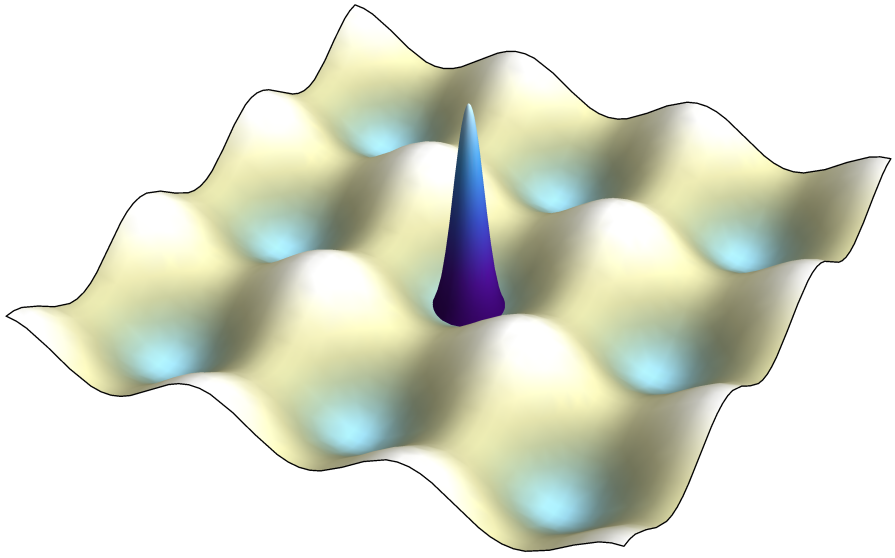

Figure 5.8: BEC initially loaded in a 2-dimensional optical lattice

well as targeting issues of thermalization and quantum phase transitions [75, 76].

Before we proceed to analyze the dynamics of the setup described above, we need to formulate the initial conditions in the language of the on-site mean field amplitude, the single particle excitations statistical two-time functions and the spectral two-time functions. Furthermore we want to constrain our analysis to commensurable systems, i.e., we only consider systems whose particle numbers equals a multiples of the total number of sites $I \times I$, where I is the number of sites in one direction, and from now on we assume to be an odd number for simplicity. The filling factor ρ is defined by $N = \rho \cdot I^2$, where N is the total particle number. The initial conditions thus read

$$a_i(0) = \sqrt{\rho \cdot I^2}\, \delta_{i0}, \tag{5.65}$$

$$F^G_{ij}(0,0) = -i\frac{\delta_{ij}}{2}, \tag{5.66}$$

$$F^F_{ij}(0,0) = 0, \tag{5.67}$$

where $i, j \in \{(i_x, i_y) |\, i_x, i_y = -(I-1)/2, \ldots, 0, \ldots, (I-1)/2\}$. Similar to the study of the TSBH in the previous section, we must fix the initial values of the components of the non-condensate spectral function, i.e., $A^G_{ij}(0,0) = \delta_{ij}$ and $A^F_{ij}(0,0) = 0$. This values are fixed for $A^{G/F}$ evaluated at equal time arguments due to the bosonic commutation relations. Moreover, similar to the discussion of the TSBH it is convenient to give all energies in units of the tunneling J, and absorb the large particle numbers appearing in the equations of motion into the dimensionless parameter $u = NU/J$, where N is the total particle number.

In section 4.2.2 as well as in Appendix B, we discussed that the numerical calculations for the full second-order approximation are time, cpu and memory consuming. Unless we make any further approximations, systems with large number of lattice sites $I \times I$ are not accessible with this approach. Moreover the on-site repulsion u possess an extra limitation on numerical analysis of the equations of motions in this approximation, since the non-linearities in the equations increase with u. This means that large numbers for the interactions parameter u require a smaller time step in the numerical analysis while solving the equations. For this reason we will only study the dynamics of a BEC loaded on a lattice with 3×3 sites by the means of the full second-order approximation (see section 5.4.2). But before we do so, we will present results for systems with larger number of lattice sites obtained using the BHF approximation.

5.4.1 BHF-Approximation Results for a BEC Loaded on a Lattice

In the following we will discuss the time evolution of a Bose condensed gas on a 2-dimensional lattice within the BHF approximation. Although this approximation lacks the ability to take memory effects into account, which could lead to thermalization, we observe very interesting physics. The initial setup was described above and in the language of the condensate amplitudes and the two-time correlation functions read according to eqs. 5.65 - 5.67. As we discussed in sec. 5.2.2, it is not necessary to consider the two-time single particle excitations spectral functions A^G_{ij} and A^F_{ij} because they decouple completely from the eqs. 5.44 and 5.45. The dynamics of the system will be summarized in terms of the density profile of the particles and the quantum fluctuations $N_i^{(0)} + N_i^{(\varphi)}$ and $N_i^{(\varphi)}$ normalized to the total number of particles $\rho \cdot I^2$, as well as the 2-dimensional quasi-momentum distribution function n_k of the atoms. We study the system for various initial conditions, i.e., different numbers of lattice sites $I \times I$, filling factors ρ, and interactions u.

In figure 5.9 we depict the time evolution of a Bose-condensed gas on a lattice with 21×21 sites with filling factor $\rho = 1$ and on-site interaction $u = 3$. The left and middle column show snapshots of the density profile of the particles and quantum fluctuations for increasing time Jt. The right column shows snapshots of the corresponding 2-dimensional quasi-momentum distribution. The initial condition is depicted at the top, where all the particles are prepared in a coherent state in the center of the lattice and the corresponding quasi-momentum distribution is homogeneous in k-space ($Jt = 0$). After switching on the the tunneling J, particles tunnel to the neighboring sites and quantum fluctuations are excited. This can be observed in fig. 5.10c and 5.10d, where we plotted the time evolution of the single particle excitations population profile along the $i_y = 0$ axis and diagonal axis, respectively. We see that after releasing the gas, it expands over the lattice (see the snapshots for $1.0 \leq Jt \leq 4.0$ in fig 5.9). The cone-like shape of the condensate population profile along the $i_y = 0$ and the diagonal axes seen in fig. 5.10a and 5.10b suggest that the expansion is ballistic. The edges of the expanding cloud have a higher density than the center. During the expansion, the shape of the quasi-momentum distribution changes, becoming a broad distribution with its maximum at the edge of the first Brillouin zone. The number of single particle excitations per site exhibits a similar pattern. While the density in the high density regions diminishes, the occupation per site of the quantum fluctuations becomes indistinguishable in the density scales, under consideration but it is still finite. This is due to the fact that the appearance of the single particle excitations is linked to the on-site interaction. As we will explain later, the higher the interaction energy, the more single particle excitations can be excited out of the coherent state. For times $Jt > 4$, finite

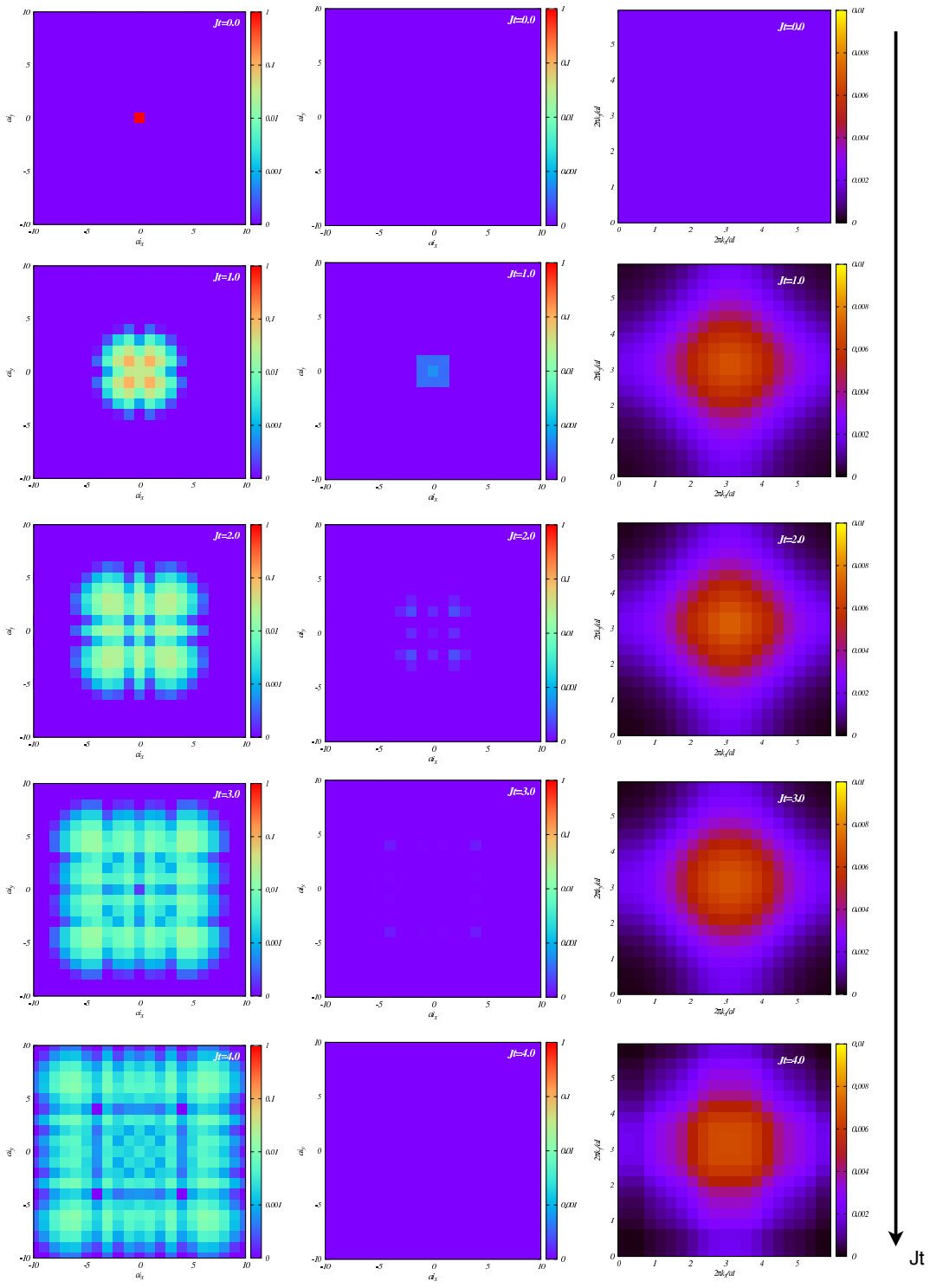

Time interval: $0 \leq Jt \leq 4$

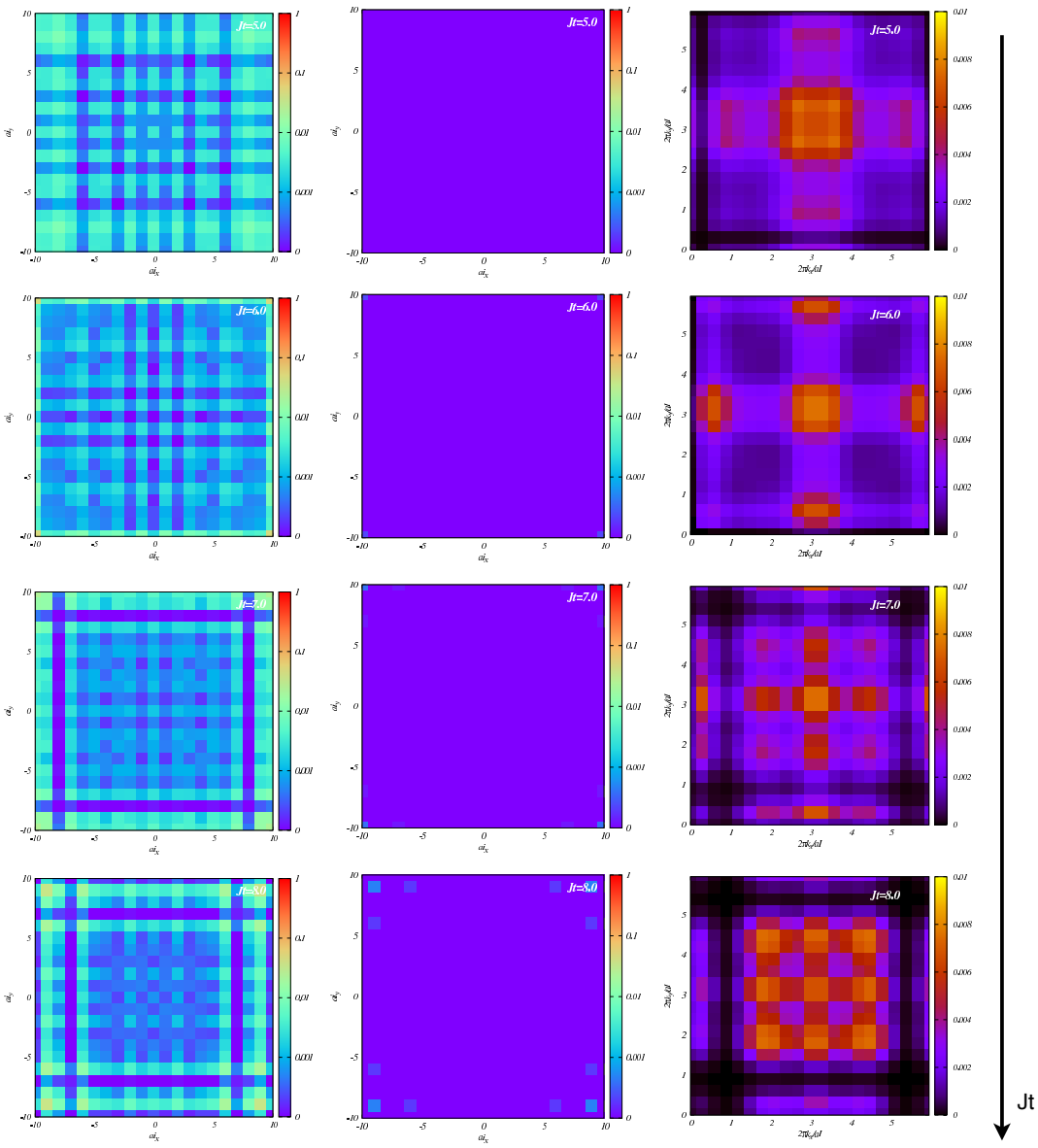

Time interval: $4 < Jt \leq 8$

Figure 5.9: The left and central columns display the time evolution of the density profile of the atoms $N_i^{(0)} + N_i^{(\varphi)}$ and quantum fluctuations $N_i^{(\varphi)}$ on a lattice with 21×21 sites, respectively. The right column shows the time evolution of the 2-dimensional quasi-momentum distribution n_k. The arrow on the right side, beside the plots depicts the time direction. The snapshots on the previous page correspond to the time interval $0 \leq Jt \leq 4$, and the ones on this page to $4 < Jt \leq 8$. The data corresponds to interaction parameter $u = 3$ and filling factor $\rho = 1$.

size effects become visible. The particles have reached the boundaries of the lattice and are reflected. The quasi-momentum distribution shows interference patterns that change in time. In order to compare the results with a system with different number of sites, we show the time

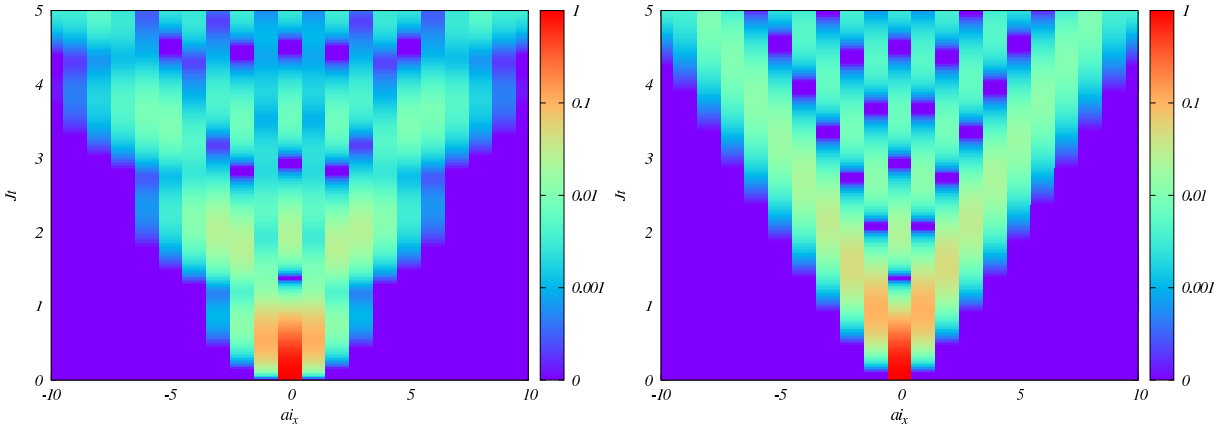

(a) Condesate population along the axis $i_y = 0$

(b) Condesate population along the axis $i_y = i_x$

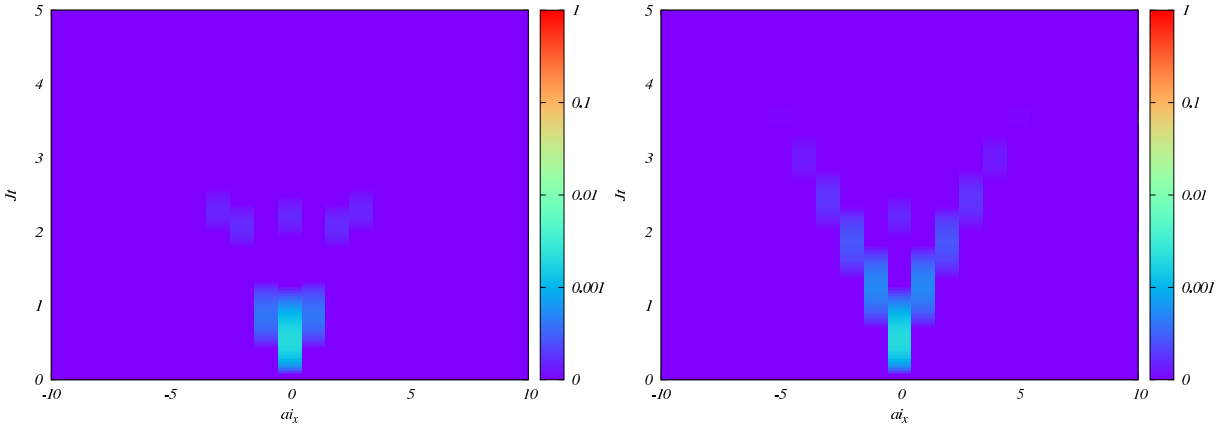

(c) Fluctuations population along the axis $i_y = 0$

(d) Fluctuations population along the axis $i_y = i_x$

Figure 5.10: On the top: Time evolution of the condensate population profile $N_i^{(0)}$ along the $i_y = 0$ and diagonal axes on a lattice with 21×21 sites during the expansion for $u = 3$ and $\rho = 1$. On the bottom: Time evolution of the population profile $N_i^{(\varphi)}$ of the single particle excitations along the same axis.

evolution of a BEC released on a lattice with 15×15 sites with the same interaction parameter u and filling factor ρ in fig. C.3 and C.2.

The situation becomes different if we increase the interaction parameter u for the same number of sites $I \times I$ and filling factor ρ. Once again, the initial condition is depicted at the top of fig. 5.11 for interaction parameter $u = 7$. Immediately after switching on the coupling J, atoms tunnel to the neighboring sites and single particle excitations appear, as it is shown in fig. 5.12c and 5.12d. Comparing the expansion of the atomic cloud for $u = 7$ and $u = 3$, we observe that for the former the expansion is slowed down (see the snapshots for $0 \leq Jt \leq 4$ in fig. 5.11). The majority of the atoms reside in an expanding cloud of spherical shape on the two dimensional plane. The rest of the particles appear to be forming lower density regions outside the expanding spherical cloud. They can be associated with atoms possessing enough kinetic energy to tunnel through the high density edges of the expanding cloud. This behavior becomes more evident in fig. 5.12a and 5.12b, where we plotted the density profile of the condensate

along, the $i_y = 0$ and the diagonal axis as functions of time. The shape observed in these plots suggests that for $u = 7$ the expansion has a diffusive nature. Similar to the lower on-site interaction case, the single particle excitations are localized in the higher density regions, which in this case is the expanding spherical cloud (see fig. 5.12c and 5.12d). Unlike the $u = 3$ case, the quasi-momentum becomes strongly peaked at the edge of the first Brillouin zone. The reason for this is that the motion of the majority of the particles coincides with the expansion of the spherical cloud. This also explains the quasi-stationary shape of the quasi-momentum distribution after the particles were reflected at the edges of the lattice.

We distinguish between the time during which the expansion takes places and the time after which the atoms have reached the edge of the lattice and are reflected to the lattice center. In the former regime we recognize two types of behavior. We observe an initial expansion, for which the on-site interactions do not play a big role. In this regime, multiple occupation of sites surrounding the center has not taken place yet, and the kinetic energy of atoms on those sites overweights the on-site repulsion. Once the sites away from the center are multiply occupied, the interaction energy becomes comparable to the kinetic energy, and consequently slows down the expansion of the gas. In case of $u = 3$, this regime is characterized by the formation of islands of higher density at the edge of the expanding cloud, which prevent the inner particles to tunnel outwards to the edges of the lattice. For this interaction parameter u, we observe that the single particle excitations and condensate particles have a similar density profile. In $u = 7$ case, more particles are excited out of the condensate.

In section 5.2 we gave the expression for the mean energy of an interacting bosonic gas. We argued that in the framework of a conserving approximation the energy is a conserved quantity. In the following, we regroup the different terms in eqs. 5.34 and 5.35 in order to introduce mean the interaction energy and the kinetic energy of the atomic gas[3],

$$\begin{aligned} E_{\text{int}} &= E_{\text{int}}^{(0)} + E_{\text{int}}^{(\varphi)} \\ &= \frac{i}{4}\sum_i \text{Tr}\left[\boldsymbol{S}_i^{HF}\boldsymbol{C}_{ii}\right] + \frac{i}{4}\sum_i \text{Tr}\left[\boldsymbol{\Sigma}_i^{HF}\boldsymbol{F}_{ii}\right], \end{aligned} \tag{5.68}$$

$$\begin{aligned} E_{\text{kin}} &= E_{\text{kin}}^{(0)} + E_{\text{kin}}^{(\varphi)} \\ &= \frac{i}{2}\sum_i \text{Tr}\left[-J\left(\boldsymbol{C}_{i+1,i} + \boldsymbol{C}_{i-1,i}\right)\right] + \frac{i}{2}\sum_i \text{Tr}\left[-J\left(\boldsymbol{F}_{i+1,i} + \boldsymbol{F}_{i-1,i}\right)\right], \end{aligned} \tag{5.69}$$

which will be used for the further analysis. The superscripts (0) and (φ) refer to the fraction of the mean energies related to the condensate atoms and the single particles excitations of the gas, respectively. In fig. 5.13 we show the time evolution of the interaction and the kinetic energy normalized to the total energy for a Bose-condensed gas on a lattice of 21×21 sites with filling factor $\rho = 1$. The upper panel shows the energies corresponding to the time evolution with an on-site interaction $u = 3$ that is depicted in the snapshots in fig. 5.9. We see that initially the interaction energy of the gas equals the total energy. Then, after switching on the tunneling amplitude J, atoms can tunnel to the neighboring sites. This manifests itself in a sudden increase of the kinetic energy and a decrease of the interaction energy. While the gas continues to expand, we observe a crossing of the energies. The kinetic energy increases further, approaching an asymptotic value close to the total mean energy. This implies that interactions energy is not strong enough to slow down the expansion anymore. In the proximity of the

[3] Throughout this section we are studying the temporal dynamics by the means of the BHF approximation.

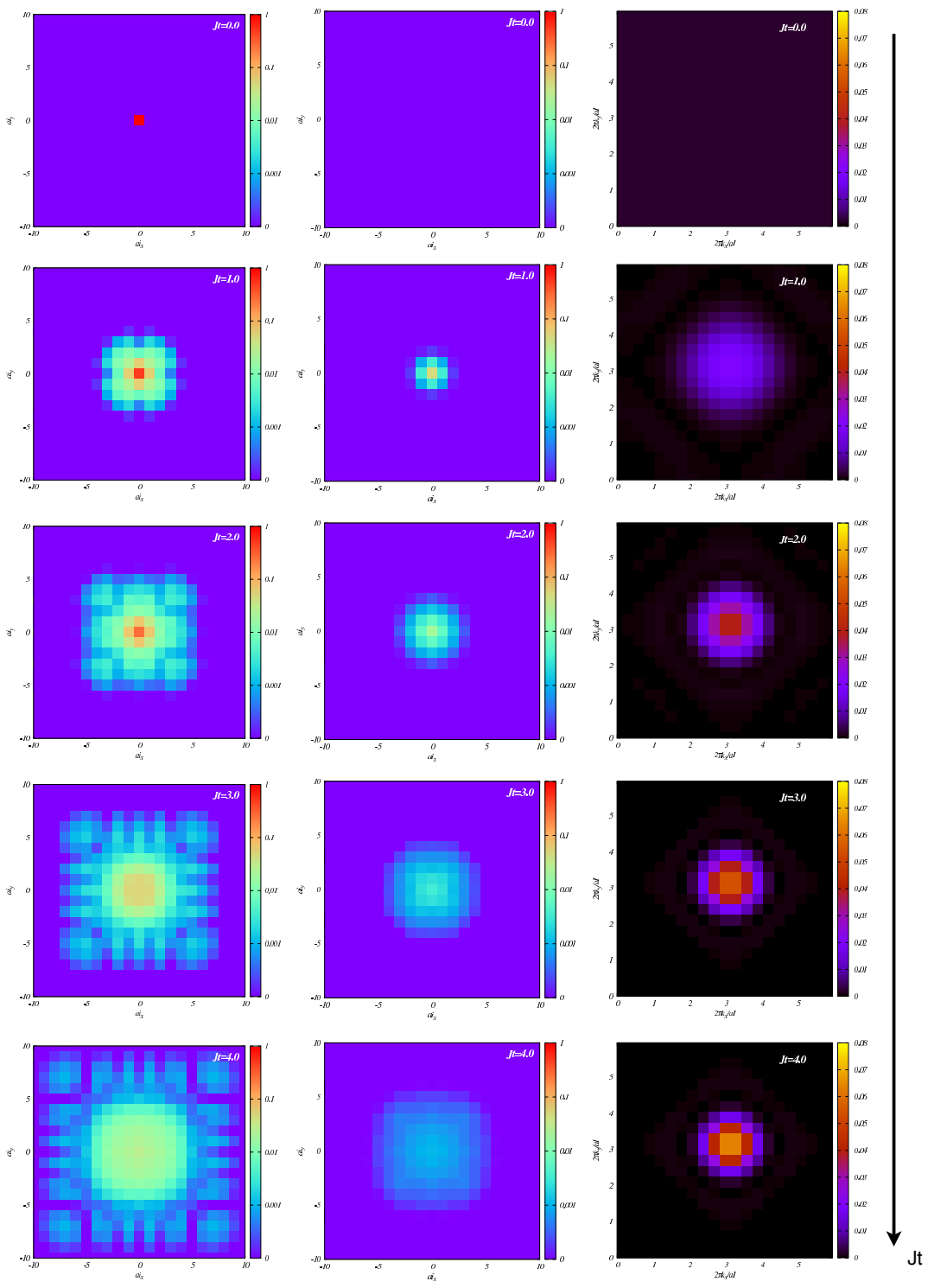

Time interval: $0 < Jt \leq 4$

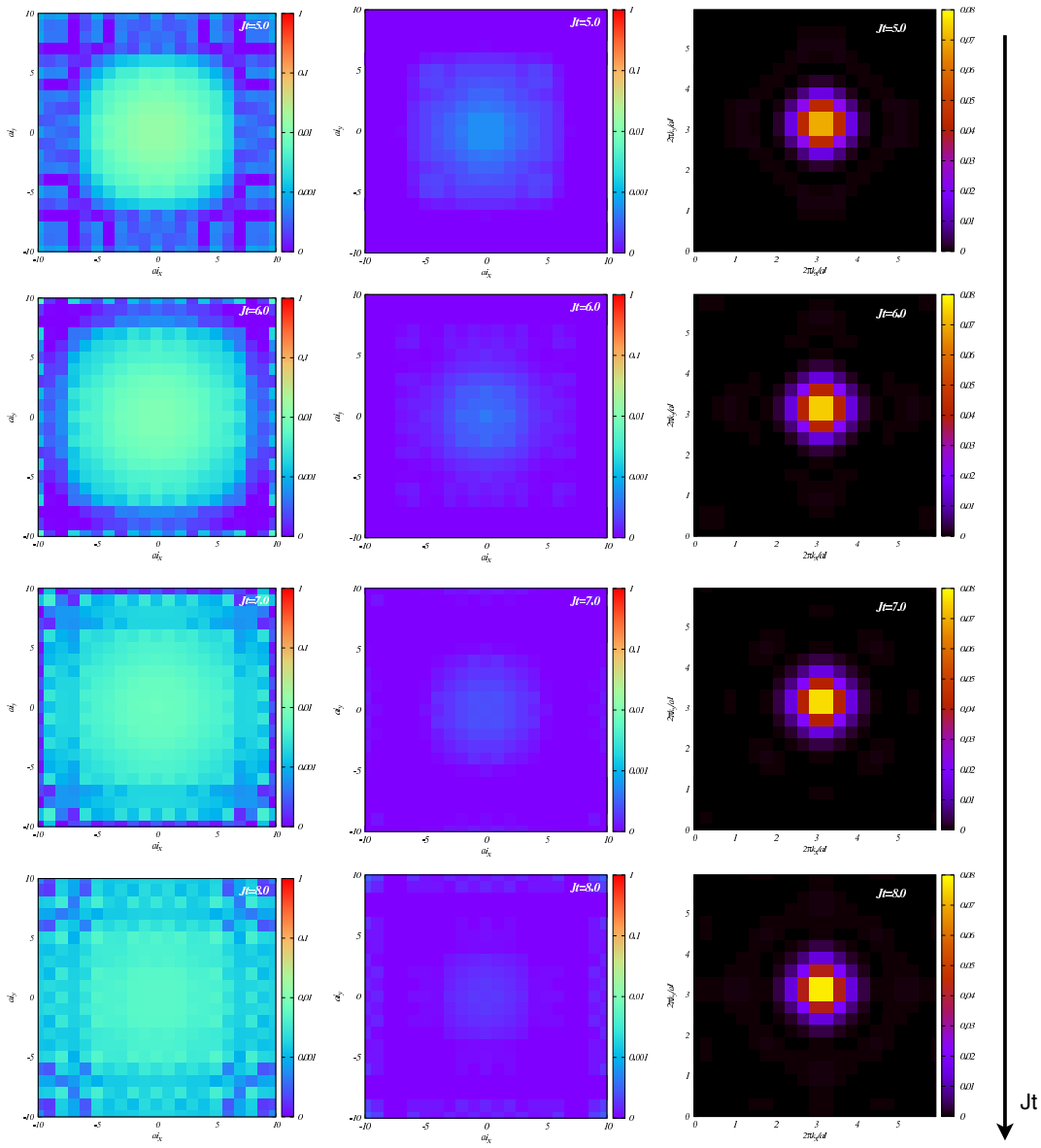

Time interval: $4 < Jt \leq 8$

Figure 5.11: The left and central columns display the time evolution of the density profile of the atoms $N_i^{(0)} + N_i^{(\varphi)}$ and quantum fluctuations $N_i^{(\varphi)}$ on a lattice with 21×21 sites, respectively. The right column shows the time evolution of the 2-dimensional quasi-momentum distribution n_k. The arrow on the right side, beside the plots depicts the time direction. The snapshots on the previous page correspond to the time interval $0 \leq Jt \leq 4$, and the ones on this page to $4 < Jt \leq 8$. The data corresponds to interaction parameter $u = 7$ and filling factor $\rho = 1$.

total mean energy, the kinetic energy presents small amplitude time oscillations, which could mean that multiple occupancy in some regions of the lattice is possible due to the relatively small on-site interaction (finite size effects). The inset of the upper panel shows the behavior

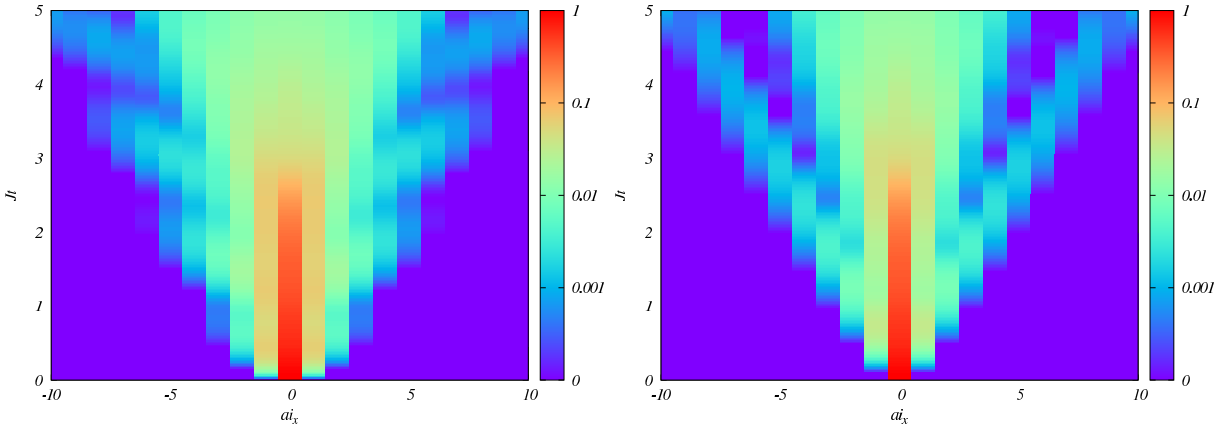

(a) Condesate population along the axis $i_y = 0$

(b) Condesate population along the axis $i_y = i_x$

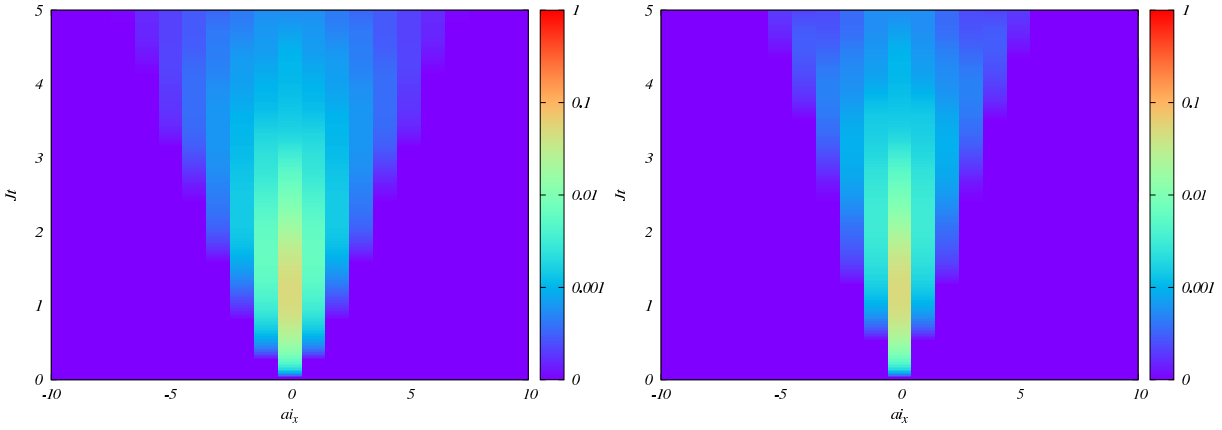

(c) Fluctuations population along the axis $i_y = 0$

(d) Fluctuations population along the axis $i_y = i_x$

Figure 5.12: On the top: Time evolution of the condensate population profile $N_i^{(0)}$ along the $i_y = 0$ and diagonal axes on a lattice with 21×21 sites during the expansion for $u = 7$ and $\rho = 1$. On the bottom: Time evolution of the population profile $N_i^{(\varphi)}$ of the single particle excitations along the same axis.

of the energy fractions related to the single particle excitations in time. Both kinetic and interaction energies of the single particle excitations exhibit a sudden rise after switching on the tunneling amplitude. During this increase, the interaction energy of the single particle excitations is larger than the kinetic energy, until it reaches a maximum. Then it suddenly goes down, crosses with the kinetic energy, and decreases further approaching an asymptotic finite value. On the other hand, the kinetic energy continues to increase slowly. The two energies continue to be comparable within the time interval under consideration, although the kinetic energy of the single particles is still larger. This means that the single particle excitations can be localized or delocalized.

The situation becomes different for on-site interaction $u = 7$. The kinetic and interaction energy of the atoms qualitatively show a similar behavior to the $u = 3$ case (lower panel of fig. 5.13). The small amplitude oscillations in the kinetic energy are not visible at the energy scales we are considering, but they are still there and can be linked to the formation and decay of the

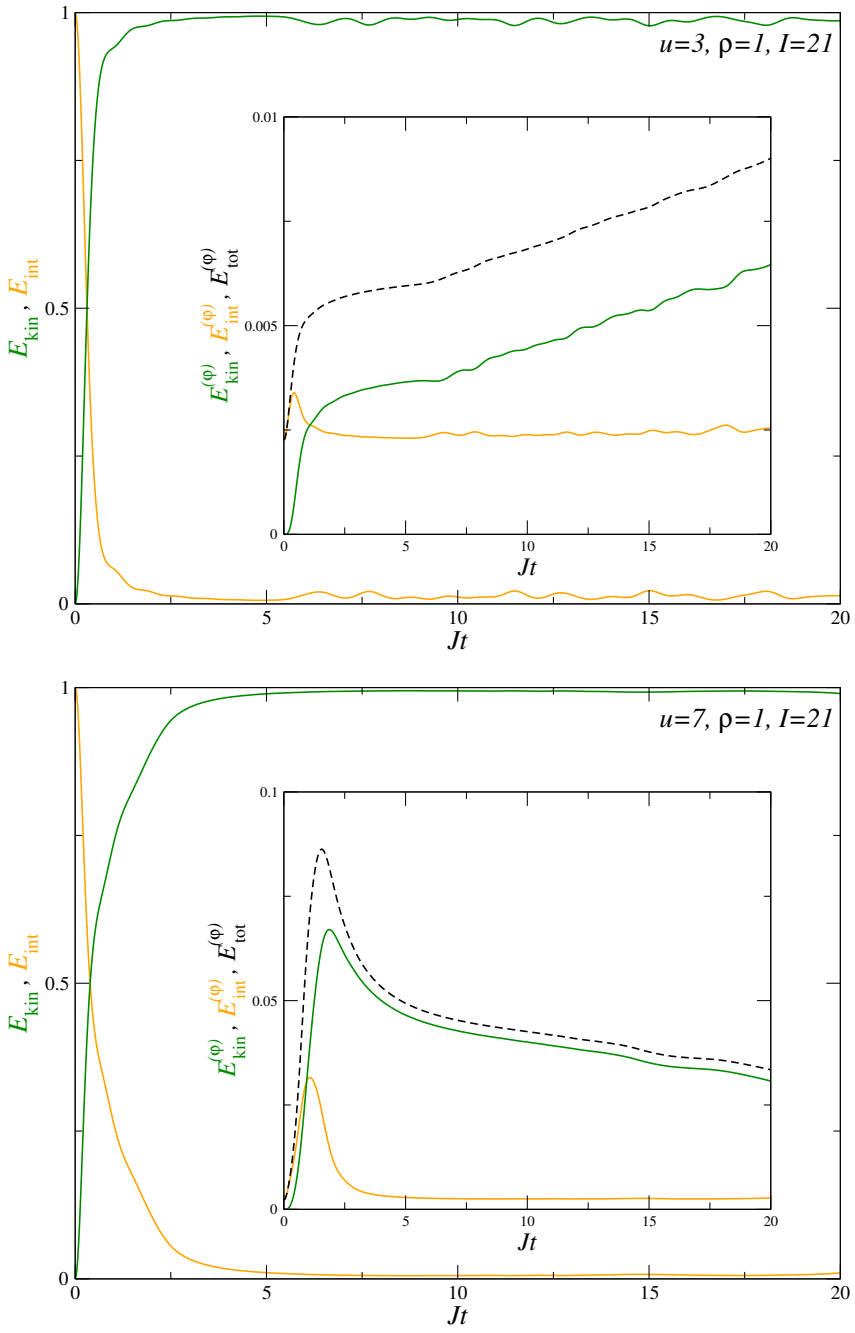

Figure 5.13: In the upper panel, the interactions and kinetic energy normalized to the total energy of a gas loaded on a lattice with 21×21 sites with filling factor $\rho = 1$ and on-site interaction $u = 3$ are plotted as a functions of time (orange and green). The inset displays the time behavior of the energy fractions corresponding to the single particle excitations, according to eqs. 5.68 and 5.69. The black dashed line in the inset corresponds to the total mean energy of single particle excitations. The lower panel shows the same quantities, but for $u = 7$.

high density islands (finite size effects). The difference resides in the time evolution of the kinetic and the interaction energy of the single particle excitations (inset of the lower panel). Similar to case with a smaller u, both energies related to the single particle excitations increase in time after switching on the tunneling. Initially, the interaction energy take larger values. Then, its increase slows down until $E_{\text{int}}^{(\varphi)}$ reaches a maximum, while the kinetic energy increases further and becomes larger than the interaction energy. The interaction energy decreases rapidly, approaching a value close to zero. The kinetic energy reaches a maximum and then decreases, approaching a finite value about two orders of magnitude larger than the one approached by the interaction energy.

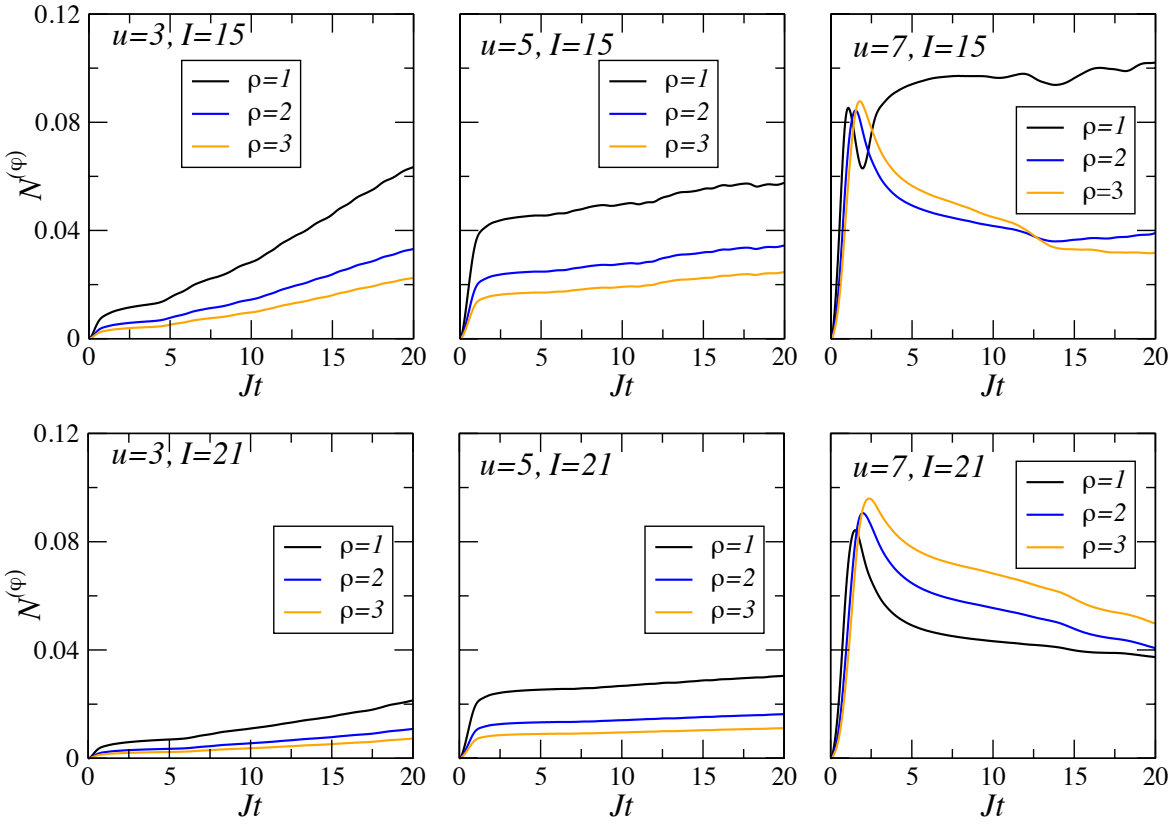

Figure 5.14: Time evolution of the overall quantum fluctuations particle number $N^{(\varphi)}$ as a function of the interaction parameter u, number of lattice site in on direction I, and filling factor ρ.

In order to compare the results for systems with different numbers of sites $I \times I$, filling factors ρ and interaction parameters u, in fig. 5.14 we plotted the time evolution of the overall condensate depletion normalized to the total number of particles $N = \rho \cdot I^2$ as a function of these parameters. We observe that for $u = 3$ the overall number of single particle excitations increases in time for lattices with 15×15 and 21×21 sites (see the left column of fig. 5.14). However, the overall depletion of the condensate decreases with the number of lattice sites and the filling factor ρ. The single particle excitations appear immediately after turning on the tunneling amplitude J and the condensate depletion shows a sudden increase. Then it appears to saturate, until it presents a bend. After it, the condensate depletion increases further and

almost linearly in time. The slope decreases with the filling factor ρ. For all interaction parameters u, the condensate depletion qualitatively shows a similar behavior, apart from the fact that the bend occurs later in time and the the slope is smaller (middle column of fig. 5.14). This is due to the stronger on-site repulsion, since for a smaller u the system is more likely to allow multiple occupancy of a single site, which leads to the excitation of quantum fluctuations. A further increase of the on-site parameter u poses an even higher energy penalty for multiple occupancy. As we have seen in fig. 5.13, for $u = 7$ the interaction energy for both condensate and non-condensate fraction of the gas approaches a value close to zero, which reflects the fact that multiple occupancy of sites is less likely to occur. The decrease of the particle number of quantum fluctuations for $u = 7$ (right column in fig. 5.14) is well explained by the lower probability to encounter multiply occupied sites on the lattice.

5.4.2 BEC Loaded on a Lattice with 3×3 Sites and Memory Effects

In the previous section we studied the BHF dynamics of an expanding BEC cloud on a 2-dimensional lattice of finite size. In spite of the very interesting behavior discussed in the previous section, the BHF approximation excludes the memory effects. Even though we observed that for very large on-site repulsion u the quasi-momentum distribution for a relative large number of sites $I \times I$ tends to reach a stationary shape (see 5.11), the question remains wether or not this would be the case for smaller systems. Previously we mention that the BHF approximation does not take memory effects into account, and we expect that the finite size effects will prevent the quasi-momentum distribution function become stationary. However, the inclusion of higher order terms in u according to the full second-order approximation will eventually drive the system into a stationary state despite of the finite size effects. In addition we explained before that the numerical analysis of the equations of motion in the framework of the full second-order approximation is time consuming. This limits the calculations. We therefore constrain our numerical analysis to the study of the dynamics of a Bose-condensed gas on a lattice of 3×3 sites. The initial setup is exactly the same as the one used in the previous section in the context of the BHF approximation (see fig. 5.8): $\rho \cdot I^2$ bosonic atoms loaded on the center of a lattice with $I \times I$ sites, where $\rho \in \mathbb{N}^+$ is the filling factor. For times $t < 0$, the system is prepared such that the atoms in the center of the lattice are in a coherent state. Then, at $t = 0$ the tunneling amplitude J is non-adiabatically turned on, permitting the atoms to tunnel to all neighboring sites. As we have mentioned previously, this initial condition is not an eigenstate of the system and, consequently, it will evolve in time in a non-trivial way. The initial condition in the language of the condensate amplitudes and the two-time correlation functions are described by eqs. 5.65 - 5.67. In sections 5.2.2 and 5.4.1, we explained that is not necessary to consider the components of the single particle excitations spectral function $\boldsymbol{A}_{ij}$ while solving the equations of motion within the BHF approximations. On the contrary, the numerical analysis within the full second-order approximation requires the knowledge of all previous steps. Thus, we have to include the equations for $\boldsymbol{A}_{ij}$ into our analysis. In addition, we also have to propagate the solutions for time for two different time arguments for the two-time correlations functions. In appendix B we summarize the numerical scheme used to solve the equations of motion in the full second-order approximation.

In the following we summarize the temporal dynamics of the system for different filling factors ρ and on-site interaction parameters u. In order to do so, we plot the time evolution of the atom and condensate population $N_i^{(0)} + N_i^{(\varphi)}$ and $N_i^{(0)}$ at every site i. In addition we plot the overall condensate depletion $N^{(\varphi)} = \sum_i N_i^{(\varphi)}$ as a function of time. All these quantities are

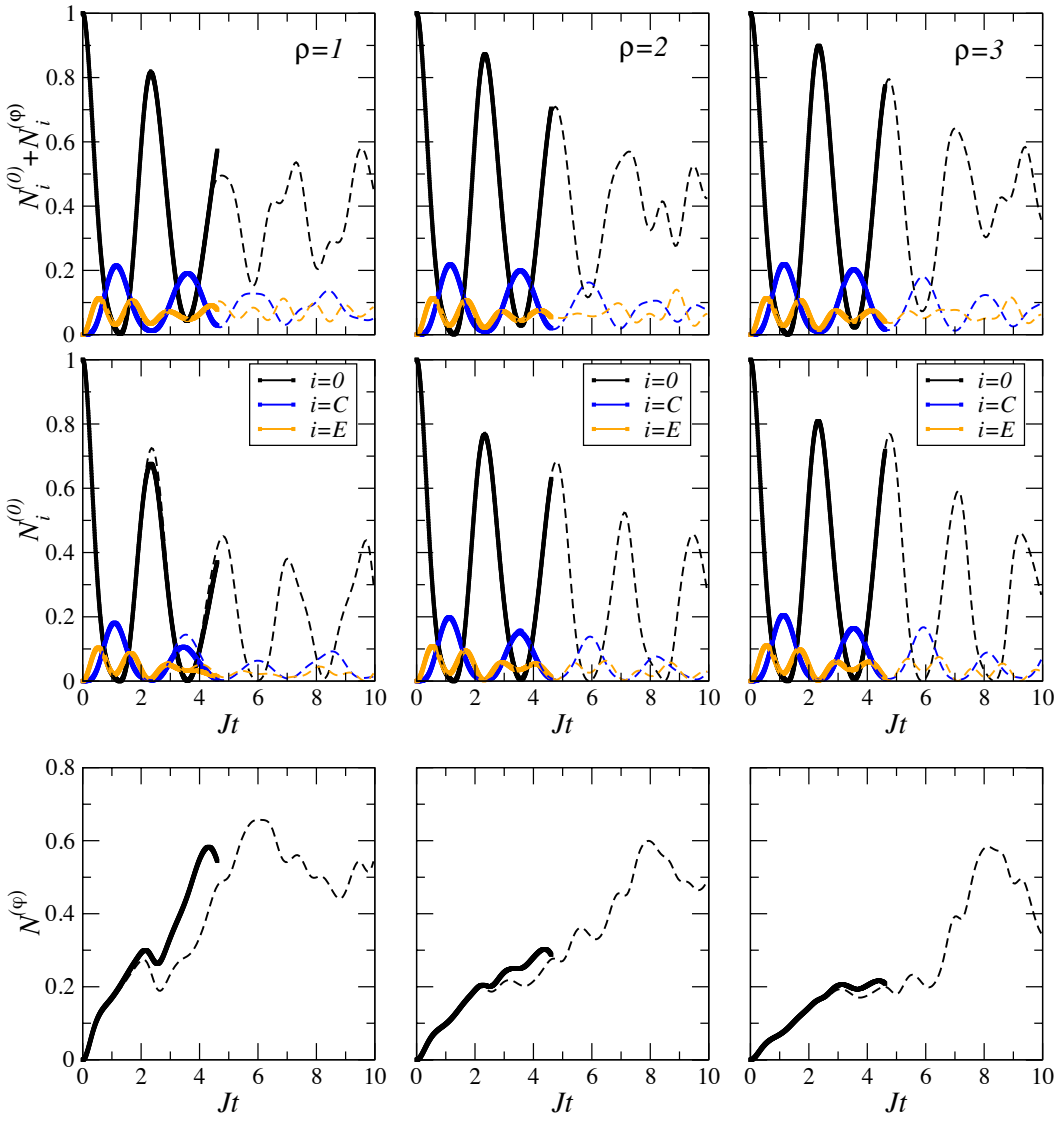

Figure 5.15: In the upper and middle row the population and condensate population $N_i^{(0)} + N_i^{(\varphi)}$ and $N_i^{(0)}$ per site on a 3×3-sites lattice with interaction parameter $u = 3$ are plotted as a functions of time for different filling factors $\rho = 1, 2, 3$ from left to right. The black lines correspond to the center of the lattice with $i = 0 \equiv (0, 0)$, the blue lines to the corners with $i = C \equiv (-a, -a), (-a, a), (a, -a), (a, a)$, and the orange lines to the edges with $i = E \equiv (-a, 0), (0, -a), (a, 0), (0, a)$. In the lower row the plots correspond to the time evolution of the overall fluctuations particle number for the different ρ's. The dashed lines correspond to the solutions obtained within the BHF approximation, and serve as reference.

given in units of the total particle number $\rho \cdot I^2$. In fig. 5.15 we show the time evolution for $u = 3$ and different filling factors ρ. We observe, that after turning on the tunneling J, the sites at the edges of the lattice, $i = E \equiv (-a, 0), (0, -a), (a, 0), (0, a)$, are populated (orange

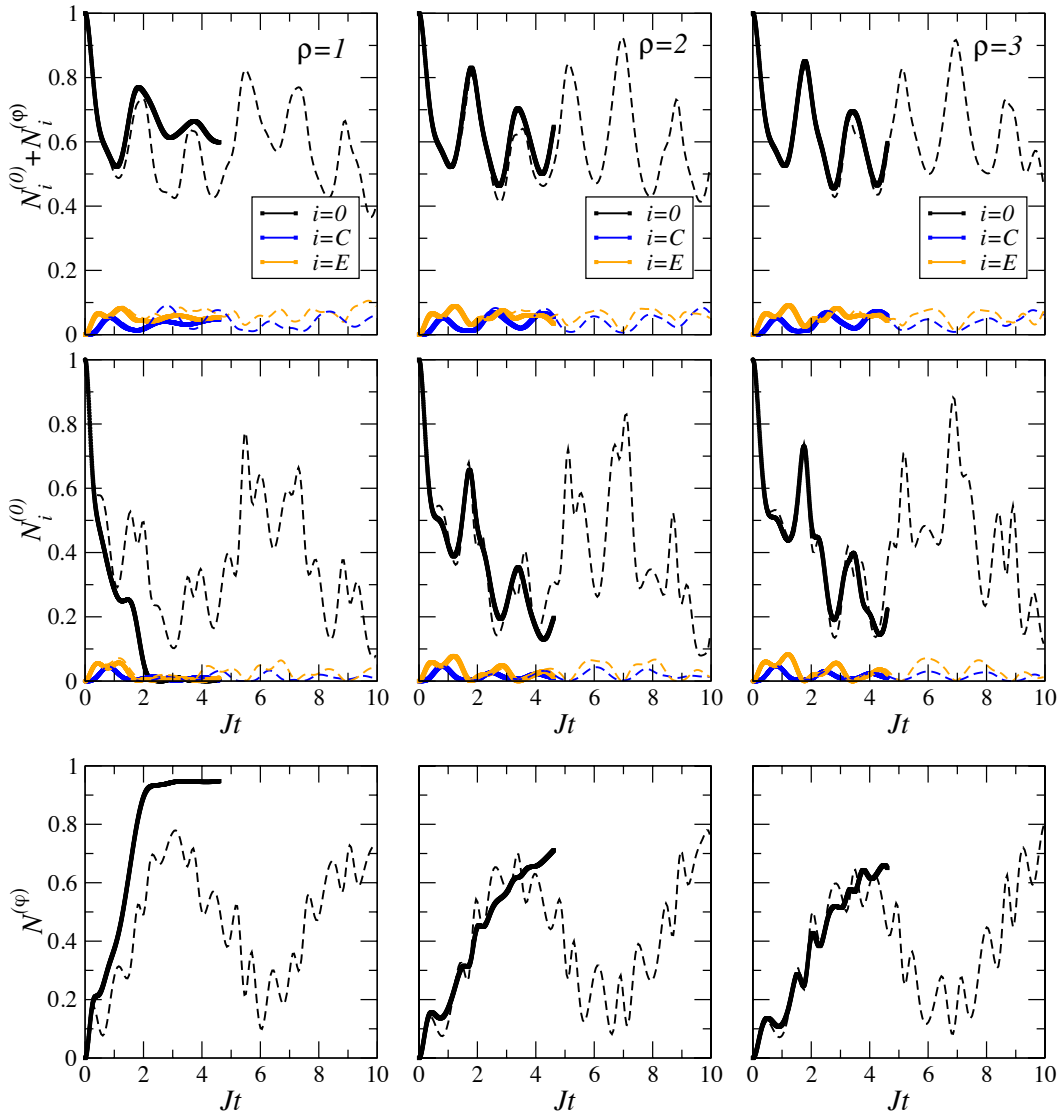

Figure 5.16: In the upper and middle row the population and condensate population $N_i^{(0)} + N_i^{(\varphi)}$ and $N_i^{(0)}$ per site on a lattice with 3×3 sites with interaction parameter $u = 7$ are plotted as a functions of time for different filling factors $\rho = 1, 2, 3$ from left to right. The black lines correspond to the center of the lattice with $i = 0 \equiv (0, 0)$, the blue lines to the corners with $i = C \equiv (-a, -a), (-a, a), (a, -a), (a, a)$, and the orange lines to the edges with $i = E \equiv (-a, 0), (0, -a), (a, 0), (0, a)$. In the lower row the plots correspond to the time evolution of the overall fluctuations particle number for the different ρ's. The dashed lines correspond to the solutions obtained within the BHF approximation, and serve as reference.

line in the upper row). The thick solid lines in the plots correspond to the results obtained from the full second-order approximation and the thin dashed lines to the results obtained from the BHF approximation. While the population in the center of the lattice $i = 0 \equiv (0, 0)$ goes

down to nearly zero (black lines), the atoms start to accumulate at the corners of the lattice $i = C \equiv (-a,-a),(-a,a),(a,-a),(a,a)$ (blue lines). Then, the atoms are reflected back over the edges to the center of the lattice. We observe that the majority of the atoms repopulate the center of the lattice at $Jt \approx 2.5$ and this repopulation increases with the filling factor ρ. In the next cycle the center of lattice is not completely depopulated. This feature becomes more pronounce with increasing ρ. In the middle row we show the condensate fraction $N_i^{(0)}$ per site. $N_i^{(0)}$ shows a behavior similar to the atom population per site, which suggests that at every site the temporal dynamics are dominated by the condensate fraction, even though the overall depletion of the condensate takes values up to 60% of the total number of particles (bottom of fig. 5.15). Although the overall depletion of the condensates accounts for such a large fraction of the total number of atoms, we observed that for $u = 3$ the dynamics of the system are still well described within the framework of the BHF approximation, and the accordance between the two approximations increases with the filling factor ρ. Unfortunately, the time scales reached within the BHF approximation are numerically not accessible by the means of the full second-order approximation without making any additional approximations. Naively, we expect the congruence between the results obtained from the two approximations to decrease in time due to the memory effects. This effect will become more visible for an increased interaction parameter u.

In contrast to the dynamics observed for $u = 3$, the overall condensate depletion saturates for $u = 7$ within the time interval that is accessible with the numerical analysis in the full second-order approximation (lower row of fig. 5.16). The overall depletion approaches a constant value. For a filling factor $\rho = 1$, the condensate fraction is depleted almost completely. The depletion decreases with the filling factor ρ. Taking a closer look at the atom population per site, $N_i^{(0)} + N_i^{(\varphi)}$, we see that the initially prepared coherent state is locked in the center of the lattice (black lines in the upper row in fig. 5.16). Once again the thick solid lines correspond to the results obtained from the full second-order approximation and the thin dashed lines to the ones obtained from the BHF approximation. Upon switching on the tunneling J, only a few atoms tunnel to the neighboring sites, to the edges of the lattice. Unlike in the case of a smaller u, the atoms leaving the center do not appear to be accumulating at the corners (orange and blue lines). The amplitude of the time oscillations in the occupation number of site $i = 0 \equiv (0,0)$ decreases with time and for increasing filling factor ρ. For $\rho = 1$, the oscillations are almost completely suppressed, while for larger filling factors only a tendency can be observed (within this time interval). Moreover, the situation depicted by the condensate atom number per site $N_i^{(0)}$ is quite different. We have argued before, that the larger the interaction parameter u and the more particles are confined on a site, the more likely the system will be to generate single particle excitations. This explains the decrease of the condensate fraction on site $i = (0,0)$ with the time (middle row). Since only a small fraction of the particles initially placed in the center of the lattice is able to tunnel to the neighboring sites, the effective on-site energy on those sites will be small. Consequently we will observed a smaller depletion of the condensate there. In agreement with the overall depletion observed for different filling factors ρ, we note that the depletion of the condensate fraction on every site increases with ρ.

Comparing the results obtained from the two approximations under consideration, we observed that the larger the filling factor ρ, the better the agreement between the two approximations. The memory effects, that could lead to thermalization of the system or drive it into a steady state, increase with the interaction parameter u, decrease with ρ, and become more evident with increasing time. In order to get a better insight into the dynamics, we consider

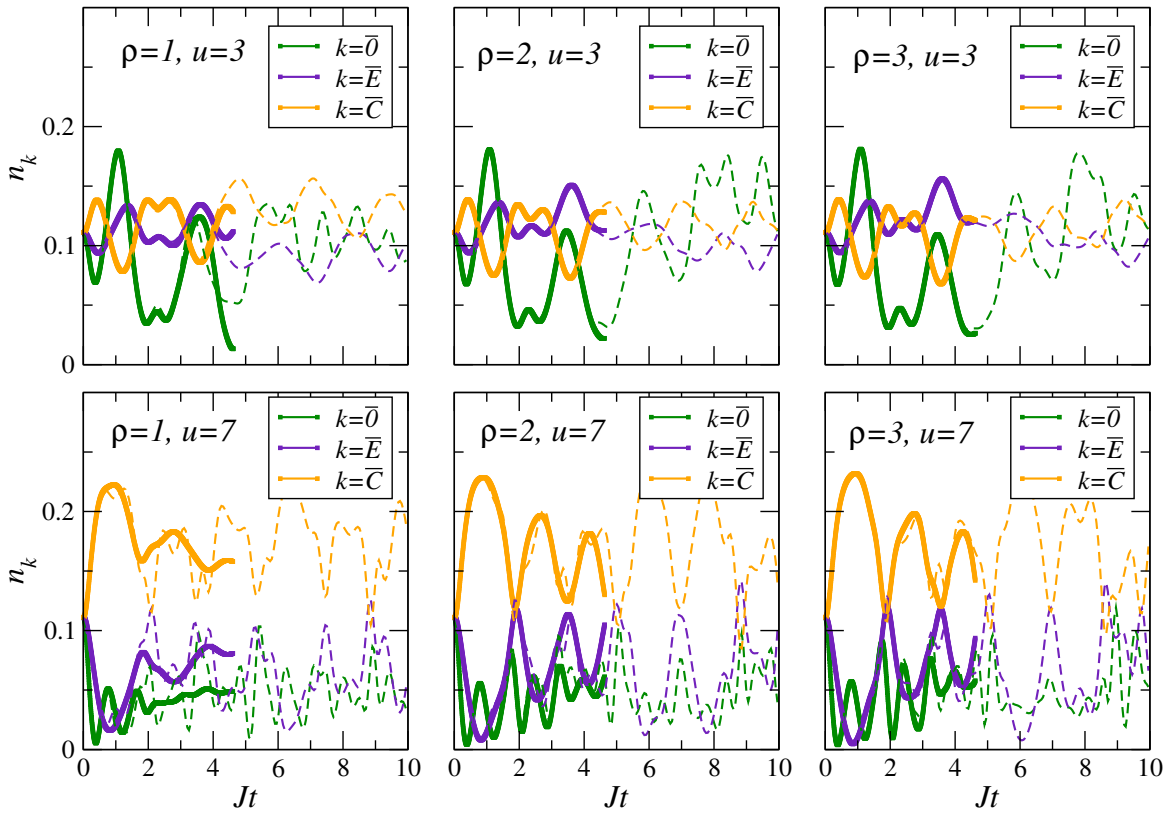

Figure 5.17: The upper row shows the time evolution of quasi-momentum distribution of atoms n_k loaded on a lattice with 3×3 sites with interaction parameter $u = 3$ and different filling factors $\rho = 1, 2, 3$ from left to right. The green line corresponds to the quasi-momentum $k = \overline{0} \equiv (0, 0)$, the violet to $k = \overline{E} \equiv (0, \frac{2\pi}{3a}), (0, \frac{4\pi}{3a}), (\frac{2\pi}{3a}, 0), (\frac{4\pi}{3a}, 0)$, and the orange to $k = \overline{C} \equiv (\frac{2\pi}{3a}, \frac{2\pi}{3a}), (\frac{2\pi}{3a}, \frac{4\pi}{3a}), (\frac{4\pi}{3a}, \frac{2\pi}{3a}), (\frac{4\pi}{3a}, \frac{4\pi}{3a})$. In the lower row the same quantities are plotted for $u = 7$. The dashed lines correspond to the solutions obtained within the BHF approximation, and serve as reference

the quasi-momentum distribution n_k defined by eq. 5.36. In fig. 5.17 we plotted the time evolution of n_k for different interaction parameters and filling factors. The thick solid lines correspond to the solutions obtained from the full second-order approximation and the thin dashed lines from the BHF-approximation. In agreement with the discussion above, we observe a bigger accordance between the two approximations for decreasing u and increasing ρ. For $u = 3$ the momentum modes are more equally distributed than for $u = 7$. We observed a similar behavior in the previous section as shown in fig. 5.9 and 5.11. The repeated crossing between the occupation number of the different quasi-momentum modes corresponds to the interference patterns observed in fig. 5.9. Unlike for the systems with large number of lattice sites, the quasi-momentum distribution does not become stationary for $u = 7$ within the BHF approximation (thin dashed lines in the lower row of fig. 5.17). Consequently, we can attribute the tendency of the occupation of the different quasi-momentum modes to reach a constant value solely to the higher order processes (thick solid lines). Even though this tendency is

very pronounced for the filling factor $\rho = 1$, we can not tell for sure if the quasi-momentum distribution will remain constant.

5.4.3 Discussion

In section 5.2 we introduced an extensive mathematical apparatus to study non-equilibrium situations in systems consisting of an interacting Bose-condensed gas loaded on an optical lattices. Using these mathematical tools, we study in particular the non-trivial time evolution of a coherent state placed in the center of a 2-dimensional lattice. In the non-equilibrium formulation used to described the system, quantum fluctuations were included and treated within the BHF and the full second-order approximations. The analysis was done systematically for systems with different numbers of sites $I \times I$, numbers of atoms $\rho \cdot I^2$, and interatomic interaction parameters u. Unfortunately, the numerical analysis within the full second-order approximation is restricted to systems with a small number of sites due cpu and memory limitations. In addition, the memory integrals on the right side of the equations of motion pose an additional restriction on the time scales accessible by numerics. For this reason, we first studied the expansion of a coherent state on lattices of 21×21 and 15×15 sites for different filling factors ρ and on-site interaction parameters u. Then, in the succeeding section we presented a detailed numerical analysis of a system with 3×3 sites with the same initial condition as those studied by the means of BHF approximation. The results obtained within the full second-order approximation were discussed and compared to those obtained from the BHF approximation.

The BHF-approximation provided us a good insight into the dynamics of the expanding gas. We observed that the expansion of the gas has a ballistic nature for a fixed filling factor, unless the interatomic interaction u exceeds a critical value. In this case the expansion occurs diffusively, as the outwards motion of the atoms is slowed down due to the relatively high interaction. Moreover, the Bogoliubov prescription allowed us to treat the coherent state and the quantum fluctuations separately. We found out that regions of high density lead to increased number of atoms excited out of the condensate, which follow the density profile of the majority of the atoms. We also observed that for increasing interaction parameters, the quasi-momentum distribution becomes strongly peaked at the corner of the first Brillouin zone, and the peak becomes more pronounce, the larger the interactions parameter gets. For the number of sites, filling factors, and interaction parameters under consideration, the overall depletion of the condensate accounted for 10% or less, and it decreases with the filling factor, as it is expected. All this implies that the larger the system and the number of atoms, the better the predictions by BHF approximation and its agreement with the GPE description.

Due to the restrictions impose by the memory integrals to the numerical analysis of the full second-order equations of motion, we constrained our analysis to a lattice with 3×3 sites. Comparing the results to those obtained from the BHF for such a system, we found out that the quasi-momentum distribution as well as the overall condensate depletion show a tendency to reach a constant shape and value due to the inclusion of memory effects. This effect becomes more pronounced, the smaller the filling factor and the bigger the interactions parameter gets. For such a small system, the BHF is only a good a approximation for small time scales, and it is necessary to include the higher order terms.

Despite having the capability to describe an expanding coherent state on a lattice and being able to study the condensate amplitude and the quantum fluctuations separately, the approach we used lacks the ability to describe a time dependent transition between the Mott-insulating

and the superfluid phase.

CHAPTER 6

Conclusion

In this work we have generalized the field theoretical description for an interacting Bose gas at low temperatures using the Keldysh formalism to study situations away from equilibrium. The theory is expressed in terms of integro-partial-differential equations for the condensate wave function and the two-point correlation functions related to the non-condensed particles. We have used the Bogoliubov-Hartree-Fock approximation for the self-energies to study the short time dynamics of weakly interacting Bose-condensed gases in atomic traps. In this approximation the equations of motion reduce to a system of coupled partial-differential equations. However, this approximation does not include the correlations between the initial and the intermediate states. In order to address the question of thermalization and equilibration, we have considered the full second-order approximation for the self-energies.

We have used the non-equilibrium formalism described above to study the temporal dynamics of Bose-condensed gases in situations out equilibrium, such as Josephson junctions between condensates and the non-trivial time evolution of a coherent state placed at the center of a 2-dimensional optical lattice. A model including interatomic interactions as well as single particle excitations was proposed for the description of the dynamics of Josephson-coupled Bose-Einstein condensates after switching on the Josephson coupling. The temporal dynamics of the atoms on the 2-dimensional lattices were studied using the Bose-Hubbard model. In addition, we analyzed the two-site Bose-Hubbard model with the same initial conditions as the Josephson-coupled condensates in order to compare the results with the dynamics obtained from the model we have proposed.

In spite of its limitations, the Bogoliubov-Hartree-Fock approximation has revealed very interesting phenomena for short times. The model proposed for the non-equilibrium description of Bose Josephson junctions recovers the mean-field dynamics reported by Smerzi et al. [62] when neglecting the quantum fluctuations. If the initial population imbalance exceeds a critical value depending on the interaction strength, the system undergoes a transition from the delocalized regime (Josephson oscillation) into the self-trapped regime, in which the population imbalance is self-locked. Taking the single particle excitations into account, the Bose Josephson junction reveals that it can sustain multiple, undamped Josephson oscillations for an extended time period before particles get excited out of the condensates as an “avalanche” and the behavior changes abruptly to fast Josephson and Rabi oscillations. This is a consequence of the crossing of the lowest quasiparticle energy and the highest condensate eigenenergy. We observed that a state, that was initially self-trapped, will be destroyed by these fast dynamics. The time

evolution of a coherent state released at the center of a 2-dimensional lattice shows an initial expansion, which is slowed down by the on-site interactions. For small interactions the gas expands ballistically. Increasing the on-site repulsion results in a diffusive expansion with a small fraction of the particles propagating ballistically. We observe that the depletion of the coherent state increases with the interaction parameters and decreases with the total number of particles.

Beyond the Bogoliubov-Hartree-Fock approximation, the numerical analysis is very demanding and time consuming. For this reason we restricted our analysis to small systems. The results obtained using the Bogoliubov-Hartree-Fock approximation were confirmed for short times. However, deviations from these results increased with time and also when increasing the interaction parameter, and decreased while increasing the number of particles. This is due to the correlations between the initial conditions and the intermediate states. In some cases we were able to propagate the solutions long enough in time in order to observe the system approaching a steady state.

The non-equilibrium description for Bose-condensed gases used in this thesis is independent of the set up. It can be applied to a variety of situations involving weakly interacting Bose gases out equilibrium. For example, the expansion of a Bose-Einstein condensate on a disordered potential could be of great interest. Even though our approach provides a description for the quantum dynamics including scattering processes between particles, it is not able to describe non-equilibrium effects close to the transition from the superfluid to the Mott insulator phase. This would require the non-equilibrium generalization of methods that are able to characterize this transition.

APPENDIX A

Analytical Continuation Procedure

We mentioned in section 2.2, that when considering the non-equilibrium version of the Dyson's equation or the equation of motion for the closed time path Green's function, one encounters terms containing the convolution and/or product of various two-point correlators, whose time arguments reside on the CTP. However, these contour-ordered quantities are not easy to interpret and one therefore needs an approach, which brings them to a real time formulation. In this section we proceed to show how the deformation of the closed time path can lead to the required expressions.

We start considering the convolution between two two-point correlators

$$C(t_1, t_{1'}) = \int_C \mathrm{d}\tau\, A(t_1, \tau) B(\tau, t_{1'}), \tag{A.1}$$

where we left out the spacial dependence for simplicity reasons, and since we are currently only interested in temporal dynamics.

Now we will carry out the derivation for the expression for the "lesser" component of A.1. In order to do this let us assume that t_1 resides on the upper branch of the closed time path and $t_{1'}$ on the lower brach.

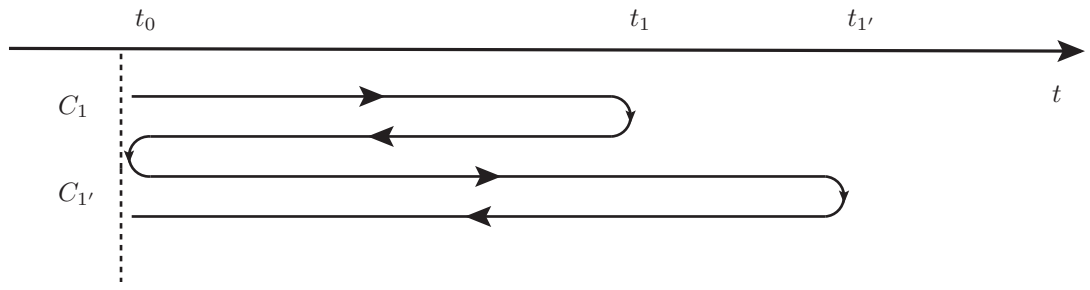

Figure A.1: Deformation of the closed time path into a contour built by the contours C_1 and $C_{1'}$.

The first step is to deform the contour, as indicated in fig. A.1. Thus, we get

$$C^<(t_1, t_{1'}) = \int_{C_1} \mathrm{d}\tau\, A(t_1, \tau) B^<(\tau, t_{1'}) + \int_{C_{1'}} \mathrm{d}\tau\, A^<(t_1, \tau) B(\tau, t_{1'}), \tag{A.2}$$

where use the "<"-sign to highlight that on the contour C_1, $t_{1'}$ appears later than $\tau \in C_1$, and on the contour $C_{1'}$, t_1 appears before $\tau \in C_{1'}$. Splitting each of the contour integrations into two parts, we get

$$\begin{aligned} C^<(t_1,t_{1'}) &= \int_{-\infty}^{t_1} \mathrm{d}t\, A^>(t_1,t)B^<(t,t_{1'}) + \int_{t_1}^{-\infty} \mathrm{d}t\, A^<(t_1,t)B^<(t,t_{1'}) \\ &\quad + \int_{-\infty}^{t_{1'}} \mathrm{d}t\, A^<(t_1,t)B^<(t,t_{1'}) + \int_{t_{1'}}^{-\infty} \mathrm{d}t\, A^<(t_1,t)B^>(t,t_{1'}) \\ &= \int_{-\infty}^{\infty} \mathrm{d}t\, \theta(t_1-t)\left[A^>(t_1,t) - A^<(t_1,t)\right] B^<(t,t_{1'}) \\ &\quad + \int_{-\infty}^{\infty} \mathrm{d}t\, A^<(t_1,t)\theta(t-t_{1'})\left[B^<(t,t_{1'}) - B^>(t,t_{1'})\right], \end{aligned} \tag{A.3}$$

where $t_0 \to -\infty$. Replacing the expressions in the integrals with the definitions of the retarded and advanced Green's function, we obtain

$$C^<(t_1,t_{1'}) = \int_{-\infty}^{\infty} \mathrm{d}t\, \left[A^{\mathrm{ret}}(t_1,t)B^<(t,t_{1'}) + A^<(t_1,t)B^{\mathrm{adv}}(t,t_{1'})\right]. \tag{2.21}$$

The equation for the greater component is derived in a similar way.

With the expressions for the lesser and greater component of the convolution A.1, we can proceed to derive the retarded/advanced component:

$$\begin{aligned} C^{\mathrm{ret}}(t_1,t_{1'}) &= \theta(t_1-t_{1'})\left[C^>(t_1,t_{1'}) - C^<(t_1,t_{1'})\right] \\ &= \theta(t_1-t_{1'}) \int_{-\infty}^{\infty} \mathrm{d}t\, \left[A^{\mathrm{ret}}(B^> - B^<) + (A^> - A^<)B^{\mathrm{adv}}\right] \\ &= \theta(t_1-t_{1'}) \left\{ \int_{-\infty}^{t_1} \mathrm{d}t\, (A^> - A^<)(B^> - B^<) \right. \\ &\quad \left. - \int_{-\infty}^{t_{1'}} (A^> - A^<)(B^> - B^<) \right\} \\ &= \int_{-\infty}^{\infty} \mathrm{d}t\, A^{\mathrm{ret}}(t_1,t)B^{\mathrm{ret}}(t,t_{1'}). \end{aligned} \tag{A.4}$$

The equation for the advanced component is obtained in the same manner.

APPENDIX B

Numerical Propagation of the Two-Time Correlation Functions

In section 4.2.2, we derived the equations of motion for the upper components of the non-condensate spectral function and the statistical function for our model describing Bose Josephson junctions out of equilibrium. In our model we absorbed the spacial dependence in the Josephson coupling, the condensate on-site energies, the overlap matrix elements related to the interatomic interactions, and other parameters. As we stated before, these parameters can be computed by solving the GPE for a double-well trap. However this is not the subject of our analysis and we, therefore, regard them all as input parameters of our model. Absorbing the spacial dependence in the input parameters simplifies the equations of motion, because instead of analyzing a system of IPDEs, we have system of integro-differential equations that resembles a "non-linear first order ordinary Volterra integro-differential equation" (see [87]). The only difference resides on the two-time arguments of the correlation functions, which we will explain in the following how to handle.

Consider now the equations of motion for the two-time correlation functions

$$
\begin{aligned}
i\frac{\partial}{\partial t}A^{G}_{nm}(t,t') &= \left[E_{n\ell}+\Sigma^{HF}_{n\ell}(t)\right]A^{G}_{\ell m}(t,t') - \Omega^{HF}_{n\ell}(t)A^{F}_{\ell m}(t,t')^{*} \\
&\quad - i\int_{t'}^{t}\mathrm{d}\bar{t}\left[\Gamma^{G}_{n\ell}(t,\bar{t})A^{G}_{\ell m}(\bar{t},t') + \Gamma^{F}_{n\ell}(t,\bar{t})A^{\overline{F}}_{\ell m}(\bar{t},t')\right], \qquad (4.77)\\
i\frac{\partial}{\partial t}A^{F}_{nm}(t,t') &= \left[E_{n\ell}+\Sigma^{HF}_{n\ell}(t)\right]A^{F}_{\ell m}(t,t') - \Omega^{HF}_{n\ell}(t)A^{G}_{\ell m}(t,t')^{*} \\
&\quad - i\int_{t'}^{t}\mathrm{d}\bar{t}\left[\Gamma^{G}_{n\ell}(t,\bar{t})A^{F}_{\ell m}(\bar{t},t') + \Gamma^{F}_{n\ell}(t,\bar{t})A^{\overline{G}}_{\ell m}(\bar{t},t')\right], \qquad (4.78)
\end{aligned}
$$

and

$$
\begin{aligned}
i\frac{\partial}{\partial t}F^G_{nm}(t,t') &= \left[E_{n\ell}+\Sigma^{HF}_{n\ell}(t)\right]F^G_{\ell m}(t,t') - \Omega^{HF}_{n\ell}(t)F^F_{\ell m}(t,t')^* \\
&\quad - i\int_0^t \mathrm{d}\bar{t}\left[\Gamma^G_{n\ell}(t,\bar{t})F^G_{\ell m}(\bar{t},t') + \Gamma^F_{n\ell}(t,\bar{t})F^{\overline{F}}_{\ell m}(\bar{t},t')\right] \\
&\quad + i\int_0^{t'} \mathrm{d}\bar{t}\left[\Pi^G_{n\ell}(t,\bar{t})A^G_{\ell m}(\bar{t},t') + \Pi^F_{n\ell}(t,\bar{t})A^{\overline{F}}_{\ell m}(\bar{t},t')\right], \qquad (4.79)\\
i\frac{\partial}{\partial t}F^F_{nm}(t,t') &= \left[E_{n\ell}+\Sigma^{HF}_{n\ell}(t)\right]F^F_{\ell m}(t,t') - \Omega^{HF}_{n\ell}(t)F^G_{\ell m}(t,t')^* \\
&\quad - i\int_0^t \mathrm{d}\bar{t}\left[\Gamma^G_{n\ell}(t,\bar{t})F^F_{\ell m}(\bar{t},t') + \Gamma^F_{n\ell}(t,\bar{t})F^{\overline{G}}_{\ell m}(\bar{t},t')\right] \\
&\quad + i\int_0^{t'} \mathrm{d}\bar{t}\left[\Pi^G_{n\ell}(t,\bar{t})A^F_{\ell m}(\bar{t},t') + \Pi^F_{n\ell}(t,\bar{t})A^{\overline{G}}_{\ell m}(\bar{t},t')\right] \qquad (4.80)
\end{aligned}
$$

For simplicity we will drop the indices referring to the single particle excitations energy levels, depicted in fig. 4.6. After time discretization, the two-time correlation functions can be regarded as matrices in the discrete "time-space". We will us F^G to illustrate the discretization scheme and the method to propagate the solutions of the equations of motion 4.77 - 4.80. The matrix F^G in time-space reads

$$
F^G = \begin{pmatrix}
F^G(0,0) & F^G(0,\Delta t) & F^G(0,2\Delta t) & \dots \\
F^G(\Delta t,0) & F^G(\Delta t,\Delta t) & \dots & \\
F^G(2\Delta t,0) & \vdots & \ddots & \\
\vdots & & &
\end{pmatrix}, \qquad (B.1)
$$

where Δt is the time difference between to time steps.

Due to the symmetry relations summarized in table 3.1, it is only necessary to consider half of the components of B.1. We start with the initial conditions 4.67 at time $t = 0$, and "artificially" expand it. This is shown in fig. B.1 in on the left. The black dot in the two-time coordinate system corresponds to the initial condition and the light blue dot is the copy of it, to which we refer to as $F^G(0',0')$. We artificially expand the system of initial conditions, because we want compute $F^G(\Delta t,0)$ and $F^G(\Delta t,\Delta t)$ from $F^G(0,0)$. $F^G(0,\Delta t)$ is obtained from $F^G(\Delta t,0)$, according to table 3.1. We propagate from $\{F^G(0,0),F^G(0',0')\}$ to $\{F^G(\Delta t,0),F^G(\Delta t,\Delta t)\}$ conforming to fourth order Runge-Kutta method. This is depicted by the green arrow pointing into the second two-time coordinate system. At time step $t = \Delta t$ we have $\{F^G(\Delta t,0),F^G(\Delta t,\Delta t)\}$. Once more we artificially add $F^G(\Delta t',\Delta t')$, which is a copy of $F^G(\Delta t,\Delta t)$. This is depicted by the additional light blue dot in the second coordinate system. This allows us now to propagate from $\{F^G(\Delta t,0),F^G(\Delta t,\Delta t),F^G(\Delta t',\Delta t')\}$ to $\{F^G(2\Delta t,0),F^G(2\Delta t,\Delta t),F^G(2\Delta t,2\Delta t)\}$. In this manner we can compute the time evolution for every time step. For instance, the n-th time step is given by the propagation from $\{F^G((n-1)\Delta t,0),\dots,F^G((n-1)\Delta t,(n-1)\Delta t),F^G((n-1)\Delta t',(n-1)\Delta t')\}$ to $\{F^G(n\Delta t,0),\dots,F^G((n-1)\Delta t,(n-1)\Delta t),F^G(n\Delta t,n\Delta t)\}$.

So far, we have explained how to propagate the two-time correlation functions numerically,

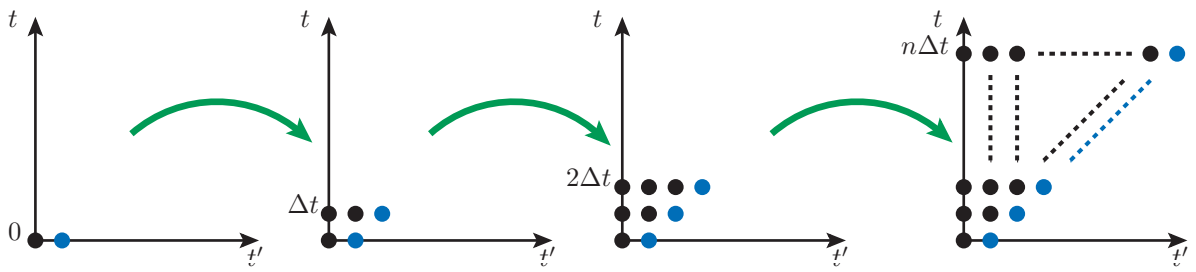

Figure B.1: The vertical and horizontal axes correspond to the left and right time arguments of the two-time correlation functions, respectively. The black dots are located on the coordinate system at the points at which the correlation functions are evaluated. Starting from the left, we initiate we the initial condition, that is located at origin of the coordinate system. The light blue dot is artificially added, in order to make to propagation along the vertical axis according to the fourth order Runge-Kutta method possible (green arrow pointing into the second coordinate system). At every time step this procedure is repeated.

but did not discuss why do we need the knowledge about all the previous step. Taking a closer look at the right side of eqs. 4.77 - 4.80, we observe that the higher order terms in the interactions contained in the "memory" integrals, involve the correlation functions calculated in the previous steps. Consequently, we need to keep track of all solutions since the initial condition while computing the two-time evolution of the correlation functions. Fortunately, the self-energies contained in the integrals fulfill similar symmetry relations to those satisfied by the two-time correlation functions (see tab. 3.2). This allows us to split the interval of integration, such that we can rewrite the integrants with the argument corresponding to the later time on the left. We now proceed to illustrate this with the integrals appearing on the right side of eq. 4.79:

$$
\begin{aligned}
&-i\int_0^t \mathrm{d}\bar{t}\left[\Gamma^G_{n\ell}(t,\bar{t})F^G_{\ell m}(\bar{t},t') + \Gamma^F_{n\ell}(t,\bar{t})F^{\overline{F}}_{\ell m}(\bar{t},t')\right] \\
&\qquad +i\int_0^{t'} \mathrm{d}\bar{t}\left[\Pi^G_{n\ell}(t,\bar{t})A^G_{\ell m}(\bar{t},t') + \Pi^F_{n\ell}(t,\bar{t})A^{\overline{F}}_{\ell m}(\bar{t},t')\right] \\
= \;& i\int_0^{t'} \mathrm{d}\bar{t}\left[\Gamma^G_{n\ell}(t,\bar{t})F^G_{m\ell}(t',\bar{t})^* + \Gamma^F_{n\ell}(t,\bar{t})F^F_{m\ell}(t',\bar{t})^*\right] \\
&\qquad -i\int_{t'}^t \mathrm{d}\bar{t}\left[\Gamma^G_{n\ell}(t,\bar{t})F^G_{\ell m}(\bar{t},t') - \Gamma^F_{n\ell}(t,\bar{t})F^F_{\ell m}(\bar{t},t')^*\right] \\
&\qquad +i\int_0^{t'} \mathrm{d}\bar{t}\left[\Pi^G_{n\ell}(t,\bar{t})A^G_{m\ell}(t',\bar{t})^* + \Pi^F_{n\ell}(t,\bar{t})A^F_{m\ell}(t',\bar{t})^*\right].
\end{aligned}
\tag{B.2}
$$

Notice that the left argument corresponds to a later time in every integrant. The integrals appearing on the right side of the equations of motion for A^G, A^F and F^F can be worked out

in the same way.

APPENDIX C

Snapshots of the Time-Evolution of a BEC Placed on a Lattice with 15×15 Sites

In section 5.4.1, we studied the non-trivial time evolution of a coherent state place at the center of a 2-dimensional lattice using the BHF approximation. The set up was analyzed for different system's sizes $I \times I$, filling factors ρ and interactions parameters u. In this section we annex the snapshots of the time evolution of a BEC on a lattice with 15×15 sites for filling factor $\rho = 1$ and interactions $u = 3$ and $u = 7$.

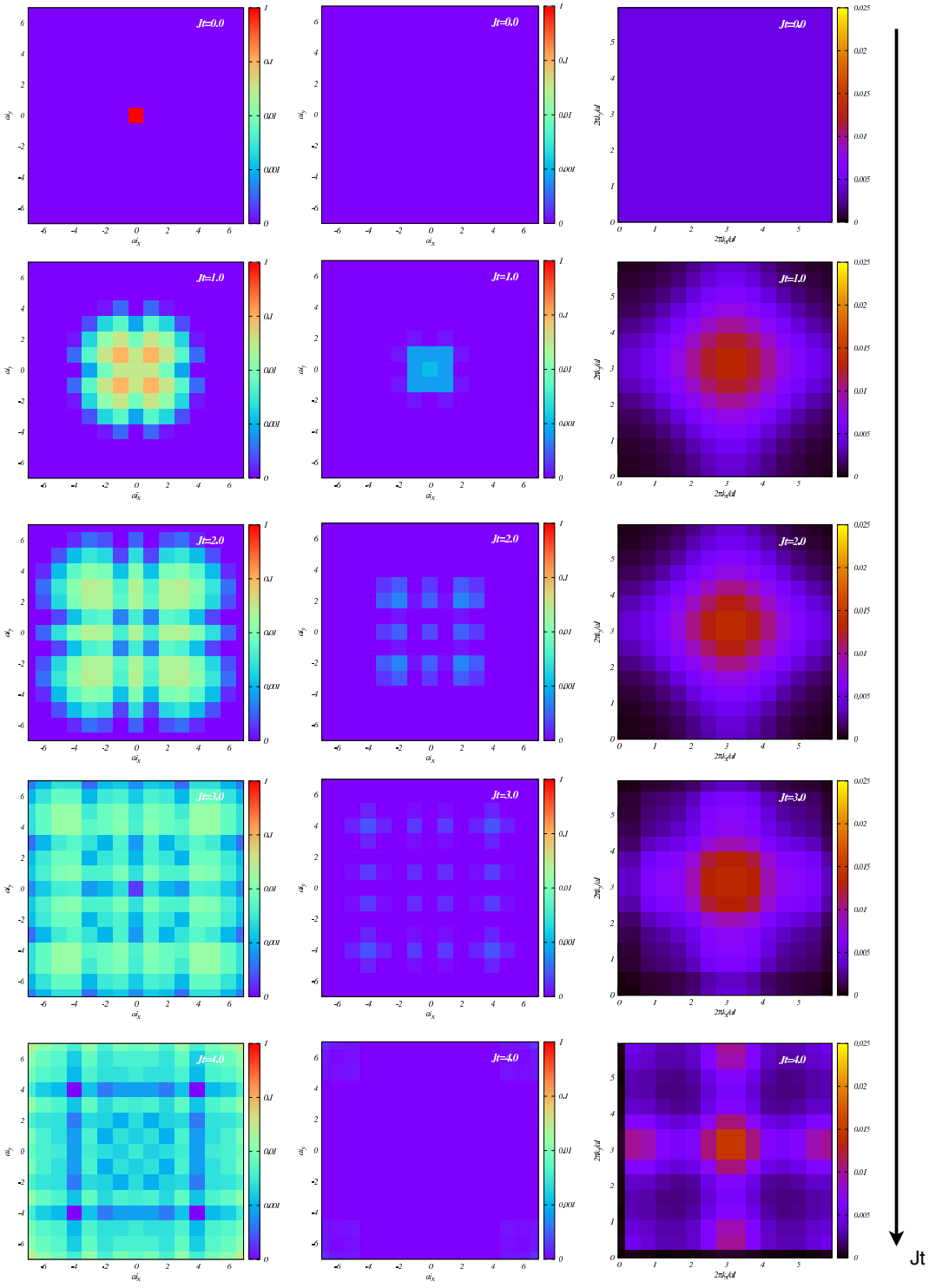

Time interval: $0 \leq Jt \leq 4$

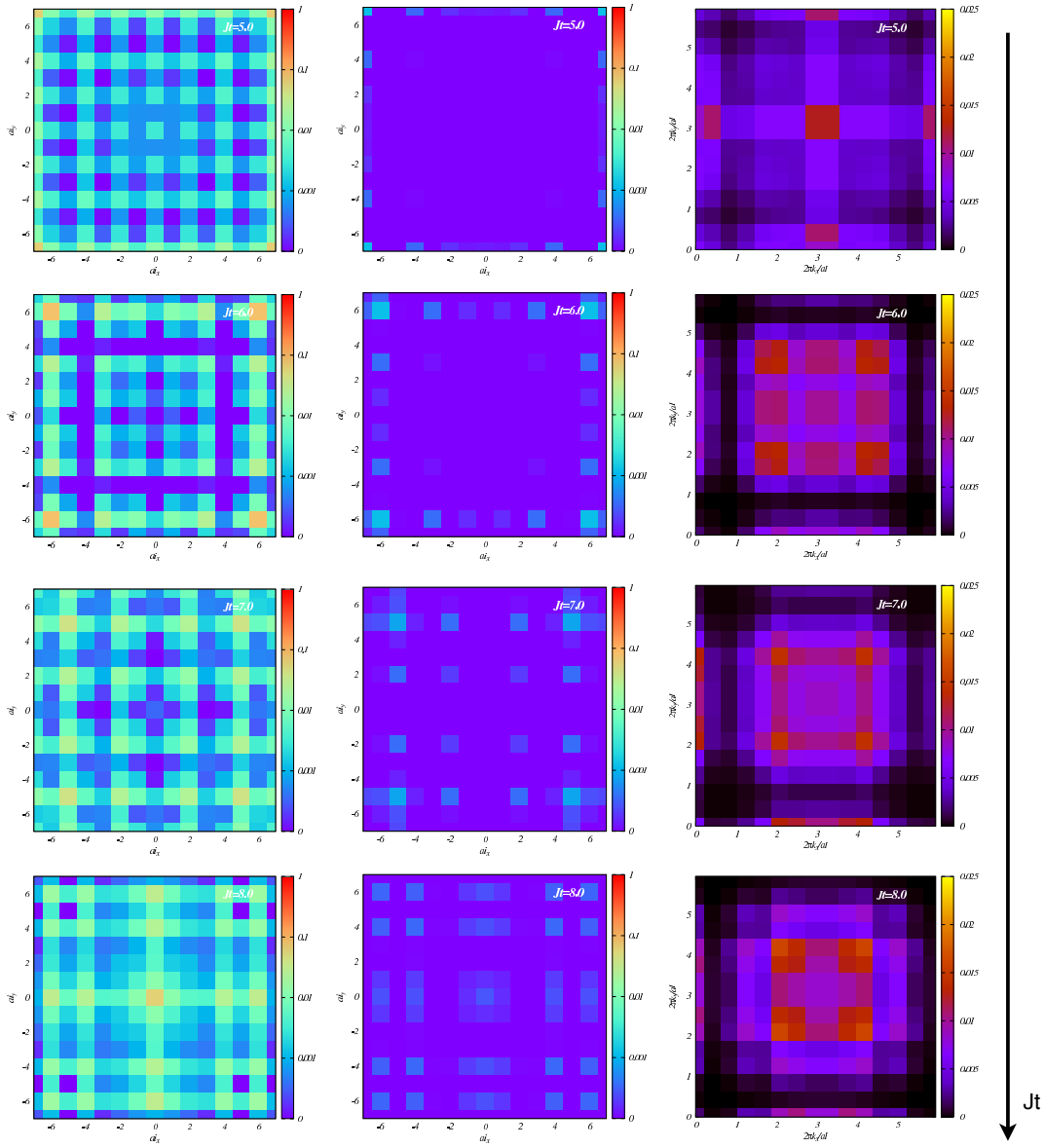

Time interval: $4 < Jt \leq 8$

Figure C.1: The left and central columns display the time evolution of the density profile of the atoms $N_i^{(0)} + N_i^{(\varphi)}$ and quantum fluctuations $N_i^{(\varphi)}$ on a lattice with 15×15 sites, respectively. The right column shows the time evolution of the 2-dimensional quasi-momentum distribution. The arrow on the right side, beside the plots depicts the time direction. The snapshots on the previous page correspond to the time interval $0 \leq Jt \leq 4$, and the ones on this page to $4 < Jt \leq 8$. The data corresponds to interaction parameter $u = 3$ and filling factor $\rho = 1$.

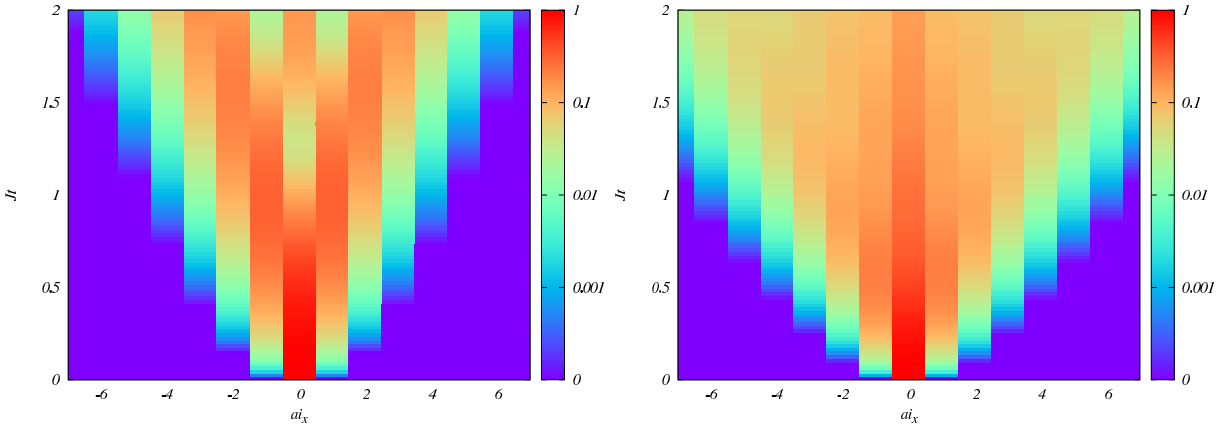

(a) Condesate population along the axis $i_y = 0$

(b) Condesate population along the axis $i_y = i_x$

(c) Fluctuations population along the axis $i_y = 0$

(d) Fluctuations population along the axis $i_y = i_x$

Figure C.2: On the top: Time evolution of the condensate population profile $N_i^{(0)}$ along the $i_y = 0$ and diagonal axes on a lattice with 15×15 sites during the expansion for $u = 3$ and $\rho = 1$. On the bottom: Time evolution of the population profile $N_i^{(\varphi)}$ of the single particle excitations along the same axis.

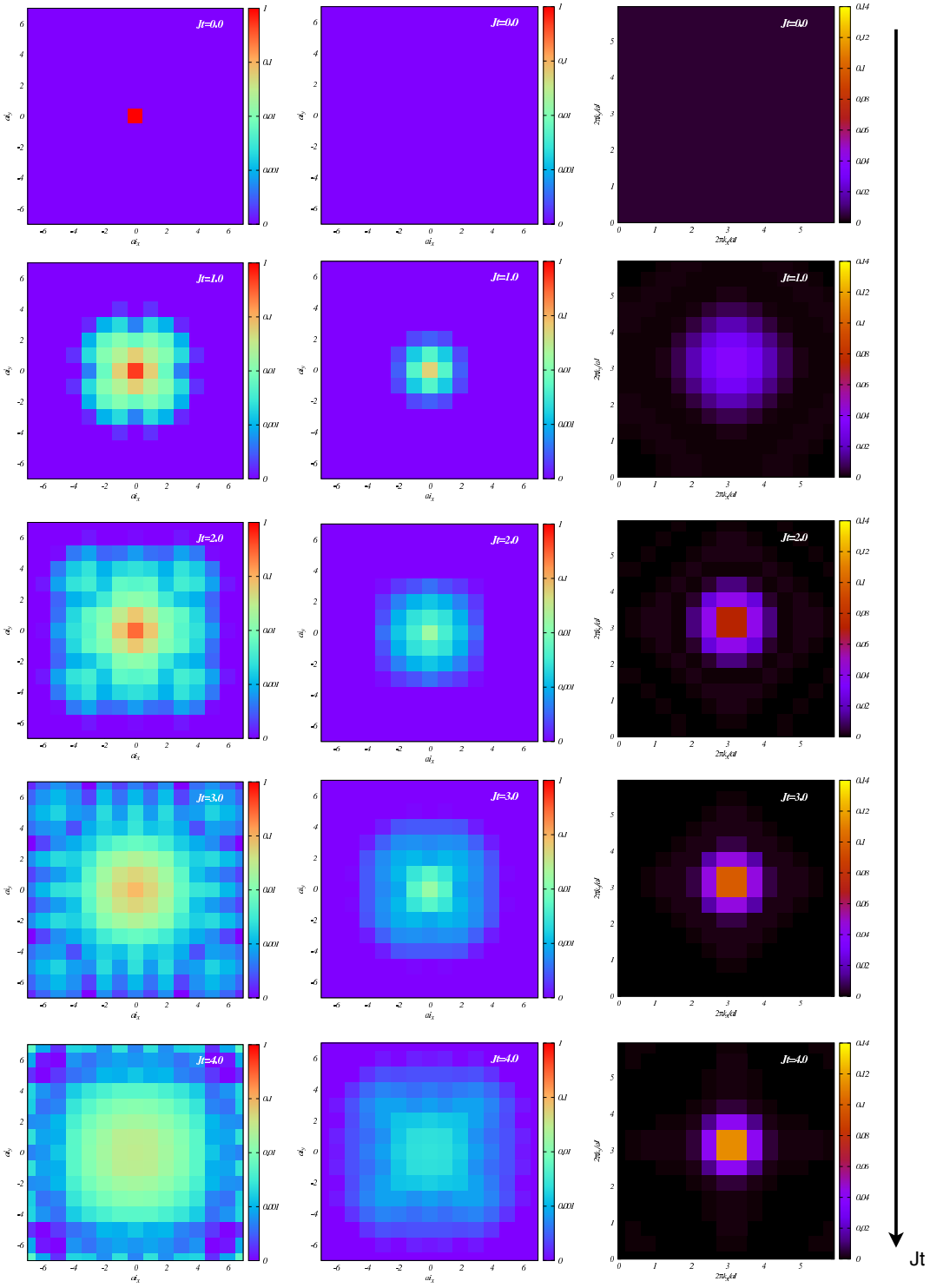

$0 \leq Jt \leq 4$

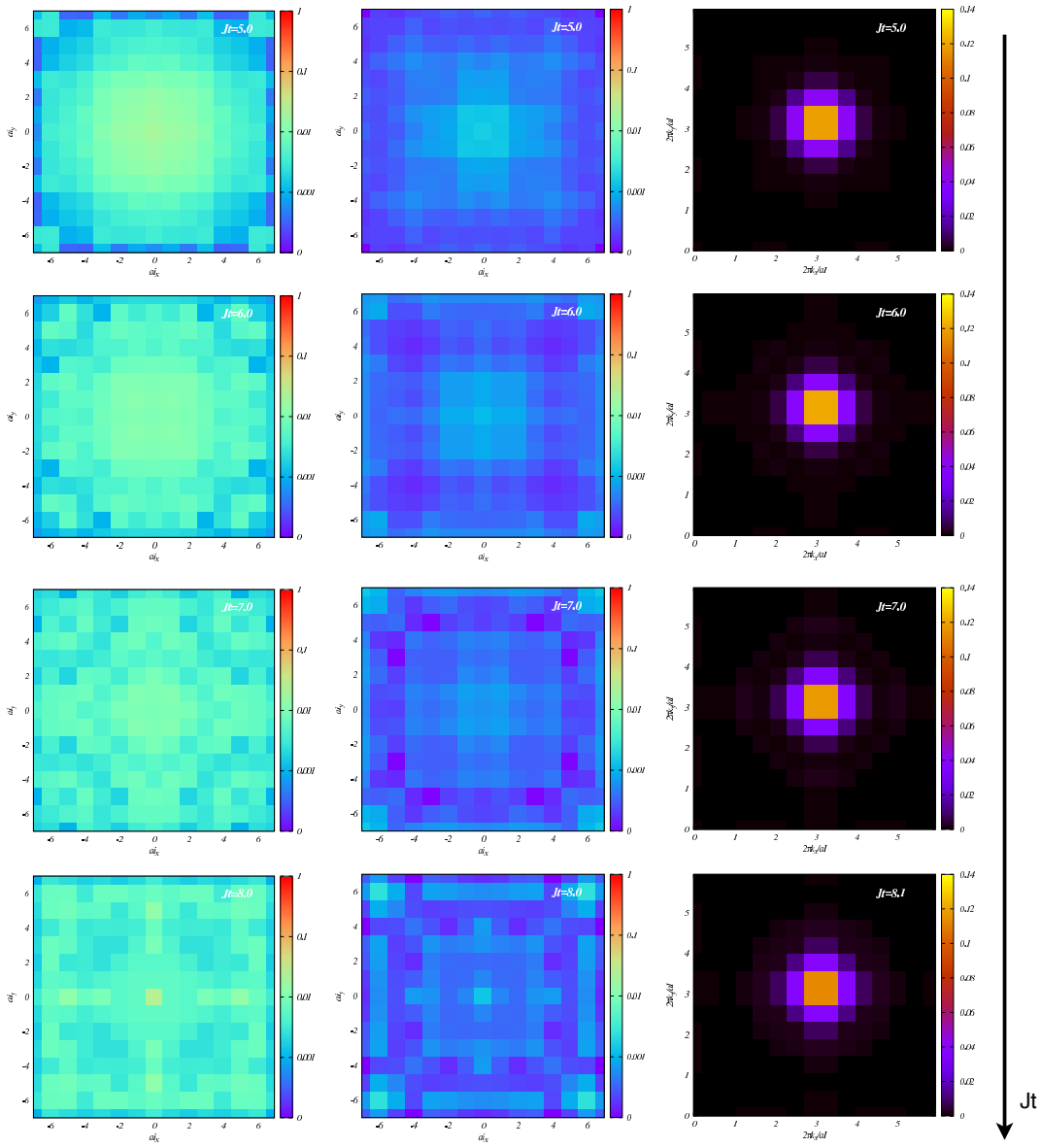

$4 < Jt \leq 8$

Figure C.3: The left and central columns display the time evolution of the density profile of the atoms $N_i^{(0)} + N_i^{(\varphi)}$ and quantum fluctuations $N_i^{(\varphi)}$ on a lattice with 15×15 sites, respectively. The right column shows the time evolution of the 2-dimensional quasi-momentum distribution. The arrow on the right side, beside the plots depicts the time direction. The snapshots on the previous page correspond to the time interval $0 \leq Jt \leq 4$, and the ones on this page to $4 < Jt \leq 8$. The data corresponds to interaction parameter $u = 7$ and filling factor $\rho = 1$.

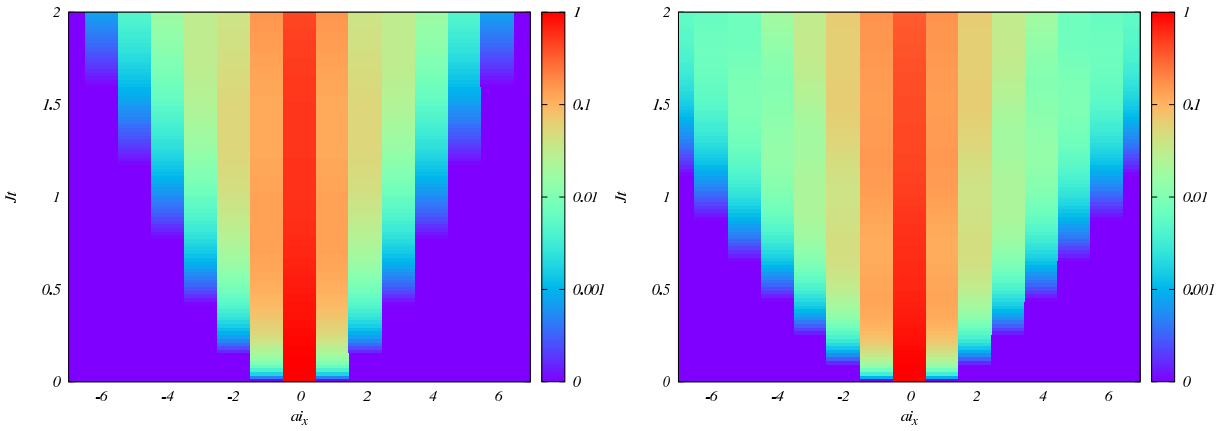

(a) Condesate population along the axis $i_y = 0$

(b) Condesate population along the axis $i_y = i_x$

(c) Fluctuations population along the axis $i_y = 0$

(d) Fluctuations population along the axis $i_y = i_x$

Figure C.4: On the top: Time evolution of the condensate population profile $N_i^{(0)}$ along the $i_y = 0$ and diagonal axes on a lattice with 15×15 sites during the expansion for $u = 7$ and $\rho = 1$. On the bottom: Time evolution of the population profile $N_i^{(\varphi)}$ of the single particle excitations along the same axis.

Bibliography

[1] A. Einstein, "Quantentheorie des einatomigen idealen Gases – Zweite Abhandlung", *Sitzungsberichte der preussischen Akademie der Wissenschaften* (1925) 3.

[2] S. Bose, "Plancks Gesetz und Lichtquantenhypothese", *Z. Phys.* 26 (1924) 178.

[3] I. F. Silvera and J. T. M. Walraven, "Stabilization of Atomic Hydrogen at Low Temperature", *Phys. Rev. Lett.* 44 (1980) 164.

[4] V. V. Goldman, I. F. Silvera and A. J. Leggett, "Atomic hydrogen in an inhomogeneous magnetic field: Density profile and Bose-Einstein condensation", *Phys. Rev. B* 24 (1980) 2870.

[5] M. Anderson et al., "Observation of Bose-Einstein Condensation in a Dilute Atomic Vapor", *Science* 269 (1995) 198.

[6] M.-O. Mewes et al., "Bose-Einstein Condensation in a Tightly Confining dc Magnetic Trap", *Phys. Rev. Lett.* 77 (1996) 416.

[7] P. Kapitza, "Viscosity of Liquid Helium below the λ-Point", *Nature* 141 (1938) 74.

[8] J. Allen and A. Misener, "Flow of Liquid Helium II", *Nature* 141 (1938) 75.

[9] F. London, "The λ-Phenomenon of Liquid Helium and the Bose-Einstein Degeneracy", *Nature* 141 (1938) 643.

[10] L. Landau, "Theory of the Superfluidity of Helium II", *Phys. Rev.* 60 (1941) 356.

[11] A. Griffin, *Excitations in a Bose-condensed Liquid*, 2nd ed., Cambridge University Press, 2005.

[12] J. Kane and L. Kadanoff, "Green's Functions and Superfluid Hydrodynamics", *J. Math. Phys.* 6 (1965) 1902.

[13] M. R. Matthews et al., "Vortices in a Bose-Einstein Condensate", *Phys. Rev. Lett.* 83 (1999) 2498.

[14] S. Burger et al., "Dark Solitons in Bose-Einstein Condensates", *Phys. Rev. Lett.* 83 (1999) 5198.

[15] M. Andrews et al., "Observation of Interference Between Two Bose Condensates", *Science* 275 (1997) 637.

[16] M. Greiner et al., "Quantum Phase Transition from a Superfluid to a Mott Insulator in a Gas of Ultracold Atoms", *Nature* 415 (2001) 39.

[17] M. Cheneau et al.,
"Light-cone-like spreading of correlations in a quantum many-body system",
Nature 481 (2012) 484.

[18] P. Barmettler et al., "Propagation front of correlations in an interacting Bose gas",
Phys. Rev. A 85 (2012) 053625.

[19] S. Li et al., "Self-trapping dynamics in a two-dimensional optical lattice",
Phys. Rev. A 88 (2013) 023419.

[20] P. Martin and J. Schwinger, "Theory of Many-Particle Systems. I",
Phys. Rev. 115 (1959) 1342.

[21] J. Schwinger, "Brownian Motion of a Quantum Oscillator", *J. Math. Phys.* 2 (1961) 407.

[22] L. Keldysh, "Diagram Technique for Nonequilibrium Processes",
Sov. Phys. JETP 20 (1965) 1018.

[23] G. Baym and L. Kadanoff, *Quantum Statistical Mechanics*, 1st ed.,
W.A. Benjamin, Inc., 1962.

[24] G. Baym and L. Kadanoff, "Conservation Laws and Correlation Functions",
Phys. Rev. 124 (1961) 287.

[25] G. Baym, "Self-Consistent Approximations in Many-Body Systems",
Phys. Rev. 127 (1962) 1391.

[26] H. Haug and A.-P. Jauho,
Quantum Kinetics in Transport and Optics of Semiconductors, 2nd ed., Springer, 2008.

[27] J. Rammer, *Quantum Field Theory of Non-equilibrium States*, 1st ed.,
Cambridge University Press, 2007.

[28] M. Trujillo-Martinez, "Non-Adiabatic Mixing of Two Bose-Einstein Condensates",
Universität Bonn, 2008,
URL: `http://library.fes.de/pdf-files/stufo/cd-0624/diplomarbeit.pdf`.

[29] M. Peskin and D. Schroeder, *An Introduction to Quantum Field Theory*, 1st ed.,
Perseus Books, 1995.

[30] A. Abrikosov, L. Gorkov and I. Dzyaloshinski,
Methods of Quantum Field Theory in Statistical Physics, 1st ed.,
Dover Publications, Inc., 1963.

[31] A. Altland and B. Simons, *Condensed Matter Field Theory*, 2nd ed.,
Cambridge University Press, 2010.

[32] J. Kroha and A. Zawadowski,
"Nonequilibrium Quasiparticle Distribution Induced Kondo Defects",
Phys. Rev. Lett. 88 (2002) 176803.

[33] P. Coleman, "New Approach to the Mixed-Valence Problem",
Phys. Rev. B 29 (1983) 3035.

[34] D. Langereth, *Linear and Nonlinear Electron Transport in Solids*,
ed. by J. Devreese and V. van Doren,
New York: Plenum Press, 21st July–2nd Aug. 1976.

[35] A. Griffin, T. Nikuni and E. Zeremba, *Bose-Condensed Gases at Finite Temperatures*, 1st ed., Cambridge University Press, 2009.

[36] M. Imamovic-Tomasovic and A. Griffin, "Generalized Boltzmann Equation for a trapped Bose-Condensed Gas Using the Kadanoff-Baym Formalism", *Progress in Nonequilibrium Green's Functions*, ed. by M. Bonitz, Singapore: World Scientific, 20th–24th Sept. 1999 404.

[37] S. Beliaev, "Application of the Methods of Quantum Field Theory to a System of Bosons", *Sov. Phys. JETP* 7 (1958) 289.

[38] J. Berges, "Introduction to Nonequilibrium Quantum Field Theory", *AIP Conf. Proc.* 739 (2004) 3.

[39] A. Branschädel and T. Gasenzer, "2PI Nonequilibrium Versus Transport Equations for an Ultracold Bose Gas", *J. Phys. B: At. Mol. Opt. Phys.* 41 (2008) 135302.

[40] A. Arrizabalaga, J. Smit and A. Tranberg, "Equilibration in φ^4 Theory in $3+1$ Dimensions", *Phys. Rev. D* 72 (2005) 025014.

[41] A. Rey et al., "Nonequilibrium Dynamics of Optical-Lattice-Loaded Bose-Einstein-Condensate atoms: Beyond the Hartree-Fock-Bogoliubov approximation", *Phys. Rev. A* 69 (2004) 033610.

[42] A. Rey et al., "Quantum Kinetic Theory of a Bose-Einstein Gas Confined in a Lattice", *Phys. Rev. A* 72 (2005) 023604.

[43] M. Imamovic-Tomasovic and A. Griffin, "Coupled Hartree-Fock-Bogoliubov Kinetic Equations for a Trapped Bose Gas", *Phys. Rev. A* 60 (1999) 494.

[44] M. Trujillo-Martinez, A. Posazhennikova and J. Kroha, "Nonequilibrium Josephson Oscillations in Bose-Einstein Condensates without Dissipation", *Phys. Rev. Lett.* 103 (2009) 105302.

[45] L. Pitaevskii and S. Stringari, *Bose-Einstein Condensation*, 1st ed., Oxford University Press, 2003.

[46] H. Stoof, K. Gubbels and D. Dickerscheid, *Ultracold Quantum Field*, 1st ed., Springer, 2009.

[47] M. Imamovic-Tomasovic and A. Griffin, "Quasiparticle Kinetic Equation in a Trapped Bose Gas at Low Temperatures", *J. Low. Temp. Phys.* 122 (2001) 617.

[48] T. Kirkpatrick and J. Dorfman, "Transport in a Dilute but Condensed Nonideal Bose Gas: Kinetic Equations", *J. Low. Temp. Phys.* 58 (1985) 301.

[49] H. Stoof, "Coherent Versus Incoherent Dynamics During Bose-Einstein Condensation in Atomic Gases", *J. Low. Temp. Phys.* 114 (1999) 11.

[50] B. Josephson, "Possible New Effects in Superconductive Tunnelling", *Phys. Lett.* 1 (1962) 251.

[51] S. Pereverzev et al.,
"Quantum Oscillations Between Two Weakly Coupled Reservoirs of Superfluid ^{3}He",
Nature 388 (1997) 449.

[52] K. Sukhatme et al., "Observation of the Ideal Josephson Effect in Superfluid ^{4}He",
Nature 411 (2001) 280.

[53] J. Javanainen,
"Oscillatory Exchange of Atoms Between Traps Containing Bose Condensates",
Phys. Rev. Lett. 57 (1986) 3164.

[54] M. Albiez et al., "Direct Observation of Tunneling and Nonlinear Self-Trapping in a Single Bosonic Josephson Junction", *Phys. Rev. Lett.* 95 (2005) 010402.

[55] S. Levy et al., "The a.c. and d.c. Josephson Effects in a Bose–Einstein Condensate",
Nature 449 (2007) 579.

[56] L. J. LeBlanc et al., "Dynamics of a Tunable Superfluid Junction",
Phys. Rev. Lett. 106 (2011) 025302.

[57] L. Radzihovsky and V. Gurarie, "Relation Between ac Josephson Effect and Double-Well Bose-Einstein-Condensate Oscillations", *Phys. Rev. A* 81 (2010) 063609.

[58] I. Zapata, F. Sols and A. Leggett,
"Josephson Effect Between Trapped Bose-Einstein Condensates",
Phys. Rev. A 57 (1998) 28.

[59] I. Zapata, F. Sols and A. Leggett,
"Phase Dynamics After Connection of Two Separate Bose-Einstein Condensates",
Phys. Rev. A 67 (2003) 021603.

[60] R. Gati et al.,
"Realization of a single Josephson junction for Bose–Einstein condensates",
Appl. Phys. B 82 (2006) 207.

[61] S. Hofferberth et al.,
"Non-Equilibrium Coherence Dynamics in One-Dimensional Bose Gases",
Nature 449 (2007) 324.

[62] A. Smerzi et al., "Quantum Coherent Atomic Tunneling Between Two Trapped Bose-Einstein Condensates", *Phys. Rev. Lett.* 79 (1997) 4950.

[63] S. Raghavan et al.,
"Coherent Oscillations Between Two Weakly Coupled Bose-Einstein Condensates: Josephson Effects, π Oscillations, and Macroscopic Quantum Self-Trapping",
Phys. Rev. A 59 (1999) 620.

[64] D. Ananikian and T. Bergeman, "Gross-Pitaevskii equation for Bose particles in a double-well potential: Two-mode models and beyond", *Phys. Rev. A* 73 (2006) 013604.

[65] G. J. Milburn et al.,
"Quantum dynamics of an atomic Bose-Einstein condensate in a double-well potential",
Phys. Rev. A 55 (1997) 4318.

[66] T. Schumm et al., "Matter-Wave Interferometry in a Double Well on an Atom Chip",
Nature Physics 1 (2005) 57.

[67] G.-B. Jo et al., "Long Phase Coherence Time and Number Squeezing of Two Bose-Einstein Condensates on an Atom Chip", *Phys. Rev. Lett.* 98 (2007) 030407.

[68] C. Gross et al., "Nonlinear atom interferometer surpasses classical precision limit", *Nature* 464 (2010) 1165.

[69] A. Ramanathan et al., "Superflow in a Toroidal Bose-Einstein Condensate: An Atom Circuit with a Tunable Weak Link", *Phys. Rev. Lett.* 106 (2011) 130401.

[70] A. Chikkatur et al., "A Continuous Source ofBose-Einstein Condensed Atoms", *Science* 296 (2002) 2193.

[71] W. Yi and L.-M. Duan, "Adiabatic and nonadiabatic merging of independent Bose-Einstein condensates", *Phys. Rev. A* 71 (2005) 043607.

[72] H. Xiong, S. Liu and M. Zhan, "Josephson effect and quantum merging of two Bose superfluids", *Phys. Rev. B* 73 (2006) 224505.

[73] F. Dalfovo et al., "Theory of Bose-Einstein condensation in trapped gases", *Rev. Mod. Phys.* 71 (1999) 463.

[74] F. Schwabel, *Quantum Mechanics*, 4th ed., Springer, 2007.

[75] G. Aarts and J. Berges, "Nonequilibrium Time Evolution of the Spectral Function in Quantum Field Theory", *Phys. Rev. D* 64 (2001) 105010.

[76] J. Berges and J. Cox, "Thermalization of Quantum Fields from Time-Reversal Invariant Evolution Equations", *Phys. Lett. B* 517 (2001) 369.

[77] D. van Oosten, P. van der Straten and H. Stoof, "Quantum Phases in an Optical Lattice", *Phys. Rev. A* 63 (2001) 053601.

[78] M. Fisher et al., "Boson Localization and the Superfluid-Insulator Transition", *Phys. Rev. B* 40 (1989) 546.

[79] D. Jaksch et al., "Cold Bosonic Atoms in Optical Lattices", *Phys. Rev. Lett.* 81 (1998) 308.

[80] S. Fölling et al., "Formation of Spatial Shell Structure in the Superfluid to Mott Insulator Transition", *Phys. Rev. Lett.* 97 (2006) 060403.

[81] G. Campbell et al., "Imaging the Mott Insulator Shells by Using Atomic Clock Shifts", *Science* 313 (2006) 649.

[82] G. G. Batrouni et al., "Mott Domains of Bosons Confined on Optical Lattices", *Phys. Rev. Lett.* 89 (2002) 117203.

[83] S. Peil et al., "Patterned Loading of a Bose-Einstein Condensate into an Optical Lattice", *Phys. Rev. A* 67 (2003) 051603.

[84] E. Calzetta and B. Hu, "Closed-Time-Path Functional Formalism in Curved Spacetime: Application to Cosmological Back-Reaction Problems", *Phys. Rev. D* 35 (1987) 495.

[85] S. Ramsey and B. Hu, "$O(N)$ Quantum Fields in Curved Spacetime", *Phys. Rev. D* 56 (1997) 661.

[86] E. Calzetta and B. Hu, "Dissipation of Quantum Fields from Particle Creation", *Phys. Rev. D* 40 (1989) 656.

[87] L. Delves and J. Mohamed, *Computational Methods for Integral Equations*, 1st ed., Cambridge University Press, 1985.

List of Figures

List of Tables

Acronyms

2PI Two-Particle-Irreducible. 18

BEC Bose-Einstein-Condensate. 1–3, 41–43, 46, 50, 51, 53, 59–62, 65, 66, 69–72, 75, 87, 96–99, 102, 109, 125, 139, 140

BHF Bogoliubov-Hartree-Fock. 18, 19, 22–27, 29, 31, 37, 55–57, 59, 66, 67, 69, 71, 84, 96, 97, 99, 103, 109–114, 125, 139

CTP closed time path contour. 6, 7, 10, 14, 53, 80, 119

DNLSE discrete non-linear Schrödinger equation. 83

GPE Gross-Pitaevskii-equation. 21, 22, 24, 26, 30, 32, 34, 39, 43, 52, 86, 114, 121

IPDE integro-partial-differential-equations. 11, 20, 31, 33, 121

PHF Popov-Hartree-Fock. 26

QBE Quantum-Boltzmann equation. 33, 34

SQUID superconducting quantum interference device. 43

TSBH two-site Bose-Hubbard model. 43, 44, 61, 75, 80, 87, 96–98, 140

ZNG Zeremba-Nikuni-Griffin equation. 38, 40

Acknowledgements

There is an extend list of people I would like to thank for their different contributions to my work. First of all, I would like to mention and thank Hans Kroha for accepting me in his research group and assigning me this interesting topic for my PhD. I have to consider me lucky for having the possibility to work together with Anna Posazhennikova. Their advice and patience made the present work possible. I would like to thank Prof. Corinna Kollath for reviewing this manuscript. Hans' research group deserves special thanks for the pleasant working atmosphere. I thank Roman Katzer and Katinka Ballmann for carefully reviewing parts of this manuscript and for their helpful recommendations. I also would like to mention and thank Patricia Zündorf, Dagmar Faßbender, Petra Weiß, Christa Börsch and Andreas Wißkirchen for helping me with bureaucratic issues. Andreas deserves additional thanks for taking care of the computer related stuff. I also would like to thank the Bonn-Cologne Graduate School of Physics and Astronomy for giving me the opportunity to travel abroad and attend conferences, which promoted the exchange with other scientists. I am very thankful to Emmi, Barbara, Brigitte and Ulrich Real for all the support since my arrival in Germany. And finally, I thank Chela, Fabio, Camilo, Maria Luisa, Nene, Yoya and Aura for believing in me and for every effort in letting me get closer to my goals - *Muchas Gracias*.